A Global Finite Element Model for Glacial Isostatic Adjustment with 3D Non-Linear Viscosity

Blank, B.

Important note
To cite this publication, please use the final published version (if applicable).
Please check the document version above.

A Global Finite Element Model for Glacial Isostatic Adjustment with 3D Non-Linear Viscosity

Bas Blank

A Global Finite Element Model for Glacial Isostatic Adjustment with 3D Non-Linear Viscosity

ii

A Global Finite Element Model for Glacial Isostatic Adjustment with 3D Non-Linear Viscosity

Proefschrift

ter verkrijging van de graad van doctor aan de

Technische Universiteit Delft,

op gezag van de Rector Magnificus, prof. dr.ir. T.H.J.J. van der Hagen,

voorzitter van het College voor Promoties,

in het openbaar te verdedigen op

Dinsdag, 25 maart 2025 om 12:30 uur

door

Bas BLANK

Master of Science in Lucht- & Ruimtevaarttechniek

Technische Universiteit Delft, Nederland

geboren te Leidschendam, Nederland

Dit proefschrift is goedgekeurd door de promotoren.

Samenstelling promotiecommissie bestaat uit:

Rector Magnificus, voorzitter

Promotor: Dr.ir. W. van der Wal	Delft University of Technology
Promotor: Prof. dr. L.L.A Vermeersen	Delft University of Technology

Onafhankelijke leden:

Prof.dr.ir. P.N.A.M. Visser	Delft University of Technology
Dr. R.E.M. Riva	Delft University of Technology
Prof.dr.ir. F.C. Vossenpoel	Delft University of Technology
Prof.dr. G. Spada	University of Bologna, Italië
Dr. G.A. Nield	Durham University, VK

Contents

Summary

Glacial isostatic adjustment (GIA) is the phenomenon where the solid Earth responds to ice shelves that grow or shrink. As the weight of an ice shelf on the Earth reduces, the Earth rebounds in that location and gravity increases. This rebound process has an instant component, elastic rebound, but also a delayed component as the mantle material slowly flows to a new equilibrium position with timescale determined by the mantle viscosity. GIA affects both the vertical land motion (VLM) and therefore relative sea level (RSL). When predicting sea-level change in the near-future ice mass and sea level changes need to be monitored. However, measurements of current ice mass change are obscured by uplift and gravity changes due to GIA. With a large portion of the world population and economic activity located in coastal areas it is important to monitor sea-level rise and therefore to understand the GIA contribution to sea level rise itself and measurements of the processes.

To understand GIA, accurate models are required. Traditionally GIA models have assumed that Earth mantle parameters only vary with depth, these models are known as 1D models. However, we know from seismic tomographic studies and surface geology that mantle parameters also vary with location, or laterally. In the last few decades GIA models have been developed that can adopt lateral variation in Earth parameters, so-called 3D models. In this thesis we present a global 3D model that is based on the commercial finite element method (FEM) software package ABAQUS.

A benefit of the ABAQUS based (or other FEM software, such as CITCOM) 3D model is that it allows for flexibility in the rheology type, for example, non-linear rheology can be used, in which effective viscosity depends on stress. Non-linear rheology is seen in laboratory experiments and will result in changes in viscosity over time for areas with rapid changes in glacial loads. Non-linear rheology can also cause the effective viscosity to change depending on the background stress present, and keeping the model global allows us to introduce long term GIA global background stress to local and short-term cases.

By converting the seismic wave speed anomalies to viscosity anomalies, a 3D linear rheology can be created. In combination with a depth dependent background viscosity, a seismic model such as SMEAN2 can be converted to mantle viscosity maps. Non-linear rheology based on olivine flow laws is also implemented in our 3D GIA model. A temperature profile of the mantle, as for example given in WINTERC-G, in combination with a flow law and material parameters grain size and the water content in the mantle is converted to diffusion and dislocation parameters. The effective viscosity of an element in the model depends on both of these parameters and the equivalent stress. Due to a specified high-resolution area that was created in the mesh, the model can achieve grid-size of 20-40 km for a designated study area. This is a stark improvement on other models based on ABAQUS that reached grid-sizes of approximately 55 km (Li et al., 2020; Zhong et al., 2022). In part due to a high-resolution

area that can be set for any area, the model has achieved greater flexibility. As such the model can be used for small study areas as well as large areas, something that previously required separate dedicated models. The mesh for the sea level and the FEM model are independent from one another, allowing for lower resolutions for either depending on the study case.

The Amundsen Sea Embayment (ASE) is a relatively small region in West-Antarctica with sparse data coverage. The region is losing mass faster than almost any other region and shows large VLM due to ice sheet loss in the last century. In Barletta et al. (2018) a GIA estimate is found by fitting 1D model with varying upper mantle viscosities to the measured VLM. In this study we show that when estimating average mantle viscosities, a 1D model would suffice for the ASE as the effect of 3D rheology is too small and the data too scarce to distinguish the 3D model from a model with 1D viscosity. For the GIA signal itself however there is a notable difference between 1D and 3D models for the ASE, especially when the stress dependent non-linear rheology is used. Due to the higher stress due to rapid deglaciation in the last decades, the uplift at the point of rapid deglaciation is larger than previously considered. This would mean that the local ice mass loss obtained after correcting with 3D GIA models might also be larger than what is obtained after correcting with simpler GIA models. An important question when using non-linear rheology is not only how much stress from the process itself influences the process, but also background stresses. The fact that we used a global model means that we can incorporate the last glacial cycle and hence its background stress as it contributes to the recent relaxation in the ASE. This revealed that the uplift pattern as observed from the data could only be matched with low local viscosity or a strong non-linear effect. Using rheological parameters with a higher average viscosity and limited non-linear effect would result in an excess of background stress lingering in the upper mantle that would prevent any reproduction of the observed uplift.

In contrast to the ASE, Europe is a large region with far more available VLM and RSL data. Europe also experiences GIA due to the deglaciation of Scandinavia and Northern Britain and meltwater filling the North Sea and Baltic Sea from glaciers and ice shelves from all over the world. Tomographic studies have identified a cold mantle underneath Eastern Europe and Eastern Scandinavia and warmer mantle underneath Britain and western Europe. This difference between the mantle in Eastern and Western Europe is not identified by 1D GIA models, as these models converge to mantle viscosities close to the global average of $0.5 \cdot 10^{21}$ Pa·s. RSL data is available from all of Europe's northern coastline and some offshore regions, and VLM data from Northern Europe. Using all this data, we investigated whether a distinct 3D signal can be observed in the combined dataset, and if individual regions would preference different rheology settings when evaluating them separately. The closest fit is obtained using the 1D model VM5a in combination with the ICE-6G ice history which is unsurprising as ICE-6G is created together with VM5a. Nonetheless the fit to data in eastern Scandinavia improved with 3D models compared to VM5a. Moreover, when ice histories were used that were developed somewhat independently from 1D Earth models, we found that 3D models

did improve the overall fit to the data as well. In these best fitting models Britain and the North Sea area have upper mantle viscosities that are likely close to the global average of 0.5 10^{21} Pa·s (0.53 10^{21} Pa·s and 0.5 10^{21} Pa·s for the shallow and deeper upper mantle respectively), data in Scandinavia tended to favor higher viscosities (4.9 10^{21} Pa·s and 1.3 10^{21} Pa·s for the shallow and deeper upper mantle respectively), which is in contrast to 1D models that did not find these differences in mantle viscosity between Eastern and Western Europe. Models with high average elastic (100-160 km) lithosphere thickness also fit Scandinavia well. Furthermore, while wet rheology seemed possible for the British Isles, it could be ruled out for Scandinavia, which is consistent with petrological findings from xenoliths.

Aside from the studies performed in the context of this thesis, this thesis contributed to applications of the model in other studies as well. The North Sea area was more closely examined in a separate study. As part of this study, we utilized the flexible mesh to change the size and study area to a grid resolution of ~25 km, showing the flexibility of the mesh. We compared our model results with a 1D model and again affirmed that for the North Sea itself 3D rheology does not improve the fit to local RSL data. This in itself questions interpretation of seismic tomography-based findings, such as in WINTERC 5.2 that have identified seismic wave speed anomalies and thus temperature anomalies underneath the North Sea. The modular nature allows for parts of the model to be used in other studies. The self-gravitation was implemented in a Python routine and used in a post-seismic study of Nield et al. (2022). Because of the versatility the model has been coupled to other physical process models. As such, the work in this thesis enabled first steps to be made to expand the model through collaboration to include polar wander and in a separate study to include mantle dynamics. The use of ABAQUS CAE provides for the RESTART option, which allows the problem to be solved incrementally so that polar wander can be calculated simultaneously with GIA. Additionally, a model was created that incorporated pre-stresses on a small scale using the high-resolution region (with a grid resolution of 25 km) of the model in this thesis. This model could be expanded to include mantle convection induced stresses when coupled with a mantle convection model, where smaller scale features such as plumes can be incorporated. The GIA model has been successfully coupled to an ice evolution model as well to investigate the cryosphere solid Earth interaction when non-linear rheology is included. Here the finer mesh for the sea level equation proved to be an advantage as the sea level equation and thus the grounding line of an ice shelf can be resolved to a higher degree than what the FEM model allowed. The grounding line must be calculated to a high degree of accuracy. In van Calcar et al. (2023) a resolution of 15-30 km was found to be the point where solutions sufficiently converged. In both cases this is far below the 55 km grid resolution, recent ABAQUS based FEM models were able to achieve.

In conclusion, we have shown that the model in this thesis is a flexible model that can be tailored to different study areas as well as be expanded to include different physical processes, such as ice evolution or rotation dynamics. We have used this flexibility ourselves to focus on the ASE and Europe to investigate whether 3D rheology would

lead to different uplift and uplift patterns than 1D models and whether these differences can be detected in the observations. For both of these areas we concluded that 3D can make a difference and the 3D effect can neither be replicated by a single 1D model nor a combination of multiple 1D models, meaning that heterogeneity in the Earth's mantle leads to unique GIA signature, more so than previously assumed.

This means that the GIA dependent estimates such as current ice mass loss or future sea level rise might be less certain than previously thought. Non-linear rheology has shown to localize GIA more than estimated with 1D models. If such a model is used to correct ice mass losses, this leads to an underestimation of both ice mass loss over the last years as well as a slight underestimation of the mass component when forecasting sea level rise. For the ASE non-linear rheology based GIA estimates are to be taken into account, although increased GPS data acquisition the ASE and surrounding regions might be vital to more accurately determine the local rheology parameters in the mantle. For Europe a dry highly viscous mantle, devoid of non-linear effects, should be considered underneath Scandinavia, while a mantle viscosity closer to the global average, possibly with a non-linear component, should be considered for Western Europe

We believe that improvements in both models as well as data acquisition are required to increase the accuracy of the GIA signal in the future. Ice histories based on 3D rheology are necessary to determine the 3D effect independently from 1D assumptions. Models with updated flow laws for non-linear rheology, compressibility and more calibrated methods to convert seismic wave speed to viscosity will improve the ability to model the actual structure, resulting in solutions with a higher accuracy and increased knowledge on the Earth's mantle structure.

Samenvatting

Postglaciale opheffing, *Engels: Glacial isostatic adjustment (GIA)*, is het fenomeen waar de Aarde vervormt als gevolg van het ontstaan en verdwijnen van ijskappen. Wanneer het gewicht van een smeltende ijskap op de Aarde afneemt, veert de Aarde terug omhoog en neemt lokaal de zwaartekracht toe. Een deel van dit terugveren gebeurt direct, elastische terugvering, maar de terugvering bevat ook een vertraagde component as gevolg van mantelmateriaal dat langzaam stroom naar een nieuwe evenwichtspositie. De tijdschaal waarop dit gebeurt wordt bepaald door de viscositeit van de mantel. GIA heeft effect op de verticale grondbeweging, *Engels: vertical land motion (VLM)*, en daardoor ook op de relatieve zeespiegel, *Engels: relative sea level (RSL)*. Wanneer we zeespiegelstijgingen voor de nabije toekomst willen voorspellen moeten de huidige zeespiegelstijgingen en veranderingen in de ijskappen nauwlettend gemonitord worden. Echter, het meten van de huidige veranderingen in de ijskappen wordt bemoeilijkt doordat opvering en zwaartekrachtveranderingen als gevolg van GIA de werkelijke veranderingen van de ijsmassa verhullen. Gegeven dat een groot deel van de wereldbevolking en de globale economische nijverheid zich bevinden in kustgebieden is het van belang om de zeespiegelstijging in de gaten te houden. Daarom is het dus belangrijk de GIA-bijdrage en de metingen hiervan goed in kaart te brengen.

Om GIA te begrijpen zijn nauwkeurige modellen nodig. Van oudsher is het gebruikelijk dat in GIA-modellen wordt aangenomen dat de mantelparameters alleen in de diepte richting veranderen, zogenaamde 1D modellen. Echter, we weten inmiddels dankzij seismische tomografie studies en geologie dat de mantelparameters ook van de locatie afhangen, ook wel laterale verschillen genoemd. In de laatste paar decennia zijn er ook GIA-modellen ontwikkeld waarin laterale verschillen in mantelparameters zijn geïmplementeerd, zogenaamde 3D modellen. In deze dissertatie presenteren we een globaal 3D model dat gebaseerd is op het commerciële softwarepakket ABAQUS, een eindige elementen methode, *Engels: finite element method (FEM)*.

Een voordeel van op ABAQUS (of andere FEM-programma's, zoals CITCOM) gebaseerde 3D modellen is dat ze een flexibiliteit verschaffen wat betreft de gekozen reologie. Hierdoor kan niet-lineaire reologie gebruikt worden, waarbij de effectieve viscositeit afhangt van de spanning. Niet-lineaire reologie is aangetoond in laboratoriumexperimenten en zal als gevolg hebben dat in gebieden waar er plotselinge grote veranderingen in de ijslading plaats vinden, de effectieve viscositeit zal variëren over de tijd. Niet-lineaire reologie kan ook zorgen voor veranderingen in effectieve viscositeit afhankelijk van achtergrondspanning in de mantel. Omdat het model globaal is, zijn we hierdoor ook in staat globale spanningen te introduceren als gevolg van lange termijn GIA voor lokale korte termijn GIA-situaties.

Wanneer we anomalieën in de seismische golfsnelheid omzetten naar anomalieën in viscositeit zijn we in staat een 3D lineaire reologie te construeren. In combinatie met een achtergrond viscositeit kunnen seismisch modellen zoals SMEAN2 omgezet worden naar een 3D mantel viscositeit. Niet-lineaire reologie gebaseerde stromingswetten vastgesteld voor olivijn, zijn geïmplementeerd in ons 3D GIA-model. Een temperatuur profiel zoals bijvoorbeeld gegeven wordt in WINTERC-G, in combinatie met een stromingswet en de materiaalparameters korrelgrootte en hoeveelheid water in de mantel, worden omgezet in diffusie- en dislocatieparameters. De effectieve viscositeit in een element in het model hangt af van deze beide parameters en de equivalente spanning. Door middel van een gespecificeerd hoge resolutie gebied in de mesh van het model, kan het model lokaal een gridgrootte van 20 km bereiken voor specifieke onderzoeksgebieden. Dit is een sterke verbetering ten opzichte van andere op ABAQUS gebaseerde modellen die gridgroottes van 55 km haalden (Li et al., 2020; Zhong et al., 2022). Mede dankzij het hoge resolutie gebied dat toegepast kan worden op ieder gebied, heeft het model een grotere mate van flexibiliteit gekregen. Zodoende kan het model zowel gebruikt worden voor kleine gebieden evenals grote gebieden, iets wat voorheen aparte gespecialiseerde modellen vereiste. De mesh voor het zeeniveau en het FEM-model zelf zijn onafhankelijk van elkaar, waardoor beide in resolutie verlaagd zouden kunnen worden mocht dat in een specifiek geval beter passen.

De Amundsenbaai, *Engels: Amundsen Sea Embayment (ASE)*, is een relatief kleine regio in West-Antarctica met een beperkt aantal metingen. De regio verliest massa in een tempo dat bijna ongeëvenaard wordt door welke andere regio dan ook en ervaart grote verticale grondbeweging als gevolg van de ijskappen die daar gedurende de laatste eeuw zijn geslonken. In Barletta et al. (2018) wordt een GIA-schatting op basis van de gemeten verticale grondbeweging gegeven door middel van het variëren van de bovenmantel in een 1D model. In ons onderzoek tonen we aan dat een 1D model volstaat voor de ASE omdat het effect van 3D reologie te klein is om in de beperkte dataset significant te onderscheiden van een model met 1D viscositeit. In het gemodelleerde GIA-signaal zelf is echter een duidelijk verschil te zien tussen 1D en 3D modellen in de ASE, zeker wanneer spanningsafhankelijke niet-lineaire reologie wordt gebruikt. Vanwege de verhoogde spanning, die het gevolg is van het snelle verdwijnen van de ijskappen in de laatste decenia, zal de verticale grondbeweging op het punt waar het meeste ijs is verdwenen een stuk hoger zijn dan tot nu toe wordt aangenomen. Dit betekent dat het lokale ijsmassaverlies dat overblijft na een GIA-correctie op basis van 3D modellen groter is dan wanneer we de correctie toepassen op basis van simpelere GIA-modellen. Een belangrijke vraag wanneer je niet-lineaire reologie toepast is niet alleen hoeveel spanning van het proces zelf effect heeft maar ook hoe de achtergrondspanning effect heeft op het proces. Het feit dat we een globaal model gebruiken betekent dat we de laatste glaciale cyclus in het model kunnen toevoegen en dus ook de achtergrondspanning die daaruit voortkomt en hoe deze bijdraagt aan de recente terugvering in de ASE. Dit heeft aangetoond dat de

terugveringspatronen die we in de data zien alleen reproduceerbaar zijn met lokale lage viscositeit of een sterk niet-lineair effect. Wanneer we reologieparameters zouden gebruiken met een gemiddeld hogere viscositeit en beperkte niet-lineaire effecten zou een overmaat aan in de mantel aanwezige achtergrondspanning het reproduceren van de geobserveerde opveringspatronen voorkomen.

In tegenstelling tot de ASE, is Europe een veel groter gebied veel meer beschikbare VLM- en RSL-data. Europa ondervindt ook GIA als gevolg van de verdwenen ijskappen in Scandinavië en het noorden van Groot-Brittannië. Verder vult smeltwater van ijskappen en gletsjers over de hele wereld de Noordzee en Baltische Zee. Tomografische studies hebben geïdentificeerd dat er een koude mantel aanwezig is onder Oost-Europa en Oost-Scandinavië en een warmere mantel onder Groot-Brittannië en West-Europa. Dit verschil tussen de mantel in Oost- en West-Europa komt echter niet naar voren in 1D GIA-studies. GIA-studies over Europa vinden een viscositeit van ongeveer het globale gemiddelde van 0.5 10^{21} Pa·s. Voor de gehele Europese Noordkust en zelfs gebieden in de Noordzee is er RSL-data beschikbaar, en VLM-data is beschikbaar voor een groot deel van Noord-Europa. Gebruikmakend van al deze data onderzochten we of we een duidelijk signaal van 3D reologie konden ontdekken in de gecombineerde dataset, en of individuele regio's voorkeuren zouden laten zien voor verschillende reologieparameters wanneer we ze afzonderlijk evalueren. De beste overeenkomst met de data is gevonden door gebruik te maken van het 1D model VM5a in combinatie met de ICE-6G ijshistorie, wat op zich niet verrassend is omdat de ijshistorie ICE-6G is gecreëerd in combinatie met VM5a. Desalniettemin blijkt dat de fit ten opzichte van de data verbetert in Oost-Scandinavië als 3D modellen gebruikt worden in plaats van VM5a. Bovendien, wanneer ijshistories gebruikt worden die onafhankelijk van VM5a zijn ontwikkeld, zien we dat 3D modellen een algehele verbetering in de fit laten zien. In de best-fittende modellen vinden we voor het Noordzeegebied en Groot-Brittannië een viscositeit dicht bij het globale gemiddelde van 0.5 10^{21} Pa·s (0.53 10^{21} Pa·s en 0.50 10^{21} Pa·s voor de ondiepe en diepere bovenmantel respectievelijk), maar dat de data in Scandinavië een voorkeur toont voor hogere viscositeiten (4.9 10^{21} Pa·s en 1.3 10^{21} Pa·s voor de ondiepe en diepere bovenmantel respectievelijk). Dit staat haaks op bevindingen van 1D modellen die tussen Groot-Brittannië en Scandinavië geen verschillen vinden. Modellen met een hoge gemiddelde elastische lithosfeer dikte (100-160 km) passen ook goed voor Scandinavië. Verder blijkt dat natte reologie mogelijk is voor Groot-Brittannië maar kan worden uitgesloten voor Scandinavië, wat consistent is met petrologische bevindingen op basis van xenolieten.

Buiten de studies die gedaan zijn in de context van deze dissertatie, heeft het werk uit deze dissertatie ook een belangrijke bijdrage kunnen leveren aan andere studies. Het Noordzeegebied is specifieke onderzocht in een aparte studie bijvoorbeeld. As onderdeel van deze studie hebben we de flexibele mesh veranderd zodat het een grid-grootte had van ~25 km over het Noordzeegebied. Dit onderstreept nogmaals de flexibiliteit die de huidige mesh-opzet biedt. We vergeleken onze modelresultaten met

de resultaten van 1D modellen en bevestigen nogmaals dat voor het Noordzeegebied zelf, 3D reologie de fit ten opzichte van RSL-data niet verbeterd. Dit op zichzelf roept vragen op over de interpretatie van seismische tomografie, zoals in WINTERC 5.2, die anomalieën in seismische golfsnelheden onder de Noordzee interpreteren als temperatuurverschillen. Het modulaire karakter van het model zorgt ervoor dat onderdelen gebruikt kunnen worden in andere studies. De zelfgravitatie is in een PYTHON routine gebouwd die vervolgens ook gebruikt is in Nield et al. (2022). Vanwege de veelzijdigheid, is het model ook gekoppeld aan andere fysieke processen. In die context heeft het werk in deze dissertatie geleid tot de eerste stappen van het uitbreiden van het model in samenwerkingsverband om poolvlucht en manteldynamica er in aparte onderzoeken in te voegen. Omdat ABAQUS CAE wordt gebruik, kan gebruik gemaakt worden van de RESTART optie, die er voor zorgt dat het probleem stap voor stap opgelost kan worden zodat het oplossen van de poolbeweging gelijktijdig met het oplossen voor GIA kan gebeuren. Er is ook een model ontwikkeld waar de voorspanningen in een kleine regio ingevoerd kunnen worden dankzij het hoge resolutie gebied (grid-grootte van 25 km) dat voor het model in deze dissertatie is ontwikkeld. Dit model kan uitgebreid worden zodat spanning die door mantelconvectie ontstaan ingevoegd kan worden. Het gevolg is dat het model uit deze dissertatie dan gekoppeld zou kunnen worden met een mantelconvectie model zodat kleinere mantelkenmerken zoals pluimen toegevoegd kunnen worden. Het GIA-model is inmiddels ook al succesvol gekoppeld aan een ijsevolutie model om de interactie te onderzoeken tussen aardmechanica en de cryosfeer als niet-lineaire reologie wordt gebruikt. In dit geval is de fijnere mesh voor de zeeniveau vergelijking een voordeel omdat het zeeniveau en dus de aardingslijn van een ijskap met een hogere resolutie gevonden lan worden dan wat met het FEM-model zou kunnen. De aardingslijn moet met een hoge mate van precisie berekend worden. In van Calcar et al. (2023) wordt aangegeven dat een resolutie van 15-30 km goed genoeg zou moeten zijn om een oplossing te vinden die in voldende mate geconvergeerd is. In beide gevallen zou een resolutie van ~55 km, zoals bij eerdere ABAQUS gebaseerde FEM-modellen het geval is, te kort schieten.

We kunnen concluderen dat het model in deze dissertatie een flexibel model is dat aangepast kan worden voor verschillende onderzoeksgebieden en uitgebreid kan worden om verschillende fysieke processen mee te nemen, zoals ijsevolutie of rotatiedynamica. We hebben zelf deze flexibiliteit gebruikt om ons te focussen op zowel de ASE als Europa om te onderzoeken of 3D reologie leidt tot andere landbewegingen en opveringspatronen ten opzichte van 1D modellen en of we deze verschillen kunnen waarnemen in de data. Voor beide gebieden kunnen we concluderen dat 3D een duidelijk verschil kan maken en dat het 3D effect niet met een enkel 1D model of een combinatie van 1D modellen kan worden nagebootst. Dit betekent dat de heterogeniteit in de mantel van de Aarde leidt tot een uniek GIA-signaal, meer nog dan eerder werd aangenomen.

Dit betekent dat op GIA gebaseerde schattingen zoals het hedendaagse ijsmassa verlies of de toekomstige zeespiegelstijging wellicht minder zeker zijn dan eerder aangenomen. Voor niet-lineaire reologie is aangetoond dat het GIA meer lokaliseert dan 1D-model gebaseerde schattingen laten zien. Als zo'n 1D model gebuikt wordt om het ijsverlies te corrigeren leidt dit tot een onderschatting van zowel het verlies in ijsmassa van de afgelopen jaren en een kleine onderschatting van de massacomponent in voorspelingen van de zeespiegelstijging. Voor de ASE moet niet-lineaire reologie gebaseerde GIA-schattingen meegenomen worden, alhoewel een toename aan GPS-metingen in de ASE en aangrenzende gebieden nodig is om de lokale mantelparameters met een hogere precisie te kunnen bepalen. Voor Europa moet een droge en hoog viskeuze mantel gebruikt worden onder Scandinavië terwijl een mantel met een viscositeit dichtbij het mondiaal gemiddelde, mogelijk met een niet-lineaire component, gebruikt moet worden voor West-Europa.

Wij zijn van mening dat verbeteringen in zowel modellen als datavergaring nodig zijn om de precisie van het GIA-signaal in de toekomst te kunnen verbeteren. IJshistories gebaseerd op 3D reologie zijn nodig om het 3D effect onafhankelijk van 1D aannames te kunnen vaststellen. Modellen met geüpdatete stromingswetten voor niet-lineaire reologie, compressibiliteit en beter gekalibreerde methodes om seismische golf anomalieën om te zetten naar viscositeit zullen zorgen dat de daadwerkelijke aardstructuren beter gemodelleerd kunnen worden. Het gevolg zal zijn dat we GIA-oplossingen vinden met een hogere precisie en we meer te weten zullen komen over de opmaak van de mantel van de Aarde.

Chapter *1*

Introduction

Bas Blank[1]

1) Delft University of Technology, Delft, Netherlands

Introduction

In the early 1700's the Swedish government was faced with complaints from fish communities on the Baltic Sea shore that they had to keep moving their docks every few years. The fishing communities believed the water level in the Baltic Sea was dropping (Ekman, 2016). The Swedish government tasked the renowned scientist Anders Celsius to investigate the phenomenon. Celsius went around the shores of the Baltic Sea inquiring about the flat stones that seals could be seen resting on just above the waves and asked when the seals moved to new stones. From this, Celius deduced that the sea level in the Baltic must be dropping at a rate of 1.4 cm/y. To later validate these findings, Celsius marked a stone in Lövgrund at the height of the current sea level in 1731. It later turned out that Celsius' estimation was only a bit off; we now know the Baltic Sea level drop near the Celsius stone is about 1 cm/y.

We now understand what caused the apparent sea level drop that Celsius observed. When the ice cap in Scandinavia receded, the local force on the Earth's crust and mantle was removed and the pressure inside the Earth around the ice-covered region pushed mantle material back underneath the location of the receded ice cap. This causes local land uplift and is called glacial isostatic uplift (GIA). As water will simply flow away when land is elevated, the sea level of the Baltic Sea effectively dropped as observed by Celsius. Thus, GIA causes sea level change because the land moves up or down. However, GIA also affects sea level because it induces changes in the gravitational field. The movement of mantle mass changes the Earth's gravitational field and with it the geoid, the gravitational equipotential surface that the Earth's oceans surface would conform to in the absence of other forces such as tides and winds. The difference between this surface and local bathymetry is the ocean depth, and changes to that depth compared to present day ocean depth what is known as relative sea level (RSL).

Coastal towns and cities in Europe and in the rest of the world are still threatened by changing sea levels. With 600 million people living in these areas (Nicholls & Cazenave, 2010) policy makers and engineers need to know how much the sea level change will be. The vertical land motion and in particular the GIA contribution to sea level to it is significant in many parts of the world. The GIA effect is not as straightforward as when land simply moves up where ice was located. Around the deflected crust a bulge of pushed away mantle material will form. This forebulge will start to collapse when deglaciation occurs. At the same time rising sea levels will increase pressure on the crust, especially on locations where the coastlines have shifted due to sea level rise.

Celsius' investigation was arguably the first time there had been a scientific inquiry into rising sea level. Today sea level is measured at many locations in the world. One of the ways to measure sea level changes during history is through archeological measurements. By dating marine fossils, a range for the sea level height at a specific time can be constructed (Muhs et al., 2014; Thompson et al., 2011; Ward et al., 2006).

Measurements that form upper or lower limits to the sea level are called limiting data, while data specifying the height itself are sea level indicator points (SLIPS).

Another way to measure sea level changes, albeit over shorter temporal range, is through tide gauges. They typically record water pressure, which can then be converted into RSL measurements. Although tide gauge data lacks the temporal range that a set of SLIPS can provide, they are relatively accurate. These measurements are crucial for understanding global sea level rise and its impact on coastal regions. While the data can be used to constrain GIA models (Davis et al., 1999) it is typically also used the other way around when monitoring climate change induced sea level rise. In these cases, GIA models are a vital tool to correct for the GIA effect in the tidal gauge data (Davis & Mitrovica, 1996; Spada & Galassi, 2012).

With the introduction of space-based measurements, sea level changes could be measured even more accurately. Radar and laser altimetry were introduced to measure the height of the sea surface using satellites. The TOPEX/Poseidon satellite, launched in 1992, was the first satellite dedicated to sea level altimetry and could measure sea level with the accuracy of a decimeter (Fu et al., 1994). Nowadays this accuracy has improved to the centimeter level with new technology and increased amounts of data collected (Escudier et al., 2017; Legeais et al., 2018).

In addition to space-based sea level altimetry, vertical land motion (VLM) could also be directly measured through geodetic leveling and Global Positioning System (GPS) stations, with their accuracies of about 0.5 mm/y depending on the region and the length of the time series (e.g. Texas 0.6 mm/y (Qiao et al., 2023), Scandinavia <0.4 mm/y (Kierulf et al., 2021)). Although measurement techniques have evolved greatly from the days of Celsius each technique still has its drawbacks. Satellite altimetry is expensive and has reduced coverage near the poles, which are important areas for GIA. Measurements on GIA through GPS stations and tide gauges are not available everywhere and sometimes the GIA signal is not as dominant in vertical motion as in the Baltic Sea. This means numerical models are used to correct for and to predict the GIA contribution to sea level change.

Not only do the different measurement techniques have their own advantages and disadvantages, but for the data, both RSL and VLM data sets, the same holds true. RSL measurements can only be taken near shores and in shallow seas, while GPS stations have to be installed on bedrock on land. This means that spatial coverage of both types of data can complement each other. Furthermore, they are in essence two different types of observations as GPS measures the motion of the bedrock, whereas SLIPS form a historical record of the height of the sea level. For this reason, SLIPS have an uncertainty in both the time dimension and height dimension. The downside of GPS measurements is that the record of most GPS points is not more than several decades, which basically means that it is snapshot of velocity on a GIA time scale, compared to RSL records which cover a substantial part of the deglaciation. Additionally, vertical land motion (VLM) can be caused by more processes than just GIA, such as tectonic movement or

local compaction making it often more complicated to filter out the GIA effect from the data.

GIA is also essential to establish historical ice mass change as the ice mass is the driving factor for the process to begin with. Uplift and sea level change depend on the interior properties of the Earth and the deglaciation history. If the Earth model can be estimated through means of e.g. tomography, the ice can be estimated such that it fits the observed uplift and sea level changes. In reality, the viscosity of Earth models is also often reconstructed using GIA, making finding an ice history and an Earth model an iterative process where both the ice history and Earth models are tailored to one another (e.g. Peltier et al., 2015). Ice models, on the other hand, are often also constructed with more data than just the GIA signal. Geological evidence on landforms, lake forms and dispersed glacier rocks are often used to estimate the extent of the ice sheet at different points in time (e.g. Clark et al., 2018). Instead of a purely data driven reconstruction, an ice history can also be constructed using ice evolution models on top of available data. Ice evolution models incorporate climate effects and ice dynamics to simulate ice growth and decline (De Boer et al., 2014). GIA models can be used as a constraint for both ice evolution models as well as empirical ice sheet reconstructions, as GIA can be used to determine the ice thickness at every location (e.g. Patton et al., 2017).

However, GIA is also invaluable to determine current ice mass loss. In this context GIA models are used to correct satellite measurements of mass changes by the satellite gravimetry measurement missions: GRACE and GRACE FO. In some regions, where GIA is the dominant signal, models can be constrained by time-variable satellite gravity data such as North America (Tamisiea et al., 2007; van der Wal et al., 2008) and Scandinavia (Steffen et al., 2008). In other regions GIA is a significant signal, that obscures the climate change signal from melting ice sheets such as in Antarctica and Greenland (Velicogna et al., 2014; Velicogna & Wahr, 2013).

Static gravity anomalies are local changes in gravity with respect to the gravity field of an ellipsoid. Their interpretation is more ambiguous than time-variable gravity as they contain contributions from the crustal and mantle structure, dynamic topography as well as GIA because the Earth's surface and deeper layers are still deflected. Here, interpretation of the gravity anomalies could benefit from more accurate GIA models to disentangle different contributions and answer questions on the support for observed high topography (e.g. in Scandinavia (Root et al., 2015), North America (Lambert et al., 2006), and the Transantarctic Mountains (Haeger & Kaban, 2019)).

Thus, we see that in some cases GIA is a source of signal noise that obscures the signal of interest, such as ice mass and sea level changes, or in finding the contribution of the mantle to topography. Therefore, GIA models are used to remove the GIA contribution. This thesis aims to add to the field of GIA studies Celsius started by establishing the GIA contributions in the Amundsen Sea Embayment (ASE), in Antarctica, and Europe. While traditionally GIA models only assume radial variation, many of the applications of prediction GIA models are in areas of considerable lateral variation in Earth structure

(West-Antarctica, Alaska, Scandinavia, European Alps). In this thesis we focus on creating a model that can model GIA with 3D variation in Earth parameters and has a multipurpose nature in terms of applications as well as study area.

The next section reviews the development of GIA models that can deal with variation in Earth structure.

1.1 Development of 3D GIA Models

Classically, in GIA models the Earth was considered to have a layered structure, with parameters only varying from one model layer to another and not in lateral direction (Peltier & Andrews, 1976). These models, where there is only 1 dimension in which the Earth parameters can vary, are henceforth referred to as 1D models. This is a simplification of reality as Earth's structural parameters vary not only in depth but also in lateral direction. However, this simplification was needed early in GIA model development as 3D models are complex and computationally expensive beyond what was possible before the 1980's. In reality, we know for example that areas with older continental crust or mountains typically have a thick cold lithosphere, whereas oceanic lithosphere is thinner and warmer.

3D anomalies in the mantle have been confirmed by seismic tomography studies (Celli et al., 2021; Debayle et al., 2016; Fichtner et al., 2018; French et al., 2013; Schaeffer & Lebedev, 2013). Seismic wave speed propagation is sensitive to density differences. These density differences can occur due to differences in temperature which translate into viscosity differences.

Density anomalies in the mantle are also seen with gravity measurements. Although observations of the gravity field are insensitive to density anomalies in radial direction for large wavelength features in lateral direction there is a high correlation between the indicated locations of density anomalies for both data sets (Root, 2020).

An additional downside of using gravity observations in GIA areas is that GIA itself influences gravitational observations and must be removed from the signal first. Gravity and seismic observations can be combined to create a model of the mantle with smaller wavelength features than are present in just tomographic models (Root, 2020). Some models that are based on inverting these data with additional data, like heat flux data, in geophysical and petrological consistent manner are models like the global model WINTERC-G (Fullea et al., 2021) and the GOCE+ model for Antarctica (Pappa et al., 2019).

With the advent of computing power, the assumption of homogenous Earth parameters for each depth could be dropped by using numerical models. The first models in which Earth parameters could be varied for all 3 dimensions, so called 3D models, were presented in the 1980's. The models utilized the finite element method (FEM) (e.g. Sabadini et al., 1986). The FEM is in its origins an engineering tool, in which a structure is modelled by a finite number of elements that can each have their own material

properties. The first FE models were flat Earth models, because of computational limitations (Kaufmann et al., 1997; Kaufmann & Lambeck, 2000). More realistic spherical 3D models were first proposed in the early 2000's (e.g. Wu, 2002; Zhong et al., 2003).

Not only did the models account for lateral variations, but the modelled physics simulating the GIA became more realistic. Most models used Maxwell rheology to model GIA (Kaufmann et al., 1997), an approach where the response of the system is conceptually modelled as that of a spring and a damper in series, where the spring simulates the elastic and the damper Newtonian viscous deformation GIA (see, section 2.4). More complicated transient rheology, like Burger rheology was initially dismissed as over complicated and of little impact on GIA, especially concerning the upper mantle viscosity (Mitrovica & Forte, 1998; Yuen et al., 1986). As the sophistication of both models and data sets progressed, more studies have challenged this notion (Boughanemi & Mémin, 2024; Lau, 2023; Simon et al., 2022), stating that simulation of regions with rapid changes in loading can be improved by applying transient rheology.

Mantle viscosity can be modelled using so-called flow laws. Flows laws originated from laboratory experiments (Hirth & Kohlstedt, 2003) on mantle rocks bring more complex rheology theory into the model. These flow laws are not perfect representations of mantle deformation as the laboratory experiments are not performed over the timescale over which these processes normally take place. Simulating the molecular level creep processes of diffusion and dislocation through flow laws allowed for non-linear rheology to be implemented in 3D models (Barnhoorn et al., 2011). In non-linear rheology stress, e.g. from deglaciation, can influence the effective viscosity (see, section 2.4) creating dependence of the rheology on the ice history which can influence the inference of ice thickness (van der Wal et al., 2010). Another source for high stresses in the mantle is from mantle dynamics. Locations such as Iceland are stressed by the mantle plume underneath it, which adds an extra ~25 MPa of stress to the mantle (Schiffer & Nielsen, 2016). Non-linear rheology is also dependent on the dominant creep mode in the mantle (See, section 2.4), which is influenced by temperature, pressure and mantle composition. As such it is important for regions where stresses are expected to be high because of rapid deglaciation or sudden ocean loading as well as regions with mantle compositions that support dislocation creep (e.g. oceanic lithosphere).

Increase in computation power did not only mean more sophisticated rheology could be incorporated but also that larger models in general could be handled. For example, in Kaufmann et al. (1997) and Kaufmann & Lambeck (2000) the model consisted of 600 elements, while current models can consist of about two hundred thousand elements (Blank et al., 2021; Huang et al., 2023). A higher number of elements in a model allows for the modelling of smaller features, and therefore, in general, the model accuracy and number of applications will increase.

While global 3D FEM based models with a resolution of ~200 km can be used to study the effect of large ice sheets and continental scale dichotomies in mantle structure, like

between East- and West-Antarctica, the low resolution of the models has hampered the study of GIA effects on smaller scale ice sheets or smaller scale differences in the Earth model. For ice caps that are only a few hundred kilometers across, like sets of glaciers, as found in Iceland or the European Alps (as shown in Figure 1.1a), a resolution of 110 km would mean that the entire ice cap is modelled with less than 10 pixels. The problem is exacerbated in these regions by the fact that important GIA features like the forebulge have a width an order of magnitude smaller (~100 km for Northern Europe, Blank et al., TBP) than the width of the ice cap. As such, the deflection cannot be accurately modelled with elements that are the same size as these features as a single element cannot model a bulge (see Section 3.5.2), regardless of how accurately the ice cap would have been discretized. A similar argument can also be made for other surface features such as complex coastlines that determine sea level induced loads on the model, as are found in Europe with the English Channel and Baltic Sea. But also, for features underneath the surface, such as possible small mantle anomalies, as is the case with part of the Iceland hotspot migration trajectory under Greenland (As shown in Figure 1.1b) and the hotspot itself in Iceland. For most of these features, grid-sizes that are in the order of 50-25 km would likely better capture these features. The challenge is to have a model with high resolution with small enough computation time to be able to explore a wide parameter range.
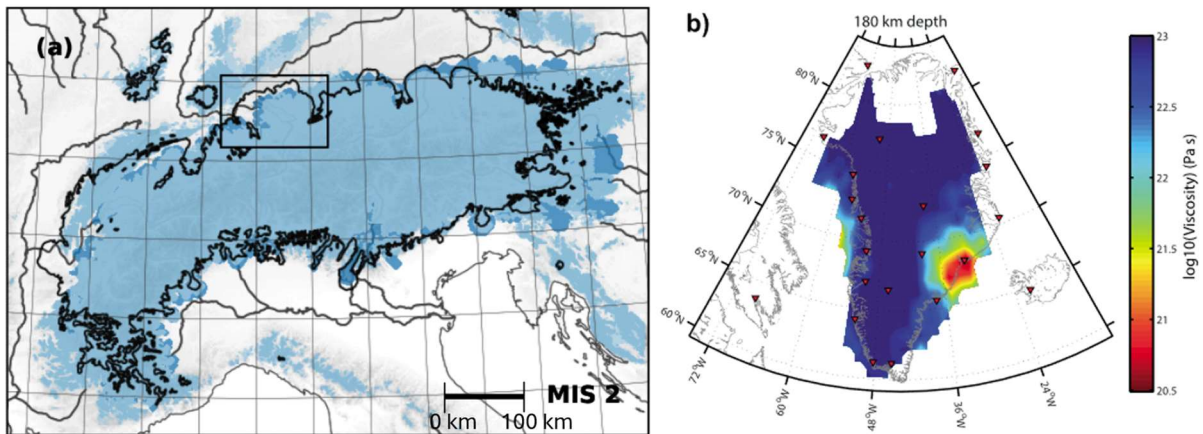
Figure 1.1: Examples of it GIA features in different regions that measure only a few hundred kilometers in size. In panel a) we can observe the extent (blue area) of the Alpine ice sheet during LGM (figure taken from Seguinot et al., 2018). In panel b) the viscosity is shown based on seismic anomalies for the lithosphere under Greenland at a depth of 180 km (figure taken from Mordret, 2018).

In this thesis we use a model based on the methodology of Wu, (2004) which couples a commercial FEM package ABAQUS to a method to solve the effect of deflection on the gravitational field (by finding a solution for the Laplace equation on a self-gravitating Earth). Subsequent applications of this method utilize an element size with surfaces of 2° by 2° (~220 by 220 km) (Wang and Wu 2006; van der Wal et al., 2015; Kierulf et al., 2014). More recent models managed to reduce the element size to about 55 by 55 km (Li et al., 2020; Zhong et al., 2022). The FEM is not the only approach to compute 3D GIA. Spectral finite element method (SFEM) based models, which use spherical

harmonic basis functions (see Section 2.2), have a comparable resolution as FEM based models, e.g. the VILMA model has a gird size of 120 km (Bagge et al., 2021; Klemann et al., 2008). The Finite volume method (FVM) has also been used to develop 3D GIA models (Latychev et al., 2005). The main difference between FVM and FEM is that for the FVM method volumes are defined for which fluxes are computed, making it a capable tool when modelling flow as it is conservative for every volume and thus the entire system in contrast to FEM. It also does not require a structured mesh. FVM, however, lacks the accuracy for structural stress analysis that FEM can provide. Latychev et al., (2005) were at the time already able to implement a model with an average grid-size of 60 km size, with recent versions managing to adopt elements of up to ~4 by 4 km for the local region of interest (Peak et al., 2022). However, as the FVM struggles more with local stresses than a FEM model these models do not use non-linear rheology and thus a FEM model is still preferred in areas where non-linear rheology is studied.

1.2 Applications of 3D GIA models

Improvements in computation time allowed 3D models to be used in different regions. Multiple studies demonstrate that including 3D rheology can yield significant differences in local uplift (Gomez et al., 2018; Kierulf et al., 2014; Nield et al., 2018; van Der Wal et al., 2013; van der Wal et al., 2015). Furthermore, it has become clear that 3D GIA can influence the corrections of tide gauge data to a significant level, while at the same time still falling short of providing a significant improvement (Davis et al., 2008).

Although 3D models can better represent the 3D variations that are thought to exist in the real Earth, these models did not show an unambiguous improvement compared to 1D models when they are compared to RSL data or VLM data. Studies for North America (Kuchar et al., 2019; Yousefi et al., 2021), Europe (Kierulf et al., 2014; Steffen et al., 2006) or Antarctica (Powell et al., 2022) showed mixed results in terms of improving the model fit to observations when including 3D variations. Both Powell et al. (2022) and Kuchar et al. (2019) argued that 3D models could improve the fit to data in respectively West-Antarctica and the Eastern US. In Kierulf et al. (2014) it was found that 1D rheology outperformed the 3D rheology in terms of the model fit to the data, although locally in Scandinavia the 3D model did lead to a lower misfit. In Yousefi et al. (2021) no improvement of the model fit to the RSL was found when applying 3D rheology. Part of the reason for the mixed success when implementing 3D rheology is that ice histories used in the modelling are being based on 1D models, such as ICE-6G (Peltier et al., 2015) and earlier versions of this ice loading history. Additionally, there can be large uncertainty in the Earth models used in the 3D GIA models as they can contain many parameters. The parameter space that is explored with 3D models is small compared to that explored with 1D models. Most 3D models use the 3D structure on observations of variations in seismic wave speed which is not linked uniquely to properties such as viscosity.

All these downsides have led to 3D models often only given marginal and local improvements compared to 1D models (Steffen et al., 2006). This means that there is a need for a 3D GIA model that offers improved accuracy compared to 1D models. This requires both increased resolution as well as a capability to simulate new flow laws and explore parameter space. This is the motivation for the research in this thesis. We focus on two regions where improvements from 3D model are both useful and expected. The first is Antarctica, as it boasts some of the highest contemporary deglaciation, especially in the ASE. Mass loss data obtained through satellite gravimetry like the GRACE mission has been essential in monitoring the year-on-year deglaciation accurately. As mentioned earlier, the most important correction for this data is the GIA correction, making accurate models of the area vital. At the same time Antarctica boasts very large differences in mantle structure between regions on the continent (Ivins et al., 2023). West-Antarctica has a thinner and warmer, relatively young, lithosphere and East-Antarctica consists of old and cold cratonic lithosphere. Within West-Antarctica there are regions that are seismically active and have a warmer and presumably less viscous upper mantle than in other regions.

Bedrock uplift influences the deglaciation speed of an ice sheet (Gomez et al., 2015; Konrad et al., 2015; Pollard & DeConto, 2012), therefore ice sheets include (simplified) GIA models. However, such simplified models cannot capture the large differences in mantle structure. The inclusion of 3D rheology has been shown to be relevant for ice sheet growth and deglaciation when a dynamic ice sheet model was coupled to a 3D GIA model in Antarctica (Gomez et al., 2018, van Calcar et al. 2023).

1.2.1 3D GIA in Antarctica

Antarctica has the largest mass of land-based ice on Earth with an average ice sheet thickness of 2 km and a volume of 25 M km^3 (Rapley, 2006), which saw considerable fluctuations in the past resulting in ongoing uplift. Its harsh climate makes research expeditions expensive to conduct, and its ice cover limits the number of locations where one can install GPS stations on bedrock. At the same time, it is especially relevant to quantify GIA because it affects measurements of current ice mass changes by satellite gravimetry (e.g. Schrama et al., 2014). Especially in West-Antarctica this is an issue as the measured high local uplift rates (up to 29.9 mm/y (Barletta et al., 2018)) have proven difficult to reconcile with most GIA models. As such, it forms an important part of the uncertainty in the number for current ice loss (Shepherd et al., 2018). Moreover, our understanding of the evolution of the ASE is limited by our understanding of GIA. That is because of the feedback mechanism between GIA and ice sheet dynamics. Ice mass loss will incur an uplift of the crust, moving the ice sheet into a colder atmosphere and more importantly reducing the RSL at the grounding line, moving the grounding line position outward and thus reducing calving (Coulon et al., 2021; Gomez et al., 2015; Konrad et al., 2015).

We know through tomography studies (An et al., 2015; Schaeffer & Lebedev, 2013) that there is a strong dichotomy in the Earth structure of Antarctica. The Transantarctic

Mountains separate East Antarctica with a cold and thick lithosphere from West Antarctica with a warmer and thinner lithosphere (Ivins et al., 2023; Pappa et al., 2019; Pappa & Ebbing, 2023). A stark difference in topography can already be observed on both sides of this divide, indicating the geological differences between East- and West-Antarctica (Paxman, 2023). In the ASE, located in West-Antarctica, the viscosity is probably even lower than neighboring regions, with the possible exception of the volcanically active Marie Byrd Land (MBL). Slow seismic wave speed found underneath the ASE using tomography (Shen et al., 2018) is an indication of higher upper mantle temperature. Moreover, space observed variations in the gravity field (Pappa et al., 2019; Pappa & Ebbing, 2023) and heat flux estimates for the ASE also point to higher-than-average temperatures, especially underneath the main ASE glacier, the Thwaites Glacier (Fisher et al., 2023).

Studies have been done on Antarctica to assess the effect of 3D rheology on the GIA in the region. In van der Wal et al., (2015) it is found that 3D rheology mainly effects the areas around the Amundsen and Weddell Sea when compared to 1D rheology, with differences in uplift around 5-6 mm/y maximum. In Nield et al. (2018) the effect of the east-west dichotomy was studied again, but with a finer grid for West-Antarctica. With a slightly different Earth model a ±3 mm/y difference was found between flat 3D and 1D models. Nield et al. (2018) also looked at the gradient of the uplift and found that 3D rheology in combination with non-linear rheology results in shorter wavelength responses than 1D models give. Yet, the aforementioned 3D models along with 1D models, see Figure 1.2, fall short of predicting the high uplift rates of up to 29.9 mm/y (Barletta et al., 2018) measured by GPS stations in the ASE area.
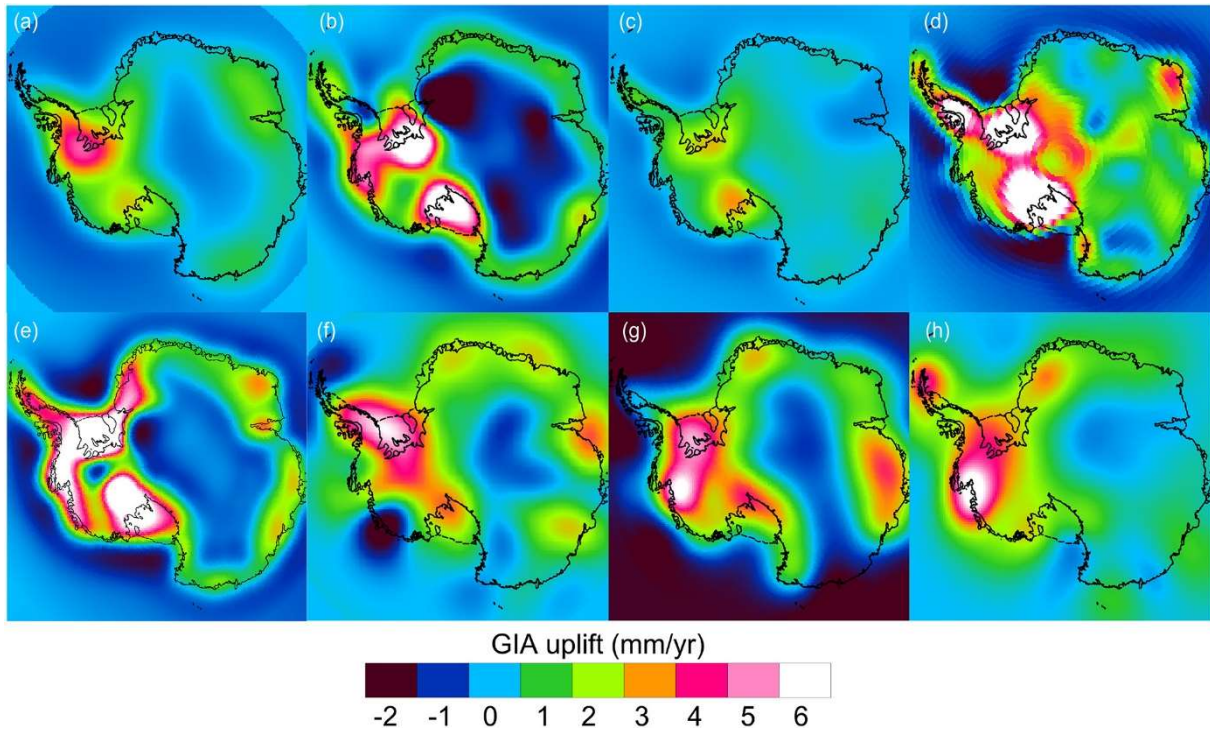
Figure 1.2: GIA induced uplift rate in Antarctica predicted by an assortment of models. (a) IJ05_R2(Ivins et al., 2013), (b) W12 (Whitehouse et al., 2012), (c) AGE-1b (Sasgen et al., 2013), (d) A13 (A et al., 2013), ICE-6G_C (VM5a) (Peltier et al., 2015), (f) R09 (Riva et al., 2009), (g) G14 (Gunter et al., 2014), and (h) RATES (Martín-Español et al., 2016). Figure from Martín-Español et al. (2016)

In Hay et al. (2017) it was found using a 3D model that measured high uplift rate (>25 mm/y) in West Antarctica can be replicated when using low local viscosities (~10^{18} Pa·s), however in the model the high uplift also extends to the Southern part of the Antarctic Peninsula and MBL, the latter of which also has a low viscosity in the model of Hay et al. (2017) and similar deglaciation. However, this modelled widespread large uplift is not in agreement with the low VLM (<5mm/y) measured in West Antarctica outside of the ASE (Whitehouse et al., 2012).

Thus, no GIA model matched the high uplift rate until Barletta et al. (2018) showed that low local viscosity in combination with recent (< 200 year) rapid local deglaciation are needed to fit these measurements (Barletta et al., 2018). In Barletta et al. (2018) a 1D model was used, which allowed for the grid search of large number of viscosities in upper mantle layers to establish the best fitting model used in the paper. The downside is that it did not include any effects due to 3D variations in the mantle below the region. 3D variations can be expected because the temperature WINTERC 3.2 shows temperature variations immediately underneath the crust and stress concentration underneath the deglaciating glaciers could lower viscosity through non-linear rheology. Furthermore, non-linear rheology influences how uplift can be localized, especially in these areas with high stress due to rapid deglaciation (Nield et al., 2018). The work in this thesis (Chapter 3, Blank et al., 2021) investigates whether 3D models could lead to changes in uplift that are statistically discernable from 1D models with the current GPS

stations in the region. It is a first step towards building an ice sheet history that is consistent with the rheology of Antarctica as shown by seismic and gravity studies.

Both van der Wal et al., 2015 and Nield et al., 2018 suggest that the changes in GIA depending on the lateral variations in Earth structure can potentially significantly affect ice sheet stability and evolution as earlier described in Pollard & DeConto (2012), and is demonstrated in Gomez et al. (2018). Using a model that couples ice sheet evolution to GIA showed that especially the ASE would have a significantly different local ice history than 1D models would imply (Gomez et al., 2018). Later work by van Calcar et al. (2023) to which this thesis contributed is discussed in chapter 2.

1.2.2 3D GIA in Europe

Europe is a densely populated continent, where a large number of people live near the coast. Accurate sea level observations and predictions are required for making policy decisions on coastal construction projects or water defenses. GIA models can be used to correct observations of sea level change to find the climate change induced sea level change, and GIA models can be used to project land subsidence and uplift in the future (Love et al., 2016).
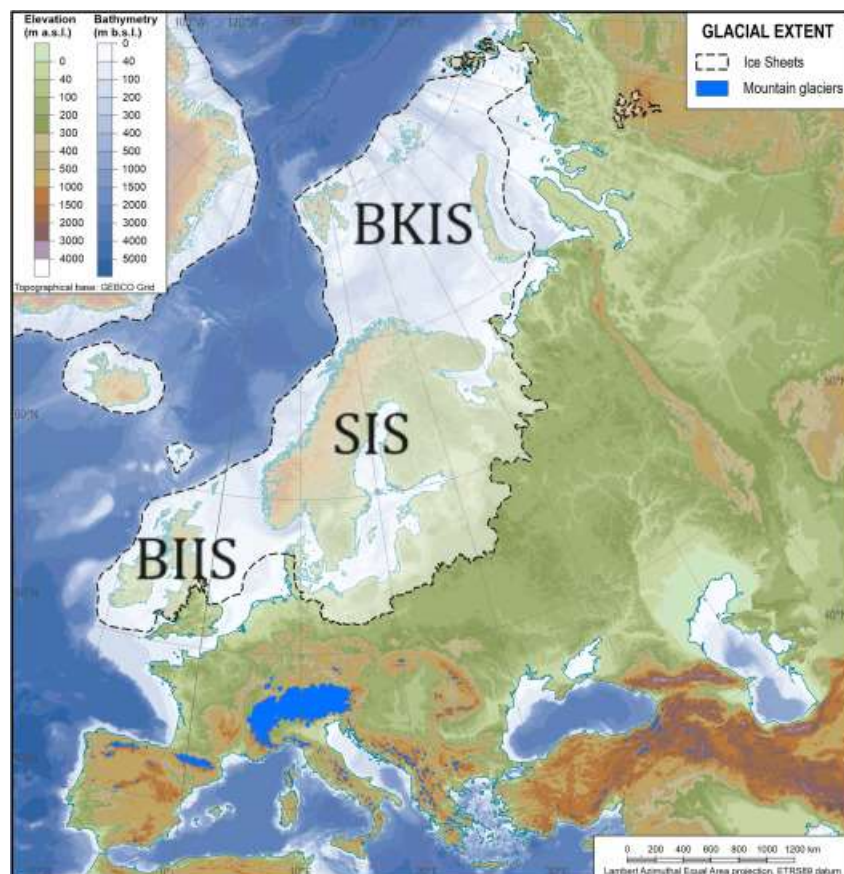

Figure 1.3: The maximum extent of the Eurasian ice sheet during the LGM and its subdivision in the smaller ice sheets: the British Isles Ice Sheet (BIIS), the Scandinavian Ice Sheet (SIS) and the Barents-Kara Ice Sheet. Figure from (Hughes et al., (2022)

The GIA signal in Europe is complex as the Eurasian ice sheet is composed of three smaller ice sheets, which disconnect at some point during deglaciation (Figure 1.3): the British Isles Ice Sheet (BIIS), the Scandinavian Ice Sheet (SIS) and the Barents-Kara Ice Sheet (BKIS). That means crustal movement can be due to one or more ice sheets, each with its uncertainty in ice thickness. The uncertainties become evident when comparing the ice reconstructions. In ICE-6G (Peltier et al., 2015) for example, ice sheet is thickness is the largest at the BKIS, while regional models like GLAC-1D (Tarasov et al., 2012), BRITICE CHRONO (Clark et al., 2022; Gowan et al., 2016), ANU (Lambeck et al., 2014) and the model of (Patton et al., 2017) have the largest ice thickness in the SIS. ICE-6G in general also shows a larger LGM ice volume in its reconstruction compared to e.g. GLAC-1D (Pollard et al., 2023). When we consider ice sheet reconstructions based on climate forcing models, independent from RSL data that GIA based reconstructions such as ICE-6G use, we still have the same uncertainties with the N05 (Näslund et al., 2005) and S04 (Siegert & Dowdeswell, 2004) reconstructions estimating the largest ice thickness in the SIS while UiT (Hubbard, 2006) again point towards the BKIS as being the most massive. An overview of some of these ice sheet reconstructions can be seen in Figure 1.4.
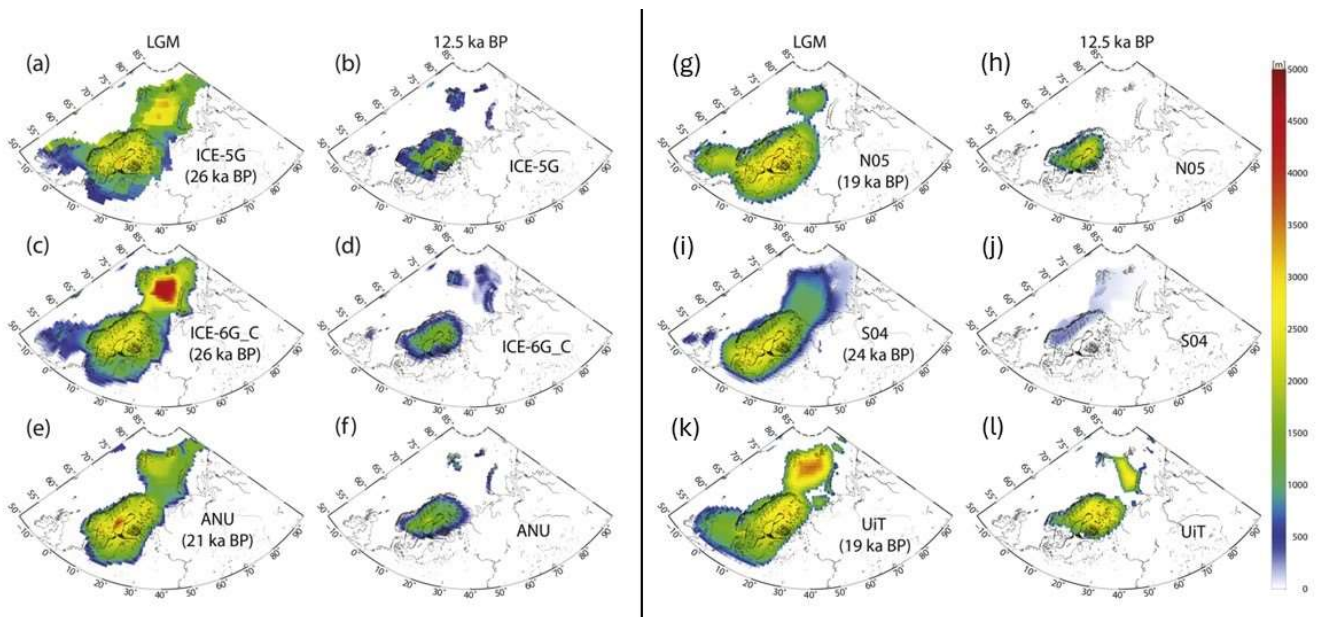
Figure 1.4: Ice height during last glacial maximum (LGM) (Figures a), c), e), g), i) and k)) and at 12.5 ky BP (Figures b), d), f), h), j) and l)) for six different ice sheet reconstructions of Europe. Figures a) and b) show ICE-5G (Peltier, 2004), c) and d) show ICE-6G (Peltier et al., 2015), e) and f) show ANU (Lambeck et al., 2014), g) and h) show N05 (Näslund et al., 2005), i) and j) show S04 (Siegert & Dowdeswell, 2004), k) and l) show UiT (Hubbard, 2006). Figure modified from Auriac et al. (2016).

The complexity in reconstructing the European GIA process is compounded by the shallow Baltic Sea and North Sea, which have at some point been open sea and land with grounded ice. This creates a dispersed sea level record as data is only available for certain epochs and at the coast, which might presently be submerged. Furthermore, the Baltic Sea has also been a lake at stages between 16 ky (Houmark-Nielsen & Henrik

Kjaer, 2003) and 8.5 ky (Berglund et al., 2005). This adds an additional problem for sea level records as the local water level will not match the global sea level at these times. Still, many sea level records have been collected for Britain (Shennan et al., 2018), the Atlantic Coast (García-Artola et al., 2018), the North Sea and Dutch coast (Hijma & Cohen, 2019), the Norwegian coasts (Creel et al., 2022), the Russian Arctic coast (Baranskaya et al., 2018), and the Baltic shores (Rosentau et al., 2021), creating a vast RSL dataset for the period of ±12.5 ky until present. The combination of these data has not been used in a single GIA analysis, although combined RSL data sets for Scandinavia and the North Sea coast (excluding Brittain) have been used in studies as Caron et al. (2018) .

Aside from RSL data, Europe has an abundance of GPS stations. Stations from the Tide Gauge working group (TIGA), BIFROST project (Kierulf et al., 2021) and the global study on stations from various working groups by Schumacher et al. (2018) give a dense coverage over the entirety of Europe. The vertical land motion measured by these GPS stations shows large uplift in central Fennoscandia of up to 9.8 mm/y (Kierulf et al., 2021). For the British Isles a slight uplift of around 1.8 mm/y can be found in Scotland (Bradley et al., 2009). Forebulge collapse can be observed north of the Netherlands and Germany (Kierulf et al., 2021).

Another complication for GIA modelling in Europe is that the ice sheets and signal cover a large area below which are large seismic velocity differences which imply rheological variations, see Figure 1.5. For example, a difference is observed between the lithosphere in the north-west of Europe and the Eastern European craton, with the region of the Eastern European craton showing higher seismic wave speeds (Celli et al., 2021; Debayle et al., 2016; Fichtner et al., 2018; French et al., 2013; Schaeffer & Lebedev, 2013; Shapiro & Ritzwoller, 2002). This results in thicker elastic lithosphere and higher viscosity mantle compared to the rest of Europe, see e.g. viscosity estimates in Barnhoorn et al. (2011) and van der Wal et al. (2013). However, GIA studies in which GIA models are fit to observations separately for different regions do not appear to show differences in viscosity. The viscosity is constrained to $0.4 - 0.6 \cdot 10^{21}$ Pa·s for the upper mantle underneath the British Isles (Bradley et al., 2011; Simms et al., 2022), and $0.3 - 0.7 \cdot 10^{21}$ Pa·s for the upper mantle beneath Fennoscandia (Kierulf et al., 2014; Lambeck et al., 1998; Steffen et al., 2008) by 1D GIA models. A notable indication from 1D modelling that different regions in Europe fit different average effective viscosities is given in Rovira-Navarro et al. (2020). By fitting 1D model results to GRACE data, the best fitting effective viscosity underneath Scandinavia is found to be twice as large as the viscosity underneath the Barents Sea.

Finally, the surface loading signal associated with GIA in Europe is a combination of ice loading, water loading (Johnston, 1995) and even erosion and sedimentation (Van Der Wal & IJpelaar, 2017). Thus, from a model perspective, multiple different loading sources are placed on the model, each requiring a fine resolution to be resolved accurately or else the model results will become unreliable.
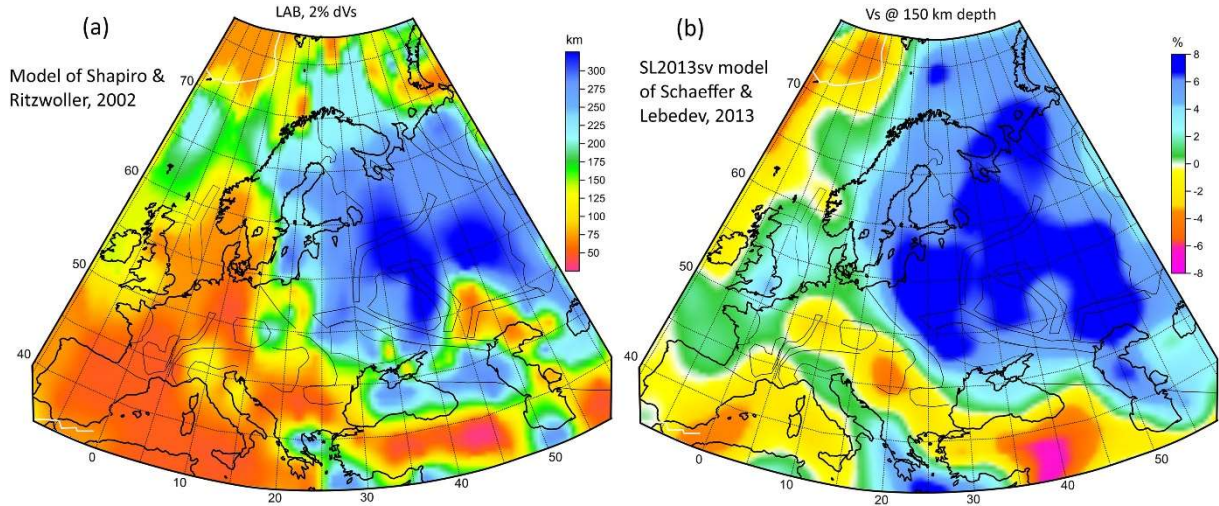
Figure 1.5: a) Lithosphere Asthenosphere boundary derived from seismic wave speed anomalies (Shapiro & Ritzwoller (2002) b) The seismic wave speed at a reference depth of 150 km according to Shaeffer & Lebedev (2015). Figure by Artemieva (2019).

3D GIA modeling has been applied to Europe (Kierulf et al., 2014; Van Der Wal et al., 2013). In Kierulf et al. (2014) it is found that 1D models in general outperform 3D models in Scandinavia when comparing the fit to VLM data, but that in certain areas, such as Northern Norway, 3D models managed to improve local fit. Van Der Wal et al. (2013) conclude that 3D models can show improvement in fit to RSL data compared to 1D models, but such models do not improve fit to the GPS data. Both studies, focused on the Scandinavian ice sheet and did not incorporate the British ice sheet in their models. Moreover, the spatial resolution of both studies was relatively low as van der Wal et al., (2013) and Kierulf et al, (2014) used 2° by 2° (~220x220 km) elements, while possibly important topographic features are already smaller (the width of the Baltic Sea in many places for example). This raises the question of whether it is possible to develop a more accurate GIA model with 3D viscosities and if such a model improves the fit to the RSL and VLM data in a larger region when using a 3D FEM model with a better resolution. In this thesis we combine VLM and RSL data sets from a larger region and use higher model resolution than the previous studies. Additionally, we have used newly created 3D rheology models for Europe and investigate a larger parameter space.

1.3 Research Questions

Based on the state-of the art describe in the previous sections We extracted 3 research questions that will be answered in the following chapters:

In this thesis we follow Wu's method which is partly based on a commercial FE program, for reasons explained in Chapter 2. Higher spatial resolution is required to make it suitable for more applications such as small ice sheets or complicated geometries for either the coastline or Earth structure, while at the same time the model should include larger scale loading such as sea level and possibly erosion.

- *How can we improve the ABAQUS based 3D GIA model such that it can be tailored to GIA in different areas for different ice sheet sizes?*

We will discuss the adaptation of the model in Chapter 2, specifically the implementation of 3D rheology, FEM mesh, and self-gravitation. Finally, we will discuss the applications that benefited from this model or modules of it, specifically the creation of a 3D GIA model coupled to ice evolution (Van Calcar et al., 2023) and additional regions that have been investigated, such as the North Sea (Hijma et al., 2025) and Greenland (Faure, 2022; Kempenaar, 2022).

- *How will GIA estimates improve when using 3D rheology on smaller scale regions, specifically the Amundsen Sea Embayment, compared to 1D models?*

In Chapter 3 a published study (Blank et al., 2021) is presented regarding the Amundsen Sea sector in Antarctica, where we use the model and compare it to the local 1D study of (Barletta et al., 2018). Here we investigate what we can learn from global 3D models for small regions like the Amundsen Sea sector.

- *Can we improve the fit to RSL and VLM data by applying 3D rheology in north-western Europe?*

A region with a wealth of both VLM and RSL data on large scale GIA can be found in the case of north-western Europe. In Chapter 4 we present a study using the model for Europe. Here we specifically try to answer if we can use the RSL and VLM data available for Europe, which has previously not been combined in a single GIA study to discover 3D effects in the data. We aim to find a 3D model that improves the fit to all the available data compared to 1D models, which can serve as GIA model for correcting for GIA effects.

In Chapter 5 we evaluate how well the research questions are answered as well as discuss future applications for the model, possible ways to improve 3D modelling relevant to the model-data fit, as well as broader recommendations for the study of GIA as a whole.

Chapter *2*

Model development and utility

Bas Blank[1]

1) Delft University of Technology, Delft, Netherlands

Abstract/summary

In this chapter we will first elaborate on the fundamental concept of the FEM and how equations of GIA can be translated to the FEM (Section 2.1). Secondly, we will discuss which elements and mesh in ABAQUS are used to create the 3D GIA model presented in this thesis in Section 2.2. It will be discussed how the model in this thesis improves the resolution in areas of interest compared to previous implementations of a 3D GIA model in combination with a FEM. Additionally, we discuss our choice for type of elements. Thirdly, we will explain how 3D rheology is implemented within the ABAQUS framework to create an Earth model with 3D varying parameters for diffusion and dislocation creep (Section 2.3). Alternatively, scaled 3D rheology has also been implemented to model 3D viscosity differences. Finally, we will discuss the applications this model or parts of it has been used for Chapter 3 and Chapter 4 in this thesis in Section 2.4. The applications relied on the model being easy to customize to different areas such as Greenland (Faure, 2022; Kempenaar, 2022) or the North Sea (Hijma et al., 2025). The model's modularity, which allows for the removal of options, was useful when only the self-gravitation module was needed in Nield et al. (2022), as well as leaving room to add extra functionality as is demonstrated e.g. in van Calcar et al. (2023) when an ice dynamic model was integrated with this model.

2.1 Basic ingredients of FEM

The FEM is a tool with which approximate solutions can be obtained for models with a high complexity, such as airplanes and composite structures. Different material properties and behavior can be dealt with, as such it lends itself well for GIA models with lateral varying parameters. However, it is necessary to correctly model the equations of motion. Here we use the method of Wu (2004) to do so, in combination with the finite element software package ABAQUS. In this section we will introduce the basic concepts of a finite element method (FEM) that are relevant to understanding the modelling of surface loading on a self-gravitating spherical incompressible Earth. We start by describing the shape function, the implementation of boundary conditions, followed by how forces, deformation and stress relate in a FEM.

The FEM is based on the approximation of the exact solution of the partial differential equations (PDEs) using the integral of the product of a set of weight functions with the partial derivatives to create a set of simpler integral equations valid for smaller subdomains, the so-called weak formulation (Zienkiewicz et al., 2005). The weight functions or test functions are based on the boundary conditions of the system and the principle of minimizing the error in the PDE. Each element is defined by a set of nodes, where the numerical solution of the PDE is calculated. Shape functions are used to interpolate the solution of the PDEs within each element using nodal values. The shape functions are chosen to satisfy conditions, such as the continuity of the solution at the

connecting nodes and nodes within the elements (integration points). The shape functions are typically chosen to be polynomial functions of the coordinates of the nodes such as linear or quadratic. The difference between both methods and the effect on the solution for our applications will be discussed in 2.3.

To solve the system, the FEM computes a stiffness matrix to relate the forces on the system to the nodal displacements. The individual stiffness matrix k of each element is based on the material properties of each individual element, the shape functions used to relate the nodes in that element and the element geometry. The stiffness matrix can therefore be seen as a quantification of how resistant an element is to deformation in every direction as a result of every possible load applied to it. The general equation that relates the nodal displacements matrix u of an element i to the forces F within the element is (Zienkiewicz et al., 2005):

$$F_{ex_i} = k_i u_i + F_i$$

Eq. 2.1

Where F_{ex_i} is the matrix of external forces applied to each node of the element when all displacements are still zero. The principal strain tensor at each integration point is related to nodal displacement matrix in principal directions by:

$$\epsilon = \nabla u$$

Eq. 2.2

In turn the strain is then related to the internal stress, q, in an element through the generalized Maxwell Model, which can be discretized to make it usable in our numerical code (Zienkiewicz et al., 2005):

$$\frac{\delta \epsilon}{\delta t} = D^{-1} q + \frac{1}{E} \frac{\delta q}{\delta t}$$

$$\downarrow$$

$$\frac{\Delta \epsilon}{\Delta t} = D^{-1} q + \frac{1}{E} \frac{\Delta q}{\Delta t}$$

Eq. 2.3

Here D is the visco-elastic stiffness matrix, which denotes the relation between stress and plastic strain rate for Maxwell materials in the form of relaxation times. As such D is related to the effective viscosity, as will be explained in Section 2.3, and is therefore material dependent. E is the elastic modulus which is also material dependent. Taking only the first term in Equation 2.3, it can be rewritten for the change of plastic strain ($\Delta \epsilon_p$) in a given time increment (Δt) which leads us to the following equation that is also used in ABAQUS to calculate the plastic deformation or creep for each time increment:

$$\Delta \epsilon_p = D^{-1} q \Delta t$$

Eq. 2.4

It is here that one can implement the laterally varying properties by assigning different material properties to an element. We will elaborate further on this in section 2.4.

When the stiffness matrix is known for each element, the PDE is then obtained by assembling the global stiffness matrix K from the element stiffness matrices, imposing the boundary conditions, and solving the resulting system of linear equations for the nodal displacements U given the forces F applied to the model:

$$F = KU \hspace{3cm} \text{Eq. 2.5}$$

As the FEM is an approximation, the accuracy largely depends on the number of elements and their shape function. A model with more nodal integrations points built-in, either through the element types used or the number of elements used in total, will require more computational resources. Thus, the mesh and element type choices will be the result of trade-off between the accuracy of the model on the one hand and the computational load on the other. Having an efficient mesh and elements with high resolution only where required, reduces the accuracy versus the computational load of a model, allowing for better accuracy, a faster model or both.

To solve the PDE's, the system must be prescribed boundary conditions. In the FEM, the boundary conditions are specified either as essential or natural. While natural boundary conditions follow automatically at the boundary of a domain if the solution is satisfied, essential boundary conditions are prescribed at the boundary of the domain, and they are necessary for the uniqueness of the solution. The boundary conditions used in our model are obtained from Wu (2004) and follow from physical limitations to the types of stress that can be present in some media and continuity that must exist between layers in terms of deflection and gravitational potential. First, we must consider that we can rewrite Equation 2.5 to (principle of virtual work):

$$F - KU = 0$$
$$\downarrow \hspace{3cm} \text{Eq. 2.6}$$
$$\nabla \cdot \tau = 0$$

Where $\nabla \cdot \tau$ is the change in stress in all directions, indicating that internal and external stresses should be in equilibrium in order to solve the system in FEM. However, in case of the Earth, we should also consider that the mantle can be pre-stressed by the hydrostatic background stress that is redistributed as the mantle material is forced to move around. This is effectively the term that introduces isostatic forces in the equation of motion. Additionally, each element should be subjected to the self-gravitation in the model. Including both the stress in an element, isostatic forces and self-gravitation results, respectively, in the equation of motions for the spherical incompressible self-gravitating Earth results in (Wu, 2004):

$$\nabla \tau - \nabla(u \cdot \rho_i g_i \hat{r}) - \nabla \phi_p \rho_i = 0 \hspace{2cm} \text{Eq. 2.7}$$

With g_i being the gravitational acceleration in the initial unperturbed state and ρ_i the initial material densities of all elements in the model in the unperturbed state. Furthermore, $\nabla \phi_p$ is the gradient of the gravitational potential after the model is

perturbed, $\hat{\mathbf{r}}$ is a unit vector in the radial direction and $\mathbf{u}$ being the displacement vector of a single point. In order for equation 2.7 to be solved in a FEM environment it must adhere to the form of equation 2.6. Therefore, a new stress tensor $\mathbf{q}$, that represents the combined stress in the FEM elements, is defined as a result of combining equation 2.6 and 2.7:

$$\mathbf{q} = \boldsymbol{\tau} - (\mathbf{u} \cdot \rho_i g_i \hat{\mathbf{r}} + \phi_p \rho_i)\mathbf{I} \qquad \text{Eq. 2.8}$$

with I being a 3 by 3 identity matrix. At the surface the only forces present are the surface loads (L), in kg/m2, that act in the radial direction; in the lateral direction, θ (as well as the longitudinal direction) there is no transfer of stress as the oceans and atmosphere cannot maintain shear stress, which means that:

$$\tau_{rr} = -Lg_0, \quad \tau_{r\theta} = 0 \qquad \text{Eq. 2.9}$$

with g_0 being the gravitational acceleration and ρ_0 being the density at the surface of the unperturbed model. Combining equation 2.8 with 2.9 then results in how the element stress is related to the geophysical properties of the model:

$$q_{rr} = -Lg_0 - \mathbf{u} \cdot \rho_0 g_0 \hat{\mathbf{r}} - \phi_p \rho_0, \qquad q_{r\theta} = 0 \qquad \text{Eq. 2.10}$$

The second term governing isostatic forces can be modelled with a spring system in the FEM model, where $\rho_0 g_0$, can be considered the spring constant. As a result, the boundary condition for the surface loads on the model simplifies to:

$$q_{rr} = -Lg_0 - \phi_p \rho_0 \qquad \text{Eq. 2.11}$$

These loads are applied in the form of a field, a grid in which the value of both terms is computed for each grid cell. ABAQUS applies a pressure to the surface elements based on an interpolation from the field values to the element face geometry in the final mesh. While $-Lg_0$ can be calculated and placed on the model, the model at the initialization, the perturbed gravitational potential, ϕ_p, needs to be computed in an iterative scheme as it depends on the model deformation. Using the solution to the Laplace equation to solve for $\boldsymbol{\phi_p}$ (Wu, 2004) will change the initial loads on the model and thus this process has to be iterated until convergence in the model solution is reached. The change in gravitational potential should be equal to the combined contribution of the change in gravitational potential caused by surface loads and the change in potential caused by the Earth's surface layer displacement:

$$\nabla \phi_p \cdot \hat{\mathbf{r}} = 4\pi GL - 4\pi G \rho_i u_r \qquad \text{Eq. 2.12}$$

Here, G the gravitational constant, ρ_0 the density of the top layer and u_r the displacement in radial direction.

At each interface between layers the continuity principle must hold. There should be no difference in gravitational potential, displacement, and stress, between the bottom of one layer and the top of the next layer. As a boundary condition this translates to:

$$[\boldsymbol{\tau} \cdot \hat{\mathbf{r}}]_-^+ = 0, \qquad [\boldsymbol{u}]_-^+ = 0, \qquad [\nabla \boldsymbol{\phi_p} \cdot \hat{\mathbf{r}} + 4\pi G \rho_l u_r]_-^+ = 0 \qquad \text{Eq. 2.13}$$

where ρ_l is the density of a layer. Applying the stress convention from equation 2.8 on Equation 2.13 results in:

$$\begin{aligned} \left[q_{rr} - u_r \rho_i g_i - \phi_p \rho_i\right]_-^+ &= 0 \\ [q_{rr}]_-^+ &= \Delta\rho(u_r g_i + \phi_p) \end{aligned} \qquad \text{Eq. 2.14}$$

where $\Delta\rho$ has become the density contrast between layers. At the core mantle boundary (CMB) only normal stress is transferred and no shear stresses as the outer core is fluid. When we apply this to equation 2.14 we obtain:

$$[q_{rr}]^+ = (\rho_f - \rho_m)g_i u_r - \rho_m \phi_p \qquad \text{Eq. 2.15}$$

here, ρ_f is the density of the outer core and ρ_m of the mantle. Additionally, as this is the deepest density difference that is modelled, the change in gravitational potential is directly proportional to the radial displacement at this boundary, resulting in the following boundary condition at the CMB as also presented in Wu, 2004:

$$\nabla\phi \cdot \hat{\mathbf{r}} = -4\pi G(\rho_f - \rho_m)u_r \qquad \text{Eq. 2.16}$$

2.2 ABAQUS mesh and elements

In this section we will look more in depth at the elements and mesh used in the model in this thesis. When choosing elements for the model the family of continuum elements is the only possible choice as it is the only element type that can have a volume and has a shape function that conveys all stresses from the full stress tensor, which are all needed when modeling Earth layers.

Continuum elements can be linear elements or quadratic elements. Linear elements have linear shape functions, while quadratic elements have quadratic shape functions. In order to fit the quadratic shape functions, the quadratic element also has integration points in between nodes, see the example of Figure 2.1.
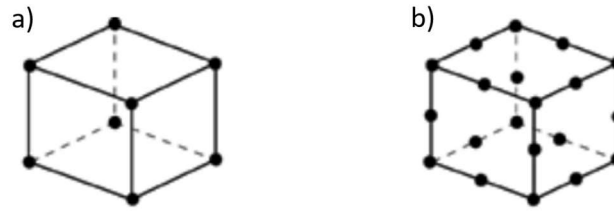
Figure 2.1: Two hexagonal continuum elements with their integration points denoted as dots. In a) the linear element C3D8 is depicted. In b) the quadratic element C3D20 is depicted. (Taken from the ABAQUS/CAE 6.1 user manual)

Quadratic elements can deal with bending as the quadratic shape function allows them to approximate a true bending element better than a linear element could. This means that an FEM model with quadratic elements can be built with less elements while reaching the same accuracy, but at the cost of higher computation time per element. However, this is a downside in the context of GIA model as less elements mean that surface loads, self-gravitation, and 3D rheology will also be evaluated at a lower resolution. Testing showed that an increased number of linear elements in both the radial and longitudinal direction will mitigate typical shortcomings associated with linear elements and approach solutions of benchmarks to a high degree of accuracy (Section 3.5.2) at a fraction of the computation time compared to quadratic elements.

One of the shortcomings associated with linear elements is shear locking, which occurs because the elements are unable to model the bending of an element accurately. As the element cannot bend when subjected to a moment it will generate artificial shear strain. These artificial shear strains result in elements that resist bending moment more than they would without the artificial shear strains. While the best solution is to use quadratic elements to avoid the issue altogether, creating a mesh with elements that are not overly thin will mitigate the issue.

Another consideration when selecting elements is volumetric locking that can occur on nearly incompressible elements. Incompressible elements can artificially cause high stiffness as the incompressibility condition cannot be estimated properly throughout the element by the shape functions. Hybrid elements can be used to mitigate this issue. Hybrid elements use multiple different interpolation functions. In ABAQUS not only displacements are computed, but an independent interpolated pressure stress variable is used alongside the displacements. Both variables are coupled through an additional variation principle to determine equilibrium equations and compatibility conditions (ABAQUS Theory Manual (2016)).

Additionally, reduced integration elements mitigate the volumetric locking as well (Doll et al., 2000). These elements have fewer integration points and are less prone to be distorted to such an extent that volumetric locking would be a problem. The downside of these elements is that they are more prone to hourglassing, which is a phenomenon that can occur in elements with a low number of integration points, unless hourglassing controls are implemented (Cangiani et al., 2015). As a result of the low number of

integration points, strain will not be calculated correctly throughout the element. The result is often a solution with elements forming hourglass shapes (see Figure 2.2). ABAQUS has forms of hourglassing controls on their reduced integration elements (ABAQUS Analysis user's manual 6.13, but it is good practice to check solution for these zigzag patterns that could indicate hourglassing. Thus, we have chosen hybrid linear reduced integration elements to be used in the 3D GIA model.
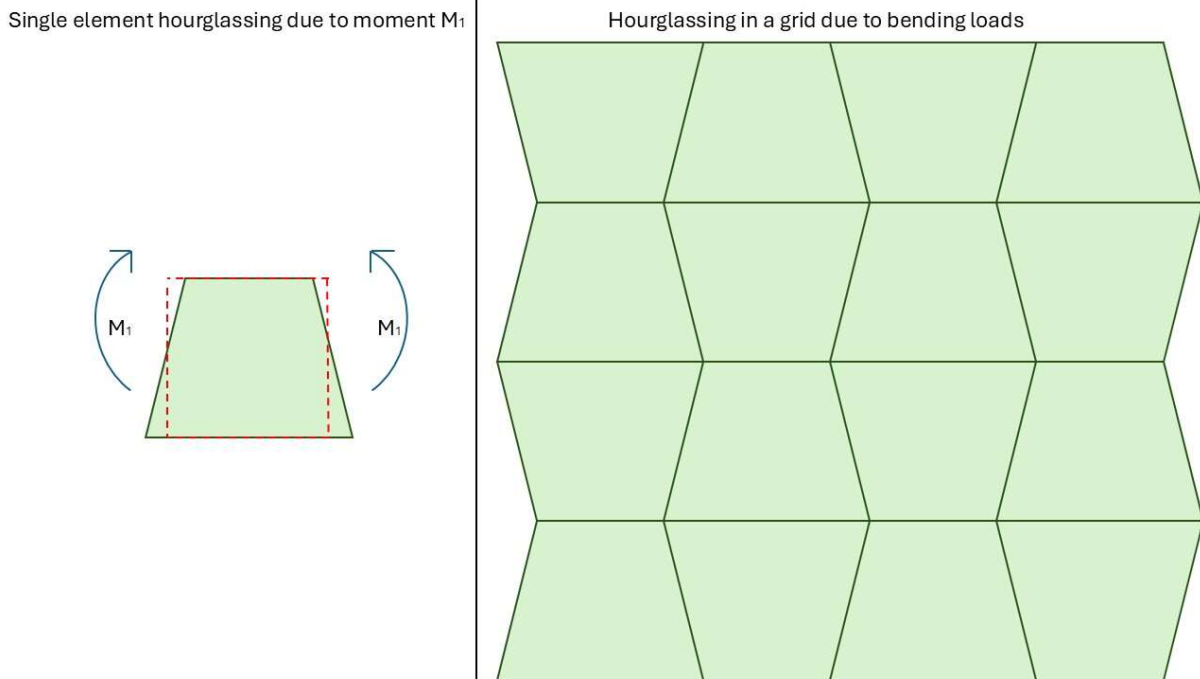
Figure 2.2: Schematic 2D representation of how hourglassing would look like for a single solid linear reduced integration element (left), which is prone to hourglassing, and the resulting grid (2D) of a structure in a FEM that experiences hourglassing (right).

The FEM model from this thesis has been benchmarked against the previously benchmarked VEGA model (Martinec, 2000), which is a spectral finite element method (SFEM) model. SFEM models use spherical harmonic basis functions instead of the regular polynomial basis function FEM uses. This can lead to computational demanding models, but SFEM models can be more accurate than FEM models (Liu et al., 2014).

As can be seen in benchmark B in section 3.5.2, the FEM model with linear elements approaches the deflection of the VEGA model (Martinec, 2000) with a maximum difference of 1.3% at the location of maximum deformation, but in all setups the FEM model always underestimates the deflection. This points to the linear elements still being slightly too stiff under bending. A difference in the effective second moment of inertia (about 1.3% in Couturier et al. (2015)), which determines the resistance to bending of the model, or maximum deflection (5% in Amirpour et al. (2017)) are known to occur when using solid elements for bending problems in FEM; meshing strategies can mitigate this issue (Couturier et al., 2015). However, both of these models are rather too flexible than too stiff, which means that these inaccuracies do not consistently lead to excess stiffness. We do see the excess stiffness when the model is compared with other incompressible FEM model solutions (section 3.5). The model in this thesis is able to

26

approach a high-resolution axisymmetric FEM model solutions within 0.2% difference in maximum deformation. Thus, it is likely that volumetric locking still plays a role in making the models overly stiff.

Now that the element type has been decided, three different meshes were tested. The first mesh is a sphere with all nodes placed at approximately the same distance from another. Almost all elements are hexagonal elements. This mesh will be referred to as the equi-distance mesh. The second mesh has nodes that are separated by the same angular distance. To increase resolution in a small area, a cone is constructed that can encompass the region of interest within which the angular distance between nodes is smaller. The central elements around the rotational axis of the cone are wedge elements, the rest of the elements is a mix of mainly hexagonal elements and some tetrahedral elements. This mesh will be referred to as the equi-angular mesh. Finally, we have a mixed model where the far field elements are based on equi-angular nodal placement and the elements within the cone have equi-distant nodal placement. This will be called the cone mesh.
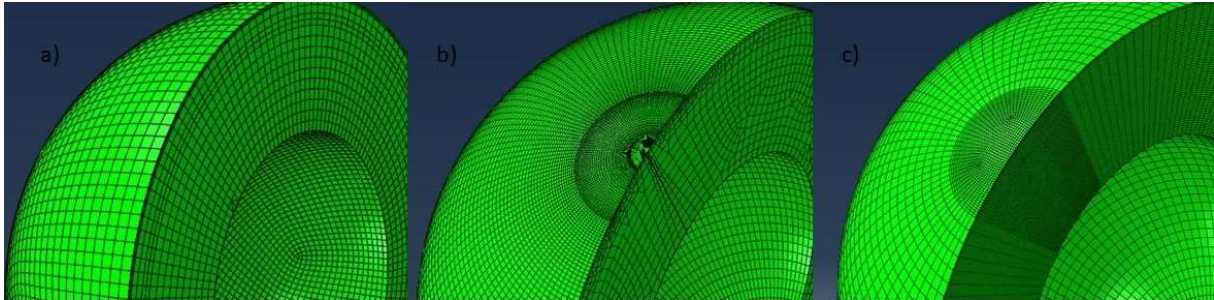
Figure 2.3: Overview of different meshes tested. In a) a mesh where all nodes are approximately the same distance from another, also called the equi-distance mesh. b) a mesh where all nodes are approximately the same angular distance from another with smaller angular distance applied for a cone region around the location of interest, also called the equi-angular mesh. In c) a mesh is shown where all nodes are approximately the same angular distance from another, but within the cone the nodes are equi-distance spaced. This is called the cone mesh.

When we apply benchmark A, an oceanless model with a cone shape ice load of 1500 m high and radius of 20° on the pole (full description in 3.5.2), to these three mesh types and compare them with the VEGA model. we see that the cone mesh (See Figure 2.3) in general performs better than the other models (Figure 2.4). The equi-angular mesh performs poorly on the point of maximum deflection compared to the other models. The central node on the rotation axis experiences compressive stresses from all adjacent wedge elements. Volumetric locking seems to occur around the central node and as a result it is unable to move. Near the forebulge the equi-distance mesh also displays an undesired locking effect. Here the wavelength of the forebulge is too small for the equi-distance mesh, and the elements start hourglassing. The cone mesh does not have issues with the point of maximum deflection as it does not have a node directly on the rotational axis. Furthermore, the cone model has the resolution required to prevent hour glassing at the forebulge. It does in the end underestimate the maximum deflection by 3.4% as computed by the SFEM model.
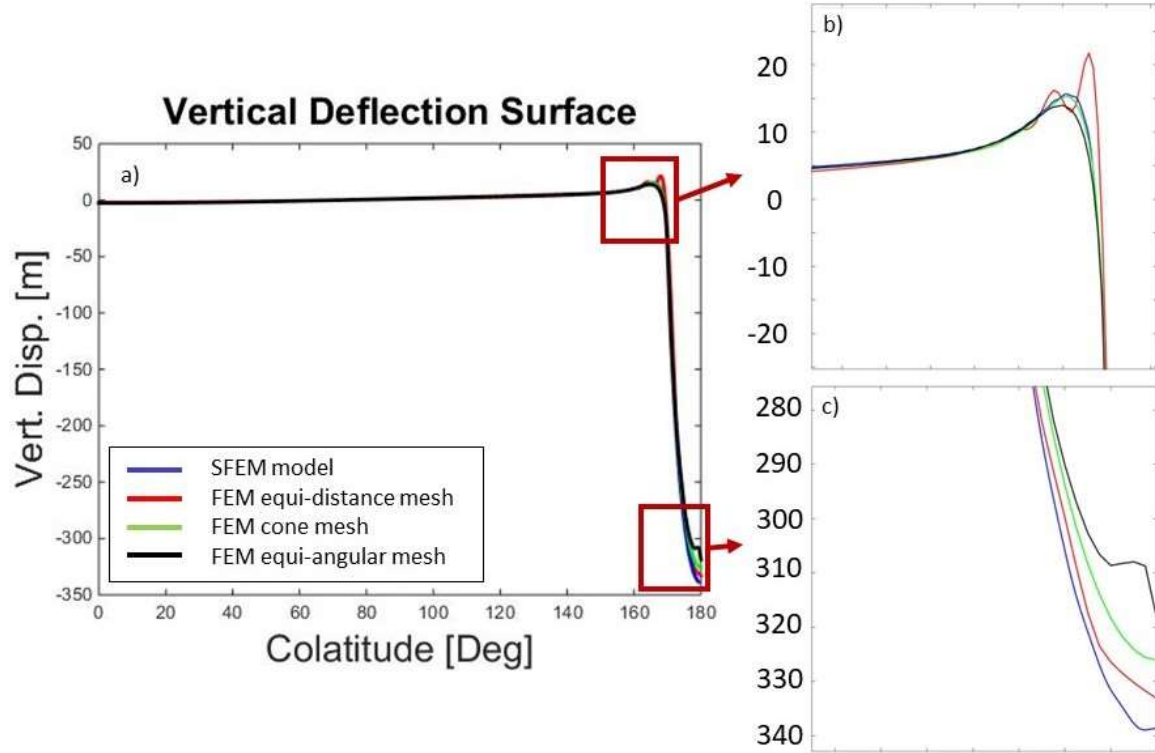
Figure 2.4: Deflection for 4 models when the cone load is applied to the south pole (Benchmark A from Martinec et al., (2018)). The normal mode model in blue is the VEGA model (Martinec, 2000) which is used as a reference for the other 3 models, which are all FEM models. The equi-angular mesh and equidistance mesh have approximately the same amount of elements, with the cone mesh having more elements than both other FEM meshes.

If we not only look at surface deflection but also examine the deflection of the layer below the top layer in the model (figure 2.5), we see that the equi-angular model has some undesired effects there as well. We observe zigzag patterns in the deflection that are not present when we use an equi-distance mesh. This again indicates that hourglassing is happening, which is detrimental to the model accuracy.
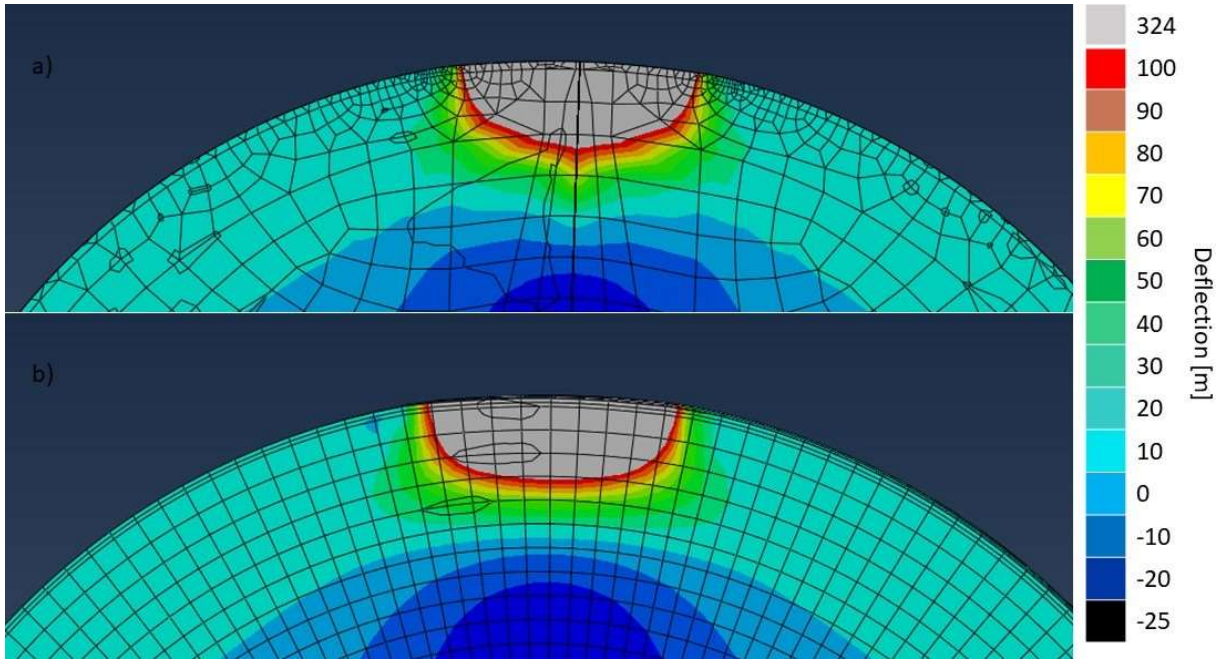
Figure 2.5: Deformation for different meshes with identical loading. a) shows the deformation when benchmark A is applied to the equi-angular mesh. b) shows the deformation when benchmark A is applied to the equi-distance mesh.

The mesh itself affects the solution also through discretization of the load applied to the model. The load input for the 3D GIA model is always on a standard predefined equi-angular grid to allow for the spherical harmonics synthesis. The ice load on the model is applied by pressure loads exerted on the elements outer surface. In order to obtain pressures for each element in our variable mesh, ABAQUS transforms the load input to a field. The input loads are the change in ice load, the change in gravitational potential and the change in sea level, all with respect to the start of the simulation where we assume all forces are in isostatic equilibrium. These loads are all calculated on a finer grid than the grid of the FEM model (0.25° x 0.25°). The fields containing these input values are used to compute the average pressure on each element face. Hence, changing the mesh also changes the discretization and thus the exact load applied at every location of the model. Having a high resolution in the region of interest mitigates this potential problem as a finer mesh decreases the differences between the input load and the actual applied load and thus it decreases the possible error made when calculating the final solution.

The cone mesh allows us to make a high-resolution area around our region of interest, however the high resolution in the cone meshed will give diminishing returns on accuracy improvement the deeper we evaluate the mesh. Therefore, we have combined the cone mesh with a reduction in elements in radial direction to reduce the total amount of elements without sacrificing accuracy. This reduction in resolution happens at the boundary between the upper and lower mantle (to elements sized 2° in all directions) and again at the core-mantle boundary (to elements sized 4° in all directions). We achieve this by implementing so-called ties between node layers in the model. The tie forms a surface from the nodes on one layer (master layer) to constrain (within a set

tolerance) the nodes on the tied layer (slave layer). As such the nodes do not need to be directly connected but can still transfer loads and deformation between nodes on different layers in both directions.

In the end, this resulted in a lateral resolution of around 25 km by 25 km for the ASE, as can be seen in chapter 3, and 40 km by 40 km for Europe, as can be seen in Chapter 4. While this cannot contest the resolution of other models that manage to go down to a grid resolution of FVM models that go as low as 4 km (Peak et al., 2022), our model is not bound to some of the downsides the FVM models have and can implement for example non-linear rheology. At the same time, our grid-size of 40 km it is an improvement to the ~55 km grid resolution (Li et al., 2020; Zhong et al., 2022) of FEM models based on ABAQUS and it allows us to investigate smaller regions such as the ASE with non-linear rheology.

2.3 Modelling 3D rheology within ABAQUS

To model the rheology of the Earth, multiple theoretical models have been proposed (Boughanemi & Mémin, 2024; Hirth & Kohlstedt, 2003; Karato, 2010; Kaufmann & Lambeck, 2000; Ohuchi et al., 2015; Ranalli, 2001; Tesauro et al., 2009). The most straightforward model of rheology is Maxwell rheology. Maxwell rheology can be visualized as a spring and damper system placed in series. The spring represents the elastic component of deformation, which is instantaneous and recoverable. The spring constant depends on the shear moduli of materials in each layer. The damper represents viscous steady-state deformation and simulates an energy loss in the form of permanent deformation. This type of deformation is non-recoverable even after stresses have been lifted.

While Maxwell rheology has proven to work well over longer geological timescales (Kaufmann & Lambeck, 2000) it does not model deformation over short timescales well, as GPS observations on post-seismic deformation show transient creep fitting better (Agata et al., 2019). To solve this problem so-called Burgers rheology has also been used in Earth models. In addition to the elements present in Maxwell rheology the schematic model of the Burgers rheology also contains a Kelvin-Voigt element. Kelvin-Voigt elements are a spring and damper in parallel. As a result, Burgers rheology has two viscosities: one for short term deformation and one for long term deformation. Burger rheology has been used in post-seismic deformation models where they are shown to fit observations better (Cannelli et al., 2010), as well as for GIA purposes (Boughanemi & Mémin, 2024).

Both rheologies are continuum approaches where the large-scale behavior of a system is described. With laboratory experiments deformation at micro-scale has been investigated. The most important types of deformation at mantle conditions have been identified as diffusion creep, dislocation creep (mainly in the upper mantle) and grain boundary sliding (in the middle and lower regions of the upper mantle) (Ohuchi et al.,

2015). The relation between mantle conditions and dominant creep mechanics can be seen in Figure 2.6.
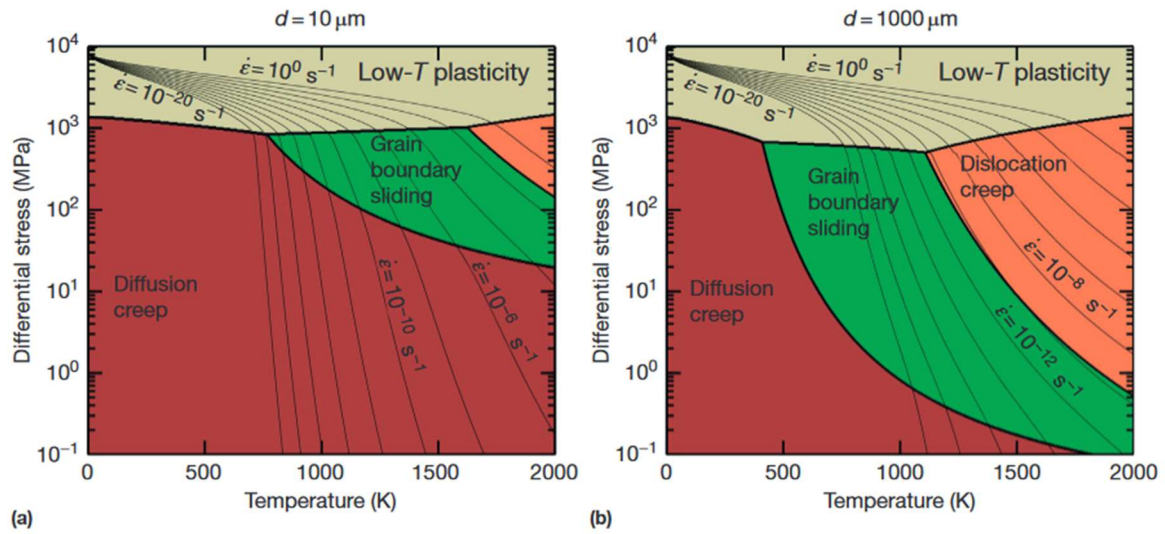
Figure 2.6: Dominant creep mechanisms for different grain sizes, a) 10 *μm and b) 1 mm, in dunite (90%olivine) depending on stress and temperature. The thin contour lines represent constant strain, whilethick contour lines form the boundaries between the different creep modes: low temperature plasticityor ductile deformation, diffusion creep, dislocation creep, and grain boundary sliding (GBS). Figuretaken from Hansen & Kohlstedt (2015)*

Diffusion creep is characterized by diffusion of vacancies in the crystalline structure of a material. As this movement becomes easier when individual particles have more energy it is sensitive to the temperature of a crystalline material. Diffusion creep is the dominant creep mechanism for low stress (Hansen & Kohlstedt, 2015).

In dislocation creep a dislocation in the crystalline structure moves under the influence of stress. For a dislocation to move in the crystalline structure the bonds along the so-called slip plane need to be broken and reformed one lattice point further. As the energy required to break and reform these boundaries comes from the work exerted on them, the dislocation mechanism is sensitive to the internal stress of a crystalline material. When a mantle material experiences high stress and low temperatures, dislocation creep is the dominant stress mechanism.

When a polycrystalline material, such as the composites in the mantle, has a homologous temperature that is greater than ~0.4 (40% of its melting point), grain boundary sliding can play a significant role in viscous deformation (Ballo et al., 2001). Grain boundaries are the planes in the crystalline structure that have a larger number of defects in the crystalline structure compared to regions within those planes or borders, called grains. While the aforementioned dislocation and diffusion creep focus on the movement of individual vacancies or dislocations within the crystalline structure, grain boundary sliding represents the movement along a grain boundary. These movements can be accommodated by dislocation or diffusion flow. The conditions for grain boundary sliding occur in the upper mantle and it can therefore not be dismissed (Ohuchi et al., 2015).

The relation for diffusion creep, or more specifically the diffusion creep parameter B_{diff}, and the dislocation creep parameter B_{disl} to the stress-strain rate relation in Equation 2.3 through D^{-1} for each element i, is as follows:

$$D^{-1} = M$$
$$M_i = B_{diff_i} + B_{disl_i} \tilde{q}_i^{n-1}$$

Eq. 2.17

Here it must be noted that there is a non-linear dependence on the equivalent stress, $\tilde{q}$, involved for dislocation creep. Where n is the creep exponent which is 3.5 for dislocation creep. In order to calculate B_{diff} and B_{disl} for every element in the model we have incorporated an experimentally based rheology that incorporates diffusion and dislocation creep equations which can be represented by (Hirth & Kohlstedt, 2003):

$$B = Ad^{-p} f_{H_2O}^r e^{-\frac{E+PV}{RT}}$$

Eq. 2.18

Here d is the grainsize, f_{H_2O} the water content in parts per million, E the activation energy of the material, V the activation volume, R the universal gas constant, P the local pressure and T the local temperature. The parameters in Equation 2.18, and as such the obtained B_{diff} and B_{disl}, are subject to uncertainties as the parameters are obtained through laboratory experiments (Hirth & Kohlstedt, 2003). Laboratory experiments suffer from scaling issues, where mantle conditions (most notably pressure) cannot be recreated in the laboratory and the experiments themselves must be done on timescales that are orders of magnitude smaller than the geological timescales the mantle relaxation times commonly are (Karato, 2010). The flow law from Equation 2.18 has also been used for other processes than GIA to model visco-elastic flow in the mantle (Agata et al., 2019; Freed & Bürgmann, 2004). An update for Equation 2.18 and its parameters is provided in Hansen & Kohlstedt, (2015), so that grain boundary sliding is included in the flow law and a distinction can be made between different forms of diffusion. We have chosen to use the flow law in Equation 2.18 as to not overcomplicate rheology with more assumptions on mantle properties than are required. The equivalent stress $\tilde{q}$, or von Mises Stress, used in Equation 2.17 can be calculated from the tensor components q_{ij}:

$$\tilde{q} = \sqrt{\frac{3}{2} q_{ij} q_{ij}}$$

Eq. 2.19

ABAQUS works with strain increments $\Delta\epsilon$, so combining the governing Equation 2.4 with 2.18 and 2.19 leads to an equation we can implement in ABAQUS to simulate non-linear rheology (Blank et al., 2021):

$$\Delta\epsilon_{ij} = \frac{3}{2}\left(B_{diff} + B_{disl}\tilde{q}^{n-1}\right)q_{ij}\Delta t$$
$$\tilde{\epsilon} = \frac{3}{2}\left(B_{diff} + B_{disl}\tilde{q}^{n}\right)\Delta t$$

Eq. 2.20

Where $\tilde{\epsilon}$ is the uni-axial strain rate. The uniaxial strain rate is applied to the stress tensor to obtain the eventual strain tensor as to model element deformation. Equation 2.19 needs to be solved for every time increment Δt in ABAQUS. The values of B_{diff} and B_{disl} are provided to ABAQUS as input while stress and strain are solved in ABAQUS using Equation 2.19. It follows that effective viscosity is (Van Der Wal et al., 2013):

$$\eta_{eff} = \frac{1}{3B_{diff} + 3B_{disl}\tilde{q}^{n-1}}$$

Eq. 2.21

Equation 2.20 implies that viscosity depends on stress, and it has to be computed after the simulation is completed to include all GIA stresses and should also include other background stresses. When we want to use a linear rheology instead of a non-linear rheology where viscosity depends on stress, we assume that $B_{disl} \cdot \tilde{q}$ is negligible, leaving us only with a linear component. This assumption can be justified either because dislocation is negligible compared to diffusion in the shallow upper part of the mantle (with low water content or small grain sizes), as assumed for linear rheology in Chapter 4, or because the Von Mises stress is negligible (which would only hold for deeper parts of the upper mantle with small loads), as assumed for linear rheology in Chapter 3. The effective viscosity η_{eff} in that case relates to B_{diff}:

$$\eta_{eff} = \frac{1}{3B_{diff}}$$

Eq. 2.22

An alternative method to compute viscosity is by computing viscosity from seismic wave speed anomaly $\frac{\delta v_s}{v_s}$ (Wu et al., 2013):

$$\log_{10}\eta = -0.4343\beta\frac{\partial T}{\partial \ln v_s}\frac{\delta v_s}{v_s}\frac{E^* + pV^*}{RT_0^2} + \log_{10}\bar{\eta}$$

Eq. 2.23

Here $\frac{\partial T}{\partial \ln v_s}$ is the temperature-seismic wave speed derivative which can be obtained from tabulated values (Karato, 2010). Furthermore, $\bar{\eta}$ is the background viscosity, for which VM5A (Peltier et al., 2015)is used here, and T_0 the reference geotherm for which we follow Turcotte & Schubert (2002) for the upper mantle (50 km - 300 km), Stacey & Davis (2008) for depths between 300 km – 420 km and Karato (2010) for the transition zone (420 km – 670 km). Here β is a scaling factor to increase or decrease the

effect of the seismic wave speed anomalies on the viscosity anomalies (Wu et al., 2013). For $\beta = 0$ Seismic wave speed variations are assumed to be due to anomalies in composition, anisotropic stress or any state parameter other than temperature, while for $\beta = 1$ all seismic wave speed variations are explained through temperature which translates to viscosity variations at a certain depth. For $\beta = 0$ the entire layer has the same reference viscosity. In this case we can derive B by combining Equation 2.21 with Equation 2.22:

$$B_{diff} = \frac{1}{3\bar{\eta}} \cdot 10^{0.4343\beta\frac{\partial T}{\partial \ln v_s}\frac{\delta v_s}{v_s}\frac{E^*+pV^*}{RT_0^2}} \qquad \text{Eq. 2.24}$$

Whichever method is used, the model requires a list with a B_{diff} and B_{disl} parameters for every element to simulate a unique effective viscosity for that element to implement 3D rheology, although for linear rheologies the value for B_{disl} is set to zero.

There are some merits and drawbacks to each approach. The benefit of using non-linear rheology is that it can incorporate the possible dependency of viscosity on stress. Areas with large changes in load in short timespans or when water content is relatively high are locations where the stress significantly influences the viscosity. However, information is needed on the composition of the mantle to use non-linear rheology, which we can only obtain by surfaced samples. We cannot verify if the surfacing process itself changes the composition of these samples. The flow law parameters themselves are also derived from laboratory experiments that do not perfectly replicate mantle conditions.

When scaling the viscosity, one still makes an assumption on mantle composition when deciding on the values for $\frac{\partial T}{\partial \ln v_s}$, with for example, large differences between olivine, iron-based garnet and calcium-based garnet (Karato, 2010). Furthermore, we have to assume a homogenous olivine mantle in order to be able to use the experimentally derived values for olivine. The experimentally derived values suffer from the same limitations in the laboratory as is the case with the flow law values. Also, we know that other things than temperature e.g. the water content or melt fraction in the mantle can influence seismic wave speed anomalies (Goes et al., 2000; Karato & Jung, 1998), as captured by using a $\beta < 1$. The benefit of working with scaled rheology is that no assumptions on the grain size, water content or melt fraction present in the mantle must be made for the model, making the problem one dimensional. This makes it both easier to implement as well as to analyse. Also, because the background viscosity is fixed to a value that matches that from a GIA study, possible viscosities for a given layer are closer to values that match GIA observations.

An important assumption for the rheology that was made in Wu (2004) to make the model work was for it to be incompressible. However, we know Earth materials are compressible. A et al. (2013) developed a 3D model that allowed for compressible rheology and showed that compressible 3D rheology can significantly influence uplift

(A et al., 2013). While in A et al. (2013) the entire model was built from the ground up, in Huang et al. (2023) a method is demonstrated in which commercial software packages like ABAQUS can be used to incorporate compressibility in the GIA model.

2.4 Applications for the 3D FEM GIA model

In previous implementations of the Wu (2004) method ABAQUS computations were combined with a Fortran routine to compute self-gravity and solve the sea-level equation (Li et al., 2020; Wang & Wu, 2006). Implementing the 3D GIA model in ABAQUS CAE allowed for large parts of the code to be written in Python. This brought a more modular style of programming such that modules of the program can be used in other models outside the 3D GIA model in ABAQUS CAE presented in this thesis.

The self-gravitation module was used in the post-seismic model presented in Nield et al. (2022). In Nield et al. (2022) ABAQUS was used to build a post-seismic-model FEM model, similar to the model in this thesis, but tailored to model slip on a fault instead of GIA. The self-gravitation module from the model in this thesis could be plugged into the model of Nield et al. (2022). Applying self-gravitation changed the deflection of the post-seismic deformation by less than 0.1% in vertical direction and an even smaller amount in horizontal direction. Thus, post-seismic simulations by themselves do not need to include self-gravitation but it does allow the model in Nield et al. (2022) to include other geophysical processes, such as modelling GIA near active faults.

Furthermore, the transition to ABAQUS CAE has allowed the model to have a more flexible mesh instead of a hard coded mesh that has been used in previous GIA studies utilizing ABAQUS (Li et al., 2020; van der Wal et al., 2015; Wang & Wu, 2006; Wu, 2004). This has allowed for the model in this thesis to have finer meshes in the area of interest, which can easily be shifted and changed in size when the area of interest changes. For small study regions the benefits of increasing the model resolution is self-explanatory but even large regions benefit from the reduced grid-size. An example of an area requiring high spatial resolution is at the glaciers at the end of large ice streams. The highest ice mass loss in deglaciating regions is generally at the end of large ice streams that accumulate ice mass loss from a wide area and experience high rates of calving at their end (Robel & Tziperman, 2016). The erosion caused by the rapidly deglaciating coastal glaciers often form fjord-type coastlines, deep throughs that can cut a long way inland. Large grid-sizes might obscure these features, changing the local force representation from both ice mass loss and changes in sea level in an inaccurate manner.

Because of the flexible grid, the 3D GIA model has not only been used in the areas presented in this thesis (West-Antarctica and Europe), but also for Greenland (Faure, MSc thesis 2022; Kempenaar, MSc thesis 2022). Greenland hosts a plethora of glaciers on its coasts that have grown and shrunk over the last glacial cycle, some of which are

currently melting. This is in contrast with the interior of the ice sheet which is stable and has accumulated precipitation over the glacial cycle. As a result, the elements representing the relatively small strip of coastal glaciers need loads that are higher in magnitude but smaller in scale than the interior of Greenland, as can be seen in the input (as computed by ANICE on with a 20 km grid-size) for the first timesteps in the simulations by Kempenaar (2022) that are shown in Figure 2.7. The reduced grid-size allows the model to accommodate these localized differences in ice loading. The earlier discussed (Chapter 1) viscosity differences that exist for the mantle underneath Greenland amplify this need for a small grid-size as it can result in a relatively shallow response and local high uplift in southern Greenland (Faure, 2022). Kempenaar (2022) has used a version of the model that is coupled with an ice evolution model (van Calcar et al., 2023), which requires a global sea level equation (explained in Subsection 3.5.1) to be present and an even finer grid for the sea level equations (as mentioned in section 2.3) to accurately model grounding line retreat along the jagged coast of Greenland.
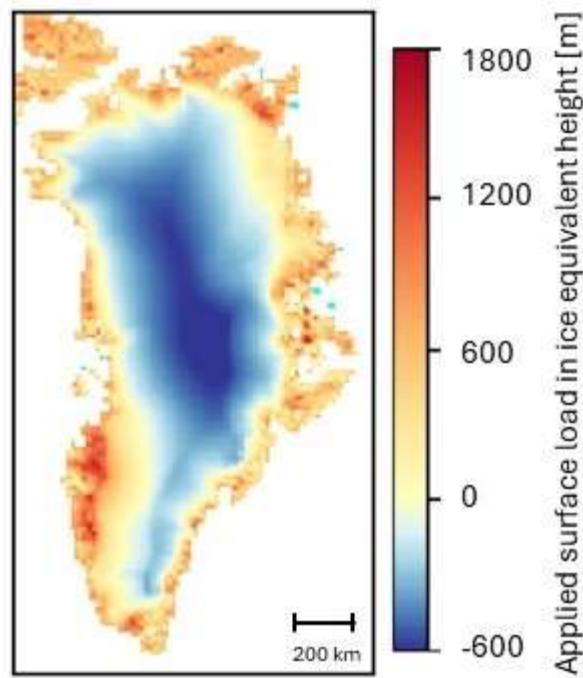
Figure 2.7: ice load in [m} applied in the first time step of the GIA model. The ice thickness was simulated by ice dynamic model ANICE. From Kempenaar (2022).

It was demonstrated in a preliminary study to this thesis that it is possible to study areas with important small wavelength details, such as Europe with the Baltic Sea coastlines, and British-Irish Ice Sheet (BIIS), using the model presented in this thesis (van Casteren, 2019). In van Casteren (2019) it was demonstrated that the model with a grid-size of approximately 80 km could find combinations of rheology parameters for 3D viscosity that could reproduce RSL curves and uplift that would match both data sets reasonably well. In Chapter 4 we expanded on these first findings, reduced the grid-size even further and included more data to compare the model to. While the rheology parameters found

in Chapter 4 differ somewhat from what was found in van Casteren (2019). In van Casteren (2019) it was already concluded that including wet rheology or small grain sizes would result in insufficient uplift in Scandinavia and that including a viscosity change in the European mantle to simulate the Eastern European Craton is beneficial when comparing the model results to the data in Scandinavia.

Because the grid-size was reduced to 40 km when studying Europe, some results of Chapter 4 could also be used for studying newly acquired sea level data in the North-Sea area (Hijma et al., 2025). The advantage of the high-resolution area in the global model was that we can simulate realistic global RSL curves, based on global GIA, while also including the stresses of continental sized ice shelves without resorting to assumptions for boundary conditions in contrast to for example flat Earth models, similar to what we have done in for the ASE in Chapter 3 (Blank et al., 2021). The separate and even finer grid for the global sea level equation is an important asset for the North Sea study as the sea is so shallow. Having a fine grid for the sea level module therefore helps with accurately modelling shoreline migration in general, but specifically for the shallow area around the Dogger Bank and the North Sea ice sheet. With the model, we can reconstruct a range for the GIA signal due to the Eurasian ice sheet to the observations presented in Hijma et al. 2025. Similar to Chapter 4, it was shown that viscosity differences underneath the North Sea are either not present or only have a small influence as the newly acquired RSL data agreed best with 1D models and 3D models with small viscosity differences.

Additionally, the flexibility of the model has also led to a coupled model in which the 3D GIA model has been coupled with the ice sheet evolution model ANICE (de Boer et al., 2014), to study the effect of 3D rheology on ice sheet evolution (Kempenaar, 2022; van Calcar et al., 2023). The fine mesh elements in the 3D GIA model allow for better resolution at the coastline. Additionally, the grid-size for the grid on which the global sea level equation is solved is finer, which helps accurately implementing the grounding line. An accurate grounding line is paramount as ice calving is the main deglaciation source for Antarctica's coastal ice shelves and the change in bedrock elevation influences the grounding line making it important to ice sheet stability in Antarctica (Pattyn & Morlighem, 2020). Failing to accurately model the grounding line can lead to convergence issues in areas with large grounding line retreat.

The models themselves could be coupled because in ABAQUS the RESTART feature allows the basic model described in this thesis to be paused and subsequently generate output on deformation. This is useful as the output can be used by ANICE to compute the ice evolution over the timestep for the specified GIA deformation, which can be reintroduced to the GIA model. The GIA model can then continue the iteration of the current timestep. This entire process continues until the ice loading and deformation during the timestep converge (van Calcar et al., 2023). An important feature of the model resulting from the use of ABAQUS is that non-linear rheology can be simulated. Calcar et al. (2023) found that the uplift rates are potentially greater in models with a strong

non-linear component. This slows grounding line retreat and ice mass loss, which shows that the earlier found stabilizing effect with 3D viscosity (Gomez et al., 2018; Konrad et al., 2015) is even stronger when we apply non-linear rheology.

The possibility to incorporate the non-linear rheology has also led to insights on the effects of background stress in GIA (Blank et al., 2021). In a non-linear rheology the viscosity is dependent on stress, which also includes stress from non-GIA processes. In the MSc. Thesis of Morra (2021) it is shown that the model could be adopted to include mantle stresses. By changing the stress tensor and thus the uni-axial stress used in Equation 2.19, the ABAQUS user subroutine can compute the uni-axial strain rate as a consequence of multiple stress sources (e.g. GIA induced stress and mantle convection induced stress). It must be remembered, however, that the stress in Equation 2.19 is transformed according to Equation 2.8 to fit the FEM. This means that adding stresses must firstly be done in Equation 2.8, so the stress tensor can be transformed and recomputed by adding the mantle stresses. Transforming the changed stress tensor back according to Equation 2.8 allows the new stress tensor to be used by the ABAQUS subroutine. A full integration of this process into the GIA model for every timestep would open the possibility of coupling a mantle dynamics model with the GIA model to study the effects of mantle induced stresses on the GIA process.

Finally, the model has also been used to study polar wander on Earth (Weerdesteijn, 2019; Weerdesteijn et al., 2019). The transport of the Earth's water (liquid and solid) during a glacial cycle and deformation of the Earth in the wake of this redistribution of mass all change the Earth's moment of inertia which shifts the rotational axis. The secular, long-term part of this is called polar wander. The change in rotational axis causes a shift in rotational induced (centrifugal) forces. The changes in the centrifugal potential can be applied to the 3D GIA model to account for the polar wander on Earth, after which the moment of inertia is updated. Although the combined model did not utilize the high-resolution region (grid-size used was 200 km), the RESTART feature was used by Weerdesteijn (2019) in order to pause the model for each timestep. ABAQUS could then be coupled with a different physics model for which is was necessary to step through time instead of compute all time steps before computing self-gravity. The developed model was used to understand if 3D rheology has a significant impact in how the Earth deformed due to polar wander, which in turn influences polar wander itself.

Considering all studies that have used this model in the short time it has been available to a few researchers shows the usefulness of the model in general, and the different topics it has been used for demonstrating the model versatility. The adaptable high-resolution area makes the model usable for most GIA regions as it has been used for the ASE, Antarctica, Greenland, Europe and specifically the North Sea. The modular set-up of the model makes the model or parts of the model useable for GIA, post-seismic evaluation, a GIA-ice sheet evolution coupled model, a GIA-mantle dynamics coupled model and a GIA-rotational dynamics coupled model

Chapter 3

Effect of Lateral and Stress-Dependent Viscosity Variations on GIA Induced Uplift Rates in the Amundsen Sea Embayment

B. Blank[1], V. Barletta[2], H. Hu[3], F. Pappa[4], and W. van der Wal[1]

1) Delft University of Technology, Delft, Netherlands

2) University of Technology Denmark, Anker Engelunds Vej 1 Bygning 101A, Kgs. Lyngby, Denmark

3) Imperial College London, South Kensington, Londen, England

4) Kiel University, Otto-Hahn-Platz 1, Kiel, Germany

Abstract

Accurate GIA models are required for correcting measurements of mass change in Antarctica and for improving knowledge of the sub-surface, especially in areas of large current ice loss such as the Amundsen Sea Embayment (ASE). Regionally, seismic and gravity data suggests lateral differences in viscosity (3D). Furthermore, mantle flow laws allow for a stress-dependent effective viscosity which changes over time (3D-s). In this study we investigate whether models with 3D/3D-s have significant effects on the uplift in the region. We use a finite element model with composite rheology consisting of diffusion and dislocation creep, forced by an ice deglaciation model starting in 1900. We use its uplift predictions as synthetic observations to test the performance of 1D model inversion in the presence of viscosity variations. Stress-dependent rheology results in lower viscosity beneath the load and a more localized uplift pattern. We demonstrate that the background stress from earlier ice load changes can both increase and decrease the influence of stress-induced effective viscosity changes. For the ASE, fitting 1D models to 3D model uplift results in a best fitting model with viscosity that represents the average of a large area, while for 3D-s rheology, local viscosity is more influential. 1D models are statistically indistinguishable from 3D/3D-s viscosity with current GPS stations. However, 3D and 3Ds models should be taken into account when accurate uplift and gravity rate patterns are needed, as uplift can differ up to 45% compared to 1D models in between existing GPS stations.

3.1 Introduction

Glacial isostatic adjustment (GIA) is the response of the solid Earth to the melting of large ice sheets, and the accompanying changes in the relative sea level, and gravitational field. It is ongoing in areas of former large Pleistocene ice sheets such as North America and Scandinavia, but also in currently glaciated areas such as Antarctica. There, modelling of GIA is necessary to correct satellite measurements of mass change for GIA. in order to reveal current ice mass change (Caron & Ivins, 2020; M. A. King et al., 2010; Shepherd et al., 2018). Additionally, comparing output of GIA models to observations that are dominated by GIA or corrected for current ice mass change effects can give us insight in the structure of the Earth. GIA is sensitive to a viscosity distribution in radial direction, but also in lateral directions. This is particularly relevant in Antarctica, where it is known that a large contrast in viscosity between East and West Antarctic mantle exists. Furthermore, GIA plays an important role in the deglaciation process itself through a feedback loop of the solid-earth response with the Antarctic ice sheet (Barletta et al., 2018; Gomez et al., 2018; Whitehouse et al., 2019). Still 1D models, which can be described as models that only have radially varying parameters (Ivins et al., 2013; Peltier, 2004; Whitehouse et al., 2012), have mostly been used to correct satellite gravimetry measurements (King et al., 2010; Shepherd et al., 2018) because of their computational simplicity. 1D models have also been used to model

small regions in West Antarctica which have lower than average viscosity (Nield et al., 2014; Samrat et al., 2020; Wolstencroft et al., 2015).

GIA induced uplift rate and horizontal rate is altered when using 3D rheology(A et al., 2013; Kaufmann et al., 2005; Nield et al., 2018; van der Wal et al., 2015), especially near the boundary between low viscosities in West Antarctica and high viscosities in East Antarctica. In Kaufmann et al., (2005) Kaufmann et al., (2005) a 3D model was used to investigate the effects of lateral viscosity variations in the Antarctic mantle. While the results of Kaufmann et al., (2005) showed that their 3D Maxwell rheology has some influence on GIA (most notably horizontal motion), they concluded that the differences in ice models have a larger impact. A et al. (2013) showed that a compressible 3D rheology affects GIA model uplift predictions to a large degree in Antarctica (up to 60%), although it must be noted that this figure was found when the 3D rheology was compared to a continent-wide average viscosity. The differences for the ASE specifically were negligible. However, as these studies were not focused on finding accurate rheology parameters or quantifying rheology differences in terms of GIA movement, both Kaufmann et al., (2005) and A et al. (2013) tested a single set of 3D rheology parameters and used ice models that did not incorporate the recent ice loss in the ASE. It is shown by van der Wal et al. (2015) using multiple different sets of rheology parameters that the effect of unknown lateral viscosity changes can be larger than these previous studies suggested. This raises the question under what condition 3D viscosity variations become significant.

The Amundsen Sea Embayment (ASE) exhibits the largest observed ice mass loss of the Antarctic continent in the last few decades (Rignot et al., 2019; Shepherd et al., 2018, 2019) of about -130Gt/y (Barletta et al., 2018). The destabilization of the Amundsen glaciers could start a collapse of the whole West Antarctic ice sheet (Seroussi et al., 2017) even though solid earth response could provide positive feedback that acts to slow down the acceleration of ice melt (Konrad et al., 2015). The largest ice loss currently occurs at the Pine Island Glacier (PIG), the glaciers near the Crosson Ice shelf and at the Thwaites Glacier (TG) (Gourmelen et al., 2018; Konrad et al., 2016). The ASE is the region where the highest uplift is measured by means of GPS stations. Only a small part of the uplift rates is explained by the elastic response of present-day melt, which indicates that the region either has an ice history in which large Pleistocene or early Holocene loads were present, or it is underlain by a low viscosity which makes it more sensitive to more recent ice load changes. Global or large-scale GIA models (Martín-Español et al., 2016; Nield et al., 2018) (either 3D or 1D) are unlikely to included recent ice mass losses to a high temporal resolution and are therefore unable to predict the GPS measured uplift values observed in the ASE because they do not model the deglaciation in the last century. Barletta et al. (2018) demonstrated with a 1D model that the ice loss

of the last few decades in combination with a low viscosity is necessary to explain the high uplift values.

In Barletta et al. (2018), a good fit was achieved between GPS-data and simulations with a GIA model in which viscosity only varies in radial direction. However, seismic models suggest lateral changes in Earth properties below or near the region(An et al., 2015a; Lloyd et al., 2015) but it is not clear if these viscosity contrasts have significant effects on the uplift rate. Furthermore, it is not clear whether the viscosities found for the ASE by means of a 1D model are a good representation of the average 3D viscosity, and whether inferences from 1D models can be used as local constraints on 3D viscosity maps. Viscosity is a macroscopic description of deformation that takes place at micro-scale. Experiments on mantle rocks show different deformation mechanisms which depend on the grain size of the rock, but also mechanisms which depend on stress with an exponent larger than one (Hirth & Kohlstedt, 2003). Such behavior is also called power-law creep. Because of the non-linear stress dependence effective viscosity decreases as stress increases. This could lead to further stress changes and changes in effective viscosity.

Nield et al. (2018) showed that the use of a representative 1D model may not only affect the magnitude of the GIA uplift compared to 3D non-linear rheology, but also the uplift gradient in their GIA uplift profile. Non-linear rheology results in steeper gradient and makes the pattern more localized. More recently there have even been efforts through the combination of multiple 1D models, to simulate 3D lateral differences in Earth structure. In Hartmann et al. (2020) Antarctica was modelled by different 1D models for the Eastern and Western parts of the continent. The results showed large conformity with the 3D finite volume model used in Hay et al. (2017). Finally, in Powell et al. (2020) a direct comparison is made between 3D models and 1D models for Antarctica and West Antarctica specifically. Their conclusion is that introducing lateral viscosity differences lead to measurable differences in horizontal bedrock movement and smaller differences in the vertical component for the stations in ASE at present day. However, there is strong emphasis on recent ice mass solely which leaves the question how past changes in both ice loading and Earth parameters would affect their conclusions.

Using power-law rheology the viscosity becomes stress-dependent, with higher stresses causing lower viscosity. Therefore, large ice mass changes and the subsequent stress changes can lower local viscosity. Furthermore, in a power-law rheology viscosity is also dependent on background stresses (Gasperini et al., 1992; Schmeling, 1987; Wu, 2001). Processes such as mantle convection, post-seismic deformation, and stresses from earlier ice loads could contribute to the total stress in the mantle and could change the effective viscosity. To express the fact that steady-state effective viscosity changes

with location and under influences of stress (Von Mises stress, specifically), which is itself is dependent on time, we will use the term 3D-s viscosity, or even 3D-s model, which means a model with laterally varying and stress-dependent viscosity. Stress-dependent models are not widely considered when computing GIA corrections although the effective viscosity can change in time by up to two orders of magnitude in viscosity (Barnhoorn et al., 2011). A GIA model with stress-dependent viscosity has been used for Antarctica (van der Wal et al., 2015), but for the ASE there has been no study detailing the effect on non-linear rheology, and the effect from background stress.

While stress-dependence can lead to effective viscosity that changes in time, it is not the same as transient rheology in which the solid Earth response is dependent on the loading frequency. The (extended) Burgers rheology is a notable example of a rheology that includes transient creep (Ivins et al., 2020; Jackson & Faul, 2010), It is used for example for post-seismic deformation (Nield et al., 2022) and seismic wave response (Carcione et al., 2014). It is possible that the response of the loading to ice load changes since is also governed by transient creep. Lau & Holtzman (2019) place different rheologies in one frame-work that can be used for different geodynamics processes. However, here we focus on the Maxwell model that combines elastic and viscous response, with the viscous response taken to be steady-state non-linear creep, with creep properties that can vary with location.

We identified the following research question: *What is the influence of 3D/3D-s effective viscosity profiles in GIA models on uplift rates in the Amundsen Sea Sector?* This question is divided into the following sub-questions:

- How representative is the best fitting viscosity in a 1D Earth model of average 3D viscosity?

- Can 3D viscosity be discerned in a statistical significant manner from 1D models using current uplift rate measurements?

- How important is stress-dependent viscosity for the uplift?

- What is the influence of background stresses on 3D-s effective viscosity and uplift?

In this study we will use 3D and 3D-s GIA models to simulate uplift rates at GPS station locations. The simulated GPS values will be used to perform an inversion for viscosity in a 1D model, similar to van der Wal et al. (2015). The best fitting 1D viscosities found will be compared to an average of the local 3D viscosities. This will provide insight in whether the best fitting 1D viscosity model is an average of the 3D model, or whether 1D samples the 3D viscosities in a different way. Furthermore, we will also investigate

the uplift pattern of the 3D and 3D-s models and see to what extent they can be represented by a 1D model. Finally, a comparison will be made between 3D and 3D-s models to study the effects of the stress-dependent viscosity. Here we also include a full glacial history to investigate whether the background stresses in the mantle due to earlier deglaciation influence our findings for the recent ice-load changes.

The structure of this paper is as follows. In section 2 we will start by introducing the FE model. After that, we will describe Earth model parameters and ice input for the model. This will be followed by a short description of the 1D model used for the inversion. In section 3 the research questions are addressed, after which main conclusions are summarized in the last section.

3.2 Method

3.2.1 3D finite element model

The 3D/3D-s model used in this study is a FE model based on the commercial software ABAQUS^{TM}, following the method of Wu (2004). In this approach a stress transformation is applied so that the equations of motion are transformed into a form in which they can be implemented in the FE model. Self-gravitation is applied by computing the change in gravitational potential and applying it to the model as a new force at each density interface after which a new deformation can be computed and the process is repeated until convergence. The FE model that formed the basis of the rotational dynamics model in Hu et al. (2017) has been modified to incorporate GIA, lateral varying viscosity, and variable resolution. A high resolution region (HRR) has been introduced to the model to simulate GIA in small regions, such as the ASE. A global model with high resolution is not computationally feasible. Therefore, the model was divided in sections with different element sizes, with the smallest elements located in the HRR around the ASE and larger elements located in the far-field (FF) (Figure 1). For this study the HRR is centered around the ASE and its smallest elements surfaces are 25 by 25 km. The element size of the far-field for this study is based on similar models without a HRR and a focus on continent scale GIA (van der Wal et al., 2015) and measure 200 km by 200 km near the equator. All element sizes are given in Table 1. Furthermore, deeper layers such as the lower mantle are meshed with a lower resolution to further reduce the total amount of elements. Depending on the model the computation time of the model would be in the order of 5 to 10 days. A benchmark of the FE model in this configuration for different test cases can be found in the supplementary material. The code has been benchmarked with results from Martinec et al. (2018) for a spherical cap load near the north pole (64°N 75°W). It can be seen in Figure S3.3 of the supplementary material that the deflection underneath and near ice masses differs between the FE model and the benchmark model by 1.3% for a resolution of ± 0.25° x 0.25°. This is a significant improvement from the 2° x 2° of earlier

implementations of the method of Wu (2004), including the 0.5° x 0.5° spatial resolution from the recent study of (Huang et al., 2019). It must be noted that the resolution is lower when compared to the global finite volume models used in Powell et al. (2020), or local normal mode model, such as Barletta et al. (2018) whose grid points are approximately 5 km apart.
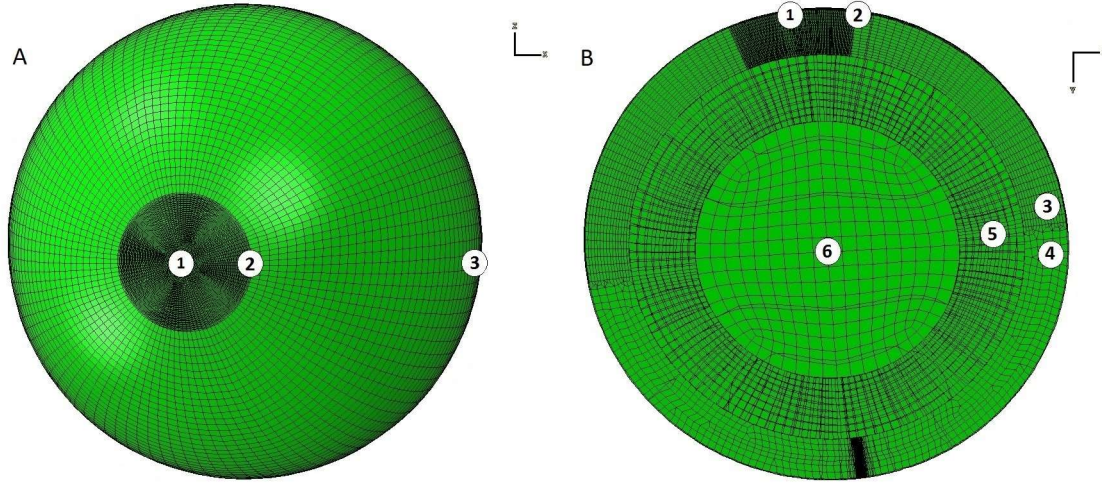
Figure 3.1: Finite-element mesh (A: top down view left, B: cross section view) used for the 3D FE GIA model. The high resolution area has a radius of 15 degrees (from point 1 to point 2) and is centered at the ASE (108.3°W, 76°S). Element dimensions for all six designated regions can be found in in Table 3.1.

Table 3.1: Approximate size of elements for sections of the model shown in figure 1, at the top of the specific layer.

Location	Latitudinal size [km]	Longitudinal size [km]	Radial size [km]
1. Center HRR	25	25	50
2. Rim HRR	27	92	50
3. FF south of equator	200	200	50
4. FF north of equator	200	200	200
5. Lower mantle	200	200	200
6. Core	400	400	400

The sea-level equation (SLE) is included according to the algorithm from Kendall et al. (2005) including changes in shorelines due to melt-water influx and changing shorelines (Johnston, 1993; Milne & Mitrovica, 1998). Small changes to the algorithm of Kendall et al. (2005) are applied to make it suitable for the FEM; these can be found in the supplementary material. The most important changes are that the 3D model can directly calculate the deflection through its FEM component of the code and the gravitational field changes by using Wu, (2004), instead of having to solve for them. Furthermore, the 3D model uses the change in ice load instead of the total ice load, for which the algorithm has to be adopted. Additionally, some functionalities were added to decrease

computation time. The effect of rotational feedback is small on the spatial scale that we consider and is not included. It is important to note that the sea-level equation can be solved at a higher resolution than the FE grid. This allows shoreline locations which experience large force changes over time as a result of ice grounding to be modeled with high spatial accuracy. Here, the SLE is solved in a global equiangular grid of $0.25°$ x $0.25°$. It must be noted that the full Sea level equation (SLE) is only used for the modelling of the ASE with a full glacial cycle ice history, to investigate the effect of Pleistocene ice history on present-day uplift rate and stress-dependent viscosity. For all other simulations an eustatic sea level with static shorelines is used to make the results comparable with a local 1D model.

3.2.2 Rheology

We use Maxwell rheology in which elastic and viscous (steady-state) deformation are summed. Elastic parameters for the Earth model are the same as the M3-L70-V01 model (Spada et al., 2011) see Table 3.1. The entire model is assumed incompressible ($v = 0.5$) as compressibility is non-trivial to add to the model (Wong & Wu, 2019). The 1D model discussed later is compressible. We have verified that differences introduced by the assumption of incompressibility are much smaller than the effect of rheology studied here (see supplementary materials).

Table 3.2: Earth model used for the 3D GIA model.

Layer	Depth top of layer [km]	Density [kg/m^3]	Youngs Modulus [Pa]	Viscosity [$Pa \cdot s$]
Top elastic layer	0	3037	$0.506 \cdot 10^{11}$	∞
Upper mantle	30	3438	$0.704 \cdot 10^{11}$	3D
Transition zone	420	3871	$1.055 \cdot 10^{11}$	Case specific[1]
Lower Mantle 1	670	4978	$2.283 \cdot 10^{11}$	$2 \cdot 10^{21}$
Lower Mantle 2	1171	4978	$2.283 \cdot 10^{11}$	$2 \cdot 10^{21}$
Core	2911	10750	0	0

The top layer of the model is fully elastic and has a thickness of 30 km. This is the minimum thickness of the lithosphere in offshore west Antarctica (Pappa et al., 2019). The lithosphere in most of Antarctica will be thicker, as the temperature results in higher effective viscosity and consequently larger effective thickness of the lithosphere. As a consequence, the density of the top mantle layer has been adjusted to 3438 kg/m3, to keep the total mass of the Earth constant. Below the top layer, the layers are viscoelastic and the effective viscosity determines whether there is significant viscous deformation over the timescale of the loading. Thus, the lithospheric thickness defined as the top part of the Earth that behaves fully elastic is defined implicitly by the effective viscosity. For the short time scales we consider in our study the lithospheric thickness will be

---

[1] Depends on the temperature and chosen rheology parameters

effectively larger than for a study for the full glacial cycle for the same Earth model (Nield et al., 2018). In the upper mantle, diffusion and dislocation creep parameters B are as calculated in Equation 3.3. The 3D variation in the creep parameters is determined by the temperature. Temperature estimates are discussed in the next section. For the transition zone the viscosity was calculated following the same procedure, however in this layer the temperature is uniform with depth and is extrapolated from the respective temperature models. Viscosity derived from shear wave velocities shows relatively high viscosity in the transition zone and smaller lateral variations (Ivins et al., 2023) which likely means little sensitivity to 3D viscosity in the transition zone for the small ice loads used here. and the load induced stresses are negligible compared to the upper mantle. Therefore, it was chosen to use linear rheology for these elements as it saves computation time without influencing the results. We assume that the rheology of the upper mantle is controlled by olivine and uses the steady-state flow law (when no melt is assumed) compiled by Hirth & Kohlstedt (2003):

$$\dot{\epsilon} = A q^n d^{-p} f_{H_2O}^r \, e^{-\frac{E+PV}{RT}}$$

Eq. 3.1

Here, A and α are experimentally determined constants. Furthermore, q represents the stress present. The parameter d represents the grain size, while f_{H2O} represents the water content within the olivine. Uncertainty in the the parameter d and f_{H2O} will lead to much larger changes in viscosity than the uncertainty in activation enthalpy resulting from experiments and these will be used as free parameters that are varied between rheology models. Viscosity changes as a result of, for example, activation enthalpy are smaller. Pressure P is assumed to increase linearly with depth Z according to $P(GPa) = 0.0333 \cdot Z(km)$ (Kearey et al., 2009). R is the gas constant and T the local temperature. Temperature and stress are the only parameters that can vary with location, with temperature variations having a larger control on viscosity. Finally, E is the activation energy and V is the activation volume.

Deformation mechanisms for olivine under upper mantle conditions include diffusion creep, dislocation creep and grain boundary sliding (Hirth & Kohlstedt, 2015) which can be combined to obtain an upper mantle flow law (e.g. (Ivins et al., 2023)). Here we use the two main mechanisms diffusion creep and dislocation creep which suffices for our goal of having a mix of linear and non-linear rheology. They can both be represented by equation 1. Diffusion creep rate is strongly dependent on grain size, with grain size exponent p of 3, but only linearly dependent on stress (stress exponent n of 1) and water content (water content exponent r of 1). Dislocation creep rate is linearly dependent on grain size ($p = 1$) and non-linearly dependent on stress ($n > 2$) and water content ($r = 1.2$). The non-linear stress-dependence gives rise to the time-dependence of effective viscosity. The deformation mechanisms have different activation energy and volume, as given in Hirth & Kohlstedt (2003). Following van der Wal et al. (2010) the two mechanisms are combined in a so-called composite rheology.

The olivine rheology is implemented in the FE model as follows. It is postulated that the relation between the stress and strain rate measured in a uni-axial experiment as compiled in Hirth & Kohlstedt (2003) also holds for the relation between the equivalent stress and equivalent strain rate which are invariants of the stress and strain tensor respectively (Ranalli, 1995):

$$\dot{\tilde{\epsilon}} = B\tilde{q}^n \qquad\qquad \text{Eq. 3.2}$$

where B is derived from equation 1

$$B = Ad^{-p} f_{H_2O}^r \, e^{-\frac{E+PV}{RT}} \qquad\qquad \text{Eq. 3.3}$$

The equivalent stress used here is the so-called Von Mises stress:

$$\tilde{q} = \sqrt{\frac{3}{2} q_{ij} q_{ij}} \qquad\qquad \text{Eq. 3.4}$$

and the corresponding uni-axial equivalent strain rate is

$$\dot{\tilde{\epsilon}} = \sqrt{\frac{2}{3} \dot{\epsilon}_{ij} \dot{\epsilon}_{ij}} \qquad\qquad \text{Eq. 3.5}$$

To get a relation between tensor components, assume that the components of the deviatoric strain rate tensor are proportional to the components of the deviatoric stress tensor with a factor λ (Ranalli, 1995):

$$\dot{\epsilon}_{ij} = \lambda q_{ij} \qquad\qquad \text{Eq. 3.6}$$

It can then be derived (Van Der Wal et al., 2013) that:

$$\dot{\epsilon}_{ij} = \frac{3}{2} B\tilde{q}^{n-1} q_{ij} \qquad\qquad \text{Eq. 3.7}$$

In ABAQUS the uniaxial equivalent strain increments are computed from time increments Δt as follows:

$$\Delta\tilde{\epsilon} = B\tilde{q}^n \Delta t \qquad\qquad \text{Eq. 3.8}$$

and components of the incremental strain tensor are computed as:

$$\Delta\epsilon_{ij} = \Delta\tilde{\epsilon}\frac{\delta\tilde{q}}{\delta q_{ij}}$$

Eq. 3.9

where the derivative is (Zhang, 2005):

$$\frac{\delta\tilde{q}}{\delta q_{ij}} = \frac{3q_{ij}}{2\tilde{q}}$$

Eq. 3.10

Combining Equations 3.8-3.10 yields:

$$\Delta\epsilon_{ij} = \frac{3}{2}B\tilde{q}^{n-1}q_{ij}\Delta t$$

Eq. 3.11

which agrees with Equation 3.7. The stress transformation of Wu, (2004) does not affect the deviatoric stress so the above equations can be used directly.

The equations in this section hold for both diffusion creep and dislocation creep. In order to implement the composite rheology we use the fact that diffusion creep and dislocation creep occur simultaneously and their components can be added for the uni-axial flow law and for the relation between the uni-axial equivalent strain rate and the Von Mises stress that is input in ABAQUS (Equation 3.8):

$$\Delta\epsilon_{ij} = \frac{3}{2}(B_{diff} + B_{disl}\tilde{q}^{n-1})q_{ij}\Delta t$$

Eq. 3.12

$$\dot{\tilde{\epsilon}} = \frac{3}{2}(B_{diff}\tilde{q} + B_{disl}\tilde{q}^{n})\Delta t$$

Eq. 3.13

Defining an effective viscosity η_{eff} as $\eta_{eff} = \frac{\tilde{q}}{\dot{\tilde{\epsilon}}}$, it follows from Equation 3.13 that (van der Wal et al., 2013)

$$\eta_{eff} = \frac{1}{3B_{diff} + 3B_{disl}\tilde{q}^{n-1}}$$

Eq. 3.14

The viscosity depends directly on temperature estimates and can vary strongly as a function of grain size and water content (Barnhoorn et al., 2011). This is in contrast to an approach whereby seismic velocity anomalies are scaled to viscosity anomalies (as for example done in Gomez et al. (2018), Hay et al. (2017) and Powell et al. (2020)). In that approach a background viscosity is needed, which can be informed by parameters from GIA or other geodynamic studies. Our approach does not require a background viscosity model and can provide viscosity values that are independent from parameters in geodynamic studies. However, they depend strongly on grain size and water content

which are unknown, and hence some guidance on these from other studies are necessary. In principal grain size and water content can also be varied with location but as we have little information on the grain size and water content across Antarctica (van der Wal et al., 2015) they are kept spatially homogeneous. We have chosen the values based on a fit with GPS uplift values, as will be explained in the results section. For the areas outside of Antarctica we no longer compute dislocation creep and diffusion creep parameters from temperature, water content and grain size (Equation 3.3), but we set them to predefined values of $1.11 \cdot 10^{-22} Pa^{-1}s^{-1}$ and the dislocation parameter to be $3.33 \cdot 10^{-35} Pa^{-3.5}s^{-1}$, with $n = 3.5$, which gives a good fit with global RSL data (van der Wal et al., 2010). This will effectively simulate a viscosity of $3.0 \cdot 10^{21} Pa \cdot s$ when no stress is considered. The composite rheology changes to a Maxwell rheology below 420 km depth for two reasons. First of the temperature models used did not contain spatial variation anymore at this depth and secondly stress at this depth turned out to be neglible for the considered load in the ASE, thus voiding the need for the more computationally heavy composite rheology type elements. For the deeper mantle (>670 km) we considered a linear Maxwell rheology with a viscosity of $2 \cdot 10^{21} Pa \cdot s$

Equation 3.14 shows that the effective viscosity always decreases with an increased Von Mises stress. The affect of adding a predefined Von Mises stress in a non-linear rheology was investigated by Wu (2001) and for composite rheology by Gasperini et al. (1992). The main conclusion from these studies is that realistic predefined mantle stresses can significantly affect the GIA process, depending on their magnitude, as they impact the stress invariant and thus the effective viscosity below the load over time.

In our composite rheology, the change in viscosity due to a load induced stress q_l in the presence of a background stress q_{bg} can be defined as follows:

$$\Delta\eta_{q_{bg}} = \frac{1}{3B_{diff} + 3B_{disl}\tilde{q}_{bg}^{n-1}} - \frac{1}{3B_{diff} + 3B_{disl}(\tilde{q}_{bg} + \tilde{q}_l)^{n-1}} \qquad \text{Eq. 3.15}$$

This equation depends on the importance of dislocation creep with respect to diffusion creep, and hence on the value of $\frac{B_{diff}}{B_{disl}}$ as well as the load induced stress. If we plot the results of Equation 15 for different values of q_l we can see the aforementioned drop in effective viscosity in the presence of background stress as a function of $\frac{B_{diff}}{B_{disl}}$, see Figure 3.2. We see that for rheologies where the contribution of dislocation creep is large ($log_{10}(B_{diff}/B_{disl}) = 10$), a large background stress will decrease the drop in viscosity as a consequence of the load induced stress. In these cases the viscosity is already lowered significantly by the background stress itself, so the extra stress from the load has little impact. If on the other hand dislocation creep has a small contribution, the drop in viscosity caused by load induced stresses will always be low, regardless of background

stress. In between the extreme cases there exists a window (around $log_{10}(B_{diff}/B_{disl}) \approx 13.5 - 18$ depending on the load magnitude) where larger background stresses will also lead to larger drops in viscosity when a load is applied. This window is relevant as it exists in the range of plausible rheologies. This means that, while the general rule is that the presence of background stress reduces the decrease in viscosity for a given load, in specific situations the presence of a background stress can also strengthen the effect of load induced stress and thus time dependency for the solid earth response.
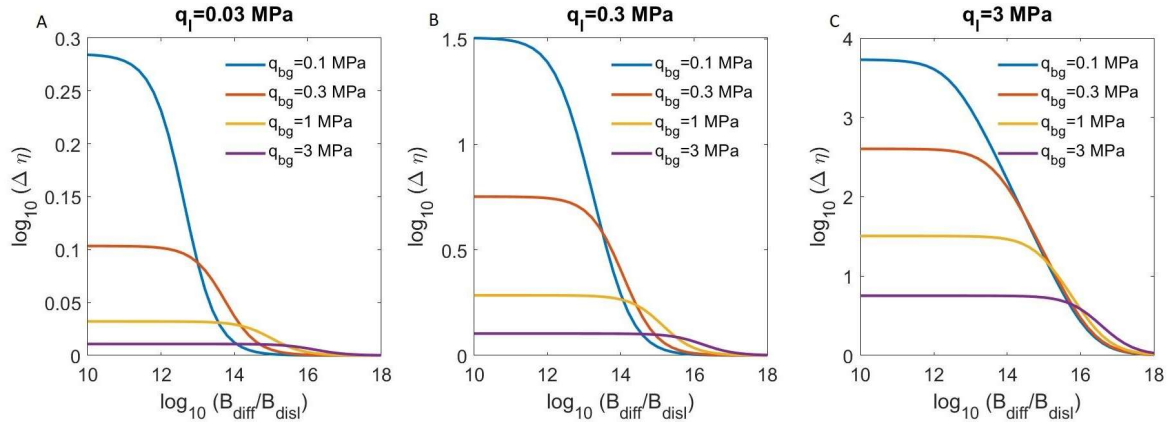
Figure 3.2: Decrease in viscosity $log_{10}(\Delta\eta)$ as a function of different non-linear rheology settings B_{diff}/B_{disl} with different values of background stress q_{bg} present. Figure A): Drop in viscosity for different background stresses as a consequence of 30 kPa of load induced stress (q_l = 0.03 MPa), which is comparable to the stress in the upper mantle at about 200-400 from the main ASE load. Figure B): Drop in viscosity for different background stresses as a consequence of 0.3 MPa of load induced stress (q_l = 0.3 MPa), which is comparable to stress in the upper mantle directly underneath the recently diminished ASE glaciers. Figure C): Drop in viscosity for different background stresses as a consequence of 3 MPa of load induced stress (q_l = 3 MPa), which is comparable to the stress from ice sheets of several kilometers thick as present during the LGM

In reality the situation is more complicated because the Von Mises stress can both increase and decrease if a background stress field is added, depending on the magnitude and direction of the individual stress components (Schmeling, 1987). In section 3.5 we investigate the effect of stresses induced by loads from the last glacial cycle on the GIA response due to recent ice loading. Both loading processes are simulated in the model, hence the stress addition takes place inside the FE model. This is the first time that the stress interaction from long timescale GIA and short timescale GIA are investigated. While we did not investigate the influence of tectonic stress, there is tectonic movement in and around West Antarctica (Eagles, Gohl, et al., 2009; Eagles, Larter, et al., 2009) that can also form an important source for background stress. This means tectonics background stress can have similar interactions with the short time scale ice load induced as the LGM induced stress and would be worth investigating in future research.

3.2.3 Temperature models of the upper mantle

For this study two new temperature models are used. Both models are created using different variants of the LitMod3D modelling framework (Fullea et al., 2009, 2018), which will be described further below. As a key characteristic, LitMod3D links thermochemical conditions in the Earth to geophysical-petrological observations. The rock composition is defined using the major oxide system CFMAS (CaO, FeO, MgO, Al_2O_3, SiO_2). These oxides represent 98% of the mantle material (McDonough & Sun, 1995) and form five independent variables, which are combined in the four main mantle mineral phases (olivine, pyroxene, plagioclase, spinel). Stable mineral assemblages are determined using Gibbs free energy minimization. The lithosphere-asthenosphere boundary is defined by the 1315°C geotherm. Heat transfer in the lithosphere is assumed to be by heat conduction; below the lithosphere the temperature follows the mantle adiabat with a potential temperature of 1345 °C (Fullea et al., 2009). There conduction and convection can both occur, while between 1400 °C and 1500 °C convection is assumed to dominate. For a certain composition, LitMod3D computes the density and elastic modulus. Different observations can be used to constrain the composition, with the most important being topography and gravity data as explained in the following.

The first temperature estimate used in this study was developed by Pappa et al. (2019) by combining data from topography, seismology and satellite gravity in a lithospheric model of Antarctica in the framework of ESA-project GOCE+. The resulting temperature model for the lithosphere and sub-lithospheric upper mantle is referred to as the GOCE+ model in the following. The authors used LitMod3D (Afonso et al., 2008; Fullea et al., 2009), which is an older variant of the LitMod3D software and provides a forward modelling framework in a finite difference discretization. Prior definitions in terms of crustal and mantle domains have been made in the GOCE+ model. The Moho is defined by a density contrast of 400 kg m^{-3}. The crust of the GOCE+ model is divided into a continental and an ocean domain. The continental crust is vertically divided into three layers, representing upper, middle, and lower crust. According to the geological provinces of Antarctica and their estimated tectonothermal age, domains of the lithospheric mantle are defined and described by different peridotitic rock compositions. Using seismologically derived models of the Moho (An et al., 2015a) and the lithosphere-asthenosphere boundary (LAB) (An et al., 2015b) as a starting model, Pappa et al. (2019) modified the Moho and LAB depths in order to achieve a fit of isostasy (topography) and gravity gradients in contrast to models that are purely constrained by seismological data. Instead, independent seismically derived Moho depth estimates from various other studies are used as an *a posteriori* benchmark to evaluate the modelled crustal thickness. As a result, the GOCE+ model simultaneously fits isostatic topography, satellite gravity gradients, and seismic Moho depth estimates to a large extent. Because LitMod3D uses adiabatic temperature gradients, dynamic topography is not included within this model. As mentioned above, mantle rock compositions are predefined in this model based on geological studies on the tectonothermal age. Since

the rock densities inside this model are modelled in a thermodynamically and internally consistent way, a 3D temperature field of the Antarctic lithosphere results. The temperature distribution of the GOCE+ model for the ASE can be seen in the top row of Figure 3.3 (A, B, and C). Compared to the seismically derived temperature distribution of An et al. (2015b), temperatures are generally lower. This could be a result of the direct conversion of S-wave velocities into mantle temperatures in the model from An et al. (2015b), which does not consider the potential existence of melt or fluid inclusions and can thus be seen as an upper bound (An et al., 2015b).

The second temperature model is the WINTERC 3.2 model (Fullea et al., 2018). A newer version of LitMod3D is used here, coming along with an inversion approach where a variety of geophysical parameters are simultaneously fit to many seismic, gravitational and heat flow observations. Isostasy is applied, as well as heat flow data, topography, and surface-wave dispersion curves analysis (Schaeffer & Lebedev, 2013) as input. The fit is performed by changing the composition (notably the aluminum content of the lithosphere), the temperature and pressure within the lithosphere model. While changing mantle composition to simultaneously fit multiple data sets in itself is a selling point for the robustness of the model, the process has its shortcomings such as the fact that converting seismic velocity to gravity through linearized scaling factors ignores known petrological non-linear effects. These non-linear petrological effects are accounted for when calculating density and seismic velocities within a thermodynamical self-consistent framework. It should be noted that in this approach the Moho depth is predefined and, in contrast to the GOCE+ model, mantle rock composition is allowed to vary. By estimating the residual isostatic topography resulting from density variations, a proxy to dynamic topography is incorporated in the model. The WINTERC 3.2 model shows good agreement with temperature patterns of seismological models. Temperature maps for the ASE and surrounding regions can be seen in the bottom row of Figure 3.3 (D, E, and F).
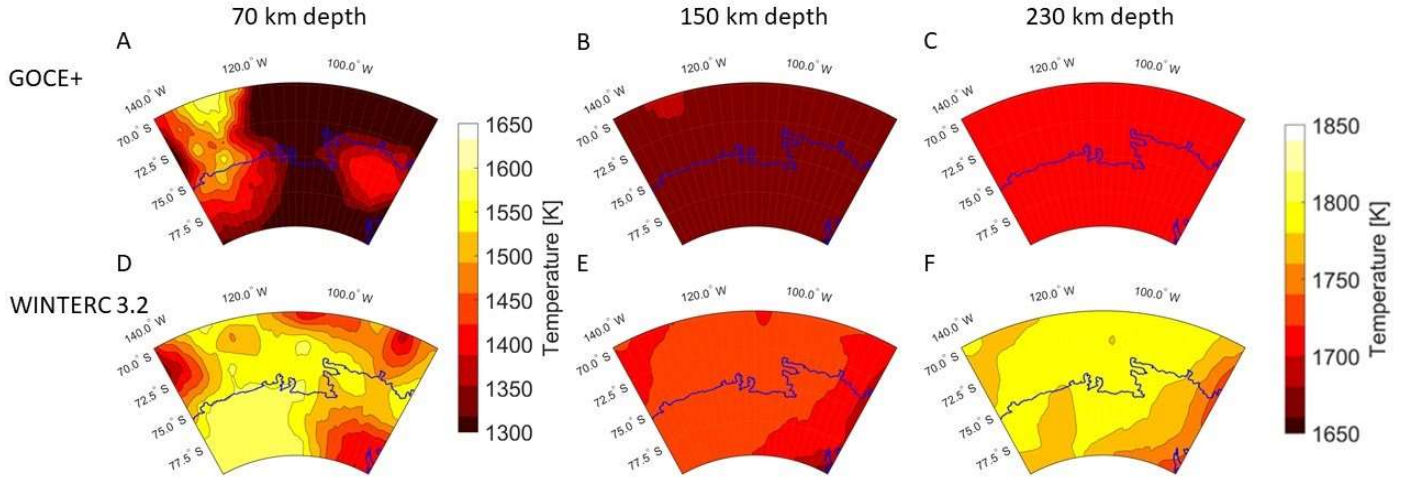
Figure 3.3. Temperature at 70 km, 150 km and 230 km depth for the GOCE+ model (top figures A), B), and C)) and WINTERC 3.2 model (bottom figures D), E), and F)) for the Amundsen Sea Embayment (ASE) and surrounding regions.

It can be seen that the GOCE+ model is colder than WINTERC 3.2 model. This is in agreement with the comparison between An et al. (2015b) and the GOCE+ temperature estimates in Pappa et al. (2019). This will result in the GOCE+ model having a higher viscosity than the WINTERC 3.2 model with the same rheology parameters, making it less responsive to short term ice loads. We also see local differences in the spatial pattern between both models. At 70 km a colder region is realized in the GOCE+ model, with warmer parts in the top part of the mantle to the east and west of the ASE. In the deeper layers of the GOCE+ model there is still a colder area north of the coast (110W°) but it is much less pronounced. In contrast, the WINTERC 3.2 model is less uniform in the top layer and has a warmer mantle underneath the ASE, near the northern coast and to the west of the ASE. This translates to a thinner elastic lithosphere in these locations. In the deeper layers of the WINTERC 3.2 model temperatures are more uniform. The most important deviations from a uniform distribution are a slightly colder area to the west of the ASE as well as a colder area in the eastern direction towards the Antarctic Peninsula. Seismic studies, for example Shen et al. (2020), predict low seismic velocities and thus high temperature directly beneath the glaciers of the ASE, showing similarities with the WINTERC 3.2 model.

It is important to note that while there is focus on the ASE itself, we use these models to construct a lateral heterogeneous viscosity map for the entire continent of Antarctica. This is done because uplift can be sensitive to viscosity in a large area, and because the simulation of the last glacial cycle was done for the entire continent.

3.2.4 Ice history model

The ice history is derived from the one proposed for the ASE in Barletta et al. (2018). In there, high resolution present-day ice changes during the time period 2002-2014 are extrapolated backwards in time until 1900 (Figure 3.4). The extrapolated ice loss trend is an overestimation of the actual trend as ice change measurements since the 1970's conclude that ice loss has been speeding up in recent years (Gardner et al., 2018; Mouginot et al., 2014). In Barletta et al. (2018) a grid search for the rheology settings for multiple ice history scenarios is performed to find the best fit to the observed GPS uplift. It is found that the ice history scenario which uses 25 % of the current trend for the period between 1900-2002, yields the best fit. We have also assumed that the rate of ice mass loss in the first half of the twentieth century is equal to that of the period of 1950-1970, which is also debatable (Ivins et al., 2002). At the start of the simulation, it is assumed that the load present in 1900 has been present for 30 ky which is practically equivalent to assuming isostatic equilibrium, which is achieved. In Powell et al. (2020) no loading is applied prior to recent satellite measured increased ice mass loss (1992). It must be noted that in our setup we initially assume no background stresses from prior ice loading, which were almost certainly present due to increased ice mass loss after 1850 (Little Ice Age) (Ivins et al., 2000). The influence of background stress on the present-day uplift cannot be assumed to be negligible and will be treated in section 3.5. The effect of pre-1900 ice loads on current uplift rates is assumed to be small. Furthermore, the ice load from Barletta et al. (2018) was tailored to fit the 1D model specifically, so it could be inconsistent with the 3D and 3Ds models introduced here, However, in this study we perform sensitivity studies comparing the different rheologies. Uncertainties in the ice history are not expected to significantly influence the characteristic differences in model behavior. Model sensitivity runs with more and slightly altered starting ice showed different uplift rates but the same characteristic difference between models. Because the ice history and the local GIA model used in Barletta et al. (2018) are of a higher resolution than the global FE model used in this study, the ice history is down sampled from ± 1 km to the size of the FE elements discussed in the method section. This down-sampling is also done for the 1D model input to eliminate possible differences as a consequence of different spatial resolution. The ice load that is used as input for the model can be seen in Figure 3.4.
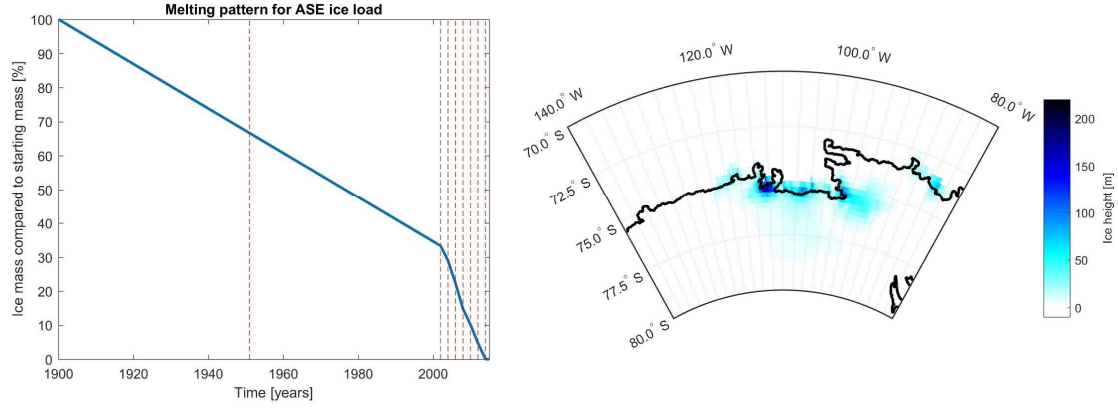
Figure 3.4: Ice model with the total mass change through time on the left and the spatial distribution on the right. The dashed red lines indicate the initial time steps at which the ice load is defined.

3.2.5 The 1D normal mode model

To evaluate the effect of 3D viscosity, the 3D model output is assumed to represent predictions for a more realistic Earth. Therefore, we seek 1D models that produce predictions compatible with those of the more granular view of the Earth's real structure. Here we use the viscoelastic uplift component for a 1D compressible Maxwell Earth model, in response to the ice mass loss, as in Barletta et al. (2018). The model is based on the normal mode viscoelastic theory where we use the VE-CL0V3RS v3.6 model (Barletta et al., 2018) to compute the elementary viscoelastic time dependent Green's functions (convolved with Heaviside function) up to degree 1500, and assume that at higher degrees they do not change with time as they sample elastic response only so the combined Green's function is negligible. The structure of the elastic parameter is PREM-based (Dziewonski & Anderson, 1981) with 31 layers, while the viscous parameters are divided into five parts. The first layer is the elastic lithosphere, which is varied in thickness from 40 km up to 70 km and represents the crust and the part of the lithosphere that behaves elastically on the timescale of loading. 40 km was used as a minimum here, because in Barletta et al. (2018) all values of 40 km showed a worse fit than those for a thicker elastic lithosphere and thin lithosphere was only observed offshore from West Antarctica (Pappa et al., 2019). The second layer is the shallow upper mantle (SUM), which is defined from the bottom of the elastic layer to a depth of 200 km. The third layer is the deeper upper mantle (DUM), which is defined from 200 km to 400 km depth. Viscosities in the SUM and DUM will be varied to achieve a good fit with respect to the uplift from the 3D and 3D-s models. The final two layers are the transition zone and the lower mantle, which are defined from 400 km to 670 km and 670 km to 2891 km (core-mantle boundary), respectively. These layers have a viscosity of $10^{21} Pa \cdot s$ in this study. In the supplementary materials we have tested this 1D setup versus the 3D setup. The maximum difference found was 1.15 mm/y and the average difference was 0.24 mm/y, which as we will later see, are not consequential to the results.

3.2.6 GPS data

For the GPS stations we have selected the same 6 GPS stations as were used in Barletta et al. (2018) with the addition of the SDLY station (Liu et al., 2018). The SDLY station is located at 125.9746°W, 77.1353°S in Marie Byrd Land, adjacent to the ASE sector. It was included to also have information on the western side of the ASE. The GPS uplift rates have been corrected with modelled elastic uplift. The elastically corrected GPS uplift, their standard deviation and length of the time-series, T_{obs}, can be seen in Table 3.3.

Table 3.3: GIA associated vertical uplift (Barletta et al., 2018; Liu et al., 2018) of GPS stations in or near the Amundsen Sea Embayment (ASE)

Stations	Uplift [mm/y]	T_{obs} [y]
BACK	10.07 ± 1.5	8.036
BERP	19.12 ± 0.7	10.386
INMN	26.05 ± 2.4	1.252
LPLY	3.93 ± 0.5	8.241
THUR	-3.99 ± 0.8	8.236
TOMO	29.90 ± 3.0	2.203
SDLY	-3.83 ± 1.04	5.0

3.2.7 Statistical model comparison

In order to compare all models evaluated in this study we use a χ^2-test with the χ^2_{cr} statistic that is also used in Barletta et al. (2018):

$$\chi^2_{cr} = \frac{1}{N_{GPS} - 1} \sum_{i=1}^{N_{GPS}} \left(\frac{M_i - m_i}{SD_{av}} \right)^2 \qquad \text{Eq. 3.16}$$

where, M_i is the uplift at the *i*th-station of the reference model, while m_i represents the 1D model uplift at the same station. Because both 1D models and 3D models provide exact results and thus no error estimate, we have assumed the standard deviation SD_{av} as the average standard deviation (1.42 mm/y) of all the real GPS-stations (see Subsection 2.6). We use the average instead of the individual standard deviation to avoid introducing a weighting bias to the stations. While the magnitude of this value might be debated, it does not change the ranking of the goodness of fit for models with respect to each other.

To determine whether or not models significantly differ from one another we used a chi-squared goodness of fit test,

$$\alpha < \int_{\chi_{cr}^2}^{\infty} \chi^2(k)$$

Eq. 3.17

where, k is the degrees of freedom for the model. In the standard case of the ASE with 7 GPS stations (as seen in Subsection 3.2.6) and a significance level α of 0.05% this would mean that if $\chi_{cr}^2 > 9.49$ the null hypotheses is rejected and the model is deemed significantly different from the (synthetic or real) measurements.

We will compare the 1D model results to 3D/3D-s models by first selecting rheology parameters for the 3D/3D-s models. We find those rheology parameters by fitting a set of rheology parameters combined with both the GOCE+ and WINTERC 3.2 temperature distribution to GPS data from the ASE region. The uplift of this best fitting model will be considered as the model standard that 1D models can then evaluate. Then, we investigate how well a best fitting 1D model will approximate the average 3D/3D-s viscosity. After this, we will investigate whether 3D viscosity results in significantly different uplift rates. Additionally, we will inquire if the results are affected by the placement of GPS stations, thus making an assessment of the robustness of any previous findings. After this, we will investigate the effect of 3D-s modelled viscosity, by comparing 3D models to a 3D-s model. Finally, we will test whether including background stress will impact our previous results significantly.

3.3 Results

3.1 Rheology parameter selection based on GPS measurements

To determine which rheology settings would fit the ASE case, we used five sets of grain sizes and water content for the GOCE+ model and four for the WINTERC 3.2 model. The number of models we can test is limited by the computational resources required. Therefore, we performed a limited grid search of the best model by varying the grain size and water content. Grain size is varied from 4 to 8 mm, close to values that give a reasonable fit to uplift in the northern hemisphere (Van Der Wal et al., 2013). Water content is varied from fully dry to fully wet (1000 ppm water content). Smaller grain size and larger water content both act to decrease viscosity. For both models we have chosen the rheologic parameters for which the chi-squared between the model results and the GPS data was minimal.

Table 3.4: χ^2_{cr} test statistics per model setting

Grain size [mm]	Water content H_2O [ppm]	GOCE+ model χ^2_{cr}	WINTERC model χ^2_{cr}
8	1000	62.4	30.3
6	1000	25.9	222.6
4	1000	10.7	710.8
4	500	10.2	231.8
4	0	109.8	-

Using Equation 3.16 we can compute the χ^2_{cr} statistic for every model we considered. The results are shown in Table 3.4. Based on the results in Table 3.4, we selected two models to focus on in this study, with a third model based on one of these first two models. The first model uses the GOCE+ temperature with a grain size of 4 mm, a water content of 500 ppm and has a transition zone viscosity of 19.3 $log_{10}(Pa \cdot s)$, which will be referred to as G405. The second model uses the WINTERC 3.2 temperature model with a grain size of 8 mm and a water content of 1000 ppm and a transition zone viscosity of 19.7 $log_{10}(Pa \cdot s)$, hence-forth referred to as W810. Two temperature models are used to differentiate between temperature model effects and general effects. Finally, a third model is used, which has the W810 settings for the rheology but dislocation creep is ignored by forcing the Von Mises stress to 0 using Equation 3.12. This is done in order to eliminate the non-linear component of the viscosity. Using a Von Mises stress of 0 will lead to an overestimation of viscosity. However, it is impossible to find a single accurate representative average Von Mises stress. The resulting model is a 3D model instead of a 3D-s model and will be referred to as W810-3D.

3.3.2 1D versus 3D/3D-s models viscosity

In Figure 3.5, the effective local viscosity is shown for G405 and W810 at two different points in time, approximately halfway through the deglaciation, in 1951, and at the end of the simulation in 2014. W810-3D is time-invariant and is shown in the bottom row. The viscosity highly correlates with the temperature map (Figure 3) for all models, with the only deviation present in high stress areas, which can be seen in Figure 3.6, near the ice load. The G405 model shows high values for the viscosity at 70 km depth with the exception of the western-most region. As the depth increases, the viscosity drops and becomes relatively uniform in horizontal directions. Changes in modelled effective viscosity over time are small for G405. This is despite the high stresses, with a maximum of 170 kPa in 1951 and 500 kPa in 2014. Due to lower water content and thus relatively small dislocation creep contribution, these high stresses do not decrease viscosity to meaningful degrees.

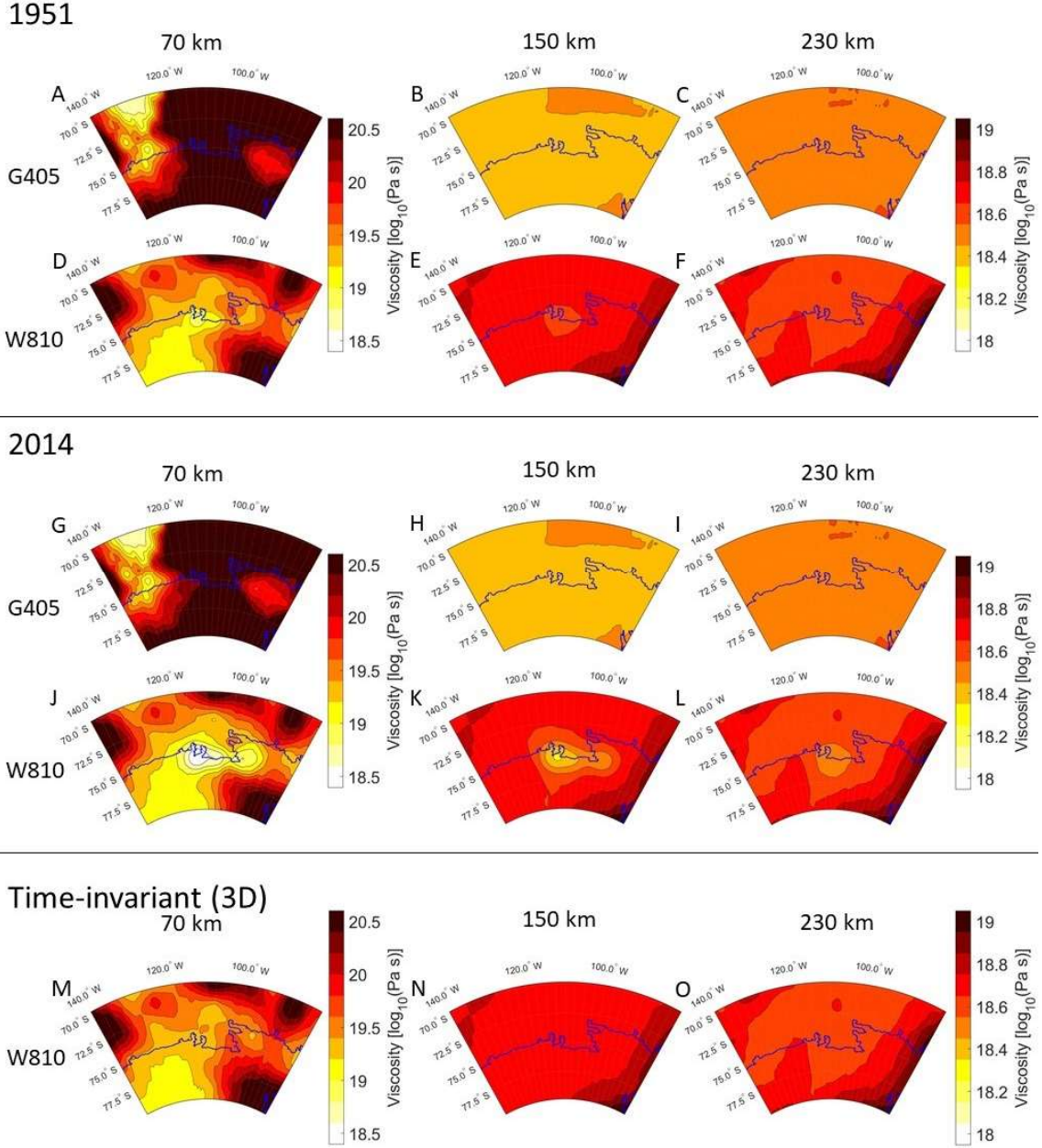*Figure 3.5: Viscosity of the ASE for three different depths: 70 km, 150 km and 230 km. The models displayed are G405, W810 and W810-3D. The top two rows show the viscosity in 1951, which is near the halfway point of the simulation. Rows 3 and 4 shows viscosities in 2014, which is the last epoch in the simulation. The bottom row shows the viscosities for the W810 version with stress independent rheology.*
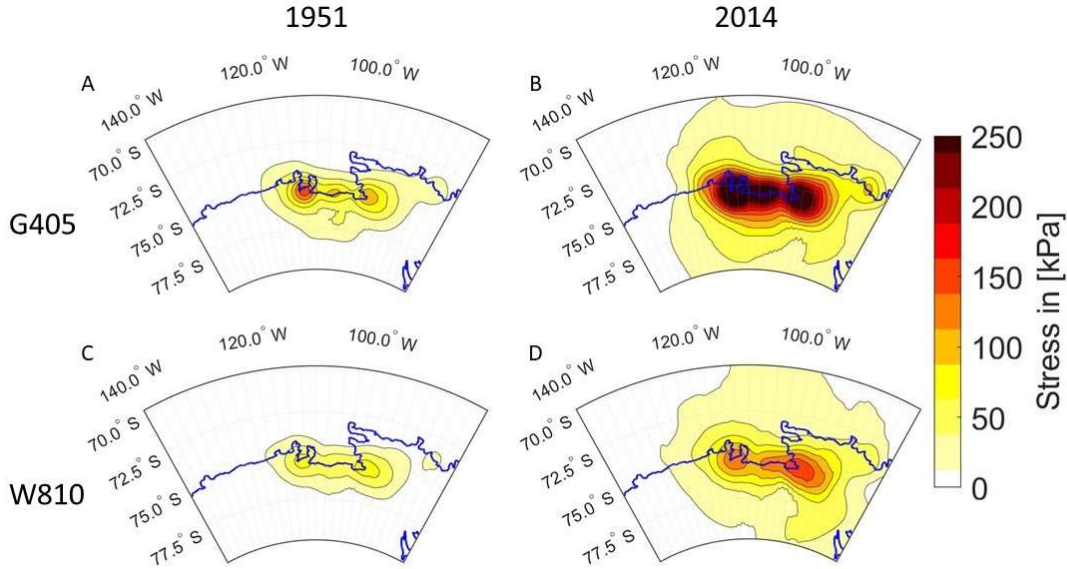
Figure 3.6. Von Mises stress in the upper mantle (70 km) of the ASE. The models displayed are G405 (Figures A) and B)) and W810 (Figures C) and D)). The left column (Figures A) and C)) show the Von Mises Stress in 1951, which is near the halfway point of the simulation. The right column (Figures B) and D)) displays the stress in 2014, which is the last epoch in the simulation.

For W810, at 70 km, there is a significant difference between the viscosities in the east and west of the ASE. In the centre of the ASE, there is an area of very low viscosity ($10^{18.0} Pa \cdot$ s) at 2014; this is where the glaciers are located with the largest mass discharge (Thwaites). This local low viscosity area is caused by the stress which is induced by the change in ice load. As the simulation approaches present day, the changes in ice load are larger than a few decades earlier. This increases the maximum stress from around 90 KPa in 1951 to approximately 175 kPa in 2014 for the final time step. The high local stresses cause dislocation creep to become a more dominant creep mechanism over a larger area which lowers the local viscosity over this area significantly. The load induced stress is reduced with increasing depth and therefore the change in effective viscosity over time is larger at 150 km than at 230 km. The last model, W8103D, has the same east-west viscosity differences in the top part of the mantle as we observed in the W810 model. In both the W810 and the W810-3D model there is an area in the east of the ASE (95°W) that has a higher viscosity compared to the neighboring coastal regions. The deeper parts of the mantle are more uniform with slightly higher viscosities towards the east in the direction of the Antarctic rift system.

To see how well the best-fitting 1D model represents the 3D structure, a representative 1D viscosity and elastic thickness of the 3D and 3D-s models has to be determined. It is not obvious how such an average should be computed from a 3D/3D-s model with a local load. The first step in order to calculate the elastic lithosphere and the average effective viscosity is determining which elements behave viscoelastic and which elements are almost exclusively elastic. Although the thickness of the purely elastic

layer is 30 km in the 3D-s model the effective elastic lithosphere thickness can be larger. The idea that elastic lithosphere thickness depends on loading duration or frequency dependent has been adopted by others as well (Lau et al., 2020). In order to estimate the viscosity for which we would consider an element elastic we consider the relation between Maxwell viscosity and relaxation time:

$$\eta = \tau G \qquad \text{Eq. 3.18}$$

As a threshold for an elastic element, 3 times a relaxation time of a 150 years of simulation is assumed. With the shear modulus G as stated in Section 3.2. We find a threshold value of $10^{21.0} \, Pa \cdot s$. By assuming elements of a viscosity larger than $10^{21.0} \, Pa \cdot s$ to be elastic we can derive an average elastic lithosphere thickness D_{litho} using relevant elements for GIA. The relevant elements are selected based on a threshold Von Mises stress, relative to the highest Von Mises stress at the depth at which the element is located in order to select elements the GIA in the ASE is actually sensitive to. For the elastic elements we did only consider elements in element layers (n_{layers}) in the elastic top layer or the SUM. We compute the fraction of elements within a selection that have a viscosity higher than $10^{21.0} \, Pa \cdot s$, $\frac{N_{\eta>21_i}}{N_{total_i}}$, and multiply this with the layer thickness D_i. Finally, the thickness of purely elastic layer, D_{crust} is added (Equation 3.19) and the results are shown in Table 3.5. We can see in Table 3.5 that G405 has a larger elastic lithosphere (53 km), while the elastic lithosphere thickness for the W810 and the W810-3D model is consistently 30 km.

$$D_{litho} = D_{crust} + \sum_{i=1}^{n_{layers}} D_i \frac{N_{\eta>21_i}}{N_{total_i}} \qquad \text{Eq. 3.19}$$

When we have defined which elements can be considered elastic, we exclude them from the viscosity averaging computations. The average viscosity for the SUM and DUM is estimated by selecting the contributing elements based on a threshold Von Mises stress, relative to the highest Von Mises stress at the depth at which an element is located. An unweighted average is taken for the selected elements in this method. An overview of the method can be seen in Figure 3.7. Using this method, it can be investigated whether the best fit 1D model viscosities are close to the average viscosity values of the FE model (Table 3.5).
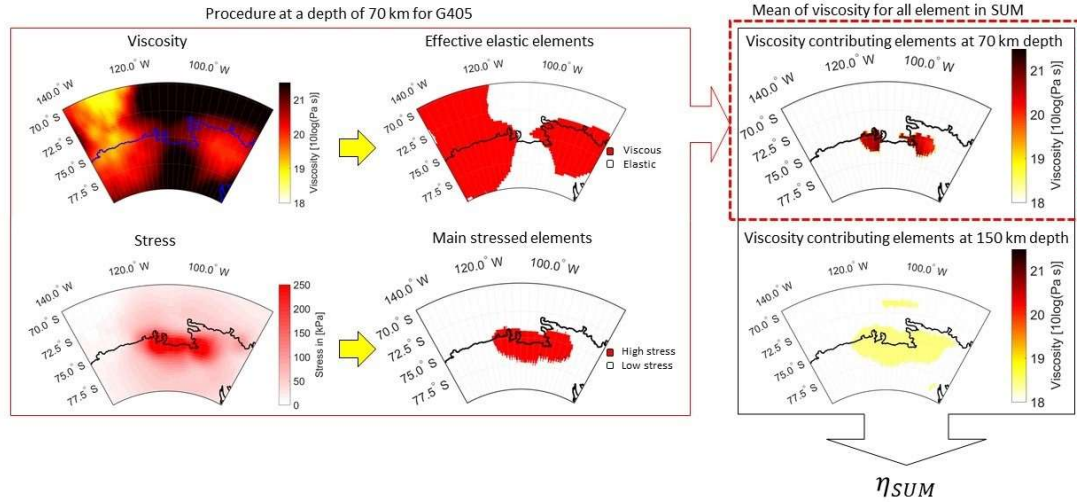
Figure 3.7: *Schematic overview of the procedure to compute an average viscosity based on stress for the SUM of the G405 model. The starting values are the viscosity and the stress at any given depth (70 km in this example). The viscosity is used to determine which elements show viscous behavior (red) over the course of the simulation ($\eta < 21.0 \log_{10}(Pa \cdot s)$). A stress threshold is used to determine the elements that contribute significantly to the uplift (red). If an element is both viscous and high stress its viscosity is used to compute η_{SUM} together with elements that also fulfil these conditions.*

Table 3.5: *Top section: Average elastic thickness (D_{litho}) and viscosity for the shallow upper mantle layer (η_{SUM}) and the deeper upper mantle layer (η_{DUM}) of the 3D and 3D-s models using stress-based selection of the elements. The SUM values are shown for both 1951 and 2014, while the DUM values are only shown for 2014 as there is little variation in this layer over time. Bottom section: Elastic thickness and viscosity for the SUM and DUM of the best fitting 1D model with respect to each of the 3D/3D-s models using the 7 GPS sites (N=7) a grid of points [71.25°S,80°S; 80.625°E,130°E] (N=1440)*

3D/3D-s model	Layer parameter	Time [AD]	G405	W810	W810-3D
Averaged values contributing elements	D_{litho} [km]	1951	59.8	30.0	30.0
		2014	53.2	30.0	30.0
	$\eta_{SUM}[\log_{10}(Pa \cdot s)]$	1951	18.94	19.22	19.08
		2014	18.91	19.02	19.08
	$\eta_{DUM}[\log_{10}(Pa \cdot s)]$	2014	18.66	18.88	18.89
Best fitting 1D models			G405	W810	W810-3D
N=7	D_{litho} [km]		70	40	50
	$\eta_{SUM}[\log_{10}(Pa \cdot s)]$		19.2	18.4	19.0
	$\eta_{DUM}[\log_{10}(Pa \cdot s)]$		18.4	18.8	18.8
N=1440	D_{litho} [km]		70	40	60
	$\eta_{SUM}[\log_{10}(Pa \cdot s)]$		19.2	18.6	19.0
	$\eta_{DUM}[\log_{10}(Pa \cdot s)]$		18.4	18.8	18.8

To benchmark how reliable the comparison is between the 1D and 3D/3D-s viscosity, a homogeneous 3D-s model was run with a top elastic layer of 40 km and non-linear rheology parameters that should correspond to an effective viscosity of 19.0 $\log_{10}$(Pa · s) for both the SUM and DUM. The best fit 1D model for this case was a model with a 40 km effective elastic lithosphere, a η_{SUM} of 18.8 $\log_{10}$(Pa · s) and a η_{DUM} of 19.0 $\log_{10}$(Pa · s). While very close to the parameters of the 3D-s model, small differences between 1D and 3D/3D-s are introduced because of difference in discretization.
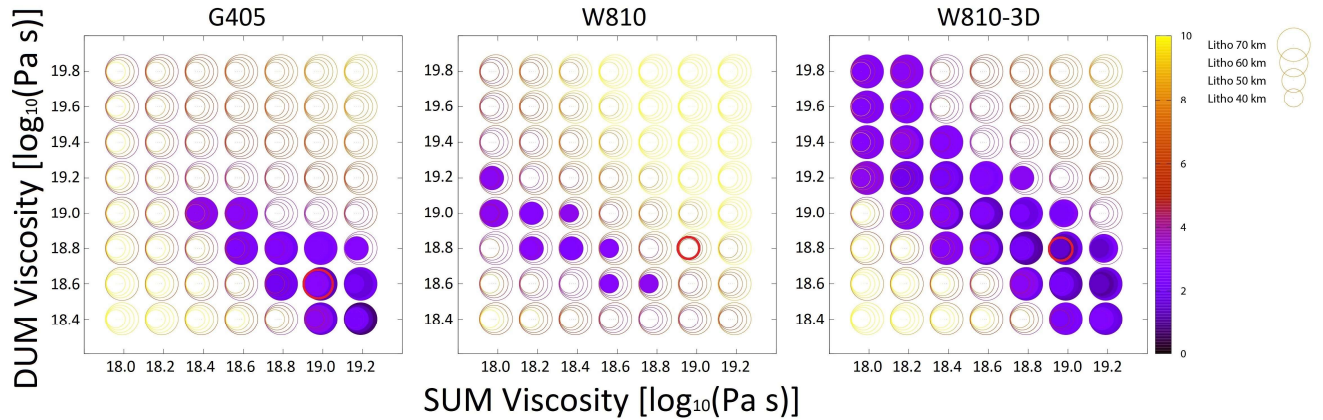
Figure 3.8: χ^2 of the 1D models with respect to simulated uplift of 3D/3D-s models as a function of viscosity in the shallow upper mantle (SUM) and the deep upper mantle (DUM). Every circle is a single 1D model, with the color indicating the χ^2. The circle size denotes models with different lithospheric thickness. All solid circles represent models that fall within the 95% confidence interval. The red circle represents the average viscosity for the 3D/3D-s model.

In Figure 8, it can be observed that there are multiple models with a good fit. The best fit 1D models in this paper for model G405 and W810-3D have a better fit to these 3D/3D-s models than to the GPS uplift rates, as was computed in Barletta et al., (2018) while model W810 has a similar value. Taking into account that for this experiment the ice history knows no discrepancy between the model standard and the 1D models approximating this, it can be concluded that G405 and W810-3D will be indistinguishable from a 1D model given the worse fit of any model to the uplift using 7 stations in reality. In order to distinguish between 1D and 3D/3D-s viscosity we would need additional GPS stations at specific points, or GPS stations with a lower standard deviation by for example increasing the length of the time-series. Longer time-series also open the possibility to investigate 3D-s in particular as the change in uplift over time would be visible and we might be able to identify the type of rheology under the ASE with more precision.

We now investigate whether the 1D viscosity obtained from the fit is close to the average 3D viscosity. In Table 3.5 we see that for all three models the viscosity for the DUM is estimated to be slightly lower (maximum of 0.3 $\log_{10}$(Pa · s)) than the average computed from the 3D/3D-s models. For both the G405 and the W810-3D models the difference

between the 1D and 3D/3D-s models in SUM viscosity is small (0.29 $\log_{10}$(Pa · s) and 0.08 $\log_{10}$(Pa · s)). For the W810 model the SUM viscosity in the 1D model underestimates the average 3D viscosity. This means that for the W810 model both the SUM and DUM 1D estimated viscosities are lower than the average viscosity. This suggests that the uplift is determined to a larger extent by a small region of low viscosity, which is not reflected in the average viscosity. The misfit of the 1D model does not strongly depend on elastic lithosphere thickness, which becomes evident from the W810-3D case. Here the 1D model prefers a thicker lithosphere but the viscosity is still the closest possible estimate. The inversion tends to prefer thicker elastic lithosphere values for the G405. In Barletta et al., (2018) it was suggested that there could be a tradeoff between upper mantle viscosity and elastic lithosphere thickness, which we see for the G405 model.

We investigate whether having limited GPS data will change the best fit 1D model with respect to the 3D/3D-s models. The best fitting model in terms of uplift is determined using 1440 reference points (all coinciding grid-points between the models) instead of only the 7 original GPS locations (Table 5). For the G405 case there is no effect of placing more stations, as 7 stations will result in the same best fit as obtained with 1440 stations. While this is not true for the W810 and W810-3D cases, we can still note that in these cases, the current 7 stations also give best fit models that have small differences in lithosphere thickness (10 km) or η_{SUM} (0.2 For the SUM) with respect to the best fit models with a large number of stations. This leads us to conclude that the current 7 stations already form an adequate data set to perform inversions when determining a representative 1D viscosity.

The resolution of the FE model is fixed to the values in Table 3.1 and Figure 3.1 to limit the computation time, and interpolation is required at multiple stages, for example from the ice history data to loads applied to the finite elements or to find uplift and locations in between model nodes. To investigate the impact of this issue we have compared GPS station uplift on their exact locations, which required interpolation, as well as on the closest model nodes to these locations, requiring no interpolation. Altering the GPS locations has a small effect on the chi-squared values of the best fit, but not enough to change the best fitting models in this paper. Changing interpolation methods for the computation of gravitational perturbation changes the average uplift by approximately 0.2%. Changing the vertical resolution can have a stronger effect on the results, because the changes in temperature in radial direction are larger than the those in lateral direction. However, GIA models cannot invert uniquely for many layers, and our results are valid for the layering in the upper mantle selected for the 1D model.

3.3.3 1D versus 3D/3D-s model uplift

To investigate whether 1D models can represent the uplift pattern of a 3D or 3D-s model, Figure 3.9 shows the difference in uplift between the 3D/3D-s models and their respective best fitting 1D model. In general, we can see that it is not possible for the best fit 1D models to fit any of the 3D models everywhere even though the models do not differ in a statistically significant fashion. This is because for most GPS locations the best fit 1D model uplift is close to the 3D/3D-s models uplift, although for every model there are 1 or 2 GPS stations that have a local bad fit (more than 2 σ difference). Locations in between the GPS sites can still show large differences (23.1 mm/y difference for W810 and 6.7 mm/y difference for W810-3D), which is more than two times the measurement error of the GPS stations. The GIA uplift pattern, for the W810 and W810-3D model, has a sharper peak with a higher uplift than the best fitting 1D model at the point of maximum unloading (cross-section a). At 76°S in cross-section a, we see more local uplift for W810 and W810-3D than the 1D model because of low local viscosity, either as consequence of the high lithosphere temperature by itself or in combination with high local stress. At cross-section b this is reversed for W810 and W810-3D, showing lower local uplift as a consequence of the local high viscosity. The different patterns in the cross-sections show that it is not possible for a 1D model to fit the uplift pattern of the 3D/3D-s model everywhere, as a change in viscosity does not only change the magnitude of the uplift but also the spatial distribution of the uplift.

We showed earlier that more stations do little to change the best 1D model for each of the 3D/3D-s models, and that with the current data the 1D models cannot statistically be distinguished from the 3D/3D-s models. However, Figure 3.9B and Figure 3.9C illustrate that this does not mean large differences do not exist and that with more GPS stations in the right locations 3D/3D-s differences could be detected. GPS stations at the point of maximum differences (dark red or dark blue areas) would be the most sensitive to differences between 1D models and 3D/3D-s models. For example, a GPS station in between the BERP and TOMO station (76°S 113°W, in the middle of cross section a) would be the most sensitive to possible low local viscosity. Another location that might give insight in the 3D effect is around 75.5°S 95°W (in the middle and to the right of cross section b) in Ellsworth Land. Large differences as a consequence of a high viscosity area are possibly present in this area. It must be noted that this high viscosity area is present because of the low temperature area in the WINTERC model; in the GOCE+ model this area has a higher temperature which would result in lower viscosity. These additional stations, if at all possible, at the mentioned locations, might provide us with data to distinguish 1D, 3D and 3D-s rheology from each other and constrain the rheological parameters to a higher accuracy. If placing extra stations is not possible another way of obtaining a data set that would be able to distinguish between rheology types is to keep the current 7 stations active for a longer time. As could already be seen in Figure 3.5G-L effective viscosity changes over time under the influences of stress,

which means uplift rates would change differently over time for these models compared to models with time-invariant effective viscosity. As the rheology in the ASE influences the WAIS stability it would be beneficial to extend the missions of these stations until their provided data can give us more insight into these possible non-linear components in the rheology.
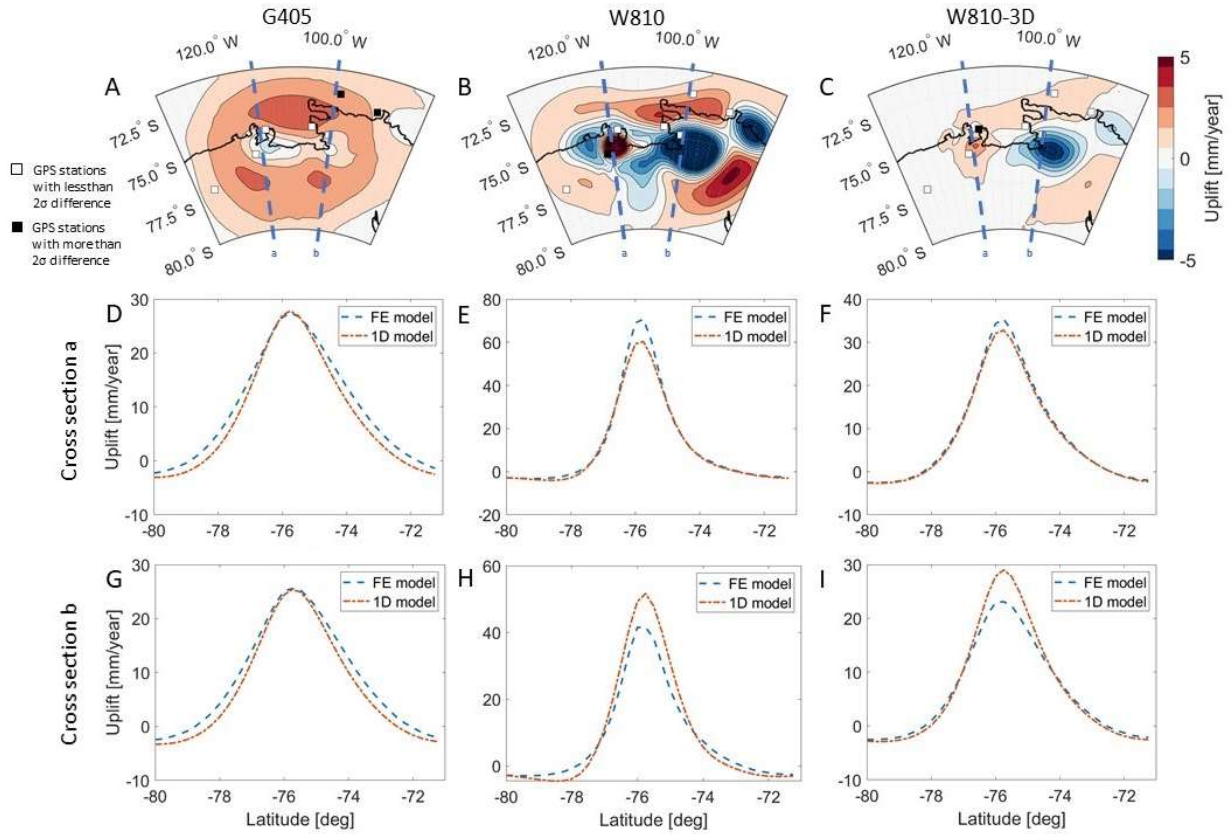
Figure 3.9: Top figures A), B), and C): uplift of the three models minus their best fitting 1D model. The black squares are GPS stations where the differences exceed 2σ (95% confidence), the white squares are stations where the differences are below 2 σ. Figures D), E), and F): cross section of the uplift of all three models and their best fitting 1D model at the 113.75W˚ meridian (a), which intersects the point of maximum uplift. Figures G), H), and I): cross section of the uplift of all three models and their best fitting model at the 97.5W˚ meridian (b), where the differences between the three models and their best fitting 1D model are the largest.

3.3.4 Effect of stress-dependent viscosity

In this section we investigate whether 3D-s rheology gives significantly different uplift compared to 3D rheology, and if any 3D rheology can approximate the effect of 3D-s rheology. We use model W810 with varying stress and compare it against W810 models in which stress is set to a constant level. Ideally, we would choose the Von Mises stress such that the time-averaged effective viscosity is the same, or the uplift differences are minimized as is done with the 1D model inversion. However, this is computationally expensive. Instead, we use a low stress (0 kPa) and a high stress (300 kPa) as lower and upper bound, respectively. This results in a significantly higher and lower average viscosity, respectively, than computed in Table 3.5. We scale these uplift patterns to

minimize the difference in maximum and minimum occurring uplift. The idea is that the pattern in uplift is largely fixed, but the magnitude will be changed as a function of Von Mises stress, which we reproduce by scaling the uplift. To support this idea, we confirmed that upscaled results and downscaled results give a similar result (Figure 3.10C and Figure 3.10D).
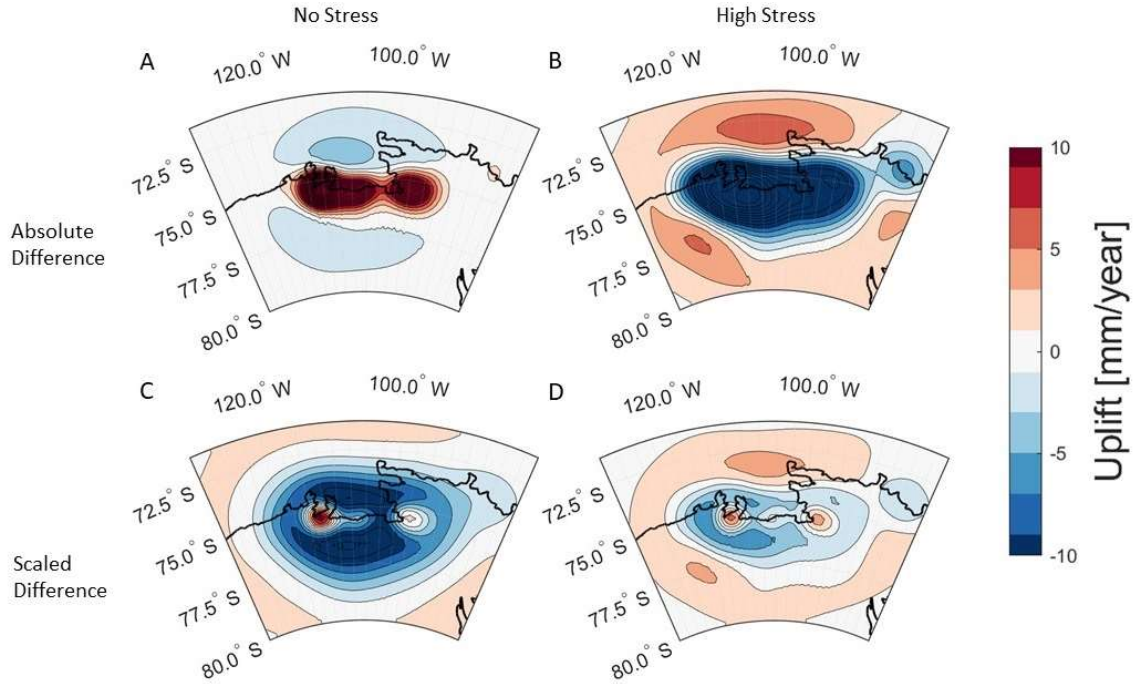
Figure 3.10: Differences in uplift: W810 a stress dependent viscosity minus W810 with a constant stress (and hence constant viscosity). Figures A) and C): Difference between W810 and W810 without stress (W810-3D) induced effective viscosity changes. Figures B) and D): Difference between W810 and W810 where a constant Von Mises stress of 300 KPa is applied. Figures A) and B): the absolute difference between aforementioned models. Figures C) and D): The difference when the constant stress models are scaled to minimize the differences, with a factor 1.73 and 0.73, for the 0 kPa case and the 300 kPa case, respectively.

In Figure 3.10A we observe that the model without stress underestimates the uplift due to the higher viscosity, while the model with 300 kPa constant stress overestimates the uplift due to the lower viscosity. The differences after scaling are positive in the center of loading and negative outside. This is the result of the constant stress models having a more spread-out uplift pattern than the 3D-s model. The average differences cannot be reduced further by scaling the uplift and when computing the the χ^2_{cr} statistics for the scaled 3D models at the location of the GPS stations we obtain values of 0.23 and 0.15, respectively for the 0 KPa scaled result and the 300 Kpa scaled result, which could be considered close fits. However, the 3D model still shows up to 14 % less uplift at the point of maximum uplift. The higher uplift in the 3D-s model can be traced back to the viscosity decrease under the load, as stress increases (see Figure 3.5G-L). It must be noted that in Figure 3.9 (A, D, and G), the G405 model did not show more localized

uplift despite it being a 3D-s model. That is because the G405 model was created using a smaller grain size and a lower water content, which results in a lower contribution of dislocation creep (Barnhoorn et al., 2011; Hansen & Kohlstedt, 2015). In conclusion, a 3D model cannot fully reproduce the uplift from 3D-s models with significant dislocation creep, which in this case is a wet model (H_2O 1000ppm) with a large average grain size (8 mm).

Nield et al. (2018) found similar differences between 1D models and models with non-linear rheology in the Antarctic Peninsula, noting the more localized uplift in the latter, as represented by differences in gradients in uplift. An important caveat in the results presented here up until this point is that no background stresses are included. The addition of long-term GIA stresses is investigated in Subsection 3.3.5 but the interaction with stresses from other processes such as mantle convection and post-seismic deformation is left to future work.

3.3.5 Effect of background stress

In all previous evaluations we only included the effects of a recent ice history as described in Subsection 3.2.4. However, as can be seen in Equation 3.14 for non-linear rheology, viscosity is a function of total stress. Larger stress will increase the contribution of dislocation creep, but at the same time it might decrease the relative importance of stress changes over time due to the loading. As stated in Subsection 3.2.2, adding a background stress can either increase or decrease the change in viscosity over time due to load induced stress changes, depending on the ratio of diffusion to dislocation creep parameter. Figure 3.2 shows us that for a ratio of around 15 orders of magnitude between diffusion and dislocation creep parameters a small load will cause a larger reduction in viscosity than a larger load. In the G405 model the ratio between diffusion and dislocation for upper mantle elements in the ASE is between 13 and 14.5, which falls in the aforementioned window where there is a larger reduction in viscosity when loads are added with a background stress present compared to the same load case without background stress. For a wet model, such as W810, this effect is less of an issue as the ratio between diffusion and dislocation is limited between 12 and 13.5 and thus the majority of the time the reduction in viscosity is less when the load is added with a background stress compared to the case without background stress. The influence of homogeneous background stress can be seen in Figure 3.11, where we look at the change in viscosity as a consequence of load induced stress. Figure 3.11A and Figure 3.11C show a viscosity reduction similar to the viscosity change we can see in Figure 3.5 between 1951 and 2014. For Figure 3.11B and Figure 3.11D a background stress of 1 Mpa is added to the load induced stress for both the G405 model and the W810 model, respectively. Only the change in stress invariant is considered here, similar to Gasperini et al. (1992) and Wu (2001).

Figure 3.11: The change in viscosity as a consequence of load induced stress by means of dislocation creep at the end of the ASE simulation. Figures A and C: the differences in viscosity when no additional background stress is considered. Figures B and D: the differences when a 1 MPa background Von Mises stress is added. Figures A and B: both background stress cases for the G405 model. Figures C and D: both background stress cases for the W810 model.

The G405 model shows an increase in viscosity change when the background stress is added. Here the increasing background stress increases the importance of dislocation creep relative to diffusion creep which makes the rheology respond stronger to stress changes, as shown in Figure 3.2B. In the wetter W810 model the dislocation mechanism is more pronounced meaning that adding background stress will dampen the viscosity changes as a consequence of time-varying stresses.

Figure 11 is essentially a snapshot of the present day viscosity if a background stress were to be introduced suddenly, which assumes it to be in the same principle direction as the load stresses and thus the Von Mises stress simply being the sum of both stresses. In reality a background stress field has different components, which means that the Von Mises stresses cannot be superimposed because stresses can cancel each other (Schmeling, 1987). Next, we take the latent stresses from GIA as a result of the millennial scale ice load changes that occurred since the LGM as a source of background stress. We introduce this stress by running the model a full glacial cycle before the simulation enters the recent ice history as described in Subsection 3.2.4. The full glacial history assumed here is the W12 model (Whitehouse et al., 2012) which continues until 500 year B.P. although the model is an interpolation between snapshots and does not have an intrinsic 1000 year resolution. No accounting is made for any changes in the past load-induced stresses from accumulation/ice loss changes in the interval between 0.5 and 0.1 ky, which could either decrease or increase the background stress, and could

influence present uplift. Including ice change in this interval could be critical for accurate modelling of the ASE, but there is great uncertainty in how to interpret the current constrains of snow accumulation and past flux gate changes in this region of WAIS where there is such complex ice dynamics and external climate drivers. The change in viscosity as a consequence of the glacial cycle stresses can be seen in Figure 3.12.
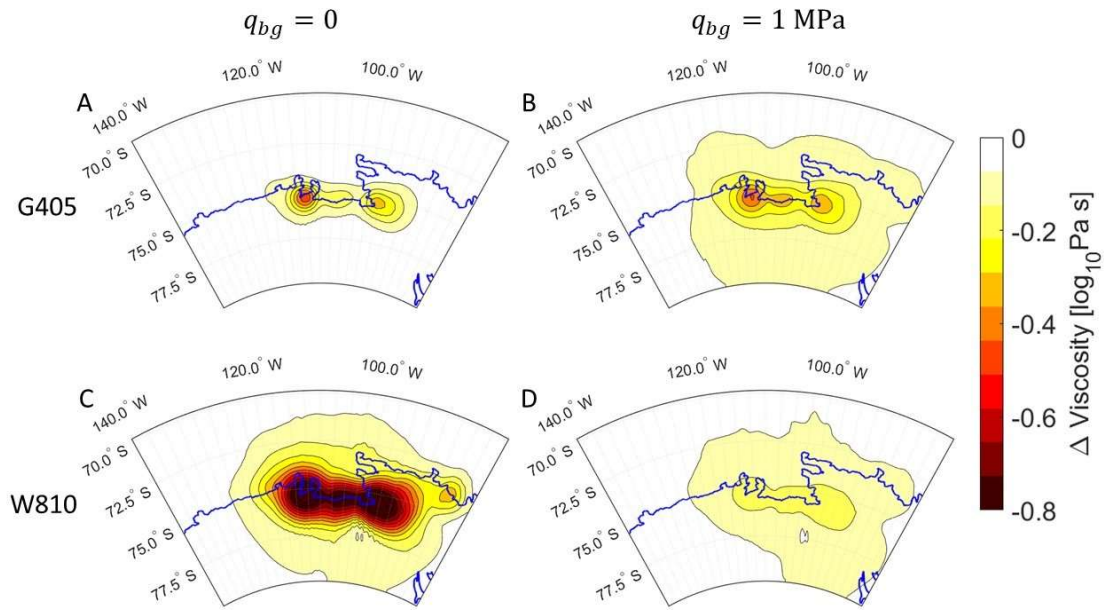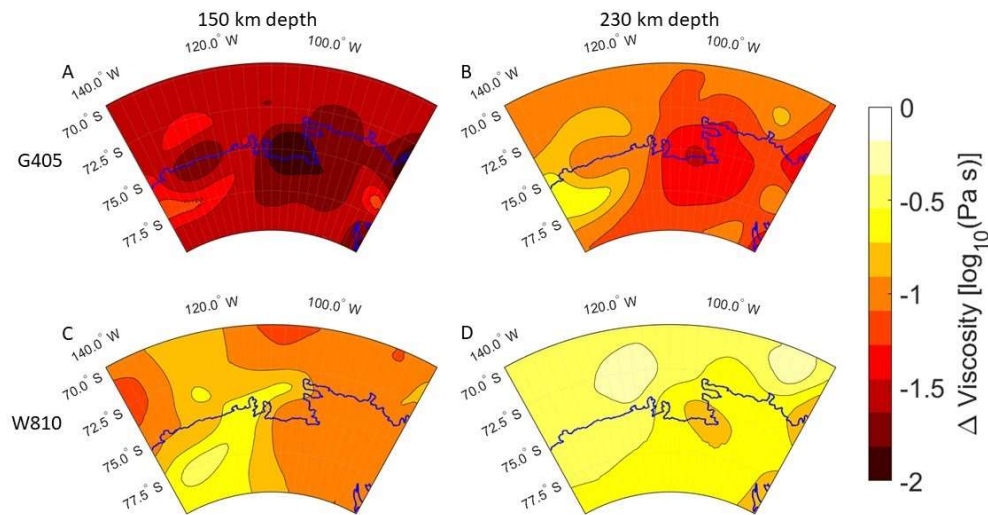

Figure 3.12: The change in viscosity as a consequence of ice age induced background stress by means of dislocation creep at the start of the ASE simulation. Figures A and C: the reduction in viscosity at 150 km depth. Figures B and D: the reduction in viscosity at 230 km depth. Figures A and B: Viscosity profiles at different depths with background stress present for the G405 model. Figures C and D: Viscosity profiles at different depths with background stress present for the W810 model.

As a consequence of the higher viscosity in the G405 model in general more stress from the ice age loads is still present at the start of the simulation, leading to a stronger reduction in viscosity compared to W810. In W810 a larger portion of the stress has dissipated in 1900 leading to a lower viscosity drop overall. This means that while wet models have a decreased viscosity drop with background stress compared to dryer models, they also have a smaller background stress, as the ductile mantle allows those models to dissipate the stress more quickly. Both the stress itself as the reduction in viscosity strongly affects the uplift for both the G405 and the W810 case. These uplift results can be seen in Figure 3.12. We now investigate the effect on the conclusions from Subsection 3.3.4 by comparing results with and without the inclusion of the W12 ice history (Figure 3.13).
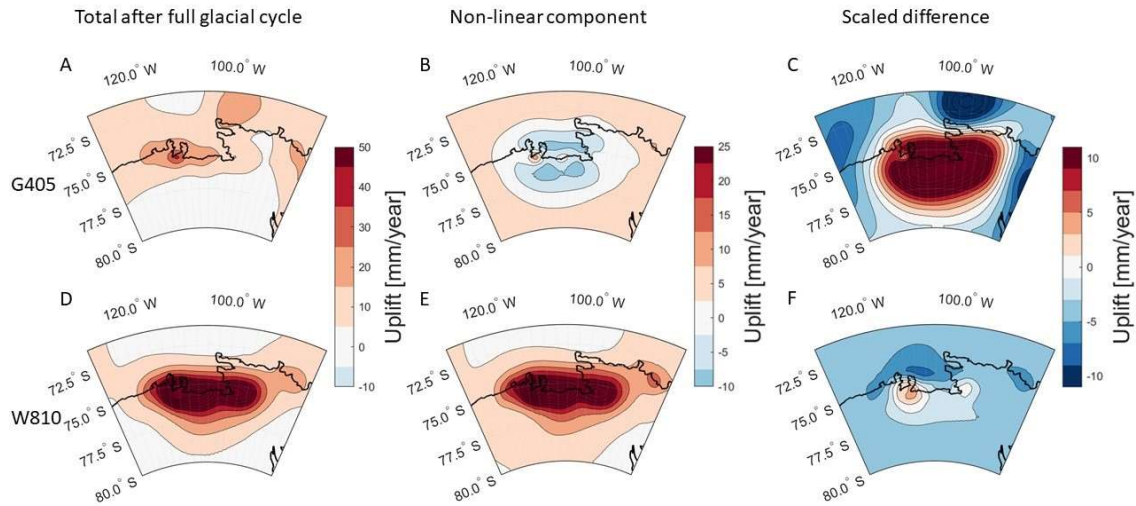
Figure 3.13: Figures A and D: uplift for both the G405 model (A) and the W810 model (D) when loaded with the W12 ice history as well as the recent ice history from Figure 4. Figures B and E: The difference between the uplift of full glacial cycle with recent loads combined in a single run and the uplift of both of those components in separate runs. This is the uplift as a consequence of the non-linear component in the rheology. Figures C and F: the uplift of the models without glacial history are scaled such that the differences squared as shown in the central column are minimized

For G405, the uplift when a full glacial history is included, is largely determined by the ice loads from before 1900. For W810 the uplift is very similar in spatial pattern to the uplift obtained from recent ice loads, with the only difference being the increase in magnitude. The fact that the G405 is influenced by the loads before 1900 and the W810 to a lesser degree is caused by the high viscosity layer in the G405 model compared to the W810 model. This high viscosity layer is still stressed at the end of the simulation from ice loads predating 1900. However, high viscosity models are unlikely given the good fit Barletta et al. (2018) achieved only considering recent ice changes. In order to understand the effect ice age stress has on current day uplift through changes in viscosity, the nonlinear component in the uplift was computed by combining the uplift from recent ice mass changes with the uplift from the ice age simulation (so there is no stress interaction) and subtract those from a single simulation where both ice histories are present (where there is stress interaction). For W810 we see that the pattern of the non-linear component matches both the uplift as a consequence of the current ice mass changes as well as the uplift from the combined ice history. If we scale the results of the combined simulation to match the results that only include recent ice changes, the resulting difference is very low. From this we can conclude that for wet models or models with low viscosity in general, background stress can have a significant effect on the total uplift as a consequence of an overall lowering in viscosity, even more so considering stress from ice mass loss in the centuries before 1900. However, as a significant portion of the background stress dissipates quickly, especially for regions that have high local stress, the overall effect on the spatial uplift pattern is limited. Areas that have experienced recent high load changes will still have more localized uplift

compared to 3D and 1D models. For G405 the situation is different as the high amount of stress in the mantle present in 1900 both changes the viscosity and local Von Mises stress such that non-linear component does not show a straightforward magnitude change in the uplift, but instead even shows areas where the non-linear component is negative. In these areas background stress and recent ice load stress have cancelled each other to some degree. The conclusion here is that for high viscosity or dryer areas, where one might expect the role of stress over time to be limited considering the small contribution of dislocation creep, non-linear rheology can still have a large impact on the final results. Even though changes in viscosity over short time frames will be less likely for these cases, the high viscosity means that stress will linger for a longer time which increases the chance of stress from different processes or time periods to interact and affect viscosity. Because of the overall lowered viscosity, the uplift response at present is stronger.

3.4 Conclusions

In the ASE region there is evidence for varying mantle structure which manifests as viscosity variations of one order of magnitude. Given the importance of dislocation creep in mantle deformation, it is also possible that stress changes induce viscosity changes over time and space. We label the model with stress-dependent viscosity as '3D-s'. Note that this still constitutes Maxwell rheology with steady-state creep. We did not include transient creep as simulated by a Burgers rheology. We simulate uplift with two different 3D-s models and a 3D model with olivine rheology with varying grain size, water content and spatial variations as a function of temperature and stress. We perform a 1D model inversion for the uplift of these models to find out how close the 1D model predictions are to those of the 3D/3D-s models.

We investigate two different temperature models based on inversion of the petrophysical-geophysical framework LitMod, with one largely based on gravity data (GOCE+) leading to more spatially homogeneous temperature and higher viscosity, and the other relying more on seismic data (WINTERC 3.2), resulting in lower viscosity and more spatial variations. For each temperature model, rheological parameters from a limited range are taken which best fit GPS uplift in the ASE. The first of the three models, G405 is based on the GOCE+ temperature profile, has a small grain size of 4 mm and a rheology between fully wet and dry olivine. The effective viscosity is rather homogeneous and has a small 3D-s effect, only dropping 0.2-0.4 $log_{10}(Pa \cdot s)$ directly under the maximum load in the last half century. The second model, W810, is based on WINTERC 3.2 and has a large grain size of 8 mm and fully wet rheology. For the latter model stress-dependence can be switched off by prescribing stress to be constant. This model is referred as W810-3D

The first main conclusion is that the best-fitting viscosity in the 1D models is close (difference of 0.3 $\log_{10}(\text{Pa} \cdot \text{s})$ maximum) to the average viscosity of the 3D and 3D-s models in the upper mantle between 200 and 400 km. At this depth the influence of 3D and 3D-s variations is small. For the viscosity estimate of depths shallower than 200 km the best fitting 1D models also find good viscosity estimates for the models with low to no stress induced variations over time in the effective viscosity. However, for W810, where stress changes reduce local viscosity more significantly, the 1D viscosity does not represent the wider regional viscosity but is biased towards local viscosity at present underneath the largest mass changes. In that case, differences in average viscosity between the standard set by W810 and the best fitting 1D model can be more than half an order of magnitude. Recent studies demonstrating abnormally low viscosity underneath the ASE are probably giving a reasonable reflection of a weighted average of a current 3D viscosity structure in the region with a stronger influence from the low viscosities under the sites of the largest mass changes.

We found that the differences between 1D and 3D models in uplift are possibly significant depending on the locations in the ASE and the 3D model assumed. This is somewhat in contrast to Powell et al. (2020), who state that 1D and 3D differences will exceed GPS measurement errors in the future but finds that for the present day the difference between regionally adapted 1D models and 3D models are around the magnitude of the measurement error and smaller. However, they did not include non-linear rheology, which as shown in this study can increase difference with 1D models significantly and had a shorter ice history, which starts from a steady state in 1992 instead of 1900. We do find that 1D models are able to fit the current regional ASE set of uplift rate measurements to a statistically significant degree and are indistinguishable from 3D/3D-s models. Despite this, this study also shows that it is also possible with certain rheologies that locations can be identified where 1D models exceed the GPS measurement error and can be distinguished from 3D/3D-s models.

For 3D-s models, the stress-dependence of viscosity creates a temporary region of low viscosity below the load. This makes uplift patterns more local for the 3D-s model compared to the 1D and 3D model. The uplift near the point of maximum stress is underestimated by the best fitting 1D model, while uplift in surrounding areas and the collapse of the forebulge is overestimated; the 1D model cannot fit both regions simultaneously. If 1D models are used to correct GIA effect in mass change measurements it could mean that GIA derived gravity rate is too low at the area of maximum mass loss and too large elsewhere. However, this result is sensitive to the magnitude of ice load changes and even more to the presence of background stresses.

When including background stresses, such as a full glacial cycle, the load induced effective viscosity drop can be amplified or weakened, depending on the relative importance of diffusion and dislocation creep. A dryer model, such as the G405 model falls within the category for which including background stress increases these viscosity drops. Due to a high viscosity in the upper mantle, G405 showed uplift patterns that were influenced by stress changes due to ice mass changes from before 1900, while the low viscosity upper mantle of the W810 model meant that stresses from earlier deglaciation were already decayed. From Barletta et al. (2018) we know that observed uplift can be modelled to a high degree by only using the recent ice history. This indicates that a low viscosity mantle such as in the W810 or W810-3D model is more likely to be representative of the actual mantle underneath the ASE. However, for both the G405 model as well as the W810 model the inclusion of stress from the LGM ice loads did change the uplift result significantly, suggesting that background stresses have to be included in areas of large past ice load changes. This likely also holds for stress in the period before recent ice melt that is not included in our model. Mass increase or decrease in the pre-1900 would influence viscosity, especially for the lower viscosity model. Stresses due to LGM ice load changes can be similar to or smaller than those of mantle convection. In the presence of large mantle convection induced background stress, the effect of 3D-s rheology used in this study is even more unpredictable. As the background stress could be spatially uncorrelated to the ice load induced stresses. The effect of mantle induced background stress is an important topic for future study.

3.5 Supplementary Materials: Effect of lateral and stress-dependent viscosity variations on GIA induced uplift rates in the Amundsen Sea Embayment

3.5.1 Sea level equation for FEM

In order to include a sea-level with migrating shorelines in the model, the theory of Kendall et al. (2005) was adopted to fit the FE model. Kendall et al. (2005) defines an increase in sea-level ΔSL as:

$$\Delta SL(\theta, \phi, t_j) = \Delta \mathcal{G}(\theta, \phi, t_j) - \Delta R(\theta, \phi, t_j) + \frac{\Delta \Phi(t_j)}{g} \qquad \text{Eq. S3.1}$$

Here t_j denotes an individual time-step within the glacial cycle. In contrast with Kendall et al. (2005), which was an SLE designed for normal mode models, the FE model is able to compute ΔG and $\Delta R(\theta,\varphi,t_j)$ in the iteration for self-gravitation; therefore an extra iteration to find these values is not needed. Furthermore, the FE model does not need the sea level directly but rather the sea level over the ice-free ocean area. This sea level over the ice-free ocean area is defined as (Kendall et al., 2005):

$$S(\theta, \phi, t_j) = SL(\theta, \phi, t_j) \cdot C^k(\theta, \phi, t_j) \qquad \text{Eq. S3.2}$$

Here the ice-free ocean function $C(\theta, \phi, t_j)$ is defined as 1 where there is ocean and no grounded marine ice and 0 for elsewhere.

The FE model is defined in terms of changes in load compared to the equilibrium situation at t_0. Therefore, the input of the FE model is the change in ice load, ΔI_j. In order to define grounded ice in terms of ΔI_j it is assumed that where the input defines a change in ice load it always refers to grounded ice. This would result in the following definition of the change in revised ice load

$$\Delta I^*(\theta, \phi, t_j) = \begin{cases} \Delta I(\theta, \phi, t_j) & \text{where } C(\theta, \phi, t_j) = 0 \\ \Delta I(\theta, \phi, t_j) & \text{where } C(\theta, \phi, t_j) = 1 \text{ and } \Delta I(\theta, \phi, t_j) > 0 \\ 0 & \text{elsewhere} \end{cases}$$

However, as most ice histories are defined in terms of ice height instead of change in ice height the model can also use the following definition of change in revised ice load

$$\Delta I^*(\theta, \phi, t_j) = \begin{cases} \Delta I(\theta, \phi, t_j) & \text{where } \mathcal{C}(\theta, \phi, t_j) = 0 \\ \Delta I(\theta, \phi, t_j) & \text{where } \mathcal{C}(\theta, \phi, t_j) = 1 \text{ and } \Delta I(\theta, \phi, t_j) + I(\theta, \phi, t_0) > |Topo(\theta, \phi, t_j)| \frac{\rho_w}{\rho_I} \\ 0 & \text{elsewhere} \end{cases}$$

To include the ocean load we need the change in ocean height ΔS with respect to t_0. Using equation S3.2 we can define ΔS as

$$\begin{aligned} \Delta S(\theta, \phi, t_j) = \Delta SL(\theta, \phi, t_j) \cdot \mathcal{C}(\theta, \phi, t_j) \\ - Topo(\theta, \phi, t_0)[\mathcal{C}(\theta, \phi, t_j) - \mathcal{C}(\theta, \phi, t_0)] \end{aligned} \qquad \text{Eq. S3.3}$$

In order to numerically solve equation 3 for every timestep t_j we have to use an iterative process in which we continuously update the ice-free ocean surface $\mathcal{C}(\theta, \phi, t_j)$ until we have reached a point of convergence for the ocean surface. Here, $Topo(\theta, \phi, t_0)$ is the topography at t_0, which is unknown initially and assumed identical to the current day topography during the first glacial cycle iteration. The iterations of glacial cycles will be denoted by index k and can be used to compute the bathymetry (topography multiplied with the ice-free ocean function) and ocean basin size through means of projections based on the previous cycle. These projections are denoted as RO and TO (Equations 68 and 70 in Kendall et al. (2005)) respectively. We will check for convergence of the topography after each iteration of k by using a convergence parameter $\zeta_{t_c}^k$ and comparing it to a convergence criterion:

$$\zeta_{t_c}^k = \left| \frac{\sum_{l,m} \left| [T_{l,m}(t_c)]^k \right| - \sum_{l,m} |[T_{lm}(t_c)]^{k-1}|}{\sum_{l,m} \left| [T_{l,m}(t_c)]^{k-1} \right|} \right| \qquad \text{Eq. S3.4}$$

Here $T_{l,m}(t_c)^k$ are the spherical harmonics coefficient of the topography at timestep t_c, where t_c is the convergence time. The convergence time is defined as the earliest time step with a considerable difference to the present-day ice load $I_{t_0} - I_{t_c} \gg 0$. In Kendall et al. (2005) it is suggested to use t_0 as convergence time. However, this might pose a problem if the initial and final load are equal and the deflection is very small, as it will lead to a very small $\zeta_{t_c}^k$ on the first iteration. Having a small initial $\zeta_{t_c}^k$ might prevent any iterations happening.

$$\xi_{t_i}^k = \left| \frac{\sum_{l,m} \left| [\Delta I_{l,m}^*(t_i)]^k \right| - \sum_{l,m} |[\Delta I_{lm}^*(t_i)]^{k-1}|}{\sum_{l,m} \left| [\Delta I_{l,m}^*(t_i)]^{k-1} \right|} \right| \qquad \text{Eq. S3.5}$$

Where i is the iteration index denoting time steps starting at $i = 0$. If $\xi_{t_i}^k > \epsilon$ it will assure at least 1 iteration for SLE module. When a convergence time is established, we can iterate the model until we reach convergence at $\zeta_{t_c}^k < \epsilon$. A typical value for ϵ is in the order of 10^{-4} (Kendall et al., 2005).

By design the algorithm will cause the ocean load to alternately be overestimated and underestimated. To reduce the computational load the algorithm checks whether the convergence is considered slow and calculates $\chi_{t_0}^k$:

$$\chi_{t_0}^k = \left| \frac{\zeta_0^k}{\zeta_0^{k-2}} \right| - 1 \qquad \text{Eq. S3.6}$$

The convergence for this study is considered slow when the change over 2 iterations in ζ_0^k is less than 33% ($\eta_3 = 0.33$). This value was chosen as it allows for near maximal reduction in computation time without introducing errors in the algorithm. When the convergence is deemed slow and an overestimated and an underestimated ocean load have been used, the average of these ocean loads is used as a new guess. This results in less iterations and continues until the $\zeta_{t_c}^k$ convergence value is met.

The projections *RO* and *TO*, together with Equation S3.1 can be used in the central equation for the SLE module to solve for the change in ocean load $\Delta S^k(\theta, \phi, t_j)$:

$$\Delta S^k(\theta, \phi, t_j) = RO^k(\theta, \phi, t_j) + \frac{\Delta \Phi^k(t_j)}{g} C^{k-1}(\theta, \phi, t_j) \qquad \text{Eq. S3.7}$$
$$- TO^k(\theta, \phi, t_j)$$

Finally, the invariant shift in geoid $\Delta \Phi^k(t_j)/g$ is given in Kendall et al. (2005) within the spherical domain as a function of the change in ice mass ΔI^*, change in bathymetry *RO* and change in basin size *TO* (Kendall et al. (2005), equation 78). A flow diagram of the entire routine can be found in Figure S3.1.
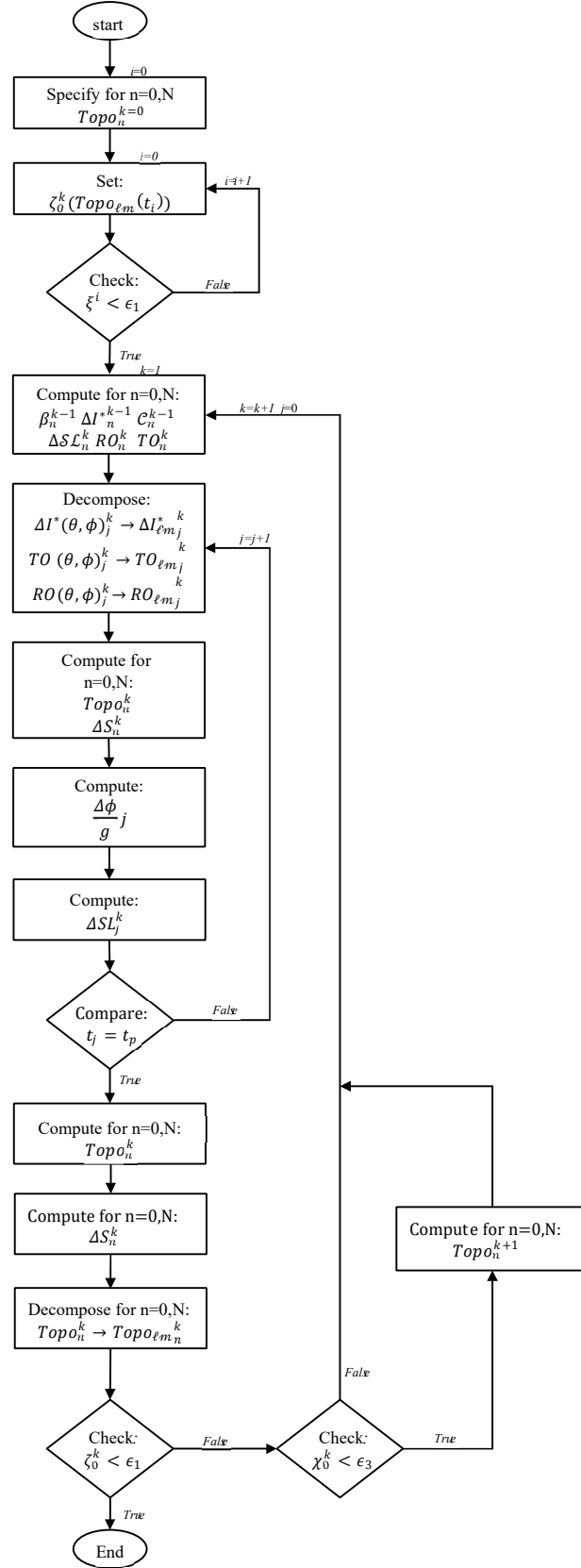
Figure S3.1: Flow chart of the migrating shoreline sea level module

3.5.2 Benchmark 1D FEM GIA model

In this subsection we will demonstrate a benchmark for the FE model for two different situations. The purpose of the benchmark is to validate the model but also to quantify the difference between the FE model and models that do not use the same methodology. We will use the benchmark setup of Martinec et al. (2018). Firstly, a benchmark will be discussed between the FE model in this paper and a rotational symmetric FE model used in Martinec et al. (2018), this test will compare deflection over time and will focus on the benefit of increasing the resolution in a target area. The second benchmark will be between the FE model and the VEGA model discussed in Martinec et al. (2018). In this test we will also include oceans with variable shorelines. This test is classified as benchmark D1 in Martinec et al. (2018). For all benchmark tests we have used the 5-layer Earth model M3-L70-V01 (Spada et al., 2011). The specifics of the M3-L70-V01 model can be found in Table S3.1.

Table S3.1: Overview of the layers and parameters in the Earth model M3-L70-V01 (Spada et al., 2011)

Radius [km]	Density [kg m^{-3}]	Shear modulus [$\cdot 10^{11}$ Pa]	Viscosity [$\cdot 10^{21}$ Pa $\cdot$ s]	Gravity [m s^{-2}]
6371	3037	0.50605	∞	9.815
6301	3438	0.70363	1	9.854
5951	3871	1.05490	1	9.978
5701	4978	2.28340	2	10.024
3480	10750	0	0	10.457

Benchmark 3D FE model versus axis symmetric FE model

In the initial benchmark we will compare the result of the 3D FE model against the benchmarked rotational symmetric FE model initially used in van der Wal et al. (2010) (Martinec et al., Klemann, van der Wal, Riva, Spada, Sun, Melini, Kachuck, Barletta, & Simon, 2018), which we will refer to as WW model for short. The ice load per unit area is defined as follows:

$$\sigma_I = \rho_I h_{max} \begin{cases} 1 & \text{if } 0 \leq \theta \leq \alpha_1 \\ 1 - \dfrac{\theta - \alpha_1}{\alpha_2 - \alpha_1} & \text{if } \alpha_1 \leq \theta \leq \alpha_2 \\ 0 & \text{elsewhere} \end{cases}$$

Here the maximum load height h_{max} is 1000 m. The load comprises of two major sections; a flat disc from $0°$ until α_1 ($10°$) followed by a linear slope until α_2 ($20°$), where the height is 0. This load minimizes differences that can occur as a consequence of discretizing the load for a random mesh it avoids high concentrated stresses one would get from a disc load.

The WW model is an axis-symmetric model with a overall resolution of 0.5x0.5 degrees. For a full 3D model this is not feasible so in this test we try to approach the rotational symmetric results by decreasing the resolution of the 3D model. The mesh of the 3D model has been changed to a rotationally symmetric mesh to better imitate the WW model.

In Figure S3.2 compare deflection for an axisymmetric FEM with a high (Polar area $1°$ x $1°$, far-field $2°$ x $2°$) and low resolution (everywhere $4°$ x $4°$) solution of the 3D model. We observe that as the resolution increases, the difference between the axisymmetric model and the 3D model reduces to less than 0.15%.
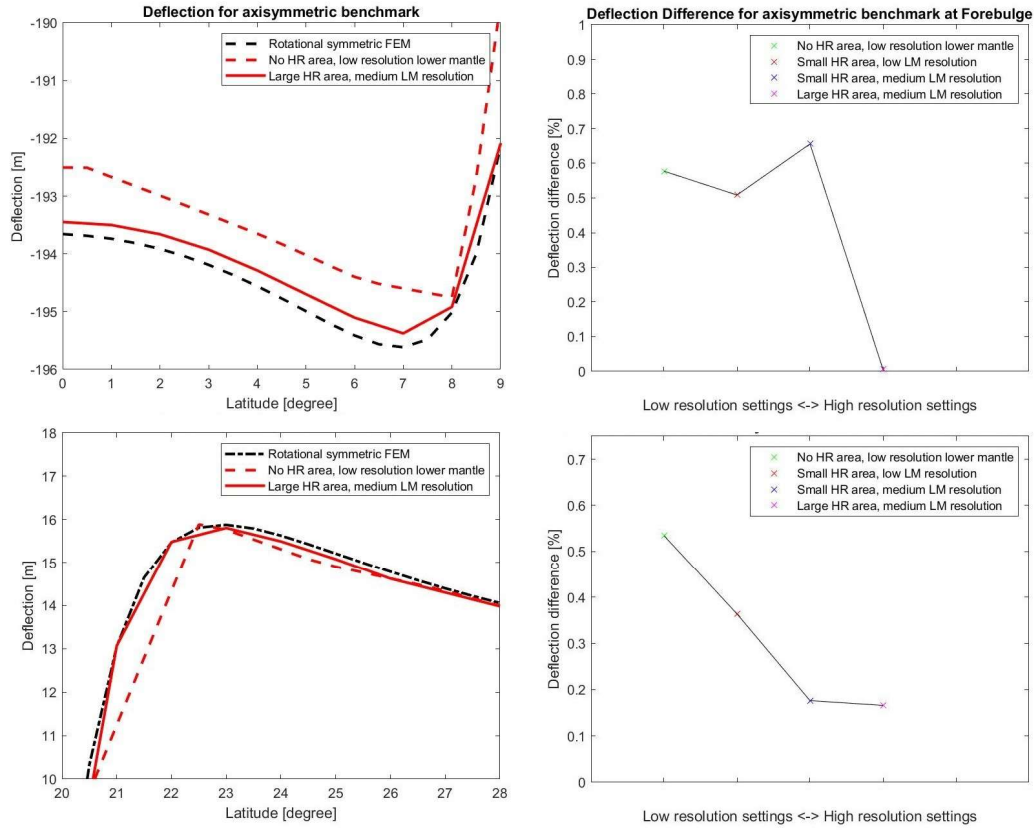
Figure S3.2: Axisymmetric benchmark deflection results for the axis symmetric model of van der Wal et al. (2010) (Black), results from the 3D FE model of this study (Red) showing the deflection results for the pole (top) and the location of the fore-bulge (bottom). The figures in the middle and right show the relative difference between the 3D model at different resolutions and the rotationally symmetric model for various locations of the model.

Benchmark D1: Ocean with dynamic shorelines

In this section we will discuss the results of the FE model in a benchmark that is referred in Martinec et al. (2018) as the benchmark D1 case. This benchmark was chosen as it bears resemblance to the ASE case and encompasses all the different components of the FE model. The benchmark will be able to provide some frame of reference on the magnitude the FE model may differ from other non-FEM GIA models. In benchmark D1 (as described in Martinec et al. (2018)) the load per unit area is defined by a parabolic cap:

$$\sigma_I(\theta) = \rho_I h_{max} \begin{cases} \sqrt{\dfrac{\cos\theta - \cos\alpha}{1 - \cos\alpha}} & \text{if } 0 \leq \theta \leq \alpha \\ 0 & \text{if } \theta > \alpha \end{cases}$$

Here, h_{max} refers to the maximum height of the ice cap, which is taken to be 1500 m. Furthermore, α is the cut-off degree, which is taken to be 10 degrees co-latitude. The

density of ice ρ_I is taken to be 931 kg m^{-3}. The ocean basin in the D1 benchmark case has the following definition:

$$b(\theta, \phi) = b_{max} - b_0 e^{-\psi^2/2\sigma_b^2}$$

<div align="right">Eq. S3.8</div>

Where

$$cos\psi = cos\theta cos\theta_b + sin\theta sin\theta_b cos(\phi - \phi_b)$$

<div align="right">Eq. S3.9</div>

Here $\sigma_b = 26^o$, $\theta_b = 100^o$, $\phi_b = 320^o$, $b_{max} = 760^o$ and, $b_0 = 1200$ m. It must be noted that an important source for discrepancies in the benchmark D1 case compared to normal runs is in the way the benchmark is set up. While the benchmark D1 case requires models to have a certain starting topography the FE model does not use the topography at t_0 as an input, but rather $t_{present}$ (see Section 4.5.1). As a consequence, the model had to be iterated several times before an input topography was found that approached (<1m) the starting topography of the benchmark model. However, the model was not iterated to full convergence because of computational and time constraints. This mainly has an influence on the found RSL near the ocean basin. The error in the RSL also influences the deformation in the basin area. Therefore, the difference between models relative to the total local deformation is higher near the basin area than in the area around the ice load. Another important factor that contributes to the errors is the limited mesh of the FE model compared to the other benchmarked models. This is especially true for the area near the ocean basin. While the VEGA model uses a resolution of 0.5° overall (~55 km on the equator) the FE model is limited to the values shown in Table 3.1. The limited resolution influences both the exact loads on the model and the structural flexibility of the model.
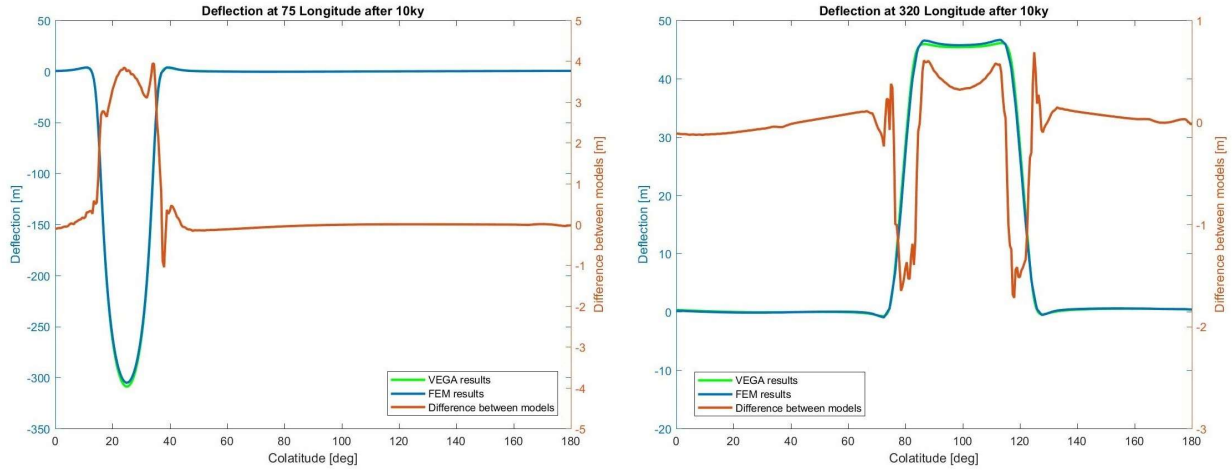
Figure S3.3: The deflection at the location of the ice load (left) and the ocean basin (right) for both the FE model and the VEGA model of Martinec (Martinec, Klemann, van der Wal, Riva, Spada, Sun, Melini, Kachuck, Barletta, & Simon, 2018). The differences for both models are represented by the orange line.

To conclude, in the benchmark D1 case the FE model shows an error of a few meters (4m or near the ice load and 1.8m near the basin). This translates into a relatively small error for the deflection, ~1.3% near the ice load and ~4% near the edges of the basin. In this paper we are only interested in uplift rates in the high-resolution area and the difference of 1.3% is deemed tolerable for the purposes of this paper. For the lateral motion the absolute errors are similar because of the inflexibility of the model, which means that a movement error in one direction leaks into the error in a different direction. This results in larger relative differences because of the smaller magnitude of the lateral movement. As the lateral differences are not discussed in this paper these differences do not influence our results.

3.5.3 Correction on movement of center of gravity for a finite element model

In this subsection we will summarize our method to correct our results for the shift between the original center of figure (OCoF) that is used as a reference origin in a FEM, and the physical gravitational center of the Earth (including ice caps and oceans), the center of mass (CoM).

The first step is to compute the shift in CoM with respect to the OCoF caused by deformation; $\vec{r}_{CoM}$. When $\vec{r}_{CoM}$ is known we can correct all forces on each interface in the model by a factor σ_{CoM}, which is defined as follows (Paulson et al. (2005):

$$\sigma_{CoM} = -\vec{r}_{CoM}\Delta\rho\cos\gamma \qquad \text{Eq. S3.10}$$

Here γ is the angle between any location on the Earth and the vector $\vec{r}_{CoM}$. Applying the correction from equation S3.10 will emulate the forces with respect to the CoM instead

of the OCoF. Because of the nature of the CoM it is also the center of the gravitational field. Following Klemann & Martinec (2011), we use the change in the gravitational field $\Delta\varphi$ to compute the change in the CoM:

$$u_{cm}^x = -\frac{1}{g_0}\sqrt{\frac{3}{2\pi}}Im\{\Delta\phi_{11}\}$$

$$u_{cm}^y = -\frac{1}{2g_0}\sqrt{\frac{3}{\pi}}\Delta\phi_{10}$$

$$u_{cm}^z = \frac{1}{g_0}\sqrt{\frac{3}{2\pi}}Re\{\Delta\phi_{11}\}$$

Eq. S3.11

It must be noted that in contrast with Klemann & Martinec (2011), who use a reference frame where the z-axis is pointed north, we have used a reference frame where the y-axis is pointed north. It is also important to note that OCoF definition in this paper differs from the definition of the CoF used in Klemann & Martinec (2011), as such we do not need to concern ourselves with the CoF motion mentioned in Klemann & Martinec (2011). The vector $\vec{r}_{CoM}$ can

now be computed using: $\vec{r}_{CoM} = [u_{cm}^x u_{cm}^y u_{cm}^z]$. In order to solve the angle γ between $\vec{r}_{CoM}$ and any point on the surface of the Earth we must first express the direction of $\vec{r}_{CoM}$ in terms of latitude ϕ and longitude θ:

$$\theta_{CoM} = \text{atan}\left(\frac{r_{CoM_x}}{r_{CoM_z}}\right)$$

$$\phi_{CoM} = \text{atan}\left(\frac{r_{Co\ y}}{\sqrt{r_{CoM_x}^2 + r_{CoM_z}^2}}\right)$$

Eq. S3.12

We can determine the angle γ by calculating the great circle angular distance on a sphere between a point 1 (θ_1, ϕ_1) and a point 2 (θ_2, ϕ_2):

$$\gamma = \text{acos}(\sin(\phi_1)\sin(\phi_2) + \cos(\phi_1)\cos(\phi_2)\cos(\Delta\theta))$$

Eq. S3.13

Combining equation 12 with equation 13 will lead to:

$$\gamma = acos\left(\frac{\frac{r_{CoM_y}}{\sqrt{r_{CoM_x}^2 + r_{CoM_z}^2}}}{\sqrt{\frac{r_{CoM_y}^2}{r_{Co\ x}^2 + r_{CoM_z}^2} + 1}}sin(\phi_p) + \frac{1}{\sqrt{\frac{r_{CoM_y}^2}{r_{CoM_x}^2 + r_{CoM_z}^2} + 1}}cos(\phi_p)cos(\Delta\theta)\right) \qquad \text{Eq. S3.14}$$

This can be simplified to:

$$\gamma = acos\left(\frac{r_{CoM_y}}{\|\boldsymbol{r}\|}sin(\phi_p) + \frac{\sqrt{r_{CoM_x}^2 + r_{CoM_z}^2}}{\|\boldsymbol{r}\|}cos(\phi_p)cos(\Delta\theta)\right) \qquad \text{Eq. S3.15}$$

Here (θ_p, ϕ_p) is the location of any point on the surface of the sphere and $\Delta\theta$ is defined as $\theta_{CoM} - \theta_p$. Now that both γ and $\vec{r}_{CoM}$ are known the factor $-\vec{r}_{CoM}\Delta\rho\cos\gamma$ as proposed by Paulson (2006) can be calculated and implemented.

In Klemann & Martinec (2011) it is suggested that σ_{CoM} only has to be applied to the CMB and the surface, as it could be assumed that density interfaces within the mantle are small enough that the σ_{CoM} can be neglected within the mantle. For the initial iteration of the FE we follow this reasoning as it saves computational time. For the iterations afterwards however, we do not need to make this assumption as we can correct the perturbed gravitational force applied to the model with σ_{CoM} without increasing the computational load for the model. An overview of the correction for the movement of the CoM can be found in Figure S3.4
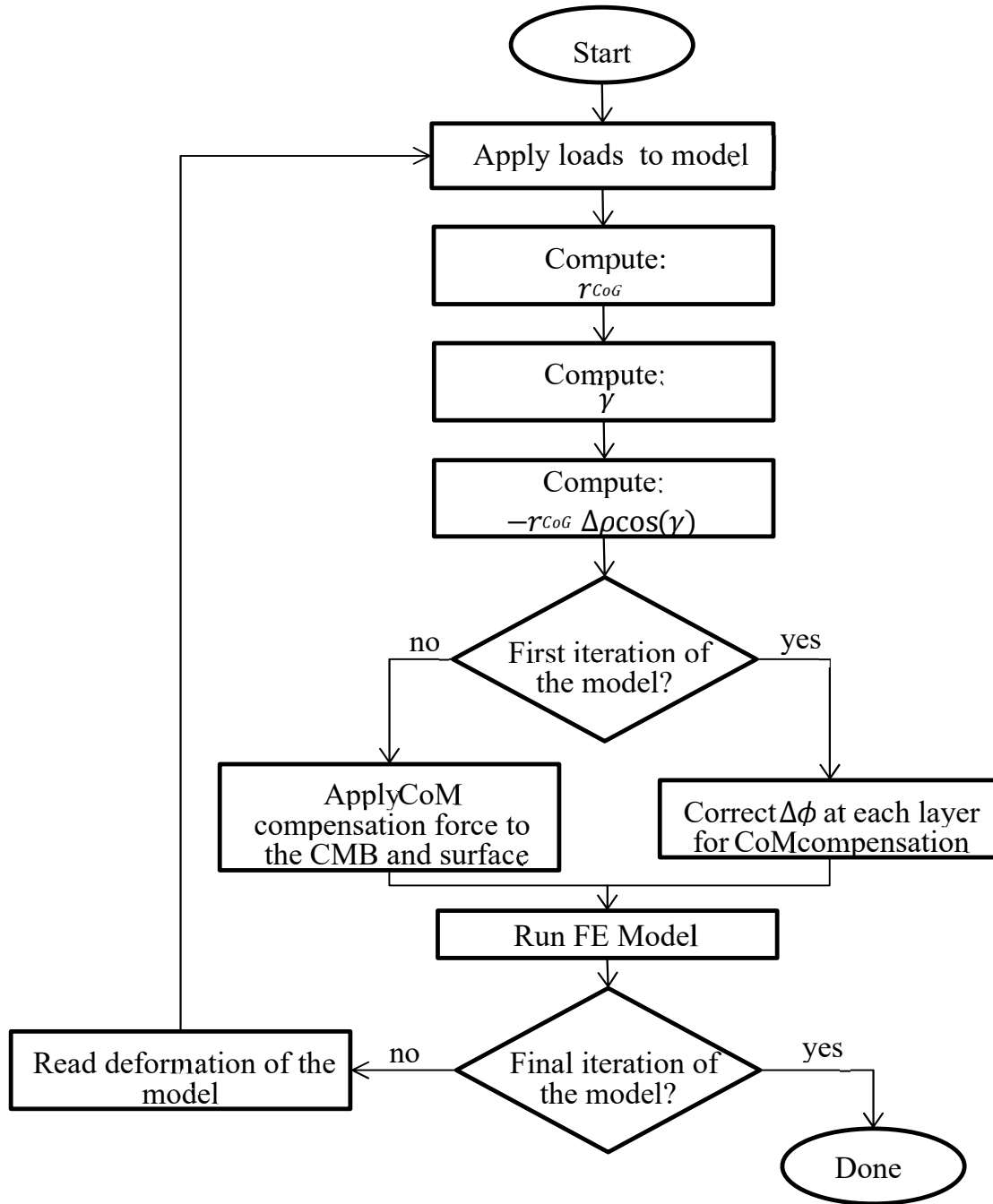
Figure S3.4: Flow chart for the movement of the CoM

3.5.4 Comparison of 3D model with 1D model from section 3.2.5

In this document we share the results of comparing the 3D FEM model described in the main text with the 1D model described in the main text. The 3D models and 1D model have some notable differences in Earth parameters. Additionally, the 1D model is compressible while the 3D model is not. In this section we set out to quantify the influence these differences have on the inversion and uplift results. In order to compare both models we have chosen a model setup for the 3D FEM model, which we assume the 1D model should be able to replicate closely even though not all model parameters described in the main text are exactly the same. Dislocation creep has been disabled so

that the 3D model only uses linear rheology. For both the shallow upper mantle (SUM) and the deeper upper mantle (DUM) in the 3D model the viscosity has been set to 19.0 $log_{10}(Pa \cdot s)$. The 1D inversion is done through a grid search with steps of 0.2 $log_{10}(Pa \cdot s)$ for both the SUM and DUM. Using model inversion, the best fitting 1D model has a SUM of 19.0 and DUM of 18.8. While a viscosity of 19.0 would be expected for both SUM and DUM, the model that we found is the closest possible alternative. We conclude that the 1D model inversion is able to replicate the 3D model viscosity to a sufficient degree, where a 0.2 $log_{10}(Pa \cdot s)$ error in either SUM or DUM viscosity is expected because of differences in the model parameters. In figure S3.5 we have compared the uplift of the 1D model with the benchmark model. The maximum error between the 1D model and the 3D model over the entire region is 1.15 mm/y which is in the range of the real GPS measurement error. The average error is 0.26 mm/y, which is well below any GPS measurement error.
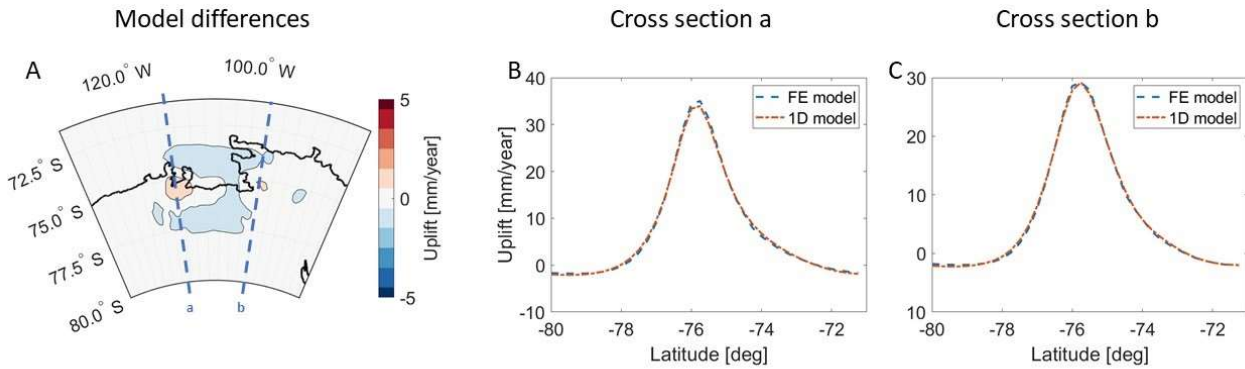
Figure S3.5: Uplift differences between 3D benchmark model and the best fitting 1D model. Figure A): uplift differences over the entire ASE region. Figure B): cross section of the uplift the 3D benchmark model and its best fitting 1D model at the 113.75° W meridian (a). Figure C: cross section of the uplift of all three models and their best fitting model at the 97.5°W meridian (b)

3.5.6 Derivation on load induced viscosity reduction

In this document we will derive the relation between the reduction of viscosity as a consequence of load induced stress, when a given background stress is present. We start with effective viscosity in composite rheology η_{eff}, which can be given as a function of diffusion and dislocation creep parameters, B_{diff} and B_{disl} respectively (Equation 3.14 main text):

$$\eta_{eff} = \frac{1}{3B_{diff} + 3B_{disl}q^{n-1}}$$

Eq. S3.16

We can rewrite the Von Mises stress q as the Von Mises stress due to the background stress q_{bg} and the load induced stress q_l to define an effect viscosity for a given background stress as function of a load induced stress $\eta_{bg}(q_l)$:

$$\eta_{bg}(q_l) = \frac{1}{3B_{diff} + 3B_{disl}(q_{bg} + q_l)^{n-1}}$$

Eq. S3.17

The change in effective viscosity as a consequence of load induced stress for a given background stress can be defined as follows:

$$\Delta\eta_{q_{bg}} = \eta_{bg}(0) - \eta_{bg}(q_l)$$

Eq. S3.18

By combining Equations S3.17 and S3.18 we end up with our final relation for the change in effective viscosity as a function of load induced viscosity for a given background Von Mises stress (Equation 3.15):

$$\Delta\eta_{q_{bg}} = \frac{1}{3B_{diff} + 3B_{disl}\tilde{q}_{bg}{}^{n-1}} - \frac{1}{3B_{diff} + 3B_{disl}(\tilde{q}_{bg} + \tilde{q}_l)^{n-1}}$$

Eq. S3.19

Uplift and RSL data constraints on 3D upper mantle viscosity in Northern Europe

Bas Blank[1]*, Sarah L. Bradley[2], Wouter van der Wal[1]

1) Delft University of Technology, Delft, Netherlands

2) The University of Sheffield, Sheffield, UK

Abstract

Northern Europe experiences vertical land motion as a response to past ice sheets in Scandinavia and the British Isles, which affects present-day sea level change. Glacial isostatic adjustment (GIA) models for the region usually adopt a homogeneous upper mantle viscosity even though seismic studies indicate contrasting elastic lithosphere and upper mantle structure between Northwestern Europe and Eastern Europe. This raises the question if in GIA observations the 3D variations in structure can be detected and if including 3D structure can improve the GIA predictions. In this study we compare model output from a finite element GIA model with 3D viscosities to relative sea level (RSL) and vertical land motion (VLM) observations. We use two different methods to derive 3D viscosities, based on seismic and upper mantle temperature estimates, and three different ice sheet reconstructions for the Eurasian ice sheet complex. We find a improvement in overall fit to the RSL and VLM data using 3D viscosities compared to standard 1D viscosity models. In particular, the fit to the RSL and VLM data across Scandinavia is improved when using an upper mantle viscosity higher than the rest of Northern Europe. Using two 1D models with different viscosities for Scandinavia and the British Isles cannot replicate the behavior of a 3D model because adjacent high and low viscosity features in 3D models redistribute GIA induced stresses differently than a combination of separate 1D models for the two regions would.

4.1 Introduction

Glacial isostatic adjustment (GIA) is the solid Earth adjustment to past ice sheet thickness changes. It plays a significant part in determining changing sea levels and evolving coastlines. For example, sea level change in northern Europe varies with location primarily due to GIA. The GIA induced vertical land motion (VLM) in the Baltic Sea leads to a sea level fall of about -7-8 mm/yr (Mäkinen et al., 2005; Richter et al., 2012), which is three to four times higher in absolute magnitude than the global mean sea level rise (Simon et al., 2021). In Scotland the present-day sea level rise has low annual change (-1.15 mm/yr) (Bradley et al., 2023) compared to the Baltic Sea, while the North-western German coast experiences a high relative sea level (RSL) rise of 8.5 mm/yr (Wahl et al., 2010) because of forebulge collapse. To quantify regional sea level change due to climate change, it is necessary to correct for the GIA signal. In the Baltic Sea, GIA is the dominant mechanism for sea level change and is measured by GPS observations with a high accuracy (±0.4 mm/yr) (Rosentau et al., 2012). However, in other areas the signal is more convoluted, and models are required to calculate the GIA contribution to ongoing sea level change (Simon & Riva, 2020), river evolution and past drainage (Peeters et al., 2015), or to separate tectonic and GIA deformation (Marotta & Sabadini, 2002).

The prediction accuracy of GIA depends on the ice history and the Earth parameters. Current models for (parts of) Northern Europe assume the rheology parameters vary only in depth (1D) (Bradley et al., 2011; Steffen et al., 2008; Lambeck et al., 1998).

However, seismic studies have shown a significant difference in wave speed between Scandinavia and Western Europe (Celli et al., 2021; Debayle et al., 2016; Fichtner et al., 2018; French et al., 2013; Schaeffer & Lebedev, 2013; Shapiro & Ritzwoller, 2002). Scandinavia and the Baltic states have been identified as having an old (>3 Gy) and thick lithosphere called the Baltic shield, which is part of the larger East European Craton. Beneath the cratonic lithosphere, relatively high seismic velocities indicate low mantle temperature. Therefore, viscosity underneath the Baltic Shield is expected to be several orders of magnitude higher than under the rest of Europe (van der Wal et al., 2013). Seismic wave speed anomalies can also be observed in the shallow upper mantle of the North Sea specifically stretching out underneath the east and south coasts of Britain (Celli et al., 2021; Fichtner et al., 2018), but these anomalies are not consistent between all models (Debayle et al., 2016; French et al., 2013). Therefore, including this 3D viscosity into GIA models could arguably improve the accuracy of the predictions.

GIA models which adopt 1D viscosities and are constrained by data from either Scandinavia or the British Isles, have similar upper mantle viscosities, $0.3 - 0.7 \times 10^{21}$ Pa·s (Kierulf et al., 2014; Lambeck et al., 1998; Steffen et al., 2008) for Scandinavia, $0.4 - 0.6 \times 10^{21}$ Pa·s for the British Isles (Bradley et al., 2011; Simms et al., 2022). Thus, GIA inferences do not support the large contrast in Earth properties found in seismic data. The only aspect in which regional GIA models of the British Isles and Scandinavia differ is the elastic lithosphere thickness. Bradley et al., (2011) find a best fitting lithosphere of 70 km for the British Isles compared to 120 km (Steffen et al., 2006) and 140 km (Kierulf et al., 2014) for Scandinavia and 75 km for the entirety of Europe (Lambeck et al., 1998). Contrary to this, a comparison of GIA models with GRACE data for Scandinavia and for the Barents Sea region find an upper mantle viscosity in Scandinavia of a factor of 2 higher compared to the Barents Sea, which agrees with viscosity ratios between the two regions derived from seismic models (Rovira-Navarro et al., 2020).

Two studies (van der Wal et al., 2013; Kierulf et al., 2014) compared the vertical land motion (VLM) (and RSL in van der Wal et al., (2013)) results for spherical finite element method (FEM) GIA models with 3D variations in viscosity against results with 1D viscosity. Van der Wal et al. (2013) concluded that some 3D models outperformed the 1D models. Kierulf et al., (2014) found the 1D model outperformed the 3D model, apart from Northern Norway. Here it must be noted that the ice history used, ICE-5G, is built by fitting a 1D Earth model to the data and will therefore have an inherent bias towards 1D models. However, data driven GIA models also show the largest discrepancies with 1D models such as ICE-6G in Scandinavia (Simon & Riva, 2020), which could be explained by 3D viscosities that are not in the 1D model. Both Van der Wal et al. (2013) and Kierulf et al. (2014) focused only on the Scandinavian Ice Sheet (SIS) and used less data than is currently available. Furthermore, both only considered a single ice sheet history and the resolution for both models ($2° \times 2°$) is too coarse to model details in coastlines reliably.

3D GIA models have been used in other regions with marked lateral viscosity variations. Results show that using 3D viscosity can improve the fit to observed data, in e.g. Antarctica (Powell et al., 2022) and North America (Kuchar et al., 2019), compared to 1D but other studies were unable to find unambiguous improvements for 3D models in both North America (Yousefi et al., 2021) and Antarctica (Blank et al., 2021). Possible reasons why the fit for 3D models might not always improve even though lateral viscosity variations are very likely to exist are the limited parameter studies of 3D models because of the large computation time, the input ice models that are created based on 1D Earth models and uncertainties in 3D viscosities (Steffen et al., 2006).

In this study we address the discrepancy between seismic studies that show lateral variations in the mantle underneath Europe and the relatively homogeneous upper mantle viscosity found with regional 1D GIA models. *We do so by comparing the fit of 3D and 1D model with measured RSL and VLM data* and by using recent ice histories that are less biased by the 1D Earth model

Our main objective is to find out to what extent can GIA models with 3D rheology in north-western Europe improve the fit to RSL and VLM data compared to conventional 1D rheology? The research questions are (i) do 1D or 3D viscosity models fit the data in Europe better and why? (ii) is the data sensitive to 3D structure even when averaged viscosities are close to 1D viscosity models? (iii) do the British Isles and Scandinavia favour a 3D model which results in different average/median viscosities below the regions? Answering these questions will also provide constraints on Earth structure underneath Europe. Secondly, if improvements to the GIA model could be achieved it can improve climate-related sea level change estimates by providing a better GIA correction on tide gauges or help interpretation of GPS or RSL data for tectonic or landscape evolution studies.

4.2 Method

4.2.1 GIA model

The 3D GIA model used is the spherical FEM from Blank et al., (2021). It is based on the formulation of Wu (2004) which uses the commercial software package ABAQUS in combination with stress transformation and iteration to create a self-gravitating GIA model. Self-consistent sea levels with migrating shorelines (e.g. Kendall et al., 2005) as well as geocenter motion (e.g. Tanaka et al., 2009) are also included in the model. In our implementation, the grid resolution in the region of interest is around 40 km in a spherical cap centred around the Danish Islands (58°N 11°E) with a radius of 17 spherical degrees (see Section 4.5.2). The grid-size for the sea level equation is higher than the FEM (~25 km) to be able to include an increased resolution around the complex coastline. The present-day topography is interpolated to this grid from ETOPO1 (Amante & Eakins, 2009).

The layering is the same as in Blank et al., (2021) with a minimum elastic lithospheric layer of 70 km based on the minimal elastic thickness found by GIA studies underneath

the British Isles (Bradley et al., 2011). The upper mantle is divided into the shallow (70-180 km), deeper (180-420 km) and transition zone (420-670 km), as in Barletta et al., (2018) and Blank et al., (2021). The 3D viscosities are applied in the shallow and deep upper mantle layers, as the flow laws and seismic wave anomaly conversion methods we use to determine viscosity are not applicable below 400 km. Additionally, the transition zone has less lateral variation in seismic velocities in the study region (Schaeffer & Lebedev, 2013). 3D viscosity models in the upper mantle are discussed in the next section. Viscosity in the transition zone and lower mantle is set to 3×10^{21} Pa·s in agreement with the VM5A profile (Peltier et al., 2015). Changing transition zone viscosity affects VLM and RSL and thus possibly the best fit, as can be seen in Section 4.5.8.

4.2.2 3D viscosity

We use two different input upper mantle models to derive the input 3D viscosities: temperature model WINTERC-G (Fullea et al., 2021) and seismic model SMEAN2 (Jackson et al., 2017). WINTERC-G is an Earth model obtained from an integrated geophysical–petrological approach, in which seismic data, gravity data and thermobarometric data are inverted. The model assumes isostasy and the fit to the datasets is obtained by changing the mantle's mineralogical composition, creating a temperature estimation for the upper 400 km of the Earth. SMEAN2 is an average of three tomography models, SAVANI, GyPSuM, and S40RTS. As SMEAN2 is an averaged model, it is by its nature a smoother model with less pronounced features. To convert the seismic wave anomalies into temperatures for SMEAN2 the following relationship is used:

$$T(z) = T_{ref} + \frac{\partial T}{\partial v_s} \frac{\delta v_s}{v_s} \qquad \text{Eq. 4.1}$$

Here T_{ref} is the global reference temperature at a certain depth from Turcotte & Schubert, (2002), $\frac{\partial T}{\partial v_s}$ the temperature-wave speed derivative (Karato, 2008) and $\frac{\delta v_s}{v_s}$ the seismic wave speed anomaly.

The first method we use is a scaling of seismic velocity anomalies (Ivins & Sammis, 1995) used here in the form of Wu et al. (2013), which can only be applied to SMEAN2 for our study:

$$\log_{10} \eta = -0.4343\beta \frac{\partial T}{\partial \ln v_s} \frac{\delta v_s}{v_s} \frac{E^* + pV^*}{RT^2} + \log_{10} \bar{\eta} \qquad \text{Eq. 4.2}$$

with $\bar{\eta}$ the 1D background viscosity, β a scaling factor that is equal to 1 when all seismic velocity anomalies are caused by thermal anomalies, and 0 when seismic velocity anomalies are caused by for example compositional changes that do not manifest as viscosity anomaly. The background viscosity is taken from the reference model VM5A (Peltier et al., 2015) and is set to 0.5×10^{21} Pa·s for the upper mantle.

In the second method, the 3D rheologic parameters are derived from the temperature estimates using the flow laws for diffusion creep and dislocation creep in olivine (Hirth & Kohlstedt, 2003). The creep mechanisms are assumed to act simultaneously which results in a so-called composite rheology (e.g. van der Wal et al., 2010). The change in uniaxial equivalent strain increment $\Delta\tilde{\epsilon}$ is related to the stress tensor $\tilde{q}$ and time increment Δt with the creep coefficient B according to:

$$\Delta\tilde{\epsilon} = B\tilde{q}^n\Delta t \qquad\qquad \text{Eq. 4.3}$$

with the stress exponent n equal to 3.5 (Hirth & Kohlstedt, 2003). The strain is linearly dependent on stress for $n = 1$; the rheology is non-linear for $n > 1$. The individual contribution of either diffusion B_{diff} and dislocation creep B_{disl} is determined by:

$$B = Ad^{-p}f_{H_2o}^r e^{-\frac{E+PV}{RT}} \qquad\qquad \text{Eq. 4.4}$$

Here, A is an experimentally determined constant, E is the activation energy, R the universal gas constant, T is the temperature and P represents the pressure, which is computed based on the hydrostatic pressure that follows from the undisturbed model. For dislocation and diffusion creep, different values for the variables A, p and r are obtained experimentally (Hirth & Kohlstedt, 2003). We created different rheologies by varying the grainsize d and the water content f_{H_2o}.

The effective viscosity, η_{eff} is determined by the combined contributions from the diffusion B_{diff} and dislocation creep B_{disl} in an element according to:

$$\eta_{eff} = \frac{1}{3B_{diff} + 3B_{disl}q^{n-1}} \qquad\qquad \text{Eq. 4.5}$$

q is the Von Mises stress which is a tensor invariant. It is important to note that the effective viscosity becomes stress dependent for rheologies where dislocation creep plays a role, which is the case for most wet rheologies (Hirth & Kohlstedt, 2003). For the non-linear rheology we mostly used models with a homogeneous grain-size and water content but also created models using SMEAN2 where we increased the grainsize for the cratonic lithosphere to reflect possible grain growth over time. The threshold to identify a region as cratonic is at positive seismic wave speed anomaly of 2%. For SMEAN2 the temperature from Equation 4.1 is inserted in Equation 4.5, calculating the creep parameter. Using this approach, we developed 21 unique Earth models for 42 different model runs in total (see Section 4.5.6), varying β between $0.25 - 0.75$, grainsize between $4 - 10$ mm, and water content between $0 - 1000$ ppm. Of these 42 different model runs 18 have Earth models based on the WINTERC-G as input, 16 SMEAN2 as input and 8 are 1D models.
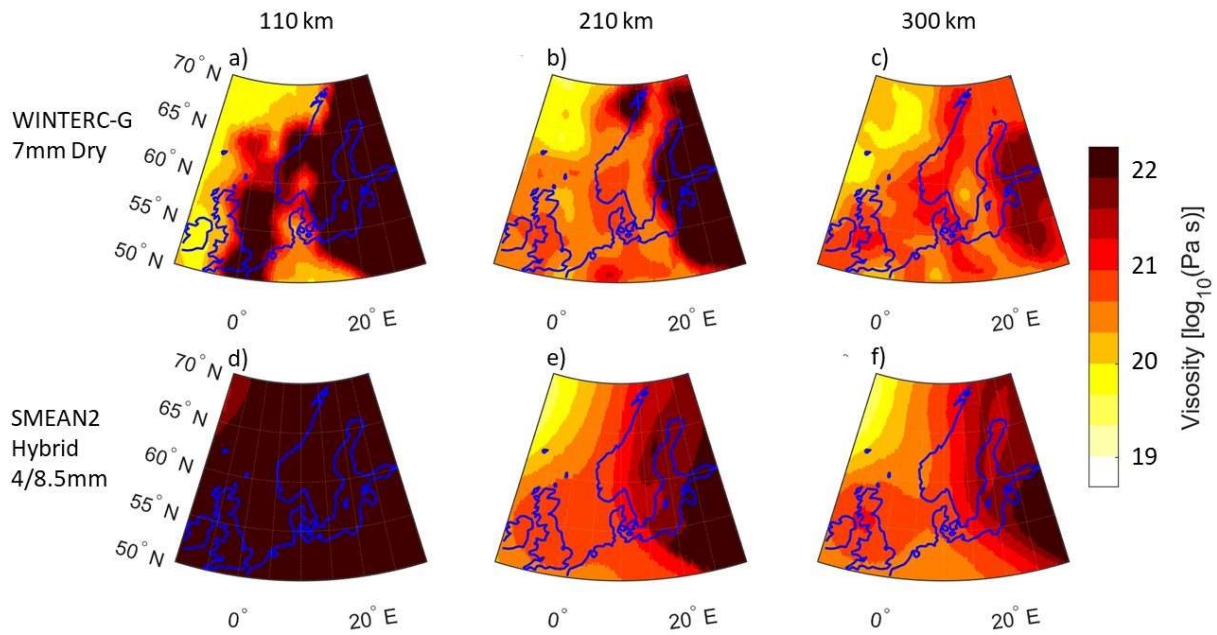
Figure 4.1: Viscosity at three depths, 110 km (Figure a and d), 210 km (Figure b and e), and 300 km (Figure c and f) for the WINTERC-G model with 7 mm grain-size and dry conditions (Figure a, b and c) and the SMEAN2 model with 8.5 mm in cratonic regions and 4 mm elsewhere (Figure d, e and f). All values are log_{10} of the viscosity in Pa·s.

Figure 4.1 shows the 3D viscosity estimates which produced the optimum fit to both the RSL and VLM data for both input upper mantle models (with ICE-6G for WINTERC-G 7 mm dry, and with BRITICE for SMEAN2 Hybrid 4/8.5 mm). Both estimates show high viscosity anomalies in Finland and North-Eastern Europe. The estimates based on SMEAN2 have a relatively homogeneous viscosity, slightly higher than the background viscosity, extending from western Norway across the North Sea and the British Isles. For the WINTERC-G based Earth models there is a high-viscosity feature from the coast of Norway, extending across the North Sea down to south of the English Channel at 110 km (Fig.4.1a), which is absent in deeper layers (Fig. 4.1b and c).

To compare 3D viscosity models against 1D viscosity models, an average viscosity is calculated from the 3D viscosity estimates in three steps. First, we select which elements contribute significantly which we define as being strained by more than 20% of the maximum element strain at that depth, similar to Blank et al. (2021). Secondly, we filter out any element that has an effective viscosity upwards of 10^{23} Pa·s as these elements are deemed to behave elastically. Finally, from the remaining selection of contributing viscous elements we take the average of the log_{10} of the viscosity. This method is similar to that used in Blank et al., (2021), with the difference being that elements are selected based on strain instead of stress. This change is made as highly viscous elements from the Baltic Shield would accumulate high stresses without contributing directly to VLM.

4.2.3 Ice history data

For this study three different ice sheet reconstructions for Europe were used, which have varying dependence on a 1D Earth model. The first is ICE-6G, which has been developed to match far field and near field RSL and VLM data using the VM5A viscosity model (Peltier et al., 2015). The data used partially overlap with the RSL and VLM data used in this paper. This ice history is inherently biased towards the VM5a viscosity model. The previous iteration of ICE-6G, ICE-5G shows relatively large misfits for areas in Scandinavia which a 3D model could possibly resolve (Kierulf et al., 2014). The second is the ice sheet created within the BRITICE-CHRONO project, which will be referred to as the BRITICE model. The focus of the BRITICE model has been with reconstructing the ice sheets over the British Isles, North Sea and Scandinavia using glacial geomorphological data (Clark et al., 2018; Hughes et al., 2016) and geochronological data as constraint for the ice sheet extent at different time steps. The ice sheet reconstruction was developed independent of RSL data. The SIS was constrained to fit the DATED-1 reconstruction (Hughes et al., 2016). To create the ice thickness for all ice sheets ICESHEET 1.0 (Gowan et al., 2016) was used. ICESHEET 1.0 is a plastic ice model underlain by a 1D Earth model with an upper mantle viscosity of 0.4×10^{21} Pa·s.

The third ice reconstruction is from Patton et al., (2017) and will be referred to as the P17 ice model. It uses a thermomechanical model to model the ice sheet build up (Patton et al., 2016) and deglaciation (Patton et al., 2017) of the European ice sheet. Observed flow channels and marginal moraines are used to calibrate the flow patterns of the model. Finally, to calibrate local ice thickness a 1D Earth model was used to model isostasy that upon iteration best fit the RSL data in combination with the ice sheet input. The ice thickness of all ice histories is shown in Section 4.5.4. Outside Europe, the ice history of ICE-6G was used for the ice thickness in all models

Because the P17 and BRITICE models are both largely constrained on geological data and ice evolution models they do not carry the strong inherent bias for a 1D Earth that ICE-6G has. While there some overlap in RSL data and geomorphological data the differences in methodology and data used are large enough that the P17 and BRITICE ice histories are distinctly different (see Subsection 4.5.4)

4.2.4 Input RSL and VLM Data and analysis

We produced RSL and VLM predictions for each of the three ice sheet reconstructions combined with up to 21 3D viscosity profiles and up to 3 1D viscosity profiles. In total we ran 43 model combinations and analyzed the fit to the RSL and VLM data.

For the RSL data we combined RSL data sets from across Europe (García-Artola et al., (2018); Hijma & Cohen, (2019) Rosentau et al., (2021); Shennan et al., (2018); Creel et al., (2022)). This results in a combined data set of 4090 SLIP's and a larger spatial coverage than in previous studies (Kierulf et al., 2014; Van Der Wal et al., 2013). To avoid spatial bias from locations with more data we weighted each sea level index point

(SLIP) data based on their proximity to other SLIP's (including itself) in terms of location (<200 km) and time (<1ka), see also Figure 4.2a.

$$W_{RSL_i} = \frac{1}{n_{SLIP(<200km \,\&<1ka)}}$$

Eq. 4.6

A large part of the data from Rosentau et al., (2021) for the Baltic Sea region is dated to time periods where the Baltic Sea was either a lake or in a transitional state. As we do not model lake effects, we removed the data when the Baltic Sea was not a sea (i.e when it was a lake) (<8.5 ky BP) (Steffen & Wu, 2011).

We filtered the data to retain RSL and VLM data which have a significant GIA signal caused by the Eurasian ice sheet, as including them would bias results towards models with little GIA response. We define these as data lying in any region in Europe where the variation between all models is at least 20% of the maximal variation between models at any point in time (as indicated by a blue square for the GPS station or circle for the SLIP's).

For the RSL data, we compute the misfit as follows:

$$Misfit_{RSL} = \frac{\sum_{i=1}^{n_{RSL}} W_{RSL_i} \sqrt{\left(\frac{RSL_{o,i} - RSL_{m,i}}{\sigma_{RSL_i}}\right)^2}}{n_{RSL}}$$

Eq. 4.7

where $RSL_{o,i}$ is the observed RSL at location i, $RSL_{m,i}$ the modelled RSL at the same location i. The difference between both is normalised by the standard deviation attributed to the observed height, σ_{RSL_i}. Furthermore, n_{RSL} is the total number of data points. The absolute distance in RSL height between model and data point is used instead of distance squared because otherwise the misfit would be controlled by a few points with very large differences between model and observations, as the measurement error is a relatively small part of the total RSL variation between models, which can be influenced by within-estuary processes or short term oscillations in sea level (Shennan et al., 2018).

We sampled the models with 2/3 of the datapoints a 1000 times in order obtain a distribution for every model. T-tests can be performed using these distributions to test whether models differ to a significant level from one another. For more consideration on this choice, we refer to Subsection 4.5.8.

For the data for the VLM we have used data from the Tide Gauge working group (TIGA), BIFROST (Kierulf et al., 2021) and Schumacher et al. (2018), which use the ITRF2008 reference frame. The ITRF2008 reference frame is defined such that there is no translation or translation rate with respect to the mean centre of mass over a certain time frame (Altamimi et al., 2011) . This can deviate from the centre of mass of the

Earth that is taken as reference in our modelling. We assume that this error is small and of such a large wavelength that it will not cause differences in misfit between models.

The VLM data is weighted according to the density of GPS observations (<200 km) around GPS station i, creating weight W_{VLM_i} to avoid a bias for more densely sampled regions (see also Figure 4.2b). The misfit is defined as:

$$Misfit_{VLM} = \frac{\sum_{i=1}^{n_{gps}} W_{VLM_i} \sqrt{\left(\frac{u_{o,i} - u_{m,i}}{\sigma_{u_i}}\right)^2}}{n_{gps}} \qquad \text{Eq. 4.8}$$

Here u_i and u_m are the measured uplift rate at station location i, and the corresponding modelled uplift rate, respectively. Before adding the misfit of both the RSL and VLM data we normalize the misfit with the value from the model with the median misfit to avoid one dataset dominating the misfit:

$$Misfit_{total} = \frac{Misfit_{RSL}}{\text{med } Misfit_{RSL}} + \frac{Misfit_{VLM}}{\text{med } Misfit_{VLM}} \qquad \text{Eq. 4.9}$$
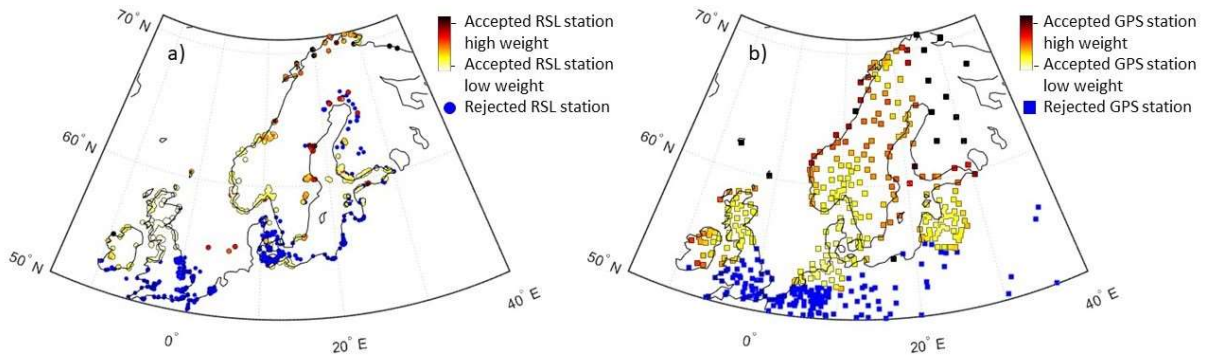
Figure 4.2: Locations of RSL data (a) and VLM data (b) used in this study. In a) the selected RSL data are shown in colors according to the color scale while discarded data are shown in blue. In figure b) discarded VLM points are shown in blue, accepted stations are shown in colors according to the color scale while. The shade of blue denotes the weight, with lighter blue points having a lower weight and dark blue points having a higher weight.

4.3 Results

To assess the importance of the 3D viscosities profiles, 7 runs are performed with 1D viscosity profiles only. Each of the three ice histories is combined with the VM5A viscosity profile, to be able to compare the effect of different ice histories. Furthermore, ICE-6G and BRITICE are combined with lower (3×10^{20} Pa·s) and higher (5×10^{21} Pa·s) upper mantle viscosity, to investigate the range of sea levels 1D viscosity models

can provide. For the 34 total 3D model runs, 16 use SMEAN2 based models and 18 are WINTERC-G based models.

Firstly, we present model comparisons to the RSL data. Secondly, we will look at how the model results compare to VLM data. Thirdly, we will combine both data sets and compare them to the models to investigate if 3D viscosity can improve the combined fit. Finally, we evaluate if the similar average upper mantles viscosities found in 1D studies for the Scandinavian and British Isles regions agree with the local viscosity of the best fitting 3D models.

4.3.1 RSL data comparison

Table 4.1 shows the misfit of the 10 models with lowest misfit with respect to the RSL data. The best performing model is a 1D model with VM5A viscosity profile and a version of VM5A with a lower viscosity in the upper mantle ($\eta = 0.3 \times 10^{21}$ Pa·s), henceforth I6-VM_η=0.3. It is not surprising that the combination of ICE-6G with its standard Earth model VM5A, henceforth I6-VM, and I6-VM_η=0.3 are performing well as ICE-6G has been developed based on VM5a to fit the majority of the data used here (Peltier et al., 2015). The second-best model is the 3D model using ice history ICE-6G and the Earth model WINTERC-G with a uniform grain-size of 7 mm (I6-W7D). For the ice histories that were not created by fitting the ice model to the RSL data for a 1D Earth model (BRITICE or P17) 3D models provide an improvement, as all best fitting models combinations for either ice history are with a 3D Earth model. This suggests that the bias in the ice history towards a viscosity profile is the main reason that no improvement in fit is found for ICE-6G in combination with a 3D rheology.

Table 4.1: Misfit of the best 10 models with respect to the RSL data. The Earth model structure is in the middle column, with additional parameters in the final column. The bars represent the total misfit, with the colors detailing the ice model used for that specific model. 1D models are highlighted in orange and 3D models are highlighted in blue. The error bar denotes the 2σ distance from the sampled mean, and thus the t-test critical values for each model.

Rank	Label	Earth model	Rheology parameters
1	I6-VM_η=0.3	VM5A profile	$\eta_{upper} = 3 \cdot 10^{20}$
2	I6-W7D	WINTERC-G	7 mm Dry
3	I6-VM	VM5A profile	Regular
4	I6-W8.5D	WINTERC-G	8.5 mm Dry
5	P17-W7D	WINTERC-G	7 mm Dry
6	BI-W7D	WINTERC-G	7 mm Dry
7	BI-W7Da	WINTERC-G	7 mm 50 ppm
8	I6-W5.5D	WINTERC-G	5.5 mm Dry
9	I6-S_β=0.75	SMEAN2	$\beta = 0.75$
10	P17-W5.5D	WINTERC-G	5.5 mm Dry

Figure 4.3 shows a map of predicted RSL for the reference 1D model (I6-VM) at 7 ky BP, and the difference between the best performing 3D model (I6-W7D) and the reference model, in terms of RSL and in terms of misfit. It is valuable to know if the
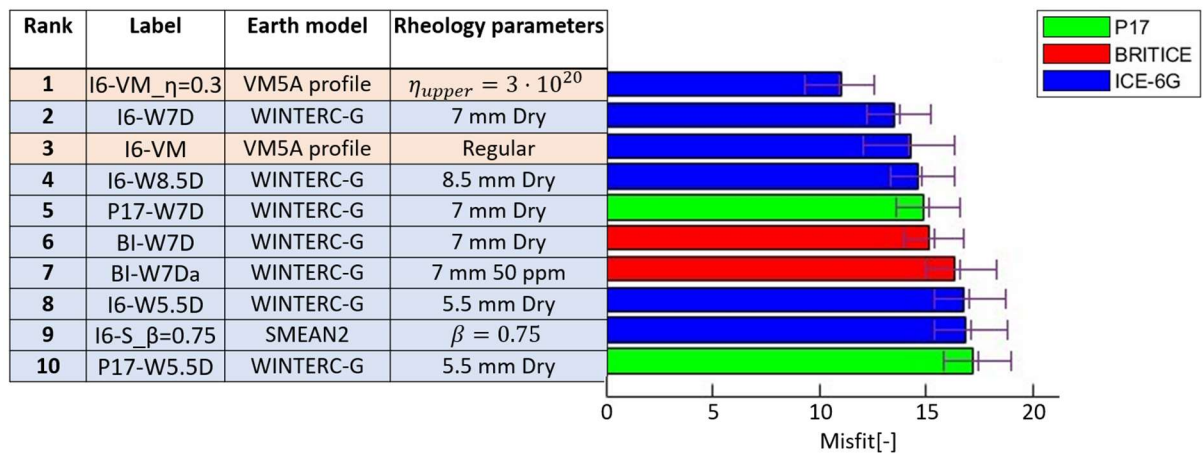
effect of 3D viscosity can be distinguished from that of the reference 1D viscosity, which is also the background viscosity for some of the 3D models. The RSL map in Figure 4.3a has a different spatial pattern than the difference in Figure 4.3d, unlike the difference between 1D models in Figure 4.3c. This suggests that the 3D viscosity could affect the results in a way that cannot be reproduced by another 1D model, which means that, given the right data, the 3D model can be expected to improve fit significantly.

To see where the best performing 3D model outperforms both the reference 1D model and the best 1D model we plot misfit difference for each location in Figure 4.3b, and selected modelled sea level curves in Figure 4.3e to g. The observed RSL in central Scandinavia (around the Eastern Baltic Sea) is lower than the 1D models predict but is captured by the I6-W7D in the entire area. The largest differences between models are at times older than 8.5 ky BP but cannot be compared to data due to the Baltic Lake phases forming a cut off for older data.

In the British Isles I6-W7D agrees better with more southern RSL sites, while the 1D models fit the Northern sites better. In Northern Wales (figure 4.3d), in the East of the British Isles, both 1D models show a rise in RSL from -12 ky till -6 ky, forming a highstand. After -6 ky, the local uplift speed outpaces the rise in global sea level, thus resulting in a net decline of the RSL. I6-W7D has a longer local relaxation time (as can be inferred from the high viscosity in Figure 4.1) and thus the uplift is slower paced. As a result, the RSL never exhibits the highstand. This matches the local RSL data better than the results of both 1D models with the highstand. This is also remarked in both Roberts et al. (2011) and Rushby et al. (2019), who exclude GIA solutions with highstands in North Wales during the Holocene.

In Samsø (Figure 4.3e) in the Danish Strait, the apparent highstand in the data over the last 5 ky in combination with a negative RSL value before this point in time is only possible with substantial initial deflection at LGM and rapid uplift during deglaciation. If we look at I6-W7D, we see it gives a more negative RSL than both 1D models initially. This is likely because the higher local viscosity (see Figure 4.1) decreases deflection at LGM (see Section 4.5.1 on evaluating deflection at the LGM) and reduces the uplift after that. The increased misfit possibly suggests that the real viscosity is lower than given by the I6-W7D (as is more consistent with Debayle et al., (2016) and French et al., (2013)). This is corroborated by the fact that I6-VM_η=0.3 produces a lower misfit than I6-VM in this location. The 3D models combined with the P17 ice model also performed better here, suggesting that the ice load and its corresponding forebulge location is also of importance.

In central Scandinavia, near Gunnarsbyn (figure 4.3f), the I6-W7D also produces a lower predicted RSL than the 1D model, likely also due to the higher viscosity in the region. This leads to a reduction in the misfit. The reference 1D model results in too much initial deformation and thus a high initial RSL (~12 ky BP), which reduces the fit with the data. Using the I6-VM_η=0.3 model reduces this high initial RSL due to the

shorter relaxation time, resulting in a reduced misfit. However, as we will see later, a viscosity of $\eta = 0.3 \times 10^{21}$ Pa·s is not preferred by VLM data.
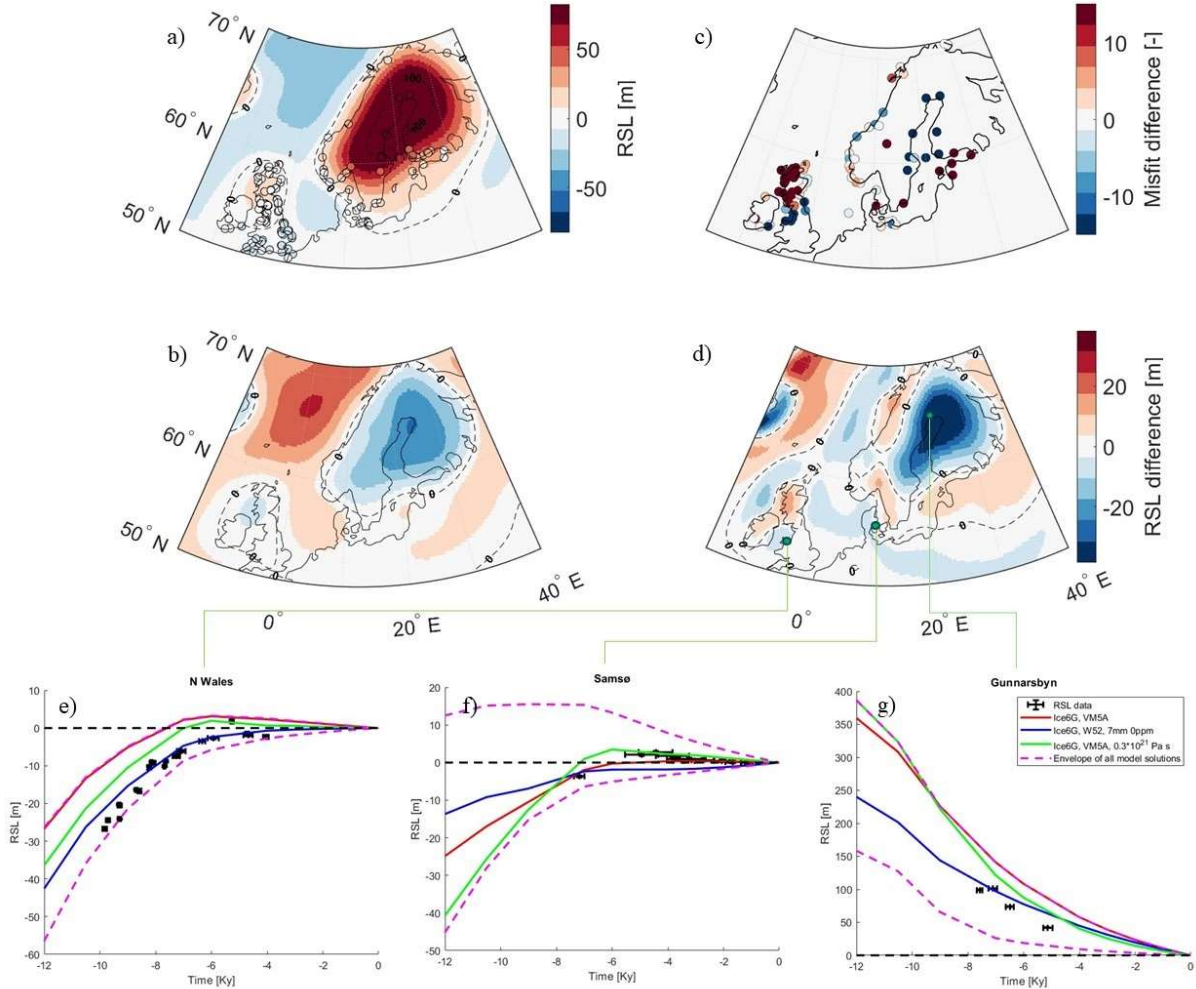
Figure 4.3; a: RSL at 7 ky for the best performing 3D model (ICE-6G with WINTERC-G dry, 7 mm grain-size). b: the difference between the best performing 1D model and the reference 1D model. c: The improvement of 3D RSL fit with respect to the reference 1D RSL fit. Blue sites indicate the 3D model fits better and red sites indicate the 1D model fits better. d: the difference between the best performing 3D model and the reference 1D model. Locations for the RSL evolution over time at individual sites, North Wales (figure e), Samsø (figure f), and Gunnarsbynn (figure g). For all individual sites (figures e-g) the RSL overtime for the 1D model is shown in red and for the 3D model in blue and the overall best model is shown in green. The magenta dotted lines indicate the range of models as it shows maximal and minimal values found among all models with the same ice history at every time step for those locations.

4.3.2 VLM data-based comparison

In Table 4.2 we can see the misfit of the ten lowest models compared to the VLM data used in this study. The central question of this study is whether 3D rheology can improve the model fit. The best performing model is I6-VM. As with the RSL data it is not surprising that this combination performs well as the ice model was fit using much of the same data and the 1D profile. Similarly to the RSL data the ice models that were not

specifically fit to local data with a 1D model we see an improvement with 3D models. The best performing 3D model is the BRITICE model with a hybrid Earth model of SMEAN2 and a global grain-size of 4 mm and a grain-size of 8.5 mm for all areas with a high (>2%) wave speed anomaly (BI-S4/8.5D).

Table 4.2: Misfit of the best 10 models with respect to the VLM data. The Earth model structure is in the middle column, with additional details used to create each model in the final column. The bars represent the total misfit, with the colors detailing the ice model used. 1D models are highlighted in orange and 3D models are highlighted in blue. The error bar denotes the 2σ distance from the sampled mean, and thus the t-test critical values for each model.

Rank	Label	Earth model	Rheology parameters
1	I6-VM	VM5A profile	Regular
2	BI-S4/8.5D	SMEAN2	4 mm/8.5 mm Dry
3	I6-S_β=0.75	SMEAN2	$\beta = 0.75$
4	BI-S_β=0.75	SMEAN2	$\beta = 0.75$
5	I6-W7D	WINTERC-G	7 mm Dry
6	I6-W5.5D	WINTERC-G	5.5 mm Dry
7	BI-VM	VM5A profile	Regular
8	BI-W4D	WINTERC-G	4 mm Dry
9	P17-S4/8.5D	SMEAN2	4 mm/8.5 mm Dry
10	I6-S_β=0.5	SMEAN2	$\beta = 0.5$
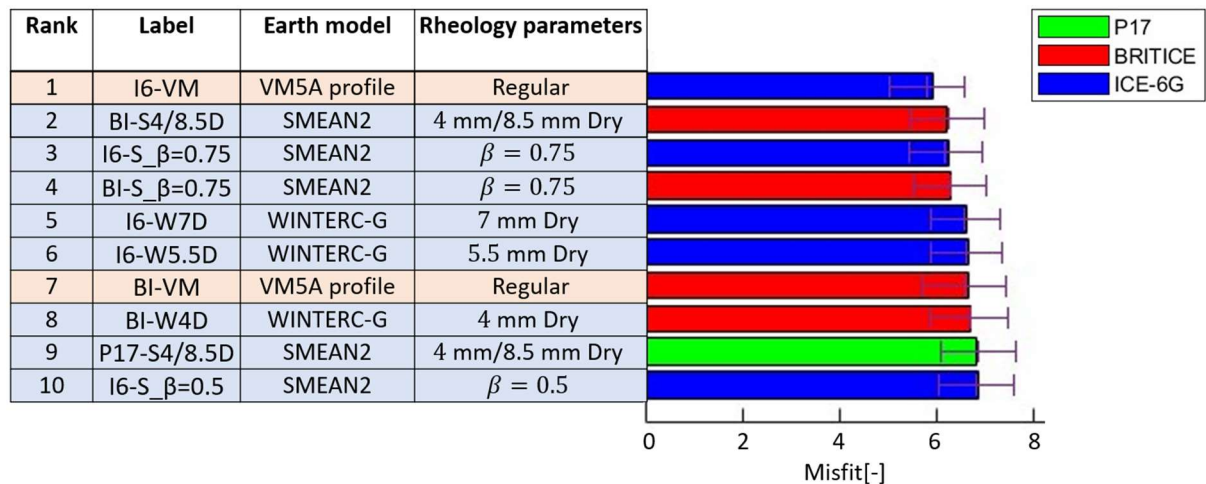
To understand if 3D models improve the fit compared to 1D models, Figure 4.4 shows the absolute uplift of BI-S4/8.5D in Figure 4.4a, the difference in uplift rate between BI-S4/8.5D and the reference 1D model (BRITICE with VM5a, BI-VM) is shown in Figure 4.4b. The differences have a spatial pattern that likely is related to the underlying viscosity as lower uplift for the 3D model in northern Finland and Sweden occurs where the local viscosity is higher (See Figure 4.1). This is a strong indicator that 3D models can improve the fit to VLM in this area.

BI-S4/8.5D predicts too low uplift rates in central and eastern Sweden but does well for other areas in Scandinavia. In Finland and around the Norwegian Swedish border there is a marked improvement compared to the 1D model which predicts too high uplift rates compared to measurements (Figure 4.4d). A larger misfit is observed for the 3D model along the Norwegian west coast, although the viscosity in this 3D model is similar to the 1D model. This is likely an example of how viscosity variations in adjacent regions can influence the uplift. This already occurs at the LGM where the deflection pattern is different from that of a 1D model as can be seen in Section 4.5.1. This demonstrates that the uplift rate pattern of a 3D model cannot always be replicated with a 1D model even if it has a local average viscosity equal to that of the 3D model, stressing the importance of using 3D rheology.

The poor performance BI-S4/8.5D in the British Isles is hard to pinpoint on one reason. It could be the viscosity of this model is too high in that region. Increasing water content of the British Isles region could be a way to lower viscosity in the region without having

to reduce grain-size below unfeasible sizes. However, BI-W7D performs better, which might indicate that the viscosity in western Scandinavia might be too high for BI-S4/8.5D and influences the results in the British Isles. Finally, it must be noted that in general the combination of BRITICE with VM5a also does not perform as well as ICE-6G models, while in Bradley et al. (2023) BRITICE models fit the RSL data better than in this study using a different Earth model.
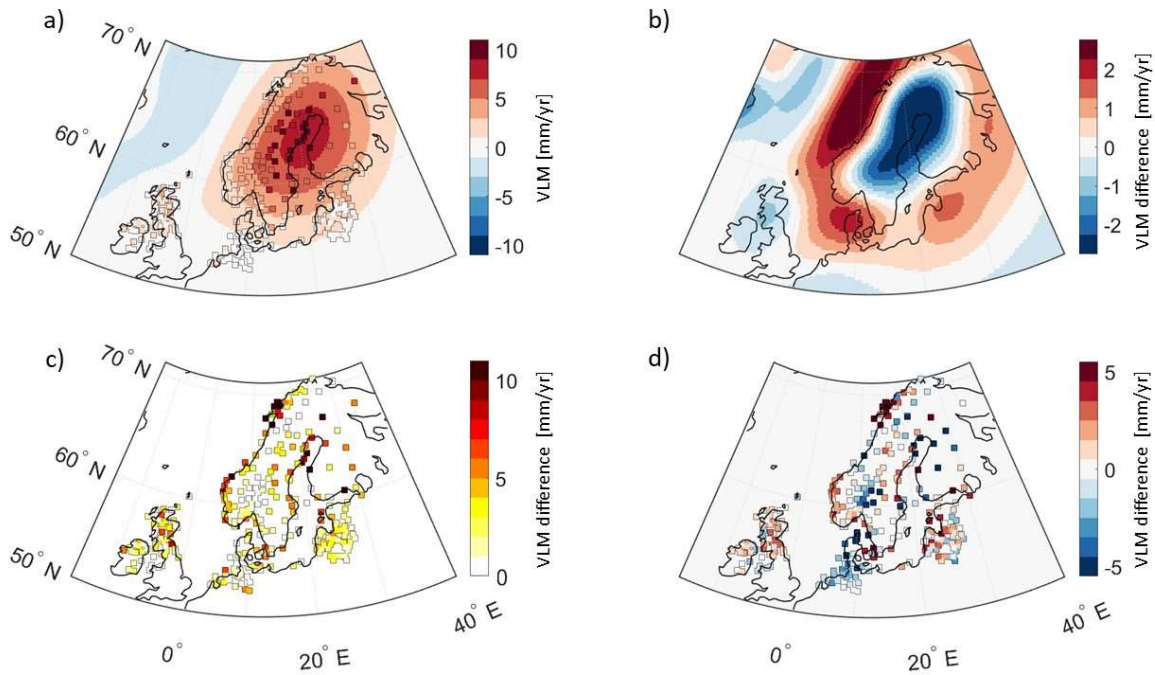
Figure 4.4: Figure a) shows the VLM for the 3D model (BRITICE with SMEAN2 model with global 4 mm grain-size and cratonic 8.5 mm grainsize) with uplift data of GPS stations as squares overlain. Figure b) shows the best fitting 3D model minus the 1D reference model (BRITICE with VM5a). Figure c) shows the absolute difference between observed uplift data and the 3D model predictions from a). Figure d) shows the VLM misfit of the 3D model minus the misfit of the 1D reference model at the GPS stations. Blue indicates improvement for the 3D model while red indicates improvement for the 1D model.

4.3.3 Combined data comparison

We tested the robustness of the assumptions, such as the selected data and sensitivity range for the weights, necessary for Equation 4.6 and Equation 4.9 that are used to compute the combined misfit and found that changing them for reasonable alternative assumptions only has a minimal effect on the ranking of the models (see Section 4.5.5). In Table 4.3 the best performing model is I6-VM, which is the optimized combination. However, 3D model I6-W7D was able to match the 1D model results in terms of misfit using the same ice history.

To see if there are regions where the results are improved using a 3D viscosity regardless of the exact Earth and ice models used, we compare a 3D model with a 1D model for

the same ice model. Figure 4.5a shows the difference between the fit of the best 3D model, I6-W7D, with the reference 1D model and Figure 4.5b shows the difference between the fit of the best fit 3D model, BI-S_β=0.75, which has a different ice history, Earth model, and rheology (linear versus non-linear rheology) with the BRITICE ice model and scaled rheology based on SMEAN2. The area that shows an improvement in fit for both 3D models is Finland and the Northern Baltic Sea. This area is in the centre of the Scandinavia ice sheet and is underlain by the Eastern European craton. It shows that including a 3D viscosity structure here helps to reproduce a locally lower uplift because the relaxation is reduced by the higher viscosity; deflection shifts westward because of lateral viscosity variations (Section 4.5.1). Areas that perform poorly in almost all 3D models are the southwestern Norwegian coast and the Danish Strait. The RSL data suggests that these areas have faster relaxation than produced by most of the 3D models.

Table 4.3: Overview of top 10 best fit models and corresponding misfit with respect to the RSL and VLM data combined. The Earth model structure is in the middle column, with additional details that are used to create each model in the final column. The bars represent the total misfit, with the colors detailing the ice model used. 3D models are highlighted in blue. The error bar denotes the 2σ distance from the sampled mean, and thus the t-test critical values for each model.

Rank	Label	Earth model	Rheology parameters
1	I6-VM	VM5A profile	Regular
2	I6-W7D	WINTERC-G	7 mm Dry
3	I6-VM_η=0.3	VM5A profile	$\eta_{upper} = 3 \cdot 10^{20}$
4	I6-S_β=0.75	SMEAN2	$\beta = 0.75$
5	I6-W5.5D	WINTERC-G	5.5 mm Dry
6	P17-W7D	WINTERC-G	7 mm Dry
7	BI-S4/8.5D	SMEAN2	4 mm/8.5 mm Dry
8	BI-S_β=0.75	SMEAN2	$\beta = 0.75$
9	BI-W4D	WINTERC-G	4 mm Dry
10	P17-W8.5D	WINTERC-G	8.5 mm Dry
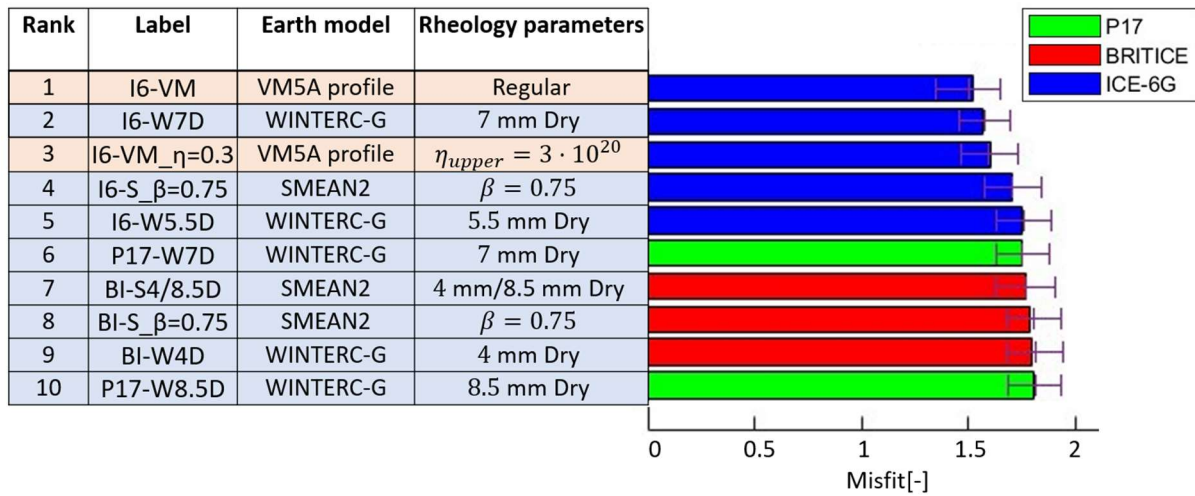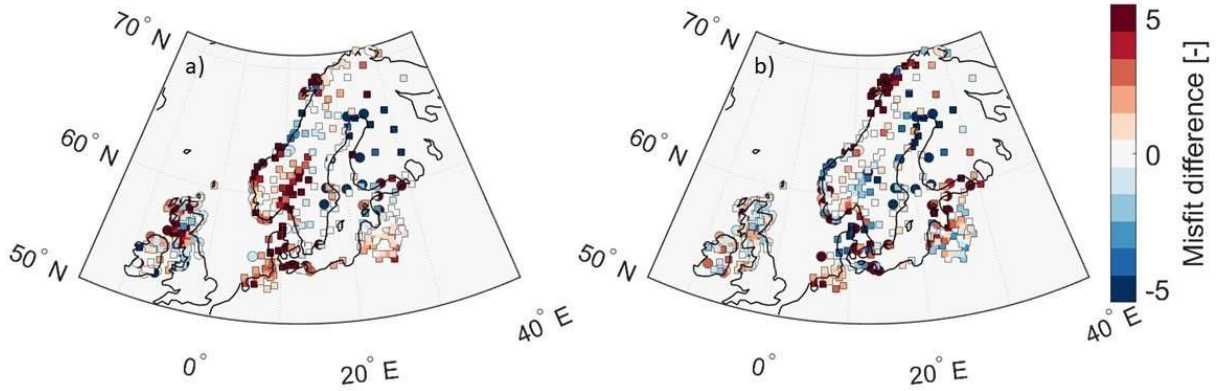
Figure 4.5: Misfit difference between models a: The misfit for ICE-6G with WINTERC-G 7mm grain-size and dry conditions minus the misfit of the reference 1D model (ICE-6G with VM5A). b: the misfit for BRITICE with SMEAN2 and $\beta = 0.75$ minus the misfit of BRITICE with VM5A. Red symbols are sites where the 1D performs better and blue symbols are where the 3D model performs better.

Finally, we want to establish if the regions underneath the BIIS and the SIS favour different 3D models and therefore we calculated the misfit for the British Isles and Scandinavia separately in Table 4.4. Although some models perform well for both regions, models with low viscosity or wet rheologies perform well for the British Isles but poorly in Scandinavia. In Scandinavia, models with higher viscosity, high lithospheric thickness or both do well.

Table 4.4: Overview of the best 10 models and their misfit with respect to the RSL and VLM data calculated separately for the British Isles region (top) and Scandinavia (bottom). Average viscosity and elastic thickness are computed as described in section 2.2. 1D models are highlighted in orange and 3D models are highlighted in blue.

Rank	Label	Earth model	Rheology parameters	Shallow upper mantle viscosity [10^{21} Pa s]	Deeper upper mantle viscosity [10^{21} Pa s]	Effective elastic lithosphere thickness [km]
1	I6-VM_η=0.3	VM5A profile	$\eta_{upper} = 3 \cdot 10^{20}$	0.30	0.30	70
2	I6-S10W	SMEAN2	10 mm Wet	6.31	0.13	115
3	BI-W7D	WINTERC-G	7 mm Dry	0.56	0.46	97
4	P17-W7D	WINTERC-G	7 mm Dry	0.33	0.58	93
5	I6-VM	VM5A profile	Regular	0.50	0.50	70
6	I6-W8.5D	WINTERC-G	8.5 mm Dry	1.01	0.49	93
7	I6-W10W	WINTERC-G	10 mm Wet	0.10	0.01	70
8	I6-S_β=0.75	SMEAN2	$\beta = 0.75$	3.97	1.16	70
9	BI-VM	VM5A profile	Regular	0.50	0.50	70
10	I6-W10W	WINTERC-G	10 mm Dry	0.77	1.26	147

Rank	Label	Earth model	Rheology parameters	Shallow upper mantle viscosity [10^{21} Pa s]	Deeper upper mantle viscosity [10^{21} Pa s]	Effective elastic lithosphere thickness [km]
1	I6-W7D	WINTERC-G	7 mm Dry	3.51	1.99	169
2	I6-VM	VM5A	Regular	0.50	0.50	70
3	I6-VM_η=0.3	VM5A	$\eta_{upper} = 3 \cdot 10^{20}$	0.30	0.30	70
4	BI-S4/8.5D	SMEAN2	4 mm/8.5 mm Dry	2.51	1.58	189
5	BI-W4D	WINTERC-G	4 mm Dry	12.59	0.50	122
6	I6-W5.5D	WINTERC-G	5.5 mm Dry	6.31	1.00	131
7	I6-S_β=0.75	SMEAN2	$\beta = 0.75$	62.6	2.76	135
8	BI-S_β=0.75	SMEAN2	$\beta = 0.75$	60.6	2.64	137
9	P17-W8.5D	WINTERC-G	8.5 mm Dry	7.41	2.40	147
10	BI-W7Da	WINTERC-G	7 mm Damp	0.16	0.05	154

The median best fitting models for the British Isles are 0.53×10^{21} Pa·s for the shallow upper mantle and 0.50×10^{21} Pa·s for the deep upper mantle. These viscosities correspond with previous viscosity findings of $0.4 - 0.6 \times 10^{21}$ Pa·s found in 1D GIA studies for the region (Bradley et al., 2023; Simms et al., 2022). For Scandinavia the median of the best fitting models is 4.9×10^{21} Pa·s for the shallow upper mantle and 1.3×10^{21} Pa·s for the deep upper mantle, which is higher than 0.3 - 0.7 $\times 10^{21}$ Pa·s that previous 1D GIA studies indicate (Steffen et al., 2008; Kierulf et al., 2014). I6-VM_η=0.3 can fit the data well. The RSL data in the Baltic is too limited temporally to distinguish between a small deflection at 10 ky and subsequent slow relaxation, as predicted by high viscosity models, or high deflection and subsequent fast relaxation because of low viscosity. However, in combination with the high uplift in Sweden, high viscosity models produce a better fit in our analysis. I6-VM_η=0.3 can even be outright rejected as it does not fit higher uplift rates (11 mm/yr) in central Scandinavia, predicting a maximum uplift of 6.5 mm/yr.

When we consider BRITICE models, which are less tuned to an Earth model, the hybrid model (see section 3.2) did better than other BRITICE models. While 1D studies in general favour low upper mantle viscosity, several studies with 1D models show misfit plots, in which a second region of low misfit exists for high upper mantle viscosity, matching the high upper mantle viscosity in the hybrid 3D earth model (J. L. Davis et al., 1999; Root et al., 2015; Schmidt et al., 2014).

Finally, we investigate the effective viscosity changes in time due to changes in stress (see equation 4). This may explain the difference in preferred models fitted to the paleo RSL data compared to the models that fit the present-day VLM data. The best fitting models for the British Isles include wet models for which viscosity depends more strongly on stress. This means that the viscosity of the mantle underneath the British Isles might change over time (Barnhoorn et al., 2011). Deglaciation induced stress lowers the effective viscosity so that the RSL curves correspond for much of the period with low viscosity model curves, but as the stress dissipates the effective viscosity increases, preventing full relaxation. In this case the modelled VLM shows uplift in accordance with the data.

In contrast, the only model in the top 10 for Scandinavia with a strong non-linear component, is the 7 mm model with 50ppm H_2O content at 10th place. The preference for dry rheology agrees with earlier conclusions on a preference for dry rheology for GIA models in van der Wal et al., (2013), as well as with Novella et al., (2015) who find that diamond samples from cratons have low amounts of water content trapped within them. The best fitting models as seen in the top 10 of Table 3 have viscosity changes of less than 0.2 Pa·s, considering elements that behave viscously (viscosity $< 10^{23}$ Pa·s) over the model simulation time.

4.4 Conclusion

In this paper we investigated to what extent a 3D rheology in a GIA model can improve the fit with relative sea level data and vertical land motion data in Northern Europe. We have run 43 models, of which 7 are 1D and 36 are 3D models that are combinations of three ice loading histories, 2 seismic models and 2 methods to obtain viscosity. 3D viscosity is used in the upper mantle, split in a shallow (70 to 180 km) and deep upper mantle (180 to 420 km depth). The average viscosity values of the shallow and deep upper mantle of these models ranges between approximately 0.1×10^{21} and 50×10^{21} Pa·s. Variation of the viscosity in the transition zone should be investigated to see the effect on fit of 3D models as it shows to be able to influence results somewhat.

3D models could match but not improve the performance of the VM5a model in combination with ICE-6G (I6-VM), which has been tuned to fit much of the same data used in this study using the VM5a viscosity profile. 3D models result in an improvement for the ice models which depend less on an a priori viscosity model, Patton et al., 2017 model (P17) and the BRITICE-CHRONO model (BRITICE). This shows the usefulness and limitations of using a 3D model, as it can improve GIA results but only when used with an ice sheet history that is not developed specifically using a 1D viscosity structure. When an ice model is used that has not been developed based on fitting ice heights to RSL data, the overall fit of the 1D reference models decreases, and some 3D models have the lowest misfit. This supports the development of ice sheet histories based on 3D viscosity (e.g. Huang et al. EPSL 2019).

Comparing our 3D model predictions to a limited number of 1D model predictions showed that, the spatial patterns and temporal patterns of the 1D and best fit 3D models are different in a way that cannot be explained by combining separate 1D models that have similar average viscosity. This can be seen in Scandinavia, where 3D rheology shifts the deflection more westward because of the high viscosity in the east. This aligns better with the low positive RSL found in the Eastern Baltic Sea and the low uplift rate in Finland.

GIA studies with 1D models show little difference in best fit upper mantle viscosity between the British Isles and Scandinavia (Bradley et al., 2023; Lambeck et al., 1998; Simms et al., 2022; Steffen et al., 2008; Kierulf et al., 2014), even though seismic models show considerable differences in Earth structure with a thick cold lithosphere underneath large parts of Scandinavia and higher local viscosities. We explored whether the data prefers 3D models with large or no contrast between the two regions. We use the median of the best 10 models instead of the average, as the median viscosity will always represent a tested model viscosity that fits the data well. For Britain we see that 1D models perform just as well as the best 3D models; for Scandinavia a 3D model can outperform 1D models. In particular in the centre and east of Scandinavia 3D models consistently fit better than 1D models. The median model viscosity for the British Isles is 0.56×10^{21} and 0.5×10^{21} Pa·s for the shallow and deep upper mantle viscosity,

respectively, together with an effective elastic thickness of 70-115 km. In Scandinavia the median viscosity is 4.9×10^{21} Pa·s for the shallow upper mantle and 1.3×10^{21} Pa·s for the deeper upper mantle and the region has a thicker elastic lithosphere (122-189 km). This is considerably higher than the global average and findings in previous GIA studies.

The performance of all 3D models enables conclusions about the solid earth parameters. Wet rheology can fit for the British Isles region, although some dry models can also still fit the data in the British Isles to an equal degree. The Earth structure underneath Scandinavia is almost certainly dry, as wet rheology leads to underpredicted uplift rate as in van der Wal et al. (2013). This agrees from petrological findings that cratons, as found under eastern Scandinavia, likely have little to no water content (Novella et al., 2015). The low temperature region underneath the North Sea in WINTERC-G had an adverse effect on the fit which means it is either not there or it does not result in a viscosity difference.

The best-fitting 3D GIA model is a 7 mm dry rheology based on WINTERC-G in combination with ICE-6G. The uplift rate is presented in figure S4.1. Its misfit of 1.57 is close to the misfit of the reference 1D model, of 1.53. While not an improvement, we suggest that the best fitting 3D GIA model can be considered as one of the correction models for various observations and purposes such as gravimetry corrections. The model accounts for variation in rheology, especially in the Baltic Sea (as in Spada & Galassi, 2012), the Norwegian Atlantic coast and for landscape evolution in Europe (Hijma & Cohen, 2011).

4.5 Supplementary materials: Uplift and RSL data fitting to constrain 3D viscosity in Northern Europe

4.5.1 Evaluating LGM deflection

In this section we evaluate the differences in the LGM deflection using a 3D viscosity profile compared to the traditional 1D profile. In Figure S4.1 we compare the differences in the total LGM deflection when using the ICE6G and P17 reconstruction combined with a 3D (SMEAN2 using β=0.5 and WINTERC-G with 7 mm and dry rheology settings respectively) and 1D viscosity profile. The total deflection beneath Scandinavia is reduced by up to 150 m using the 3D viscosity profile, with the maximum point of deflection shifted westwards. The high viscosity feature in this region also decreases the RSL. Furthermore, the stress in North Scandinavia is spread out over a larger area in the 3D model, making the deflection profile smoother as can be seen in the lower gradient for the 3D model in the cross section of Figure S4.1. For the P17 with WINTERC-G model we even see something similar happen for the northern British Isles.

The high local viscosity underneath the North Sea (see Figure 1 for viscosity profile model) in the P17 with WINTERC-G with 7 mm and dry rheology settings model decreases the local deflection in this region but also displaces the maximum deflection point below Scotland to the west, even though the viscosity below Scotland for the 3D model is similar to the 1D model. This high viscosity feature is not present in all seismic models, but it does show how the response across the British Isles can be significantly impacted by such a feature. It should be noted that using this 3D viscosity profile increase the misfit with the data across the British Isles.
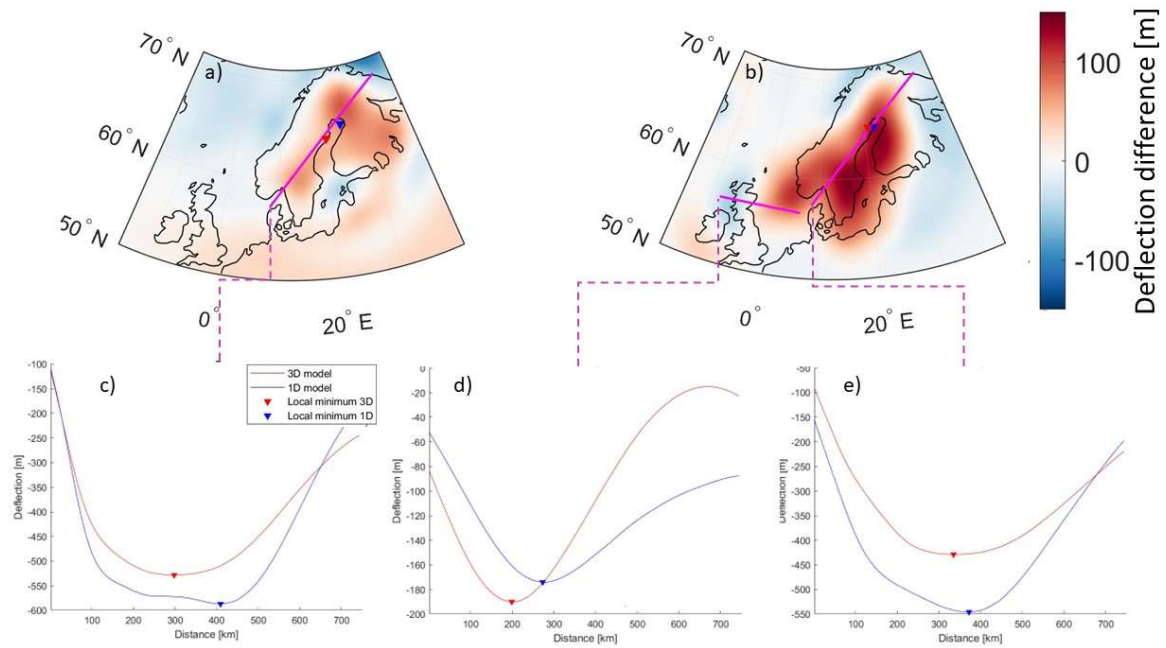
Figure S4.1: Comparison of LGM deflection. Figure a) shows the difference between the deflection at LGM between ICE-6G with SMEAN and a scaling of 0.5 and ICE-6G with VM5A. Figure b) shows the difference between the deflection at LGM between the Patton ice history (P17) with WINTERC 5.2 and 7mm dry settings and the Patton ice history with VM5A. Red regions indicate less deflection or a higher forebulge for the 3D model and the blue region indicate the reverse. The magenta lines are cross sections detailed in figures c-e. Figure c) is the cross section from the Danish coast to Murmansk in Figure a). Figure d) is the cross section from an offshore location north of Ireland to the Danish coast in Figure b). Figure e) is the cross section Danish coast k to Murmansk in Figure b). The red triangles in figure a-e indicate the point of maximal deflection for the 3D model in that figure, while the blue triangle indicates the point of maximum deflection for the 1D model in that figure.

4.5.2 Earth model mesh used

In this section the FEM mesh and initial settings are listed

Setting	Value
Spheric harmonic degree limit	360
Resolution input data	4 pixels/degree
Seed distance far field mesh	200 km
High resolution area radius	17.0
High resolution area seeding bias	5
Target seed radial direction high-resolution area	50 km
Target seed in plane high-resolution area	25 km
Centre of high-resolution area	(58.0N, 11.0E)

Loads have a linear progression between each timestep with the time vector being defined as:

Step	0	1	2	3	4	5	6	7	8
Time (ka BP)	122	63	26	22.5	20.0	17.5	15	13.5	12
Step	9	10	11	12	13	14	15	16	17
Time (ka BP)	10.5	9	7	6	4	3	2	1	present

Where the first timestep has no associated loads attributed as the load at a particular time step is defined as the difference between loads on that time step and the initial timestep.
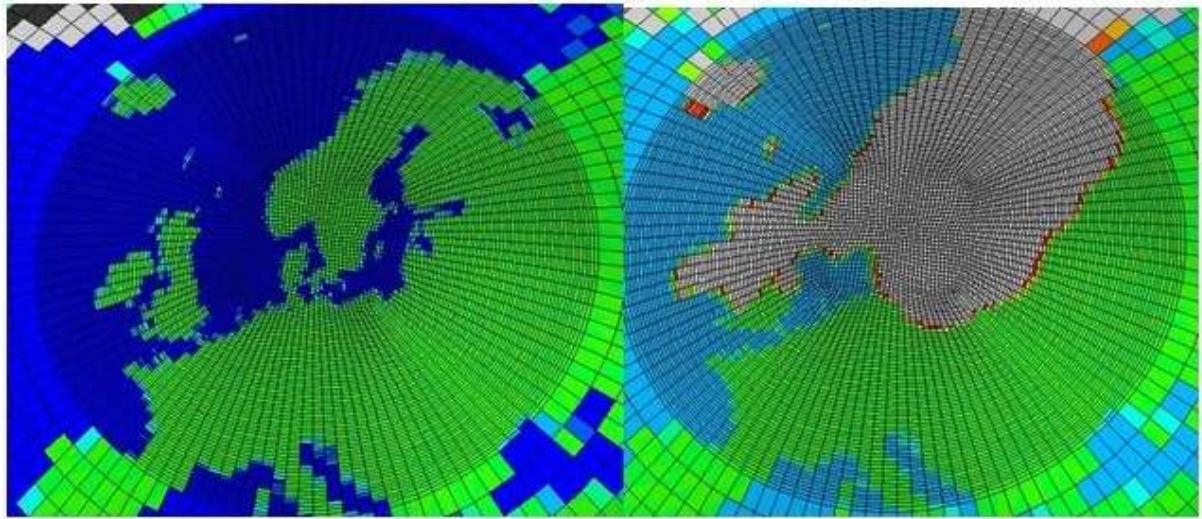
Figure S4.2: Mesh overview for the European region zoomed in on Europe with present day topography at the first time step (63 ky b.p.) of the model (left), and with the LGM extent of ICE-6G over the present day topography (right).

4.5.3 3D Viscosity profiles.

In this section we display the original values for SMEAN2 and WINTERC5.2 as used in this paper at the depths that were used to construct the viscosity profiles, followed by viscosity profiles derived from them for parameters that yielded good fit.
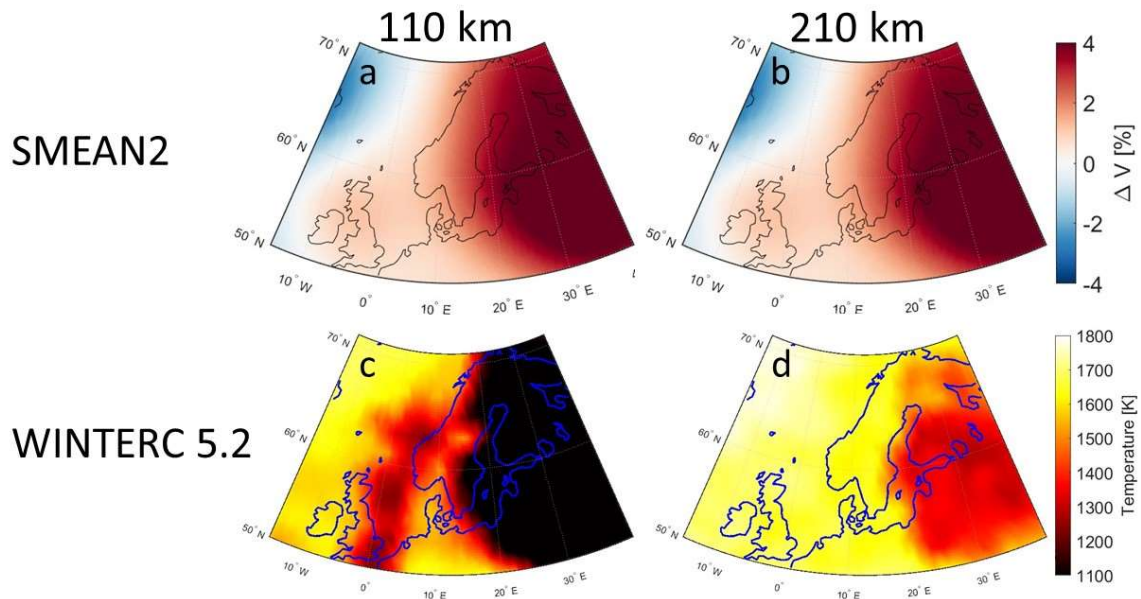
Figure S4.3: Slices of two depths, 110 km (Figure a) and c)) and 210 km (Figure b) and d)) for both the SMEAN2 model (Figure a) and b)) and the WINTERC-G model (Figure c) and d)). For figure a) and b) values represent the wave speed anomalies, while for figure c) and d) values represent the temperature in Kelvin.

Figure 4.1 of the main text shows the viscosity of the two best performing models for the RSL data and VLM data. For completeness we also show the viscosity of other Earth models that were used in models that performed well.
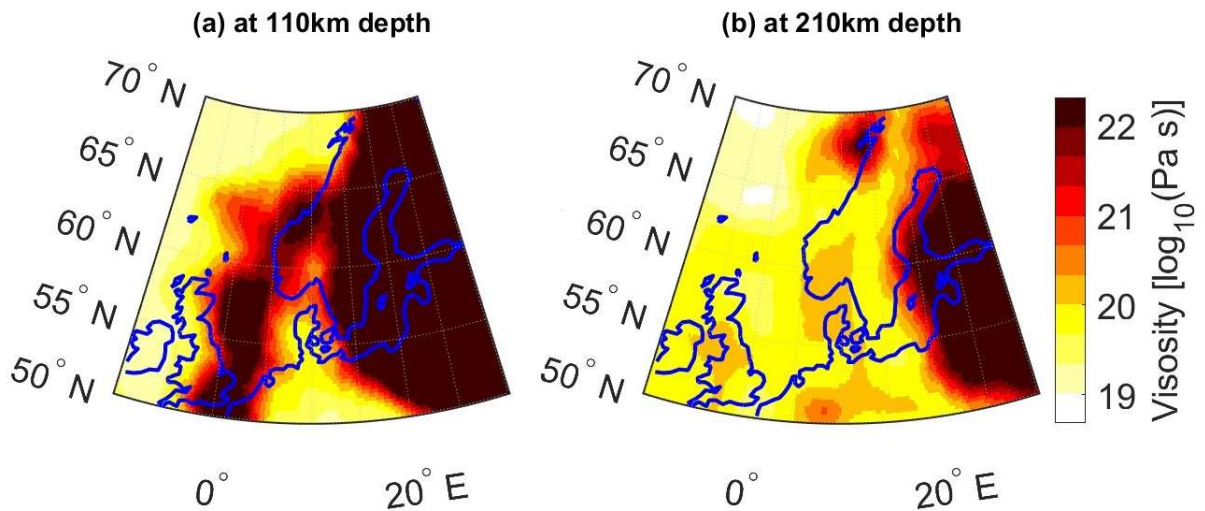
Figure S4.4: Viscosity at two depths, 110 km (Figure a)) and 210 km (Figure b)) for the WINTERC-G model with 4mm grain size and dry conditions. All values are 10log of the viscosity in Pas.

Figure S4.5: Viscosity at two depths, 110 km (Figure a) and c)) and 210 km (Figure b) and d)) for the WINTERC-G model with 5.5mm grain size and dry conditions (Figure a) and b)) and 8.5mm grainsize (Figure c) and d)). All values are 10log of the viscosity in Pa · s.
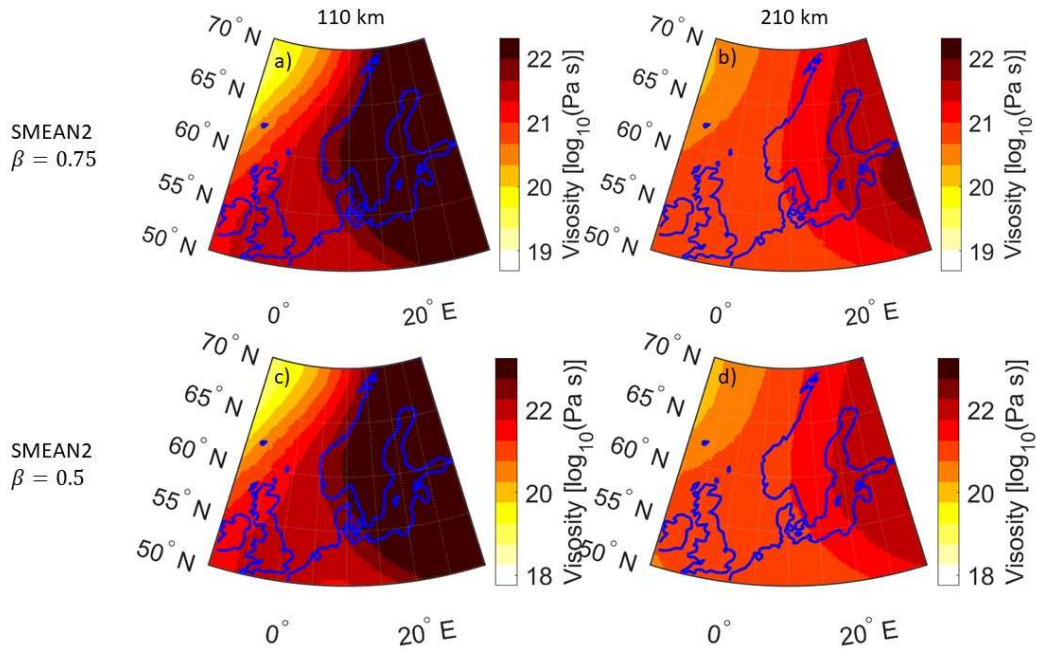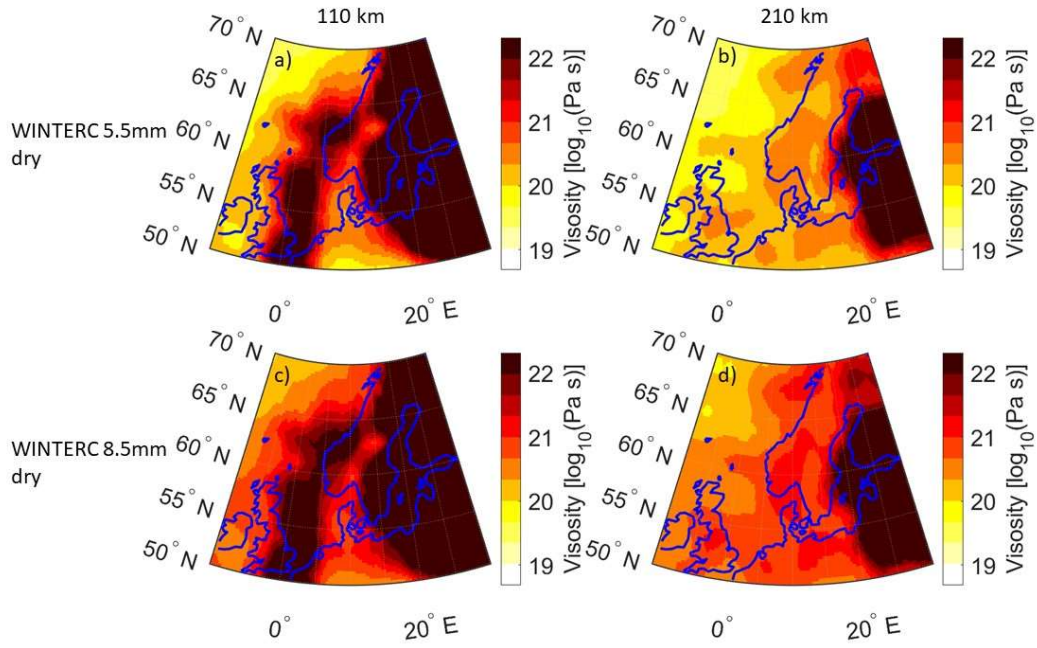
Figure S4.6: Viscosity at two depths, 110 km (Figure a) and c)) and 210 km (Figure b) and d)) for the SMEAN2 model with $\beta = 0.75$ (Figure a) and b)) and $\beta = 0.5$ (Figure c) and d)). All values are 10log of the viscosity in Pa · s.

4.5.4 Ice models

In this section we show ice height from the models used in the paper at selected t epochs.
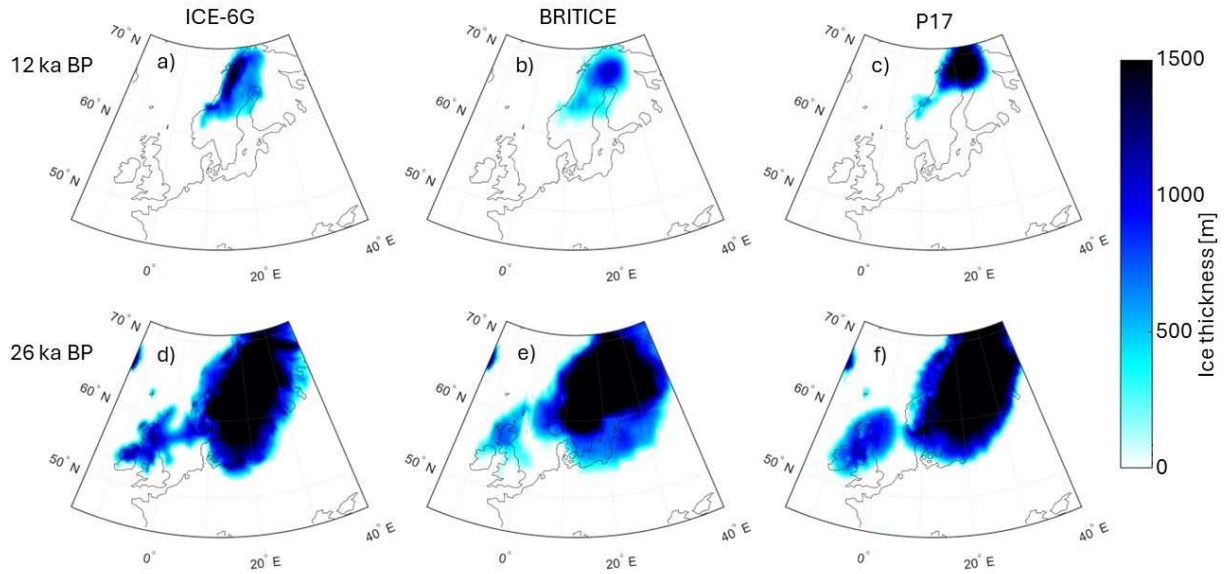
Figure S4.7: Ice history input used for this study. The top row (figure a), b) and c)) show the ice histories in Europe at 26 ky B>P. which is near each of their glacial maxima, while the bottom row show the extent of the ice for each history just before the oldest data points (12ky B.P.). Figures a) and d) shows BRITICE figures b) and e) show ICE-6G and figures c) and f) show the Patton model at the same points in time.

4.5.5 Model robustness

The methodology contains a few key design choices. In this section we will discuss the influence of those decisions on the results.

Normalization used in the misfit of individual data sets before calculating a combined misfit can be a point of discussion. An alternative for using the median to normalize the misfit for both datasets as done in the main text could be using the misfit of the best performing model instead. In Table S4.1 we can see the misfit table if we change the normalization so that Equation 7 becomes

$$Misfit_{total} = \frac{Misfit_{RSL}}{\min Misfit_{RSL}} + \frac{Misfit_{VLM}}{\min Misfit_{VLM}} \qquad \text{Eq. S4.1}$$

Table S4.1: Overview of all run models and combined misfit with respect to the RSL and VLM data for with a normalization according to equation E1. The Earth model structure is in the middle column, with additional details that are used to create each unique model in the final column. The bars represent the total misfit, with the colors detailing the ice model used for that specific model.

Rank	Earth model	Rheology parameters
1	VM5A profile	Regular
2	WINTERC-G	7 mm Dry
3	VM5A profile	$\eta_{upper} = 0.3 \cdot 10^{21}$
4	SMEAN2	$\beta = 0.75$
5	WINTERC-G	7 mm Dry
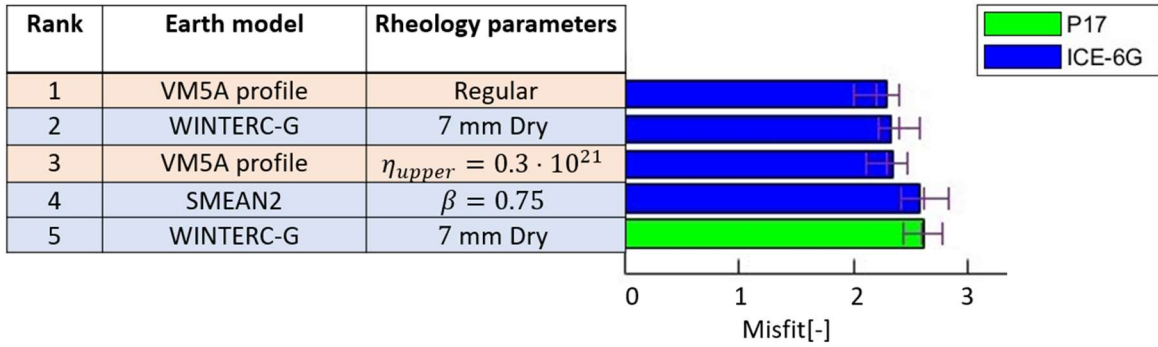
Changing the normalization changes the weighting of the RSL data with respect to the VLM data, but the weighting using the best performing models is similar using the normalization best on the median model. Consequently, the overall ranking of best performing models changes little.

The weighting matrix constructed using Equation 4.6 and 4.7 is dependent on a range of influences (spatial distance for GPS sites and both temporal and spatial distance for SLIPs) for each SLIP and GPS. For the main text the spatial range was chosen to be 200 km and the temporal range is 1000y.

Table S4.2: Top 5 best fit models and corresponding misfit with respect to the RSL and VLM data when the influence range for weighing each datapoint is altered. Figure a) shows halved influence range for weighing data points combined. Figure b) shows doubled influence range for weighting data points. The Earth model structure is in the middle column, with additional details that are used to create each unique model in the final column. The bars represent the total misfit, with the colors detailing the ice model used for that specific model.

a)

Rank	Earth model	Rheology parameters
1	VM5A profile	Regular
2	VM5A profile	$\eta_{upper} = 0.3 \cdot 10^{21}$
3	WINTERC-G	7 mm Dry
4	WINTERC-G	7 mm Dry
5	SMEAN2	$\beta = 0.75$

P17
BRITICE
ICE-6G

b)

Rank	Earth model	Rheology parameters
1	VM5A profile	Regular
2	VM5A profile	$\eta_{upper} = 0.3 \cdot 10^{21}$
3	WINTERC-G	7 mm Dry
4	VM5A profile	Regular
5	SMEAN2	$\beta = 0.75$

0   2
Misfit[-]
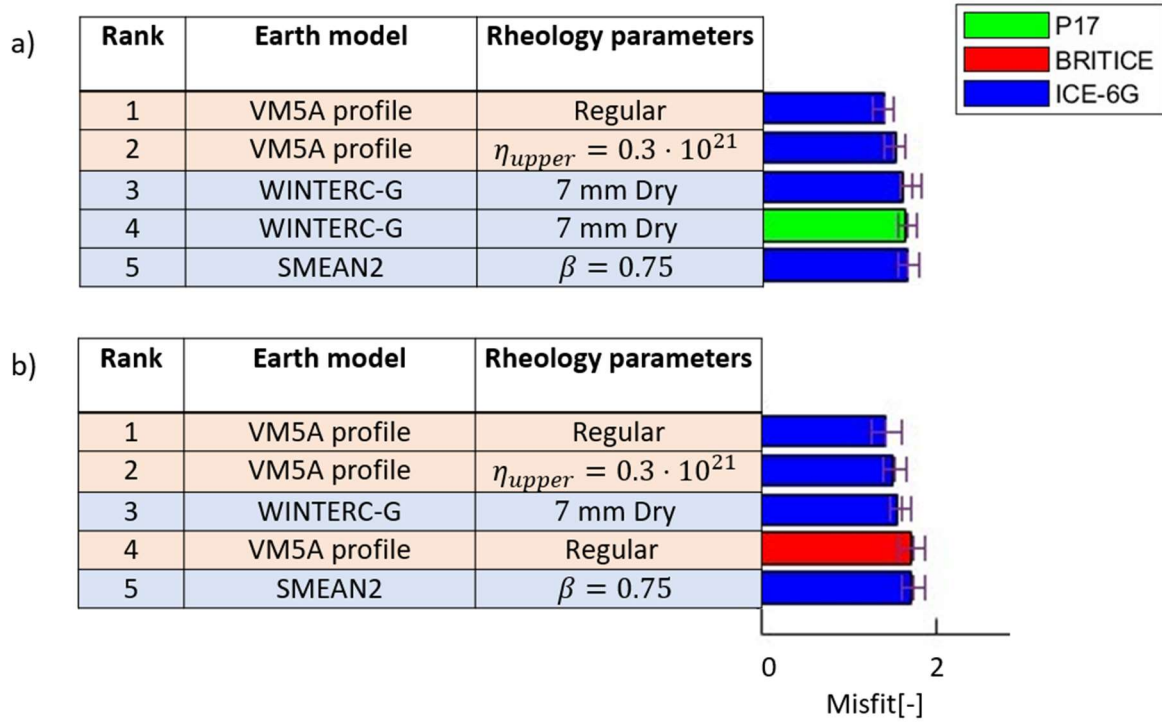
The influence radius at which data points are counted to be within the range of other data points is used to determine the weight of each station. When we half the range to 100 km spatially and 500y temporally we obtain a new list of misfits for the combined data (Table S4.2.a). Decreasing the influence radius at which data points count other data points to determine their weight increase the relative importance of two parts of the data set. Firstly, the weight of some of RSL sites with a wide temporal domain (mainly found in the British Isles) is increased, benefiting the VM5A model with lowered viscosity ($\eta = 0.3 \cdot 10^{21}$ Pa·s). The second model group that sees increased importance is the densely clustered VLM data points in southern Norway and Sweden. The P17 with WINTERC-G and 7 mm dry conditions does well in this area and therefore moves up in the ranking.

When we instead increase this range to 400 km and 2000 years, we mainly reduce the weight of VLM points in central Scandinavia. As such we see models such as the BRITICE 1D model, which had bad fit in central Scandinavia, move up in the table. The other models are four models that we also see in the top 5 with the normal influence radius.

The final choice we investigate is the cut-off point for the RSL sites we used. We use a threshold of 15% variation in RSL between the minimum and maximum model at a location and thus allow for a bigger area with data to be considered instead of the 20% used in the study. Additionally, we also used 25% variation between all models decreasing the area for which we consider the data. The result of varying this variable on the combined misfit is found in Table S4.3.

Table S4.3: Overview of all run models and corresponding misfit with respect to the RSL and VLM data combined with an altered area for which data is considered. Figure a) shows the combined misfit when more data is considered in the analysis. Figure b) shows the combined misfit results when less data is considered in the analysis. The Earth model structure is in the middle column, with additional details that are used to create each unique model in the final column. The bars represent the total misfit, with the colors detailing the ice model used for that specific model.
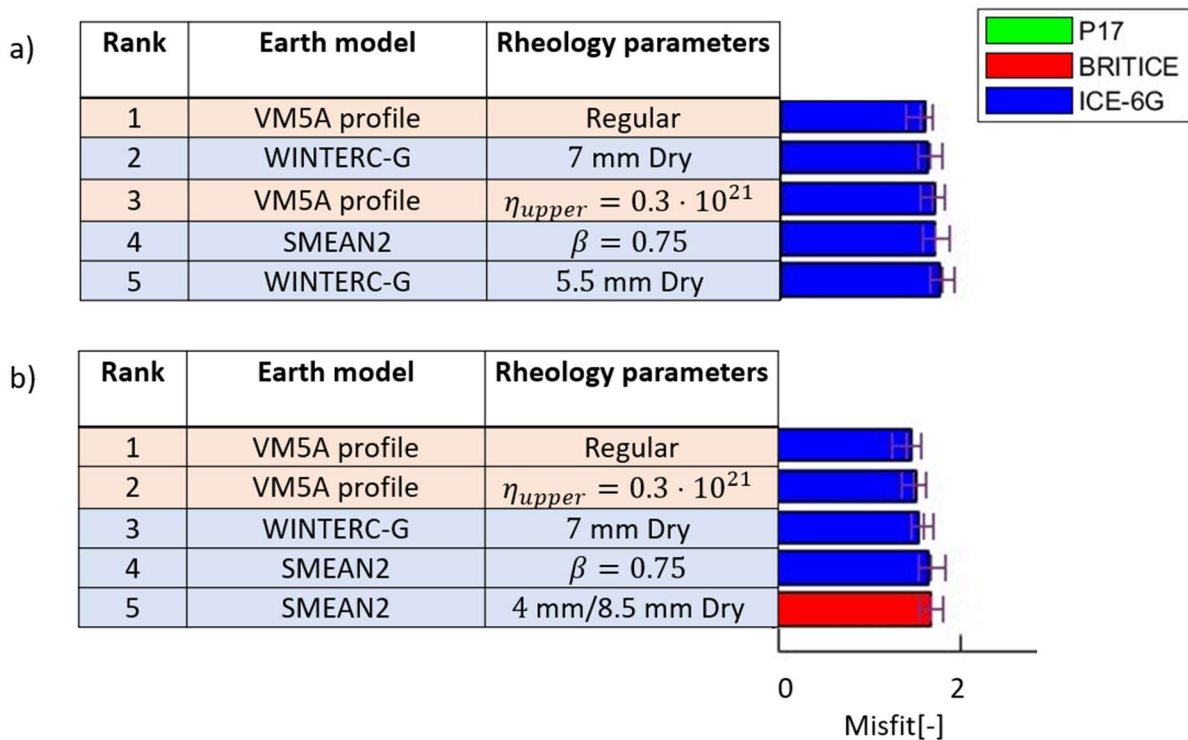
a)

Rank	Earth model	Rheology parameters
1	VM5A profile	Regular
2	WINTERC-G	7 mm Dry
3	VM5A profile	$\eta_{upper} = 0.3 \cdot 10^{21}$
4	SMEAN2	$\beta = 0.75$
5	WINTERC-G	5.5 mm Dry

Legend: P17, BRITICE, ICE-6G

b)

Rank	Earth model	Rheology parameters
1	VM5A profile	Regular
2	VM5A profile	$\eta_{upper} = 0.3 \cdot 10^{21}$
3	WINTERC-G	7 mm Dry
4	SMEAN2	$\beta = 0.75$
5	SMEAN2	4 mm/8.5 mm Dry

Misfit[-]

We can observe from Table S4.3 that the exact threshold to determine which data is considered has a limited influence on the ranking. We found that there is a wide range of reasonable thresholds for which the results vary little.

In conclusion, alternative choices for computing the misfit, would not change the conclusions in any substantial form as in most cases the same models perform well. ICE6-G with the regular VM5A model performs well under every setting, being the best model in every instance and ICE-6G with WINTERC-G set to 7 mm and dry conditions remains the best 3D model in all instances. Moreover, the median viscosities of the best fit models for Scandinavia and the British Isles remain the same and thus the conclusion on the need for 3D modelling in Europe is not affected.

4.5.6 Overview of all model combinations used
This section shows an overview of all 42 run models in Table S4.4.

Table S4.4: Overview of all run models. All models consist of basic earth model (first column) and corresponding rheology parameters to determine the exact Earth structure. Finally, these Earth models are run with one of three ice sheet reconstructions (third column).

Earth model	Rheology settings	Ice sheet reconstruction
WINTERC 5.2	4mm Dry	ICE-6G
WINTERC 5.2	4mm 500ppm H2O	ICE-6G
WINTERC 5.2	5.5mm Dry	ICE-6G
WINTERC 5.2	7mm Dry	ICE-6G
WINTERC 5.2	8.5mm Dry	ICE-6G
WINTERC 5.2	10mm Dry	ICE-6G
WINTERC 5.2	10mm 500ppm H2O	ICE-6G
WINTERC 5.2	2mm Dry	BRITICE
WINTERC 5.2	4mm Dry	BRITICE
WINTERC 5.2	5.5mm Dry	BRITICE
WINTERC 5.2	7mm Dry	BRITICE
WINTERC 5.2	7mm 50ppm H2O	BRITICE
WINTERC 5.2	7mm 100ppm H2O	BRITICE
WINTERC 5.2	8.5mm Dry	BRITICE
WINTERC 5.2	10mm Dry	BRITICE
WINTERC 5.2	4mm Dry	P17
WINTERC 5.2	5.5mm Dry	P17
WINTERC 5.2	7mm Dry	P17
WINTERC 5.2	8.5mm Dry	P17
WINTERC 5.2	10mm Dry	P17
SMEAN2	$\beta = 0.25$	ICE-6G
SMEAN2	$\beta = 0.5$	ICE-6G
SMEAN2	$\beta = 0.75$	ICE-6G
SMEAN2	4mm Dry	ICE-6G
SMEAN2	10mm Dry	ICE-6G
SMEAN2	10mm 1000ppm H2O	ICE-6G
SMEAN2	4mm Dry/8.5mm Dry	ICE-6G
SMEAN2	$\beta = 0.25$	BRITICE
SMEAN2	$\beta = 0.5$	BRITICE
SMEAN2	$\beta = 0.75$	BRITICE
SMEAN2	4mm Dry/8.5mm Dry	BRITICE
SMEAN2	5.5mm Dry/8.5mm Dry	BRITICE
SMEAN2	$\beta = 0.25$	P17
SMEAN2	$\beta = 0.5$	P17
SMEAN2	$\beta = 0.75$	P17
SMEAN2	4mm Dry/8.5mm Dry	P17

VM5A profile	Regular	ICE-6G
VM5A profile	$\eta = 5 \cdot 10^{21}$	ICE-6G
VM5A profile	$\eta = 0.3 \cdot 10^{21}$	ICE-6G
VM5A profile	Regular	BRITICE
VM5A profile	$\eta = 5 \cdot 10^{21}$	BRITICE
VM5A profile	$\eta = 0.3 \cdot 10^{21}$	BRITICE
VM5A profile	Regular	P17

4.5.7 Sensitivity of the transition zone viscosity

As ICE-6G was constrained to the VM5A Earth model, VM5A was used to model the transition zone (420-670 km) and deeper mantle. In this section investigate other choices are made regarding the transition zone viscosity. The transition zone in VM5A can be considered quite weak with a viscosity of $\eta = 5 \cdot 10^{20}$ Pa·s, therefore we have increased the transition zone viscosity with an order of magnitude to $\eta = 5 \cdot 10^{21}$ Pa·s. In this test we have used an upper mantle viscosity of $\eta = 5 \cdot 10^{20}$ Pa·s (The reference model, VM5a) and an upper mantle viscosity of $\eta = 5 \cdot 10^{21}$ Pa·s as it corresponds with the upper bound of upper mantle viscosity for parts of the Baltic Shield. The test uses ICE-6G as the ice history. In Figure S4.8 the VLM difference for both models is shown when the transition zone viscosity is changed from $\eta = 5 \cdot 10^{20}$ to $\eta = 5 \cdot 10^{21}$. For the standard VM5A model the higher viscosity in the transition zone has a non-trivial effect on the VLM (Figure S4.8 a), lowering it by as much as 4 mm/yr in central Scandinavia. This region is likely to have a higher upper mantle viscosity. Outside of Scandinavia the effects are in the range of or below the measurement error of local GPS stations. If we look at the change in VLM from changing the transition zone to a higher viscosity when a high viscosity upper mantle is used, we see that the changes are everywhere below the GPS measurement error.

Figure S4.8: Difference in uplift when the transition zone viscosity is increased by one order of magnitude for the reference model (a) and a version of the reference model where the upper mantle viscosity has also increased by one order of magnitude(b).

In Figure S4.9 we have examined the differences in RSL for both models when the transition zone viscosity is changed. For the RSL the differences are also not trivial. Especially for a weak upper mantle the differences can be quite significant at 10.5 ky

125

BP. However, the RSL differences are much smaller with a strong lithosphere, as is expected under Scandinavia, than for the model with a weak upper mantle. Therefore, the 25 m difference in RSL will not occur for the 3D models (it might be an issue with 1D models and could explain for example the relatively large misfit of BRITICE+VM5a and P17+VM5A compared to the ICE-6G+VM5a). Moreover, the largest differences also occur at 10.5 ky bp across central Scandinavia, but as the Baltic RSL sites have been filtered out for this time period the impact on the misfit results would be minimal. The only areas with RSL data that would be affected are northwestern Scotland and the area around the Lofoten on the Norwegian coast.

As with the VLM differences, the patterns of the RSL differences vary for all for cases, making it hard to draw very definitive conclusions regarding the effect of increasing transition zone viscosity

Therefore, we could not exclude the possibility that varying the lower mantle viscosity would change the overall fit and perhaps even best fitting model but considering that for both the VLM and RSL data the key regions of the Baltic and most of the North Sea coasts would only see limited changes, we think a change in transition zone viscosity will not impact the main conclusions of our work.
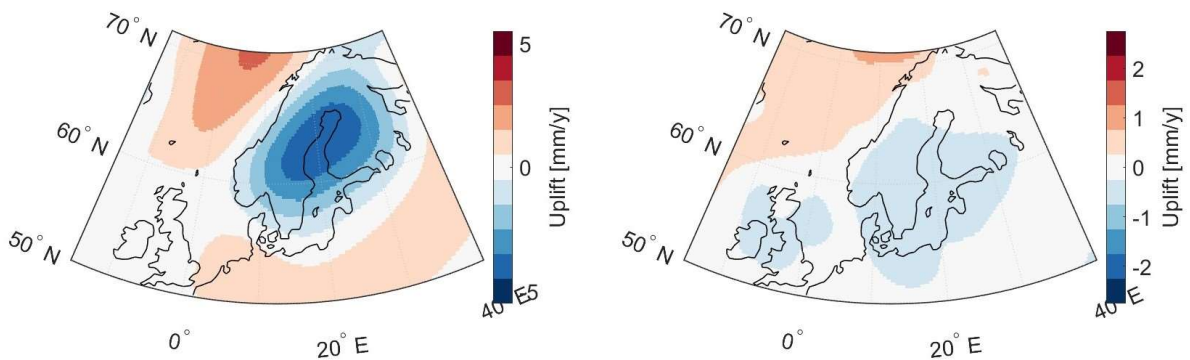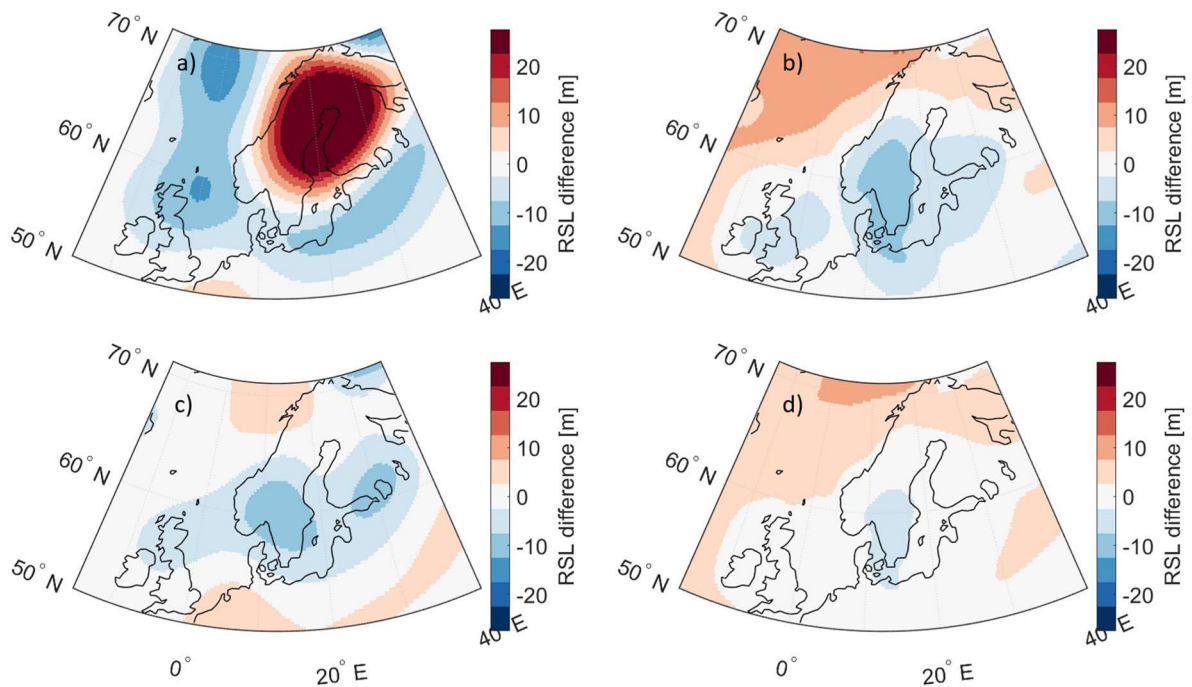

Figure S4.9: Difference in RSL when the transition zone viscosity is increased by one order of magnitude for the reference model (Figures a) and c)) and a version of the reference model where the upper mantle viscosity has also increased by one order of magnitude (Figures b) and d)). Figures a) and b) represent RSL changes at 10.5 ky bp. Figures c) and d) represent RSL changes at 7 ky BP.

4.5.8 Overview of I6-W7D results

In this section we present the results for the best performing model in our study: the combination of the Earth model based on WINTERC-G with a dry non-linear rheology with a grainsize of 7 mm and the ice history ICE-6G (I6-W7D). In Figure S4.10 the present-day uplift is shown. In Figure S4.11 the RSL is shown for 12 ky BP until 4 ky before present.
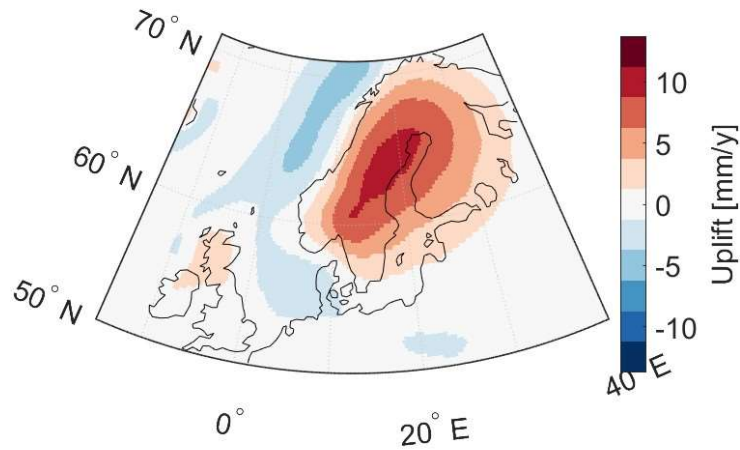
Figure S4.10: Present-day uplift in Europe for model I6-W7D.
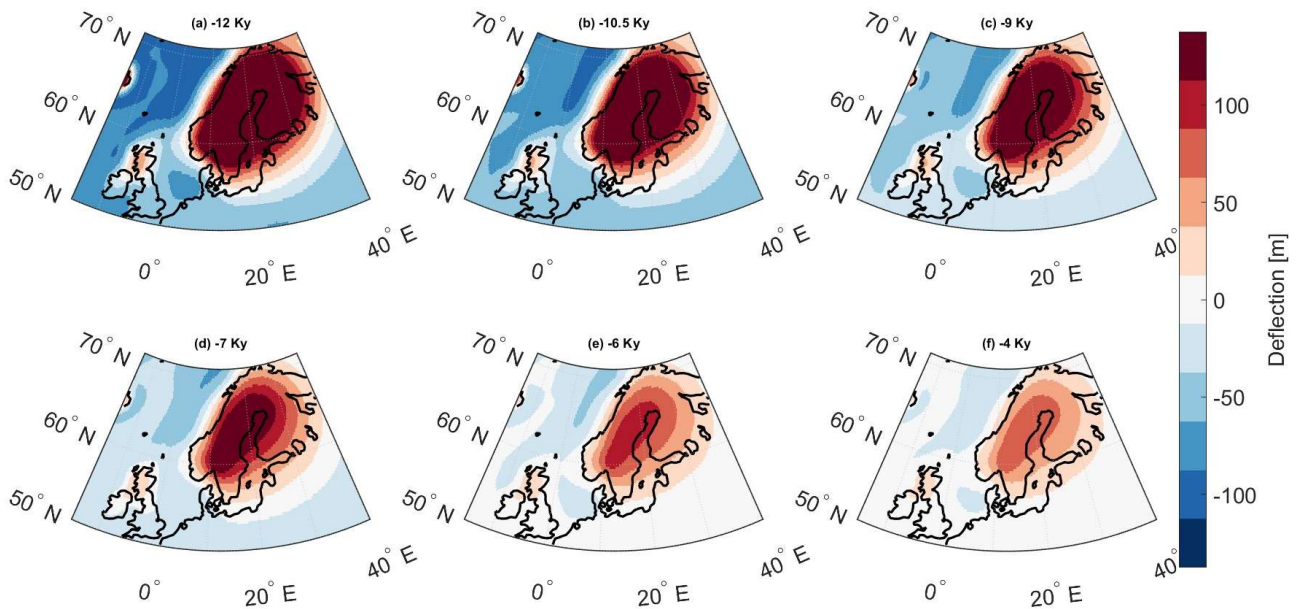
Figure S4.11: RSL in Europe for model I6-W7D for the period between 12 ky BP and 4 ky BP. Temporal cross-sections have been taken for a) 12 ky BP, b) 10.5 ky BP, c) 9 ky BP, d) 7 ky BP, e) 6 ky BP., and f) 4 ky BP

127

4.5.9 Notes on testing differences in model performance

When testing how well models perform compared to one another there are several statistical methods available. However, we found that for this study commonly used methods were difficult to incorporate without stretching assumptions too far. In Blank et al., (2021) a Chi-squared test was used to relate 3D model results to 1D model results. The difference in that study is that the 1D model results are fitted to the 3D models, which formed a simulated reality. This is contrast to this paper, where we fit both 1D and 3D models to observations instead of to one another.

When we fit the models, it is important to establish the number of parameters the model uses. While technically the load on every surface element can be varied and rheology parameters can be changed for each mantle element, we have obviously not done so. At minimum we can argue that we varied the ice history, Earth model, and two rheology parameters. In combination with the large amount of data used in this study, the result would be a critical value so high it would validate half of the tested models.

The second problem with using the Chi-Squared test is the weight matrix, as only isolated observations have a weight of 1. Normalizing the weight matrix for the modus of the weights could be argued as a solution. Alternatively, we could transform the weights so that the sum of the weights would equal the number of observations, but depending on the modus the weight matrix can push models over the critical value of the Chi-squared test just based on the normalization used.

Finally, having combined both the VLM data and RSL data complicates the issue further. The RSS of the RSL will create a bias for RSL points with a high leverage, which are often unreliable. As the RSL data set has far more high leverage data points than the VLM data set it will significantly outweigh the impact of RSL compared to GPS in these tests, defeating the point of trying to combine both datasets.

Another way to compare models is by using an F-test. However, the F-test is most suited to compare distributions to one another. While the F-test can be performed with the sampled standard deviations it only provides information on how well distributions match instead of how well the performance of those models compared to the observations match.

Other methods, such as T-tests or the log-likelihood ratio test require model solutions to have a distribution, but by the deterministic nature of the model this is not the case. As such we have chosen to simplify the problem. By random sampling 2/3 of the data set in a 1000 times repeated sampling experiment we can obtain a sampled distribution of the misfit for each model. Having a distribution for the model based on sampled data gives insight in how sensitive each model is for over or underrepresentation of areas in the data set. Models with a relatively large variation are more sensitive than other models to specific (sets of) datapoints, meaning they will likely fit some area very well or very poorly, while the reverse is true for models with small variations.

When the residual distribution for the models is assumed to be Gaussian a standard T-test (two-sided with a confidence level of 0.95) can be performed between any specific two models to determine if the models mean misfit values differ significantly from one another. The choice one must make is the sample size. If the sample size is smaller the variation for the sampled means will increase and vice versa. We feel that that sampling 2/3 of the data set strikes a balance between not allowing any variation at all in the results when we would increase the sample size on the one hand, and limiting the sample size to much so unrealistic biases for specific regions would be embedded in the sampled data on the other hand. We do recognize that this is still not a very exact method as sampling 60% or 70% of the data would fit the same criteria, while it does change the critical values for a T-test between models. A similar argument could be made for the log-likelihood ratio test; however, the T-test is easier to visualize and interpret for the reader. Therefore, we would recommend the reader to look at the T-test critical values of the models as a strong indication for when models can be considered equal in fit to the data, rather than a hard statistical boundary.

Chapter 5

Conclusions and Recommendations

Bas Blank[1]

1) Delft University of Technology, Delft, Netherlands

Conclusions and Recommendations

Abstract

In Chapter 1 we summarized the state-of-the-art in the field of 3D GIA. 3D GIA studies have been done for all regions with major GIA signal in the world, using simple rheology models or large grid-sizes that obscure potentially important features in regions. For this reason, the effect of more 3D Earth models on the GIA contribution in observables like the RSL in the North Sea area or the ice mass balance in West-Antarctica is unknown. In this thesis a global GIA model was developed for the commercial software package ABAQUS, and we applied it to the Amundsen Sea Embayment (ASE) and Europe in order to investigate the effects of 3D models in these areas. For both studies we compared the results to the available data in both areas.

In section 5.1 we will reiterate the research questions we identified in Chapter 1 and provide answers based on the experiences and results from the rest of this thesis. The studies in this thesis do not only have their caveats but also exposed issues that can be improved upon by the field. We have split recommendations about this thesis and the field in multiple subjects. In Section 5.2 we examine the issues we faced when implementing ice histories that are tuned to a 1D viscosity model and combining different types of data when fitting the model. In Section 5.3 we critically evaluate the concepts of average viscosity and lithosphere thickness as well as assumptions that are made when creating 3D viscosity models. We discuss the omittance of variations in transition zone and deeper mantle structure from much of our research in section 5.4.

5.1 Answers to research questions

As GIA is a source of noise in climate relevant topics like local sea level rise and ice mass loss numerous models have been developed to estimate the effect of GIA on vertical land motion (VLM) data, relative sea level (RSL) data and gravimetry data. Traditionally models for GIA have only assumed variations in Earth parameters in the radial direction. Tomographic studies demonstrate that variations of Earth parameters in lateral directions (3D variations) exist (Debayle et al., 2016; Fichtner et al., 2018; Schaeffer & Lebedev, 2013), and in the last two decades global GIA models have been created to incorporate the effect of these 3D variations (A et al., 2013; Latychev et al., 2005; van der Wal et al., 2023; Wu, 2004; Zhong et al., 2003, 2022). Global models that utilized the finite element method (FEM) have used a grid-size of 2° (~220 km) (Huang et al., 2019; Kierulf et al., 2014; Liu & Zhong, 2016; Van Der Wal et al., 2013; Wu, 2004) and more recently 0.5° (~55 km) (Huang et al., 2023; Zhong et al., 2022). This decrease in grid-size is important as small-scale features in a study area could be incorrectly modelled if the grid-size is too large. The Amundsen Sea Embayment (ASE)

is one of the fastest deglaciating areas in the world with an ice mass loss of 130 Gt/yr (Barletta et al., 2018) but the main glaciers like the Thwaites Glacier only measure a 120 km in width. Even in large study areas like Europe we find important features like the Baltic Sea, with an average width of 193 km. While flat models have been developed with smaller grid-sizes (e.g. Kaufmann et al. 2000; Islam et al., 2016, Marsman et al. 2021) that can model small features as found in for example Iceland, these models are ill equipped to model entire continents such as Europe because elements like self-gravitation and a global sea level are not included. They also do not allow investigation of the effect of Background stress for areas such as the ASE as the stress from the post-LGM deglaciation of the Antarctic ice sheet would be missing.

Coupling models of GIA with ice evolution already requires better resolution than the available models offered so that the grounding line retreat can be accurately modelled. To avoid this issue global finite element GIA models (Huang et al., 2023; Zhong et al., 2022) had their global grid-size reduced in recent years. The downside is that this increases the number of elements in the model, with most of the elements placed at locations in the model where the added benefit is minimal. As such, the minimal grid-size these models reached did not go below ~55 km. Recently, finite volume method (FVM) based models such as the one from Peak et al. (2022) have been able to reach much smaller grid sizes, but at the cost of not being able to run non-linear rheology with the FVM model opposed to the FEM based models. Therefore, the first question we have, was:

- *How can we improve the ABAQUS based 3D GIA model such that it can be tailored to GIA in different areas, ice sheet sizes and applications*

We have demonstrated that we were able to create a 3D model that could be adapted to a wide variety of studies. This adaptability was possible through making a global mesh with a high-resolution area that can be adopted for small and large regions. The high-resolution mesh consists of an equi-angular grid placed within the global distance grid. Radial decreases in grid-size are achieved through ties in ABAQUS, surfaces in between node layers that form a constraint on the nodes of the adjacent layers. The center point of the high-resolution area can be moved so the model is able to focus on different regions. Being able to adjust the size and position of the high-resolution area means there are few restrictions on the area of interest; continental size areas with large ice shelves have been studied using the presented model in Europe and Antarctica, but smaller areas like the ASE can also be accommodated. The setup of the model is such that the element size in the high-resolution area can be set in the model. The choice is a trade-off between increase in computation time when the total number of elements in the model increases versus size of the elements for the high-resolution area. For the ASE the high-resolution area could remain relatively small resulting in a model with around 185 000 elements for a grid-size in the center of the high-resolution area of 25 km (With small variations in size within the high-resolution area). For Europe we needed a much larger high-resolution area but allowing a larger number of elements (~225 000 elements

in total) and consequently longer computation time the grid-size could be 40 km. This way, individual regions like the North and Baltic Sea could be resolved with an adequate number of elements.

Investigating the ASE using the refined mesh (Chapter 3) was done in the framework of ESA's GOCE+Antarctica project (Ebbing et al., 2016) which, among other aims, focused on increasing our understanding of the solid Earth in Antarctica and its role in GIA processes. The relatively small grid-size for Europe also proved interesting for Hijma et al. (2025) as they needed a way to correct new SLIP data from the North Sea for GIA with 3D earth structures that could be relevant. Specifically, the small grid-size allowed 3D features in the mantle and deformation features like the forebulge to be resolved to a usable degree for correction the North Sea data set. The benefits of being able to shift the high-resolution area around to a different area of interest was also used in two MSc theses that focused on GIA in Greenland (Faure, 2022; Kempenaar, 2022). The high resolution itself proved to be beneficial for more accurately modelling Greenland's coastlines, the relatively small high-viscosity regions and small regions of high VLM in southern Greenland.

In this thesis, ABAQUS has been employed to study GIA. However, compared to previous studies using ABAQUS standard (Barnhoorn et al., 2011; Steffen & Wu, 2011; van der Wal et al., 2010; Wang & Wu, 2006; Wu, 2004), we introduced several modifications through the capabilities of ABAQUS CAE that make the model more flexible and extend its applicability. The code is independent of the previous implementation of the Wu method used in van der Wal et al. (2015). In models using ABAQUS standard all coding had to prescribed in the input files for ABAQUS. As such, elements like the grid were hard coded in ABAQUS-specific syntax. With ABAQUS CAE, the grid can be generated based on pre-coded routines with changeable parameters. Additionally, the modular nature of the code makes it possible to either take out modules for usage in other studies, as is done in Nield et al. (2022), or add modules to add functionality to the code. This last point has been best exemplified the best in the work of van Calcar et al. (2023), who coupled the GIA model presented in this thesis to the ice evolution model ANICE. This has allowed for studying the feedback of 3D GIA on ice evolution through the influence of GIA on grounding line migration.

In Section 3.5.1 it is explained that the sea level equation and self-gravitation are solved using spherical harmonics on an equi-angular grid that is separate from the actual element grid that the forces and stresses are solved on. Being able to resolve the sea level with a smaller grid-size than the element mesh allows for accurate grounding lines. However, the accurate grounding lines would not supplement the overall model accuracy if the FEM grid, on which the water and ice loads are implemented, has a significantly larger grid-size. Thus, the high-resolution area made it possible to also implement the loads based on accurate coastline into the FEM part of the model with an acceptable resolution without increase the computation time beyond unfeasible limits.

ABAQUS CAE's RESTART option (which is not available in ABAQUS Standard based models) is also instrumental in coupling the GIA code to the ice evolution model. It allows for the GIA model to be paused at every time step so that ice evolution model can be evaluated. As such the entire timestep can be iterated for both the GIA model and the ice evolution model until convergence is reached for both, before moving on to the next timestep. This timestep-by-timestep approach is, however, also practical to couple other geophysical models to the GIA model. Because of the RESTART function, first steps have been made coupling the model from this thesis to both mantle dynamics and rotational feedback in the MSc work of Morra (2021) and Weerdesteijn (2019) respectively.

- *How will GIA estimates improve when using 3D rheology on smaller scale regions, specifically the Amundsen Sea Embayment, compared to 1D models?*

The Amundsen Sea Embayment is the location where most of the ice mass loss on Antarctica occurs, with an estimated yearly ice mass loss of -130 Gt/y (Barletta et al., 2018). This makes it an important site to monitor from a global sea level perspective, however the GIA in the region is not well understood as most GIA studies of Antarctica fail to replicate the large observed VLM there. Because GIA distorts the signal when computing ice mass loss, uncertainty in the GIA causes uncertainty in the actual amount of ice loss in the region (Shepherd et al., 2018).

Barletta et al. (2018) showed that 1D rheology could model the uplift in the ASE by including an ice history from 1900 onwards in combination with low viscosity for the region. The low viscosity in the region could have a stabilizing effect on the ice shelves. As low viscosity would decrease the relaxation time it would decrease the grounding line retreat and elevate the ice shelf. In this way both calving and atmospheric induced melting are reduced, reducing the total ice mass loss. However, they did not investigate 3D viscosity. Therefore, it was unknown before this thesis whether the fit with uplift rate data is sensitive to 3D rheology, and hence whether the low viscosity is widespread.

We investigate the effects of 3D viscosity in ASE. To do so, we created different viscosity profiles, we used a temperature profile from the upper mantle model WINTERC 3.2 and GOCE+. Using flow laws for olivine (Hirth & Kohlstedt, 2003) and flow law parameters like water content and grain size, these temperature profiles are converted to different viscosity profiles for the upper mantle. Using the different 3D viscosity profiles, we synthesized uplift data in the same locations as the actual GPS stations in the ASE. 1D models fit the synthesized data better than the 1D models could fit the velocity measurements in Barletta et al. (2018). This result suggested the possible effect of 3D viscosity was not bigger than the effect from uncertainty in the ice history. As such, 3D and 1D profiles are statistically indistinguishable from one another in the ASE. This is mainly due to scarce data coverage in the region. When the modelled response of 3D non-linear rheology is compared against 1D rheology important differences between both models are revealed in locations where no GPS stations are

located. 3D non-linear rheology models had very low viscosity (~10^{19} Pa·s) due to stress concentration underneath shrinking glaciers. The resulting uplift was higher but also more local compared to 1D rheology, for which the GIA response was spread out over a larger area. The localization of GIA as a consequence of 3D non-linear rheology was also observed in Nield et al. (2018). An important conclusion in Chapter 3 was also that the background stress impacts the effect of non-linear rheology on the effective viscosity. The relation between background stress and the possible effect of load induced stress in non-linear rheology is not straightforward and depends not only on the orientation and magnitude of the stress tensors of both respective stress sources but also on the ratio of the dislocation creep parameter versus diffusion creep parameter in each element. In the end we found that a higher viscosity mantle or mantle with limited non-linear effects seemed implausible as in those cases the ASE would still experience a response from the LGM, which is not observed.

Chapter 3 shows that even on a smaller scale non-linear 3D rheology can influence local GIA effects, creating a GIA effect that is more local but higher in magnitude, especially when high stresses like in the ASE are involved. At the same time, we cannot prove nor disprove the non-linear effect affecting the GIA in the ASE to a significant degree at the present day. While this means that until more data is available 1D models like in Barletta et al. (2018) can also be used to correct for local GIA, the impact of 3D non-linear rheology can be large (chapter 3) and therefore the impact on cryosphere-solid Earth feedback is significant (Van Calcar et al., 2023).

While the ASE was the main small-scale region in this thesis our model has also been applied to the small region of the North Sea in Hijma et al. (2025). When our 3D FEM model was applied to just the North Sea, we found no improvement in the fit to the RSL (Hijma et al., 2025), corroborating findings from Chapter 4 that the North Sea likely has little 3D variations underneath it. The changes to GIA solutions by introducing 3D rheology to neighboring Scandinavia are not accurate or impactful enough to improve the data in the North Sea region.

Chapter 3 showed that Amundsen Sea Embayment (ASE) could be sensitive to 3D GIA because of low local viscosity and large changes in loads over time, but a region like Iceland could possibly also fit this description and would be good study area once a version of the model with coupled mantle dynamics is developed.

- *Can we improve the fit to RSL and VLM data by applying 3D rheology in north-western Europe?*

In Chapter 3 it became obvious that if field measurements are scarce, it is not possible to distinguish 1D models from 3D models in the data. However, it is expected that viscosity variations within a small region, such as the ASE, are smaller than variations within a larger region. Therefore, measurements over a larger region could show effects of 3D rheology. A region like Europe fits this description better as it is larger and tomographic studies indicate difference in mantle structure between Eastern and

Western Europe (Fichtner et al., 2018; Schaeffer & Lebedev, 2013). This is also confirmed by geological studies as the eastern part of Europa is believed to be a large craton, the Eastern European Craton. The older colder craton is more likely to have higher viscosity mantle underneath it than the warmer western parts of Europe (Tesauro et al., 2009). With a large part of Northwestern Europe covered by ice sheets, from the Barents Sea to Britain, we would expect these differences in viscosity to become apparent in VLM induced by GIA. However, so far, the expected viscosity differences have not become apparent from comparisons between most 1D GIA studies for Europe. Studies for Scandinavia (Kierulf et al., 2014; Lambeck et al., 1998; Steffen et al., 2008) and Britain (Bradley et al., 2011; Simms et al., 2022) both find comparable upper mantle viscosity for both regions. The exception to this is Rovira-Navarro et al. (2020), which uses GRACE data to compare 1D models from the Barents Sea to Scandinavia and finds that the viscosity in Scandinavia is expected to be a factor of 2 times larger than the viscosity underneath the Barents Sea. This aligns more with the findings from tomographic studies(Celli et al., 2021; Fichtner et al., 2018; Schaeffer & Lebedev, 2013).

To create different viscosity profiles, we used the newest iteration of the WINTERC upper mantle model, WINTERC-G. Furthermore, a seismic profile from the averaged tomography model SMEAN2 was also used to create 3D viscosity underneath Europe. As SMEAN2 is an average of multiple seismic models, Earth models based on it had a smoother viscosity profile than Earth models based on WINTERC-G, where for example a high viscosity feature can be found under the North Sea and Eastern Britain (Celli et al., 2021; Fichtner et al., 2018).

In Chapter 4 it is shown that for the entire Northwestern Europe 3D models are distinguishable from 1D models and improve the fit to the available data for certain regions, such as Eastern Scandinavia. Specifically, the high positive RSL values on the Eastern Baltic coast could only be replicated by models with longer relaxation time and thus higher viscosities, while at the same time the 3D rheology shifts uplift westward so the lower VLM in Finland could also be fitted. The only possibility for 1D to fit this region was with very low relaxation times that resulted in more deflection over the past few millennia to match the fast decline in RSL while at the same time matching the low present-day VLM. This 1D solution is rejected as it did not come close to producing the maximum observed uplift in Scandinavia and there is no tomography study that would provide any indication of low temperatures that could lead to such low upper mantle(?)viscosities (0.3×10^{21} Pa·s). This confirms that the found 3D solutions are the only way to both fit RSL and VLM in the region. we found areas in Eastern Scandinavia that are consistently improved by the best 3D rheology models, that were not highlighted in previous literature investigating the effect of 3D rheology in Europe using similar rheologies. The fit for the North Sea and North Sea coastal region often did not improve or even worsen. This indicates that the high viscosity underneath the North Sea in WINTERC-G based Earth models, and to a lesser extent also in the SMEAN2 based models is probably not present.

When we consider all ice histories, we established that 1D Earth models can fit the data as well as 3D Earth models, but this is partly because of the built-in bias for 1D models in an ice history like ICE-6G that were developed in tandem with an 1D Earth model (VM5a). When we only consider ice histories that were developed somewhat independently from 1D models (the model from Patton et al., 2017 and the BRITICE-CHRONO model) we found an improvement in the fit to RSL and VLM data when we applied 3D rheology. This illustrates that the dependence of ice models like ICE-6G on a specific 1D Earth model prohibits conclusions on how well 3D models can fit the data.

5.2 Data and Ice histories

As explained, the ice histories that use a certain 1D model in their construction form an obstacle to assess 3D model results. The ideal setup for finding earth structure through GIA studies would either be having an ice model that is independent from any Earth model or have every Earth model tested with a dedicated ice history. The former is unfeasible because, as much as can be learned from geological evidence and far field RSL on the position of ice sheets and total mass in the ice sheets, the ice sheet reconstruction will essentially be under constrained as the ice evolution models will fail to provide a unique solution that replicates the geological evidence. Therefore, local ice height must be constraint using some form of ice dynamic model that includes solid Earth feedback, and which predicts reasonable sea level and vertical motion. The option where every model is tested with its own ice history is also still far off because of computational limits. A currently achievable alternative would be to test 3D models with ice sheet reconstructions based on 3D Earth models, even if the 3D Earth models would differ from the 3D Earth model used in the ice sheet reconstruction. While currently there is no complete ice-history built using a 3D Earth model, a version where North America and Europe are fitted to VLM and RSL data with 3D rheology does exist (Huang et al., 2019). Thus, 3D based ice history development should be an immediate objective for the GIA community as these ice histories will likely result in significant improvements in the GIA estimates for locations like Antarctica and Europe.

Coupled models of 3D GIA with ice evolution are the first step to building those models. However, a single model run of a fully coupled model still takes days or even weeks. Thus, this issue can only be resolved once significant advances in computational processing power are made, or the models are innovated to be much more computationally efficient. Models like those from Zhong et al. (2022) claim to be able to do a 3D evaluation on a model with a 0.5° grid-size in 4.5 hours with 96 CPU's. Such GIA models would, once coupled with an ice evolution model, be a first step in achieving full 3D ice histories for multiple different 3D rheologies. Once these advances are made, it would be insightful to redo a study such as done in Chapter 4 with different ice histories that are all based on specific (3D or 1D) Earth rheology parameters. As such one would not simply compare Earth models, but Earth model and Ice history combinations with one another to fully assess the impact of 3D rheology on VLM and RSL data.

138

Another issue on the analysis of the data that was already stressed in Chapter 4 is how to combine RSL and GPS data. While we feel that the method in Chapter 4 is a method that finds a balance in weighting both data sets somewhat equally but without deflating statistical uncertainties for each data point, we do recognize that as a debatable point as is evident from other studies choosing a different approach(van der Wal et al., 2015; Whitehouse et al., 2012). The problem that arises when RSL data and GPS are combined is that the misfit for RSL is almost always inherently worse than the misfit for VLM, as the GPS station measurement uncertainties seem to capture the variance in data much better than is the case for the estimated measurement uncertainty of the RSL height in dated samples, as it excludes reasons why the measured RSL could deviate from the average RSL at that time (e.g. wind forcing, tidal effects etc.). If this additional uncertainty of the RSL height was estimated for the sea level indicator points (SLIPS) used in Chapter 4, then we would advocate for combining that with the measurement uncertainty in height to create a combined RSL variance. With this combined RSL height variance the method proposed in Whitehouse et al. (2012) to also include the dating uncertainty would potentially produce a more representative misfit for the RSL than has been done before.

Assuming the uncertainties perfectly represent the variation in the data, the misfit in RSL should be calculated by establishing the shortest distance between a measurement point and the modeled RSL curve, while normalizing the sea level height and its age for their respective measurement errors. However, there is more uncertainty in the RSL height than the standard deviation from the SLIP data suggests. It is not rare for contemporary SLIPS in the same location to deviate more than a few standard deviations from each other. Such outliers have a disproportionated influence on the total misfit. The variation in the RSL heights for the same location can be attributed to short term processes that are not captured in a GIA model. Ashe et al. (2019) found they always needed to include more terms than the global average and the local GIA effect to account for the variability in RSL datapoints. Physical processes that explain this variation are short term ocean oscillations, tectonics, sediment compaction, and glacier specific effects (Ashe et al., 2019). When present day tide gauge data is examined the main drivers outside of GIA are found to be the local thermal expansion, salinity related changes and atmospheric pressure related changes. However, with these effects included still only 30-85% of variability was explained, depending on the location, along the Norwegian coast (Richter et al., 2012). Non modelled influences such as wind effects and mass distribution in the deep ocean due to hydrographic changes are also mentioned as possible error sources (Richter et al., 2012). The measurement uncertainty from SLIPS in the RSL height cannot be used in combination with the temporal uncertainty to compute model fitness compared to the data if we do not include uncertainties on measured RSL compared to average RSL for each location in each time period. Either model fitness should be calculated as proposed in Chapter 4 or these variations should be incorporated into the SLIPS RSL variance.

5.2 Upper Mantle and 3D viscosity

While we have found that 3D models cannot fully replace 1D models as the difference in computational costs makes 1D models more suitable to large parameter studies, we have found that 3D models can provide new insights when the results are compared to 1D models. Two parameters which are most used to compare 3D studies to 1D studies are the average effective mantle viscosity and average elastic lithosphere thickness, because in 1D models, the mantle viscosity and lithosphere thickness are themselves parameters(e.g. Barletta et al., 2018; Peltier, 1974). These two values are also easy to compare from one GIA study to another, but harder to other geodynamics studies. Lithospheric thickness, defined for GIA as the top layer or elements which do not behave viscously on the time scale of the model is related to elastic thickness from gravity but is not the same (Eaton et al., 2009). Furthermore, lithospheric thickness should be understood as average elastic lithosphere thickness and viscosity should be understood as average effective viscosity, and they are not universal physical quantities.

This is also one of the reasons why using flow laws instead of viscosity as parameter is beneficial, as things like grain size and water content are parameters that are physical quantities which are usable in a wide variety of geodynamic models and which have been observed in sparse findings of mantle rocks (Dannberg et al., 2017; Novella et al., 2015). As GIA models have started to include 3D variations, the average effective viscosity and average elastic lithosphere thickness are no longer directly used as parameters in 3D models. This raises the question of whether they can or even should be computed from a 3D model, to compare to 1D studies. The first issue is that obviously not all elements contribute to local GIA, therefore it is not clear which elements to include when computing an average of the log values of the viscosity (Paulson et al., 2005). Global averages of 3D viscosity do not fit GIA observations as well as local averages of the same 3D viscosity profile (A et al., 2013). We must create a criterion based on which we make an element selection. In Chapter 3 we used relative stress, but we found in Chapter 4 that for Europe relative strain was a more logical choice, as stress was accumulating in highly viscous elements that are hardly contributing to any VLM. The same conclusion was reached already in Christensen (1984), where the strain rate is also used as a weighting function to compute the average effective viscosity. Whether stress or strain is used as a weighting function, a threshold of relative stress and strain must be assumed above which elements are considered as contributing. While we have also taken an unweighted average, not all elements equally contribute to VLM and so a weighted average should be taken to obtain an accurate representation of the average viscosity. If weights were to be used the number of assumptions would only increase further. If we have a non-linear rheology the viscosity of elements can also change over time, which again complicates the computation of an average viscosity only further. The only reasonable way to solve this is to fit a 1D model to the 3D model to obtain a reasonable estimate of what the average viscosity would be that best approximates the results of the 1D model (van der Wal et al., 2015).

When considering the elastic lithosphere, we define this term as the part of the lithosphere that behaves elastic over the course of the glacial cycle considered, which is similar to most other GIA studies who use (almost) the same definition (Kuchar & Milne, 2015; Nield et al., 2018; Watts et al., 2013). But for the definition of elastic lithosphere thickness the same questions as with average viscosity exists concerning element selection: which elements have a high enough viscosity that they are considered to be part of the lithosphere, and which elements are actually contributing to this number for a region when using a global model? Furthermore, the elastic lithosphere also depends on the timescale of the process considered where for longer simulation an element can behave visco-elastic which would be considered elastic for faster processes as hardly any viscous deformation would take place in the shorter time frame. The point that elastic lithosphere has a time-dependent factor to it has also been raised in Lau et al. (2020). This means lithospheric thickness is more difficult to compare between studies that focus on different periods of loading. A similar solution, similar to the effective viscosity problem, might be possible to calculate the elastic lithosphere thickness by fitting 1D models to the 3D model, and adopt the best fitting elastic lithosphere thickness as the model's effective elastic lithosphere thickness. However, this would again mean trying to let the 3D model adhere to 1D parameters that do not exist in the 3D model nor the real world. More useful would be to compare the lithospheric thickness distribution or even the viscosity distributions from area to area. While 3D distribution figures itself might be hard to interpret, simplifying it to well-known statistical measures like boxplots or kernel density plots for different depths would already provide a more insightful way of comparing lithospheric thickness or viscosity estimates between different studies. At the very least, a central statistic like effective viscosity should be accompanied by a measure of spread, such as the interquartile distance or variance in either viscosity or elastic lithosphere thickness.

An important assumption done for scaled rheology was the conversion factor for seismic wavespeed anomalies to temperature anomalies, $\frac{\delta T}{\delta v_s}$. Here we have assumed that the seismic wavespeed in a material depends only on temperature and pressure (Karato, 2008). In reality, partial melt and more importantly, local mantle composition can also influence the seismic wave speed velocity without influencing the temperature (Goes et al., 2000; Trampert & van der Hilst, 2005). While this element is captured by the β constant in our equations (following Wu et al. 2013) it is still an extra source of uncertainty when interpretating individual wave speed anomalies found by tomographic studies. However, even if we assume the composition of the mantle to be homogenous seismic wavespeed also depends on grain size in the mantle which leads to several additional issues (Priestley & McKenzie, 2013). First of all, the $\frac{\delta T}{\delta v_s}$ used in this study is based on parameters found in laboratory experiments (Goes et al., 2000). The pressures thought to be present in the mantle are hard to replicate in laboratories for constant strain experiments, nor can experiments run for the thousand or sometimes millions of years needed to replicate mantle processes. Grain sizes in laboratory experiments are two

orders of magnitude smaller than the grain sizes we think are present in the mantle, depending on the depth the experiments are performed for. Second, we do not exactly know what the grain size is of mantle materials as all our information comes from surfaced mantle material and we have no way of establishing if and how the surfacing affects the grain size in these samples. Moreso, the samples from surfaced materials are few and they would only provide information from the shallow upper part of the mantle at a few specific locations. We do not know if these samples are accurate representation for the grainsize in the upper mantle at these locations or that they are anomalies. Still, we do know that grain size is likely to vary with depth in the upper mantle (Dannberg et al., 2017) and is not constant as assumed in our current model. This last point could be remedied by adopting a depth-grainsize relation based on the results from Dannberg et al. (2017). Adopting a method that incorporates the grain size depth relation could improve 3D rheology and the accuracy of models that use it, whether a $\frac{\delta T}{\delta v_s}$ conversion is used or a flow law that contains grain size.

Dislocation creep is non-linearly dependent on stress (Hirth & Kohlstedt, 2003), as such a mantle in which dislocation creep is significant will have an effective viscosity that is also dependent on the stresses that are present. While in this thesis we looked at GIA induced stresses, processes such as mantle dynamics can also add additional stress to the mantle. The model developed in this thesis was used in the MSc thesis of Morra (2021) where schematic mantle dynamics stresses induced stresses were introduced in the 3D FEM to calculate creep based on the combined stress tensor. The GIA model could be combined in the future with stresses from a full-scale mantle dynamics model. For orogenic regions such as Cascadia or mantle plume regions like Iceland, where both mantle dynamics and relatively small ice sheets induce stress, such a model would provide more realistic viscosities and give insight how mantle dynamics affects GIA in these regions.

5.3 Transition zone and deeper mantle

In this thesis we mainly focused on the upper mantle as the differences in viscosity are more pronounced there compared to the transition zone and the lower mantle. At the same time, we also concluded in Chapter 4 that changing the transition zone viscosity can affect uplift and RSL. However, we stopped short of investigating to what extent this influences the best fitting upper mantle model. For the transition zone Hirth & Kohlstedt (2003) compute a range of possible viscosities at 400 km between $\sim 10^{19}$ and 10^{23} Pa·s depending on the activation volume used. Other studies find a transition zone viscosity of 5×10^{19} Pa·s (Liu & Zhong, 2016), 5×10^{20} Pa·s (Rudolph et al., 2015), and $\sim 5 \times 10^{21}$ Pa·s (Ricard & Wuming, 1991), , and in a future study these viscosities should be explored when modelling GIA with 3D rheology with a 1D transition zone.

While a combination of seismic models such as SMEAN2 reveals that the transition zone has less drastic variations in 3D viscosity than the upper mantle it is not completely homogenous. Viscosity variations at the base of the upper mantle, such as a low

viscosity notch have been shown to influence the GIA signal in Scandinavia (Milne et al., 1998). Furthermore, the assumption of an olivine mantle does not hold for the transition zone as olivine experiences a pressure induced transition into wadsleyite at ~410 km depth and to ringwoodite at larger depth (Ringwood, 1975). This means that the flow law and flow law parameters should be changed to match the rheology in the transition zone, as for example described in Ritterbex et al. (2020). Would research into 3D rheology be continued with this model, it is advised to incorporate transition zone viscosity variations and transition zone flow laws.

The lower mantle viscosity has not been investigated at all in this thesis. Viscosity in the lower mantle can have an observable effect on GIA (e.g. Métivier et al., 2016). Large ice caps (~6500 km in diameter and a maximum height of 3300 km) can be sensitive to mantle viscosity up to the core mantle boundary (Wu, TBP; Lau et al., 2016). Regarding the lower mantle viscosity, there is some consensus that the deeper part of the lower mantle has a viscosity of between 9×10^{21} Pa·s and 4×10^{22} Pa·s (Caron et al., 2018; King & Masters, 1992; Lambeck et al., 2017; Liu & Zhong, 2016; Métivier et al., 2016; Nakada & Okuno, 2016; Roy & Peltier, 2018). The viscosity values for the upper part of the lower mantle (until 1000-1500 km depth), however, are more contentious and are thought to range from 1×10^{21} (Roy & Peltier, 2018) to 4×10^{22} Pa·s (Caron et al., 2018). Although theoretically the resolving power of the European Ice sheet should go as deep as ~1300 km (Mitrovica & Forte, 2004), it seems that the RSL data is hardly sensitive to the lower mantle viscosity and thus the viscosity is hard to constrain based on the European GIA signal (Steffen & Kaufmann, 2005). Nonetheless, the lower mantle was constrained with 95% certainty between 5×10^{21} Pa·s and 5×10^{22} Pa·s underneath Europe using VLM data from the BIFROST network (Milne et al., 2004). The average lower mantle viscosity should be varied when the largest ice sheet, the Laurentide ice sheet, is modelled as it more sensitive to lower mantle viscosity and has been used to constrain lower mantle viscosity (Argus et al., 2021; Lambeck et al., 2017).

GIA can also be sensitive to 3D structures in the deep mantle (Lloyd et al., 2024). However, it might be hard to define parameters for non-linear rheology for the lower mantle as well as exact flow laws as little is still known about conditions in the lower mantle, let alone grain sizes that could be used in flow laws. Conditions for strain rates for lower mantle rheology are almost impossible to replicate in laboratory experiments and as such statements regarding lower mantle rheology remains controversial (Chen, 2016). Thus, 1D maxwell rheology might still be advised for the lower mantle.

5.4 Future outlook on the field

A recurring theme when trying to assess the effectiveness of 3D models is that the collected data impacts this method of assessment to a large degree. In Chapter 3 we discussed the problem of the scarcity of data in the ASE and how this data scarcity prohibits us from observing 3D effects. At the same time, in Chapter 4 we had to find solutions to areas that are over sampled compared to other areas in Europe. In the future data scarcity in Antarctica is hopefully mitigated by placing more stations there. Of course, other aspects than just scientific relevance play a role here, as placing and maintaining stations in Antarctica is expensive, logistically complex and in the absence of uncovered bedrock often not possible at all. Secondly, space-based altimetry and tide gauges have not been utilized in this thesis, while for Europe the wide coverage and accuracy would have made it a potential useful addition to the work in Chapter 4. This has already been demonstrated by studies that identify the GIA fingerprint from tide gauges (Wang et al., 2021) and altimetry (Spada, 2017). As such VLM data, paleo RSL data, tide gauge data and altimetry data together form an impressive combination of data identify GIA effects. As the length of the time series for specifically VLM data and altimetry will continue to expand over time, the potential for this data in finding a GIA solution with an increasing higher accuracy will increase with time. In the future, studies using all these data types should become more common as their potential relevance will also increase over time.

While data collection could improve GIA solutions in the future, innovations in GIA models also have the potential to improve the fit to data. Of course, increases in computing power will make it more possible for 3D models to perform parameter studies in a similar manner as 1D models have been used the past decades. However, the inherent reduced computation time needed for 1D models will mean that 1D models will also benefit from increases in computing power making it possible to always do more extensive parameter studies than contemporary 3D models can do. While just doing more model runs in the same parameter space will at some point lose its usefulness, a study such as Hartmann et al., (2020) already proves that in that case the parameter space for 1D models can still be expanded, by segmenting the study area.

Another innovation in modelling that can reduce the misfit of GIA solutions compared to data is the development of neural network type AI GIA emulators. The field currently uses two different methodologies to compute GIA solutions: statistical driven inverse modelling and physics driven forward modelling. Neural network type AI would be capable of combining elements from both methods to compute better fitting GIA solutions. At the moment a proof-of-concept model that is able to perform sufficiently accurate inversions already exists, albeit only trained and verified on the effect of varying simulated ice history input (Lin et al., 2023). For the AI to also incorporate the effect of varying Earth rheology parameters would require a large amount of training data. 3D Forward model results can be used as basis for this training data. The neural network weights such an AI model would develop to constrain solutions would far

exceed the complexity of inverse models now used as it accounts for far more parameters when determining the Earth structure. If we would expand the AI emulation to simultaneously invert for the ice history as well as the mantle parameters, we would be able to generate mantle viscosity patterns with more degrees of freedom which are no longer constrained on assumptions on mantle composition such as the set values to convert seismic wave speed to actual viscosity. Mantle viscosity patterns generated in this way should in principle be able to fit the observation to a high degree, as a larger number of parameters can be used. AI models like this would also lend themselves well for these types of parameter studies as they, just as regular inversion models, generate solutions quickly (Lin et al., 2023), much faster than for example the model in this dissertation. The additional degrees of freedom in Earth parameters will not only allow for a better fit to GIA observables like RSL and VLM and with that a better accuracy of GIA estimates in general but also provide a more defined envelope on what possible Earth rheology parameters are realistic in any area.

Acknowledgements

While PhD project are often portrayed as projects with a lone PhD working in isolation, that is only half the truth. Often it did feel like that especially during COVID, but before I even worked a day on this project other people had already poured time and effort and when I was stuck there were always people around me to help me get moving again on both a technical level as well as an emotional level.

I would like to start with thanking the people on the more technical side of the project, first and foremost both Wouter and Bert, who were responsible for the initial funding and without who I never would have been able to begin in the first place. I would also like to thank Bert for moving the process along a bit quicker in the final stages so I could start my job in Utrecht. Wouter, I would like to thank maybe most of all for just the countless hours spent on helping me get this PhD to it's final product, especially in the last year as well. Although, we have had our disagreements over this long collaboration we always held the same goal and would come around again to achieve that goal of finishing the PhD, whether it was during office hours or emailing each other in the weekend at 2 o'clock at night.

I would like to thank my main co-authors Sarah and Valentina as well. Both papers have been long journeys, riddled with a lot of email from my side asking help, data, or sending another version to you. I hope it hasn't been too bothersome. I can say from my side that I have enjoyed working with you both on a technical level as well as on a personal level. Moreover, Sarah, I would again also like to thank you for hosting me and Wouter to discuss my PhD findings in Sheffield in 2022.

I would also like to thank Folker Pappa and Javier Fullea for letting me use their products, GOCE+ANTARTICA and WINTERC (both iterations) respectively, for my work and helping me understand what exactly was done to develop these products. I would also like to mention Grace Nield here, although not a co-author and the work published in this paper, we are co-authors on papers outside of this thesis. Our interactions helped me critically think about how ABAQUS works, and your work helped get my work a bit more exposure. Aside from that, me and Sharella loved having you over at our place.

I would like to thank my office co-workers for keeping it 'gezellig' on the floor. Although, it seems like ages ago I fondly remember the Dutch lessons I had with Gunther and Gurav, cake from Svenja and sharing a laugh with Tim and Jacco. I would especially like to thank my office roommates from 9.03 as well as they have helped me beyond just keeping the atmosphere enjoyable. I would like to thank Haiyang for helping me to get started with Abaqus and the model. I would like to thank Marc for helping me finish by being the second reader and reading everything on very short notice. Finally, I would like to thank Teresa for the whole process in between. The rest of the department dubbed us office husband and wife and I cannot blame them, as we spend so much time together in and out of the office. We would complain to one another about stuff not working out and we tried to help each other on a technical level as well, although I think you helped me more than the other way around.

The final people I would like to thank who I met at the faculty are the students I (partly) supervised. Marc, you get a second mention here as you were technically my first student who I helped supervise a literature study, which now seems like ages ago! My second student who I also co-supervised on his literature study, Tim, has now become my co-worker in Utrecht or maybe it would be more correct to say I have become his co-worker. Again, this shows that nine years is a really, really long time. Rosalie was the first student who worked with the full model on her thesis, she added 2 lines of code for the model I used, but those 2 lines were the most important contribution of any student to my work as it allowed me to move the high-resolution area around. Other than that, she did a preliminary study for Europe, which encouraged me to follow that direction after we struggled a bit with sparse data and competing research interest from collaborator for Antarctica. I will remember Maaike as a very ambitious student who was the first to try and combine the GIA model with another physical process, as a result she found the RESTART option, so vital for combining the model with other models. With Fabri I am very happy that we even finished the thesis, as the topic was also very ambitious and times were even more challenging with COVID pinning everybody down, while we were seeing the worst images possible from Italy every day. The last student I want to mention and really thank is Caroline. You took the model I created here and combined it with the ice history evolution model over the course of your master thesis and later your own PhD to make something special in my opinion. Your final model showed how my model could *ahum* easily *ahum* fit into something that is truly cutting edge in the field. It made me feel I did something useful as well. Thank you for that.

From outside my academic bubble I would like to start by thanking the mother of our beautiful daughter and my girlfriend, Sharella. I was a bit of a mess when we met, got my act together, became a mess again, got my act together again and became a mess again, and frankly I have lost track of where we are in that cycle now, but you supported me through this whole ordeal wherever we were in this cycle. Eight years has been a long time and we went from 'just dating' to having a daughter, a new house, 2 cars and 2 PhD's in that timeframe. You didn't only help in the moral support department but engaged in discussion with me on my research forcing me to reflect on the problems I faced, which sometimes directly lead to implemented solutions in the final product. You pushed me to keep engaging with Wouter when at times I was hesitant to do so. You even redid part of a figure after I deleted it and was stressed to finish it for a deadline. You did your best to free up time for me in the final stages of the PhD when I was juggling that with my job as a teacher, while you were also busy wrapping up your own PhD. Even when you were stressed about preparing for your own defense you found time to help me with my cover. At this point almost everything we have is shared in ownership in some way between us anyway and I think this title will fit the bill as well.

Furthermore, I would like to thank both of my parents. First of all, I'm very grateful that both of my parents are present for this moment, something I wasn't very sure of for some time. While both my parents have been incredibly supportive during this whole process, I would like to specifically thank my dad for all the insightful discussions we had regarding the statistics applied in this thesis, and my mom I would like to specifically thank for all the extra time she freed up for me by taking care of Julia so much. I would also like to thank my sister, Joy, for doing most of the work to create the cover and finally my brother for just being a fun distraction, whether we would play games, watch series or see a football game.

I would also very much like to thank my parents in law who have also taken care of Julia, but also Sharella, every Monday evening, during my time in Japan, but also after I got back from Japan when I had so little time to spare. Beste Harold en Sonja, jullie staan altijd voor ons klaar, zelfs op korte termijn. Ik had me geen betere schoonouders kunnen wensen. I would also like to mention my brother in law, Chris and my sister in law, Shamara. Chris, you have been a great listener during our bike rides and was always interested to hear if I had made progress with my PhD. Shamara, thank you for opening up your house at all times for Sharella and Julia during the time I needed our house for myself.

I would also like to thank my former employers, IPSE studies and het Christelijk Lyceum Delft, for putting faith in me and hiring me while it was clear I had a very time-consuming side project in my PhD. Organizations are of course the sum of its people and if these people would have not put their trust in me or be as accommodating as they were, I would have been forced to abandon my PhD project years ago.

Finally, my friends have been a great source of fun distraction, always providing me with something on the horizon to look forward to. Game nights with Douwe and Sebas, diners with Orhan and Jeroen, hanging out with Chris and Zayra or just having a 'papadag' with the whole Zoetermeergang and all our daughters. But the final person who I want to thank, specifically here is Thomas. You were of course also present at said game night and diners, but you've also been listening to my PhD drama for the full nine years, laughing about how ridiculous it sometimes got, supporting me when I was down about it, or just distracting me when I didn't even want to think about it. We even still shared a few 'scriptiedagen' working on both our PhD's forever ago, but over time they have been supplanted with Friday lunches with our daughters. I hope we'll continue that new tradition for long after the point that finishing this thesis will also feel like forever ago.

Thank you all,

Bas

Bibliography

A, G., Wahr, J., & Zhong, S. (2013). Computations of the viscoelastic response of a 3-D compressible Earth to surface loading: an application to Glacial Isostatic Adjustment in Antarctica and Canada. *Geophysical Journal International*, *192*(2), 557–572. https://doi.org/10.1093/gji/ggs030

Afonso, J. C., Fernandez, M., Ranalli, G., Griffin, W. L., & Connolly, J. A. D. (2008). Integrated geophysical-petrological modeling of the lithosphere and sublithospheric upper mantle: Methodology and applications. *Geochemistry, Geophysics, Geosystems*, *9*(5).

Agata, R., Barbot, S. D., Fujita, K., Hyodo, M., Iinuma, T., Nakata, R., Ichimura, T., & Hori, T. (2019). Rapid mantle flow with power-law creep explains deformation after the 2011 Tohoku mega-quake. *Nature Communications*, *10*(1), 1385.

Altamimi, Z., Collilieux, X., & Métivier, L. (2011). ITRF2008: an improved solution of the international terrestrial reference frame. *Journal of Geodesy*, *85*, 457–473.

Amante, C., & Eakins, B. W. (2009). *NOAA Technical Memorandum NESDIS NGDC-24 ETOPO1 1 ARC-MINUTE GLOBAL RELIEF MODEL: PROCEDURES, DATA SOURCES AND ANALYSIS.*

Amirpour, M., Das, R., & Flores, E. I. S. (2017). Bending analysis of thin functionally graded plate under in-plane stiffness variations. *Applied Mathematical Modelling*, *44*, 481–496.

An, M., Wiens, D. A., Zhao, Y., Feng, M., Nyblade, A. A., Kanao, M., Li, Y., Maggi, A., & Lévêque, J. (2015a). S-velocity model and inferred Moho topography beneath the Antarctic Plate from Rayleigh waves. *Journal of Geophysical Research: Solid Earth*, *120*(1), 359–383.

An, M., Wiens, D. A., Zhao, Y., Feng, M., Nyblade, A., Kanao, M., Li, Y., Maggi, A., & Lévêque, J. (2015b). Temperature, lithosphere-asthenosphere boundary, and heat flux beneath the Antarctic Plate inferred from seismic velocities. *Journal of Geophysical Research: Solid Earth*, *120*(12), 8720–8742.

Argus, D. F., Peltier, W. R., Blewitt, G., & Kreemer, C. (2021). The Viscosity of the Top Third of the Lower Mantle Estimated Using GPS, GRACE, and Relative Sea Level Measurements of Glacial Isostatic Adjustment. *Journal of Geophysical Research: Solid Earth*, *126*(5), e2020JB021537. https://doi.org/https://doi.org/10.1029/2020JB021537

Artemieva, I. M. (2019). Lithosphere structure in Europe from thermal isostasy. *Earth-Science Reviews*, *188*, 454–468. https://doi.org/https://doi.org/10.1016/j.earscirev.2018.11.004

Ashe, E. L., Cahill, N., Hay, C., Khan, N. S., Kemp, A., Engelhart, S. E., Horton, B. P., Parnell, A. C., & Kopp, R. E. (2019). Statistical modeling of rates and trends in Holocene relative sea level. *Quaternary Science Reviews*, *204*, 58–77.

Auriac, A., Whitehouse, P. L., Bentley, M. J., Patton, H., Lloyd, J. M., & Hubbard, A. (2016). Glacial isostatic adjustment associated with the Barents Sea ice sheet: A modelling inter-comparison. *Quaternary Science Reviews*, *147*, 122–135. https://doi.org/https://doi.org/10.1016/j.quascirev.2016.02.011

Bagge, M., Klemann, V., Steinberger, B., Latinović, M., & Thomas, M. (2021). Glacial-Isostatic Adjustment Models Using Geodynamically Constrained 3D Earth Structures. *Geochemistry, Geophysics, Geosystems*, *22*(11), e2021GC009853. https://doi.org/https://doi.org/10.1029/2021GC009853

Ballo, P., Kioussis, N., & Lu, G. (2001). Grain boundary sliding and migration: Effect of temperature and vacancies. *Phys. Rev. B*, *64*. https://doi.org/10.1103/PhysRevB.64.024104

Baranskaya, A. V, Khan, N. S., Romanenko, F. A., Roy, K., Peltier, W. R., & Horton, B. P. (2018). A postglacial relative sea-level database for the Russian Arctic coast. *Quaternary Science Reviews*, *199*, 188–205. https://doi.org/https://doi.org/10.1016/j.quascirev.2018.07.033

Barletta, V. R., Bevis, M., Smith, B. E., Wilson, T., Brown, A., Bordoni, A., Willis, M., Khan, S. A., Rovira-Navarro, M., Dalziel, I., Smalley, R., Kendrick, E., Konfal, S., Caccamise, D. J., Aster, R. C., Nyblade, A., & Wiens, D. A. (2018). Observed rapid bedrock uplift in Amundsen Sea Embayment promotes ice-sheet stability. *Science*, *360*(6395), 1335–1339. https://doi.org/10.1126/science.aao1447

Barnhoorn, A., van der Wal, W., & Drury, M. R. (2011). Upper mantle viscosity and lithospheric thickness under Iceland. *Journal of Geodynamics*, *52*(3–4), 260–270. https://doi.org/10.1016/j.jog.2011.01.002

Berglund, B. E., Sandgren, P., Barnekow, L., Hannon, G., Jiang, H., Skog, G., & Yu, S.-Y. (2005). Early Holocene history of the Baltic Sea, as reflected in coastal sediments in Blekinge, southeastern Sweden. *Quaternary International*, *130*(1), 111–139.

Blank, B., Barletta, V., Hu, H., Pappa, F., & van der Wal, W. (2021). Effect of Lateral and Stress-Dependent Viscosity Variations on GIA Induced Uplift Rates in the Amundsen Sea Embayment. *Geochemistry, Geophysics, Geosystems*, *22*(9), e2021GC009807. https://doi.org/https://doi.org/10.1029/2021GC009807

Boughanemi, A., & Mémin, A. (2024). Effects of Andrade and Burgers rheologies on glacial isostatic adjustment modeling in Antarctica. *Geodesy and Geodynamics*, *15 (5),* 429-440, https://doi.org/10.1016/j.geog.2023.12.008

Bradley, S. L., Ely, J. C., Clark, C. D., Edwards, R. J., & Shennan, I. (2023). Reconstruction of the palaeo-sea level of Britain and Ireland arising from empirical constraints of ice extent: implications for regional sea level forecasts and North American ice sheet volume. *Journal of Quaternary Science*, *38*(6), 791–805.

Bradley, S. L., Milne, G. A., Shennan, I., & Edwards, R. (2011). An improved glacial isostatic adjustment model for the British Isles. *Journal of Quaternary Science*, *26*(5), 541–552. https://doi.org/10.1002/jqs.1481

Bradley, S. L., Milne, G. A., Teferle, F. N., Bingley, R. M., & Orliac, E. J. (2009). Glacial isostatic adjustment of the British Isles: new constraints from GPS measurements of crustal motion. *Geophysical Journal International*, *178*(1), 14–22. https://doi.org/10.1111/j.1365-246X.2008.04033.x

Cangiani, A., Manzini, G., Russo, A., & Sukumar, N. (2015). Hourglass stabilization and the virtual element method. *International Journal for Numerical Methods in Engineering*, *102*(3–4), 404–436.

Cannelli, V., Melini, D., & Piersanti, A. (2010). Post-seismic stress relaxation with a linear transient rheology. *Annals of Geophysics*, *53*(2), 89–99.

Carcione, J. M., Poletto, F., Farina, B., & Craglietto, A. (2014). Simulation of seismic waves at the earth's crust (brittle–ductile transition) based on the Burgers model. *Solid Earth*, *5*(2), 1001–1010. https://doi.org/10.5194/se-5-1001-2014

Caron, L., & Ivins, E. R. (2020). A baseline Antarctic GIA correction for space gravimetry*, Earth Planet. Sc. Lett., 531, 115957*.

Caron, L., Ivins, E. R., Larour, E., Adhikari, S., Nilsson, J., & Blewitt, G. (2018). GIA model statistics for GRACE hydrology, cryosphere, and ocean science. *Geophysical Research Letters*, *45*(5), 2203–2212.

Celli, N. L., Lebedev, S., Schaeffer, A. J., & Gaina, C. (2021). The tilted Iceland Plume and its effect on the North Atlantic evolution and magmatism. *Earth and Planetary Science Letters*, *569*, 117048. https://doi.org/https://doi.org/10.1016/j.epsl.2021.117048

Chen, J. (2016). Lower-mantle materials under pressure. *Science*, *351*(6269), 122–123.

Christensen, U. (1984). Convection with pressure- and temperature-dependent non-Newtonian rheology. *Geophysical Journal International*, *77*(2), 343–384. https://doi.org/10.1111/j.1365-246X.1984.tb01939.x

Clark, C. D., Ely, J. C., Greenwood, S. L., Hughes, A. L. C., Meehan, R., Barr, I. D., Bateman, M. D., Bradwell, T., Doole, J., & Evans, D. J. A. (2018). BRITICE Glacial Map, version 2: a map and GIS database of glacial landforms of the last British–Irish Ice Sheet. *Boreas*, *47*(1), 11-e8.

Clark, C. D., Ely, J. C., Hindmarsh, R. C. A., Bradley, S., Ignéczi, A., Fabel, D., Ó Cofaigh, C., Chiverrell, R. C., Scourse, J., Benetti, S., Bradwell, T., Evans, D. J. A., Roberts, D. H., Burke, M., Callard, S. L., Medialdea, A., Saher, M., Small, D., Smedley, R. K., … Wilson, P. (2022). Growth and retreat of the last British–Irish Ice Sheet, 31 000 to 15 000 years ago: the BRITICE-CHRONO reconstruction. *Boreas*, *51*(4), 699–758. https://doi.org/https://doi.org/10.1111/bor.12594

Coulon, V., Bulthuis, K., Whitehouse, P. L., Sun, S., Haubner, K., Zipf, L., & Pattyn, F. (2021). Contrasting response of West and East Antarctic ice sheets to glacial isostatic adjustment. *Journal of Geophysical Research: Earth Surface*, *126*(7), e2020JF006003.

Couturier, P. J., Krenk, S., & Høgsberg, J. (2015). Beam section stiffness properties using a single layer of 3D solid elements. *Computers & Structures*, *156*, 122–133.

Creel, R. C., Austermann, J., Khan, N. S., D'Andrea, W. J., Balascio, N., Dyer, B., Ashe, E., & Menke, W. (2022). Postglacial relative sea level change in Norway. *Quaternary Science Reviews*, *282*, 107422.

Dannberg, J., Eilon, Z., Faul, U., Gassmöller, R., Moulik, P., & Myhill, R. (2017). The importance of grain size to mantle dynamics and seismological observations. *Geochemistry, Geophysics, Geosystems*, *18*(8), 3034–3061. https://doi.org/https://doi.org/10.1002/2017GC006944

Davis, J. E., Latychev, K., Mitrovica, J. X., Kendall, R., & Tamisiea, M. E. (2008). Glacial isostatic adjustment in 3-D earth models: Implications for the analysis of tide gauge records along the U.S. east coast. *Journal of Geodynamics*, *46*(3), 90–94. https://doi.org/https://doi.org/10.1016/j.jog.2008.04.007

Davis, J. L., & Mitrovica, J. X. (1996). Glacial isostatic adjustment and the anomalous tide gauge record of eastern North America. *Nature*, *379*(6563), 331–333.

Davis, J. L., Mitrovica, J. X., Scherneck, H., & Fan, H. (1999). Investigations of Fennoscandian glacial isostatic adjustment using modern sea level records. *Journal of Geophysical Research: Solid Earth*, *104*(B2), 2733–2747.

De Boer, B., Stocchi, P., & Van De Wal, R. S. W. (2014). A fully coupled 3-D ice-sheet–sea-level model: algorithm and applications. *Geoscientific Model Development*, *7*(5), 2141–2156.

Debayle, E., Dubuffet, F., & Durand, S. (2016). An automatically updated S-wave model of the upper mantle and the depth extent of azimuthal anisotropy. *Geophysical Research Letters*, *43*(2), 674–682. https://doi.org/https://doi.org/10.1002/2015GL067329

Doll, S., Schweizerhof, K., Hauptmann, R., & Freischläger, C. (2000). On volumetric locking of low-order solid and solid-shell elements for finite elastoviscoplastic

deformations and selective reduced integration. *Engineering Computations*, *17*(7), 874–902. https://doi.org/10.1108/02644400010355871

Dziewonski, A. M., & Anderson, D. L. (1981). Preliminary reference Earth model. *Physics of the Earth and Planetary Interiors*, *25*(4), 297–356.

Eagles, G., Gohl, K., & Larter, R. D. (2009). Animated tectonic reconstruction of the Southern Pacific and alkaline volcanism at its convergent margins since Eocene times. *Tectonophysics*, *464*(1–4), 21–29.

Eagles, G., Larter, R. D., Gohl, K., & Vaughan, A. P. M. (2009). West Antarctic rift system in the Antarctic Peninsula. *Geophysical Research Letters*, *36*(21).

Eaton, D. W., Darbyshire, F., Evans, R. L., Grütter, H., Jones, A. G., & Yuan, X. (2009). The elusive lithosphere–asthenosphere boundary (LAB) beneath cratons. *Lithos*, *109*(1–2), 1–22.

Ebbing, J., Pappa, F., Forsberg, R., Barletta, V., Jensen, T., van der Wal, W., & Blank, B. (2016, January 29). *GOCE+ Antarctica project*.

Ekman, M. (2016). *The Man behind "Degrees Celsius": A Pioneer in Investigating the Earth and its Changes, Åland Islands, 159 pp*.

Escudier, P., Couhert, A., Mercier, F., Mallet, A., Thibaut, P., Tran, N., Amarouche, L., Picard, B., Carrere, L., & Dibarboure, G. (2017). Satellite radar altimetry: Principle, accuracy, and precision. In *Satellite altimetry over oceans and land surfaces* (pp. 1–70). CRC Press.

Faure, N. (2022). *GIA modelling of Greenland using an ice history from the last glacial cycle to present day with lateral varying viscosity profiles on a spherical Earth*.

Fichtner, A., van Herwaarden, D.-P., Afanasiev, M., Simutė, S., Krischer, L., Çubuk-Sabuncu, Y., Taymaz, T., Colli, L., Saygin, E., Villaseñor, A., Trampert, J., Cupillard, P., Bunge, H.-P., & Igel, H. (2018). The Collaborative Seismic Earth Model: Generation 1. *Geophysical Research Letters*, *45*(9), 4007–4016. https://doi.org/https://doi.org/10.1029/2018GL077338

Fisher, A. T., Mankoff, K. D., Tulaczyk, S. M., Tyler, S. W., Foley, N., & Team, and the W. S. (2023). High geothermal heat flux measured below the West Antarctic Ice Sheet. *Science Advances*, *1*(6), e1500093. https://doi.org/10.1126/sciadv.1500093

Freed, A. M., & Bürgmann, R. (2004). Evidence of power-law flow in the Mojave desert mantle. *Nature*, *430*(6999), 548–551.

French, S., Lekic, V., & Romanowicz, B. (2013). Waveform Tomography Reveals Channeled Flow at the Base of the Oceanic Asthenosphere. *Science*, *342*(6155), 227–230. https://doi.org/10.1126/science.1241514

Fu, L., Christensen, E. J., Yamarone Jr, C. A., Lefebvre, M., Menard, Y., Dorrer, M., & Escudier, P. (1994). TOPEX/POSEIDON mission overview. In *Journal of Geophysical Research: Oceans* (Vol. 99, Issue C12, pp. 24369–24381). Wiley Online Library.

Fullea, J., Afonso, J. C., Connolly, J. A. D., Fernàndez, M., García-Castellanos, D., & Zeyen, H. (2009). LitMod3D: An interactive 3D software to model the thermal, compositional, density, seismological, and rheological structure of the lithosphere and sublithospheric upper mantle. *Geochemistry, Geophysics, Geosystems*, *10*(8).

Fullea, J., Lebedev, S., Martinec, Z., & Celli, N. ~L. (2018). WINTERC: a new Global thermochemical model constrained by seismic waveforms, heat flow, surface elevation and gravity satellite data. *AGU Fall Meeting Abstracts*, *2018*.

Fullea, J., Lebedev, S., Martinec, Z., & Celli, N. L. (2021). WINTERC-G: mapping the upper mantle thermochemical heterogeneity from coupled geophysical–petrological inversion of seismic waveforms, heat flow, surface elevation and gravity satellite data. *Geophysical Journal International*, *226*(1), 146–191. https://doi.org/10.1093/gji/ggab094

García-Artola, A., Stéphan, P., Cearreta, A., Kopp, R. E., Khan, N. S., & Horton, B. P. (2018). Holocene sea-level database from the Atlantic coast of Europe. *Quaternary Science Reviews*, *196*, 177–192.

Gardner, A. S., Moholdt, G., Scambos, T., Fahnstock, M., Ligtenberg, S., Broeke, M. van den, & Nilsson, J. (2018). Increased West Antarctic and unchanged East Antarctic ice discharge over the last 7 years. *The Cryosphere*, *12*(2), 521–547.

Gasperini, P., Yuen, D. A., & Sabadini, R. (1992). Postglacial rebound with a non-Newtonian upper mantle and a Newtonian lower mantle rheology. *Geophysical Research Letters*, *19*(16), 1711–1714.

Goes, S., Govers, R., & Vacher, P. (2000). Shallow mantle temperatures under Europe from P and S wave tomography. *Journal of Geophysical Research: Solid Earth*, *105*(B5), 11153–11169. https://doi.org/https://doi.org/10.1029/1999JB900300

Gomez, N., Latychev, K., & Pollard, D. (2018). A coupled ice sheet–sea level model incorporating 3D earth structure: variations in Antarctica during the last deglacial retreat. *Journal of Climate*, *31*(10), 4041–4054.

Gomez, N., Pollard, D., & Holland, D. (2015). Sea-level feedback lowers projections of future Antarctic Ice-Sheet mass loss. *Nature Communications*, *6*(1), 8798.

Gomez, N., Yousefi, M., Pollard, D., DeConto, R. M., Sadai, S., Lloyd, A., Nyblade, A., Wiens, D. A., Aster, R. C., & Wilson, T. (2024). The influence of realistic 3D mantle viscosity on Antarctica's contribution to future global sea levels. *Science Advances*, *10*(31), eadn1470. https://doi.org/10.1126/sciadv.adn1470

Gourmelen, N., Escorihuela, M. J., Shepherd, A., Foresta, L., Muir, A., Garcia-Mondéjar, A., Roca, M., Baker, S. G., & Drinkwater, M. R. (2018). CryoSat-2 swath interferometric altimetry for mapping ice elevation and elevation change. *Advances in Space Research*, *62*(6), 1226–1242.

Gowan, E. J., Tregoning, P., Purcell, A., Lea, J., Fransner, O. J., Noormets, R., & Dowdeswell, J. A. (2016). ICESHEET 1.0: a program to produce paleo-ice sheet reconstructions with minimal assumptions. *Geoscientific Model Development*, *9*(5), 1673–1682. https://doi.org/10.5194/gmd-9-1673-2016

Gunter, B. C., Didova, O., Riva, R. E. M., Ligtenberg, S. R. M., Lenaerts, J. T. M., King, M. A., Van den Broeke, M. R., & Urban, T. (2014). Empirical estimation of present-day Antarctic glacial isostatic adjustment and ice mass change. *The Cryosphere*, *8*(2), 743–760.

Haeger, C., & Kaban, M. K. (2019). Decompensative gravity anomalies reveal the structure of the upper crust of Antarctica. *Pure and Applied Geophysics*, *176*(10), 4401–4414.

Hansen, L., & Kohlstedt, D. L. (2015). 2.18 constitutive equations, rheological behavior, and viscosity of rocks. *Treatise on Geophysics, 2*, 441–472.

Hartmann, R., Ebbing, J., & Conrad, C. P. (2020). A Multiple 1D Earth Approach (M1DEA) to account for lateral viscosity variations in solutions of the sea level equation: An application for glacial isostatic adjustment by Antarctic deglaciation. *Journal of Geodynamics*, *135*(January), 101695. https://doi.org/10.1016/j.jog.2020.101695

Hay, C. C., Lau, H. C. P., Gomez, N., Austermann, J., Powell, E., Mitrovica, J. X., Latychev, K., & Wiens, D. A. (2017). Sea level fingerprints in a region of complex Earth structure: The case of WAIS. *Journal of Climate*, *30*(6), 1881–1892.

Hijma, Blank, Bradley, Cohen, van der Wal, Barlow, Frechen, Hennekam, van Heteren, Kiden, Mavritsakis, Meijninger, Reichart, Reinhardt, Rijsdijk, Vink, & Busschers. (2025). Two phases of accelerated ice-sheet melt in the Early Holocene revealed from North Sea peats. *Nature*.

Hijma, M. P., & Cohen, K. M. (2011). Holocene transgression of the Rhine river mouth area, The Netherlands/Southern North Sea: Palaeogeography and sequence stratigraphy. *Sedimentology*, *58*(6), 1453–1485. https://doi.org/10.1111/j.1365-3091.2010.01222.x

Hijma, M. P., & Cohen, K. M. (2019). Holocene sea-level database for the Rhine-Meuse Delta, The Netherlands: Implications for the pre-8.2 ka sea-level jump. *Quaternary Science Reviews*, *214*, 68–86. https://doi.org/https://doi.org/10.1016/j.quascirev.2019.05.001

Hirth, G., & Kohlstedt, D. (2003). Rheology of the upper mantle and the mantle wedge: A view from the experimentalists. *Geophysical Monograph-American Geophysical Union*, *138*, 83–106.

Hirth, G., & Kohlstedt, D. L. (2015). The stress dependence of olivine creep rate: Implications for extrapolation of lab data and interpretation of recrystallized grain size. *Earth and Planetary Science Letters*, *418*, 20–26. https://doi.org/https://doi.org/10.1016/j.epsl.2015.02.013

Houmark-Nielsen, M., & Henrik Kjaer, K. (2003). Southwest Scandinavia, 40–15 kyr BP: palaeogeography and environmental change. *Journal of Quaternary Science*, *18*(8), 769–786.

Hu, H., van der Wal, W., & Vermeersen, L. L. A. (2017). A numerical method for reorientation of rotating tidally deformed viscoelastic bodies. *Journal of Geophysical Research: Planets*, *122*(1), 228–248.

Huang, P., Steffen, R., Steffen, H., Klemann, V., Wu, P., van der Wal, W., Martinec, Z., & Tanaka, Y. (2023). A commercial finite element approach to modelling Glacial Isostatic Adjustment on spherical self-gravitating compressible earth models. *Geophysical Journal International*, *235*(3), 2231–2256. https://doi.org/10.1093/gji/ggad354

Huang, P., Wu, P., & Steffen, H. (2019). In search of an ice history that is consistent with composite rheology in Glacial Isostatic Adjustment modelling. *Earth and Planetary Science Letters*, *517*, 26–37. https://doi.org/https://doi.org/10.1016/j.epsl.2019.04.011

Hubbard, A. (2006). The validation and sensitivity of a model of the Icelandic ice sheet. *Quaternary Science Reviews*, *25*(17–18), 2297–2313.

Hughes, A. L. C., Gyllencreutz, R., Lohne, Ø. S., Mangerud, J., & Svendsen, J. I. (2016). The last Eurasian ice sheets–a chronological database and time-slice reconstruction, DATED-1. *Boreas*, *45*(1), 1–45.

Hughes, P. D., Palacios, D., García-Ruiz, J. M., & Andrés, N. (2022). Chapter 64 - The European glacial landscapes from the Last Glacial Maximum - synthesis. In D. Palacios, P. D. Hughes, J. M. García-Ruiz, & N. Andrés (Eds.), *European Glacial Landscapes* (pp. 507–516). Elsevier. https://doi.org/https://doi.org/10.1016/B978-0-12-823498-3.00005-4

Islam, Md. T., Sturkell, E., LaFemina, P., Geirsson, H., Sigmundsson, F., & Ólafsson, H. (2016). Continuous subsidence in the Thingvellir rift graben, Iceland: Geodetic observations since 1967 compared to rheological models of plate spreading. *Journal of Geophysical Research: Solid Earth*, *121*(1), 321–338. https://doi.org/https://doi.org/10.1002/2015JB012306

Ivins, E. R., Caron, L., Adhikari, S., Larour, E., & Scheinert, M. (2020). A linear viscoelasticity for decadal to centennial time scale mantle deformation. *Reports on Progress in Physics*, *83*(10), 106801.

Ivins, E. R., James, T. S., Wahr, J., O. Schrama, E. J., Landerer, F. W., & Simon, K. M. (2013). Antarctic contribution to sea level rise observed by GRACE with improved GIA correction. *Journal of Geophysical Research: Solid Earth*, *118*(6), 3126–3141.

Ivins, E. R., Raymond, C. A., & James, T. S. (2000). The influence of 5000 year-old and younger glacial mass variability on present-day crustal rebound in the Antarctic Peninsula. *Earth, Planets and Space*, *52*(11), 1023–1029.

Ivins, E. R., Raymond, C. A., & James, T. S. (2002). Late-Pleistocene, Holocene and present-day ice load evolution in the Antarctic Peninsula: Models and predicted vertical crustal motion. *Ice Sheets, Sea Level and the Dynamic Earth*, *29*, 133–155.

Ivins, E. R., & Sammis, C. G. (1995). On lateral viscosity contrast in the mantle and the rheology of low-frequency geodynamics. *Geophysical Journal International*, *123*(2), 305–322. https://doi.org/https://doi.org/10.1111/j.1365-246X.1995.tb06856.x

Ivins, E. R., van der Wal, W., Wiens, D. A., Lloyd, A. J., & Caron, L. (2023). Antarctic upper mantle rheology. *Geological Society of London Memoir*.

Jackson, I., & Faul, U. H. (2010). Grainsize-sensitive viscoelastic relaxation in olivine: Towards a robust laboratory-based model for seismological application. *Physics of the Earth and Planetary Interiors*, *183*(1), 151–163.

Jackson, M. G., Konter, J. G., & Becker, T. W. (2017). Primordial helium entrained by the hottest mantle plumes. *Nature*, *542*(7641), 340–343. https://doi.org/10.1038/nature21023

Johnston, P. (1993). The effect of spatially non-uniform water loads on prediction of sea-level change. *Geophysical Journal International*, *114*(3), 615–634.

Johnston, P. (1995). The role of hydro-isostasy for Holocene sea-level changes in the British Isles. *Marine Geology*, *124*(1–4), 61–70.

Karato, S. (2008). Deformation of earth materials. *An Introduction to the Rheology of Solid Earth*, *463*.

Karato, S. (2010). Rheology of the Earth's mantle: A historical review. *Gondwana Research*, *18*(1), 17–45.

Karato, S., & Jung, H. (1998). Water, partial melting and the origin of the seismic low velocity and high attenuation zone in the upper mantle. *Earth and Planetary*

Science Letters, *157*(3), 193–207. https://doi.org/https://doi.org/10.1016/S0012-821X(98)00034-X

Kaufmann, G., & Lambeck, K. (2000). Mantle dynamics, postglacial rebound and the radial viscosity profile. *Physics of the Earth and Planetary Interiors*, *121*(3), 301–324. https://doi.org/https://doi.org/10.1016/S0031-9201(00)00174-6

Kaufmann, G., Wu, P., & Ivins, E. (2005). Lateral viscosity variations beneath Antarctica and their implications on regional rebound motions and seismotectonics. *Geophysics Journal International*, *161*, 679–706.

Kaufmann, G., Wu, P., & Wolf, D. (1997). Some effects of lateral heterogeneities in the upper mantle on postglacial land uplift close to continental margins. *Geophysical Journal International*, *128*(1), 175–187. https://doi.org/10.1111/j.1365-246X.1997.tb04078.x

Kearey, P., Klepeis, K. A., & Vine, F. J. (2009). *Global Tectonics* (3rd ed.). Wiley–Blackwell.

Kempenaar, G. (2022). *Modelling The Greenland Ice Sheet following The Mid-Eemian: A study of the impact of including lateral variations in the sub-Greenland Earth rheology on the GrIS'evolution since the mid-Eemian in a coupled 3D ice sheet and 3D GIA model*.

Kendall, R. A., Mitrovica, J. X., & Milne, G. A. (2005). On post-glacial sea level–II. Numerical formulation and comparative results on spherically symmetric models. *Geophysical Journal International*, *161*(3), 679–706.

Kierulf, H. P., Steffen, H., Barletta, V. R., Lidberg, M., Johansson, J., Kristiansen, O., & Tarasov, L. (2021). A GNSS velocity field for geophysical applications in Fennoscandia. *Journal of Geodynamics*, *146*, 101845. https://doi.org/https://doi.org/10.1016/j.jog.2021.101845

Kierulf, H. P., Steffen, H., Simpson, M. J. R., Lidberg, M., Wu, P., & Wang, H. (2014). A GPS velocity field for Fennoscandia and a consistent comparison to glacial isostatic adjustment models. *Journal of Geophysical Research: Solid Earth*, *119*(8), 6613–6629.

King, M. A., Altamimi, Z., Boehm, J., Bos, M., Dach, R., Elosegui, P., Fund, F., Hernández-Pajares, M., Lavallee, D., Mendes Cerveira, P. J., Penna, N., Riva, R. E. M., Steigenberger, P., van Dam, T., Vittuari, L., Williams, S., & Willis, P. (2010). Improved Constraints on Models of Glacial Isostatic Adjustment: A Review of the Contribution of Ground-Based Geodetic Observations. *Surveys in Geophysics*, *31*, 465–507.

King, S. D., & Masters, G. (1992). An inversion for radial viscosity structure using seismic tomography. *Geophysical Research Letters*, *19*(15), 1551–1554.

Klemann, V., & Martinec, Z. (2011). Contribution of glacial-isostatic adjustment to the geocenter motion. *Tectonophysics*, *511*(3–4), 99–108.

Klemann, V., Martinec, Z., & Ivins, E. R. (2008). Glacial isostasy and plate motion. *Journal of Geodynamics*, *46*(3), 95–103. https://doi.org/https://doi.org/10.1016/j.jog.2008.04.005

Konrad, H., Gilbert, L., Cornford, S. L., Payne, A., Hogg, A., Muir, A., & Shepherd, A. (2016). Uneven onset and pace of ice-dynamical imbalance in the Amundsen Sea Embayment, West Antarctica. *Geophysical Research Letters*, *44*(2), 910–918.

Konrad, H., Sasgen, I., Pollard, D., & Klemann, V. (2015). Potential of the solid-Earth response for limiting long-term West Antarctic Ice Sheet retreat in a warming climate. *Earth and Planetary Science Letters*, *432*, 254–264.

Kuchar, J., & Milne, G. A. (2015). The influence of viscosity structure in the lithosphere on predictions from models of glacial isostatic adjustment. *Journal of Geodynamics*, *86*, 1–9.

Kuchar, J., Milne, G., & Latychev, K. (2019). The importance of lateral Earth structure for North American glacial isostatic adjustment. *Earth and Planetary Science Letters*, *512*, 236–245. https://doi.org/10.1016/j.epsl.2019.01.046

Lambeck, K., Purcell, A., & Zhao, S. (2017). The North American Late Wisconsin ice sheet and mantle viscosity from glacial rebound analyses. *Quaternary Science Reviews*, *158*, 172–210. https://doi.org/https://doi.org/10.1016/j.quascirev.2016.11.033

Lambeck, K., Rouby, H., Purcell, A., Sun, Y., & Sambridge, M. (2014). Sea level and global ice volumes from the Last Glacial Maximum to the Holocene. *Proceedings of the National Academy of Sciences*, *111*(43), 15296–15303.

Lambeck, K., Smither, C., & Johnston, P. (1998). Sea-level change, glacial rebound and mantle viscosity for northern Europe. *Geophysical Journal International*, *134*(1), 102–144. https://doi.org/10.1046/j.1365-246X.1998.00541.x

Lambert, A., Courtier, N., & James, T. S. (2006). Long-term monitoring by absolute gravimetry: Tides to postglacial rebound. *Journal of Geodynamics*, *41*(1), 307–317. https://doi.org/https://doi.org/10.1016/j.jog.2005.08.032

Latychev, K., Mitrovica, J. X., Tromp, J., Tamisiea, M. E., Komatitsch, D., & Christara, C. C. (2005). Glacial isostatic adjustment on 3-D Earth models: a finite-volume formulation. *Geophysical Journal International*, *161*(2), 421–444. https://doi.org/10.1111/j.1365-246X.2005.02536.x

Lau, H. C. P. (2023). Transient rheology in sea level change: Implications for Meltwater Pulse 1A. *Earth and Planetary Science Letters*, *609*, 118106.

Lau, H. C. P., & Holtzman, B. K. (2019). "Measures of Dissipation in Viscoelastic Media" Extended: Toward Continuous Characterization Across Very Broad Geophysical Time Scales. *Geophysical Research Letters*, *46*(16), 9544–9553.

Lau, H. C. P., Holtzman, B. K., & Havlin, C. (2020). Toward a Self-Consistent Characterization of Lithospheric Plates Using Full-Spectrum Viscoelasticity. *AGU Advances*, *1*(4), e2020AV000205.

Legeais, J.-F., Ablain, M., Zawadzki, L., Zuo, H., Johannessen, J. A., Scharffenberg, M. G., Fenoglio-Marc, L., Fernandes, M. J., Andersen, O. B., & Rudenko, S. (2018). An improved and homogeneous altimeter sea level record from the ESA Climate Change Initiative. *Earth System Science Data*, *10*(1), 281–301.

Li, T., Wu, P., Wang, H., Steffen, H., Khan, N. S., Engelhart, S. E., Vacchi, M., Shaw, T. A., Peltier, W. R., & Horton, B. P. (2020). Uncertainties of Glacial Isostatic Adjustment Model Predictions in North America Associated With 3D Structure. *Geophysical Research Letters*, *47*(10), e2020GL087944. https://doi.org/https://doi.org/10.1029/2020GL087944

Lin, Y., Whitehouse, P. L., Valentine, A. P., & Woodroffe, S. A. (2023). GEORGIA: A Graph Neural Network Based EmulatOR for Glacial Isostatic Adjustment. *Geophysical Research Letters*, *50*(18), e2023GL103672. https://doi.org/https://doi.org/10.1029/2023GL103672

Liu, B., King, M., & Dai, W. (2018). Common mode error in Antarctic GPS coordinate time-series on its effect on bedrock-uplift estimates. *Geophysics Journal International*, *214*(3), 1652–1664.

Liu, X., & Zhong, S. J. (2016). Studying the geoid and viscosity structure in a thermochemical model based on seismic tomographic data. *Geochem. Geophys. Geosyst.*

Liu, Y., Teng, J., Lan, H., Si, X., & Ma, X. (2014). A comparative study of finite element and spectral element methods in seismic wavefield modeling. *Geophysics*, *79*(2), T91–T104.

Lloyd, A. J., Crawford, O., Al-Attar, D., Austermann, J., Hoggard, M. J., Richards, F. D., & Syvret, F. (2024). GIA imaging of 3-D mantle viscosity based on palaeo sea level observations – Part I: Sensitivity kernels for an Earth with laterally varying viscosity. *Geophysical Journal International*, *236*(2), 1139–1171. https://doi.org/10.1093/gji/ggad455

Lloyd, A. J., Wiens, D. A., Nyblade, A. A., Anandakrishnan, S., Aster, R. C., Huerta, A. D., Wilson, T. J., Dalziel, I. W. D., Shore, P. J., & Zhao, D. (2015). A seismic transect across West Antarctica: Evidence for mantle thermal anomalies beneath the Bentley Subglacial Trench and the Marie Byrd Land Dome. *Journal of Geophysical Research: Solid Earth*, *120*(12), 8439–8460.

Love, R., Milne, G. A., Tarasov, L., Engelhart, S. E., Hijma, M. P., Latychev, K., Horton, B. P., & Törnqvist, T. E. (2016). The contribution of glacial isostatic adjustment to projections of sea-level change along the Atlantic and Gulf coasts of North America. *Earth's Future*, *4*(10), 440–464.

Mäkinen, J., Lilje, M., Ågren, J., Engsager, K., Eriksson, P.-O., Jepsen, C., Olsson, P.-A., Saaranen, V., Schmidt, K., Svensson, R., Takalo, M., & Vestøl, O. (2005). *Regional Adjustment of Precise Levellings around the Baltic*.

Marotta, A. M., & Sabadini, R. (2002). Tectonic versus glacial isostatic deformation in Europe. *Geophysical Research Letters*, *29*(10), 73-1-73–74. https://doi.org/https://doi.org/10.1029/2001GL013865

Martinec, Z. (2000). Spectral–finite element approach to three-dimensional viscoelastic relaxation in a spherical earth. *Geophysical Journal International*, *142*(1), 117–141.

Martinec, Z., Klemann, V., van der Wal, W., Riva, R. E. M., Spada, G., Sun, Y., Melini, D., Kachuck, S. B., Barletta, V., Simon, K., A, G., & James, T. S. (2018). A benchmark study of numerical implementations of the sea level equation in GIA modelling. *Geophysical Journal International*, *215*(1), 389–414. https://doi.org/10.1093/gji/ggy280

Martín-Español, A., King, M. A., Zammit-Mangion, A., Andrews, S. B., Moore, P., & Bamber, J. L. (2016). An assessment of forward and inverse GIA solutions for Antarctica. *Journal of Geophysical Research: Solid Earth*, *121*(9), 6947–6965.

Martín-Español, A., Zammit-Mangion, A., Clarke, P., Flament, T., Helm, V., King, M., Luthcke, S., Petrie, E., Remy, F., Schön, N., Wouters, B., & Bamber, J. (2016). Spatial and temporal Antarctic Ice Sheet mass trends, glacio-isostatic adjustment, and surface processes from a joint inversion of satellite altimeter, gravity, and GPS data. *Journal of Geophysical Research: Earth Surface*, *121*, 182–200.

McDonough, W. F., & Sun, S. -s. (1995). The composition of the Earth. *Chemical Geology*, *120*(3), 223–253.

Métivier, L., Caron, L., Greff-Lefftz, M., Pajot-Métivier, G., Fleitout, L., & Rouby, H. (2016). Evidence for postglacial signatures in gravity gradients: A clue in lower mantle viscosity. *Earth and Planetary Science Letters*, *452*, 146–156. https://doi.org/https://doi.org/10.1016/j.epsl.2016.07.034

Milne, G. A., & Mitrovica, J. X. (1998). The influence of time-dependent ocean-continent geometry on predictions of post-glacial sea level change in Australia and New Zealand. *Geophysical Research Letters*, *25*(6), 793–796.

Milne, G. A., Mitrovica, J. X., & Forte, A. M. (1998). The sensitivity of glacial isostatic adjustment predictions to a low-viscosity layer at the base of the upper

mantle. *Earth and Planetary Science Letters*, *154*(1), 265–278.
https://doi.org/https://doi.org/10.1016/S0012-821X(97)00191-X

Milne, G. A., Mitrovica, J. X., Scherneck, H.-G., Davis, J. L., Johansson, J. M., Koivula, H., & Vermeer, M. (2004). Continuous GPS measurements of postglacial adjustment in Fennoscandia: 2. Modeling results. *Journal of Geophysical Research: Solid Earth*, *109*(B2).
https://doi.org/https://doi.org/10.1029/2003JB002619

Mitrovica, J. X., & Forte, A. M. (1998). New insights obtained from joint inversions for the radial profile of mantle viscosity. *Physics and Chemistry of the Earth*, *23*(9), 857–863. https://doi.org/https://doi.org/10.1016/S0079-1946(98)00105-0

Mitrovica, J. X., & Forte, A. M. (2004). A new inference of mantle viscosity based upon joint inversion of convection and glacial isostatic adjustment data. *Earth and Planetary Science Letters*, *225*(1), 177–189.
https://doi.org/https://doi.org/10.1016/j.epsl.2004.06.005

Mordret, A. (2018). Uncovering the Iceland Hot Spot Track Beneath Greenland. *Journal of Geophysical Research: Solid Earth*, *123*(6), 4922–4941.
https://doi.org/https://doi.org/10.1029/2017JB015104

Morra, F. (2021). *Influence of the combination of ambient and glacial stresses on the response of a viscoelastic Earth*. MSc dissertation, Delft University of Technology

Mouginot, J., Rignot, E., & Scheuchl, B. (2014). Sustained increase in ice discharge from the Amundsen Sea Embayment, West Antarctica, from 1973 to 2013. *Geophysical Research Letters*, *41*(5).

Muhs, D. R., Meco, J., & Simmons, K. R. (2014). Uranium-series ages of corals, sea level history, and palaeozoogeography, Canary Islands, Spain: An exploratory study for two Quaternary interglacial periods. *Palaeogeography, Palaeoclimatology, Palaeoecology*, *394*, 99–118.
https://doi.org/https://doi.org/10.1016/j.palaeo.2013.11.015

Nakada, M., & Okuno, J. (2016). Inference of mantle viscosity for depth resolutions of GIA observations. *Geophysical Journal International*, *207*(2), 719–740.
https://doi.org/10.1093/gji/ggw301

Näslund, J.-O., Jansson, P., Fastook, J. L., Johnson, J., & Andersson, L. (2005). Detailed spatially distributed geothermal heat-flow data for modeling of basal temperatures and meltwater production beneath the Fennoscandian ice sheet. *Annals of Glaciology*, *40*, 95–101.

Nicholls, R. J., & Cazenave, A. (2010). Sea-Level Rise and Its Impact on Coastal Zones. *Science*, *328*(5985), 1517–1520. https://doi.org/10.1126/science.1185782

Nield, G. A., Barletta, V. R., Bordoni, A., King, M. A., Whitehouse, P. L., Clarke, P. J., Domack, E., Scambos, T. A., & Berthier, E. (2014). Rapid bedrock uplift in the Antarctic Peninsula explained by viscoelastic response to recent ice unloading. *Earth and Planetary Science Letters*, *397*, 32–41.

Nield, G. A., King, M. A., Steffen, R., & Blank, B. (2022). A global, spherical finite-element model for post-seismic deformation using Abaqus. *Geoscientific Model Development*, *15*(6), 2489–2503.

Nield, G. A., Whitehouse, P. L., van der Wal, W., Blank, B., O'Donnell, J. P., & Stuart, G. W. (2018). The impact of lateral variations in lithospheric thickness on glacial isostatic adjustment in West Antarctica. *Geophysical Journal International*, *214*(2), 811–824.

Novella, D., Bolfan-Casanova, N., Nestola, F., & Harris, J. W. (2015). H2O in olivine and garnet inclusions still trapped in diamonds from the Siberian craton: Implications for the water content of cratonic lithosphere peridotites. In *Lithos* (Vol. 230, pp. 180–183). Elsevier B.V. https://doi.org/10.1016/j.lithos.2015.05.013

Ohuchi, T., Kawazoe, T., Higo, Y., Funakoshi, K., Suzuki, A., Kikegawa, T., & Irifune, T. (2015). Dislocation-accommodated grain boundary sliding as the major deformation mechanism of olivine in the Earth's upper mantle. *Science Advances*, *1*(9), e1500360.

Pappa, F., & Ebbing, J. (2023). *Gravity, magnetics and geothermal heat flow of the Antarctic lithospheric crust and mantle*. The Geochemistry and Geophysics of the Antarctic Mantle, A. P. Martin, W. van der Wal. https://doi.org/10.1144/M56-2020-5

Pappa, F., Ebbing, J., Ferraccioli, F., & van der Wal, W. (2019). Modeling Satellite Gravity Gradient Data to Derive Density, Temperature, and Viscosity Structure of the Antarctic Lithosphere. *Journal of Geophysical Research: Solid Earth*, *124*(11), 12053–12076. https://doi.org/https://doi.org/10.1029/2019JB017997

Patton, H., Hubbard, A., Andreassen, K., Auriac, A., Whitehouse, P. L., Stroeven, A. P., Shackleton, C., Winsborrow, M., Heyman, J., & Hall, A. M. (2017). Deglaciation of the Eurasian ice sheet complex. *Quaternary Science Reviews*, *169*, 148–172. https://doi.org/10.1016/j.quascirev.2017.05.019

Patton, H., Hubbard, A., Andreassen, K., Winsborrow, M., & Stroeven, A. P. (2016). The build-up, configuration, and dynamical sensitivity of the Eurasian ice-sheet complex to Late Weichselian climatic and oceanic forcing. *Quaternary Science Reviews*, *153*, 97–121.

Pattyn, F., & Morlighem, M. (2020). The uncertain future of the Antarctic Ice Sheet. *Science*, *367*(6484), 1331–1335. https://doi.org/10.1126/science.aaz5487

Paulson, A. (2006). *Inference of the Earth's Mantle Viscosity from Post-glacial Rebound*. University of Colorado.

Paulson, A., Zhong, S., & Wahr, J. (2005). Modelling post-glacial rebound with lateral viscosity variations. *Geophysical Journal International*, *163*(1), 357–371.

Paxman, G. J. G. (2023). Antarctic palaeotopography, *Geological Society, London, Memoirs, 56,* 231-251, https://doi.org/10.1144/M56-2020-7

Peak, B. A., Latychev, K., Hoggard, M. J., & Mitrovica, J. X. (2022). Glacial isostatic adjustment in the Red Sea: Impact of 3-D Earth structure. *Quaternary Science Reviews*, *280*, 107415. https://doi.org/https://doi.org/10.1016/j.quascirev.2022.107415

Peeters, J., Busschers, F. S., & Stouthamer, E. (2015). Fluvial evolution of the Rhine during the last interglacial-glacial cycle in the southern North Sea basin: A review and look forward. *Quaternary International*, *357*, 176–188. https://doi.org/https://doi.org/10.1016/j.quaint.2014.03.024

Peltier, W. R. (1974). The impulse response of a Maxwell Earth. *Reviews of Geophysics*, *12*(4), 649–669.

Peltier, W. R. (2004). Global glacial isostasy and the surface of the ice-age Earth: the ICE-5G (VM2) model and GRACE. *Annu. Rev. Earth Planet. Sci.*, *32*, 111–149.

Peltier, W. R., & Andrews, J. T. (1976). Glacial-isostatic adjustment—I. The forward problem. *Geophysical Journal International*, *46*(3), 605–646.

Peltier, W. R., Argus, D. F., & Drummond, R. (2015). Space geodesy constrains ice age terminal deglaciation: The global ICE-6G_C (VM5a) model. *Journal of Geophysical Research: Solid Earth*, *120*(1), 450–487. https://doi.org/https://doi.org/10.1002/2014JB011176

Pollard, D., & DeConto, R. M. (2012). Description of a hybrid ice sheet-shelf model, and application to Antarctica. *Geoscientific Model Development*, *5*(5), 1273–1295.

Pollard, O. G., Barlow, N. L. M., Gregoire, L., Gomez, N., Cartelle, V., Ely, J. C., & Astfalck, L. C. (2023). Quantifying the Uncertainty in the Eurasian Ice-Sheet Geometry at the Penultimate Glacial Maximum (Marine Isotope Stage 6). *The Cryosphere Discussions*, *2023*, 1–31. https://doi.org/10.5194/tc-2023-5

Powell, E., Gomez, N., Hay, C., Latychev, K., & Mitrovica, J. X. (2020). Viscous effects in the solid Earth response to modern Antarctic ice mass flux: Implications for geodetic studies of WAIS stability in a warming world. *Journal of Climate*, *33*(2), 443–459.

Powell, E., Latychev, K., Gomez, N., & Mitrovica, J. X. (2022). The robustness of geodetically derived 1-D Antarctic viscosity models in the presence of complex 3-

D viscoelastic Earth structure. *Geophysical Journal International*, *231*(1), 118–128. https://doi.org/10.1093/gji/ggac129

Priestley, K., & McKenzie, D. (2013). The relationship between shear wave velocity, temperature, attenuation and viscosity in the shallow part of the mantle. *Earth and Planetary Science Letters*, *381*, 78–91. https://doi.org/https://doi.org/10.1016/j.epsl.2013.08.022

Qiao, X., Chu, T., Tissot, P., Ali, I., & Ahmed, M. (2023). Vertical land motion monitored with satellite radar altimetry and tide gauge along the Texas coastline, USA, between 1993 and 2020. *International Journal of Applied Earth Observation and Geoinformation*, *117*, 103222.

Ranalli, G. (1995). *Rheology of the Earth*. Cambridge University Press.

Ranalli, G. (2001). Mantle rheology: radial and lateral viscosity variations inferred from microphysical creep laws. *Journal of Geodynamics*, *32*(4–5), 425–444.

Rapley, C. (2006). The Antarctic ice sheet and sea level rise. *Avoiding Dangerous Climate Change*, 25–28.

Ricard, Y., & Wuming, B. (1991). Inferring the viscosity and the 3-D density structure of the mantle from geoid, topography and plate velocities. *Geophysical Journal International*, *105*(3), 561–571.

Richter, A., Groh, A., & Dietrich, R. (2012). Geodetic observation of sea-level change and crustal deformation in the Baltic Sea region. *Physics and Chemistry of the Earth*, *53–54*, 43–53. https://doi.org/10.1016/j.pce.2011.04.011

Richter, K., Nilsen, J. E. Ø., & Drange, H. (2012). Contributions to sea level variability along the Norwegian coast for 1960–2010. *Journal of Geophysical Research: Oceans*, *117*(C5). https://doi.org/https://doi.org/10.1029/2011JC007826

Rignot, E., Mouginot, J., Scheuchl, B., Van Den Broeke, M., Van Wessem, M. J., & Morlighem, M. (2019). Four decades of Antarctic Ice Sheet mass balance from 1979–2017. *Proceedings of the National Academy of Sciences*, *116*(4), 1095–1103.

Ringwood, A. E. (1975). Composition and Petrology of the Earth's Mantle. *MacGraw-Hill, 618*.

Ritterbex, S., Carrez, P., & Cordier, P. (2020). Deformation across the mantle transition zone: A theoretical mineral physics view. *Earth and Planetary Science Letters*, *547*, 116438. https://doi.org/https://doi.org/10.1016/j.epsl.2020.116438

Riva, R. E. M., Gunter, B. C., Urban, T. J., Vermeersen, B. L. A., Lindenbergh, R. C., Helsen, M. M., Bamber, J. L., van de Wal, R. S. W., van den Broeke, M. R., & Schutz, B. E. (2009). Glacial isostatic adjustment over Antarctica from combined

ICESat and GRACE satellite data. *Earth and Planetary Science Letters*, *288*(3–4), 516–523.

Robel, A. A., & Tziperman, E. (2016). The role of ice stream dynamics in deglaciation. *Journal of Geophysical Research: Earth Surface*, *121*(8), 1540–1554.

Roberts, M., Scourse, J., Bennell, J., Huws, D., Jago, C., & Long, B. (2011). Late Devensian and Holocene relative sea-level change in North Wales, UK. *Journal of Quaternary Science*, *26*, 141–155. https://doi.org/10.1002/jqs.1443

Root, B. C. (2020). Comparing global tomography-derived and gravity-based upper mantle density models. *Geophysical Journal International*, *221*(3), 1542–1554. https://doi.org/10.1093/gji/ggaa091

Root, B. C., van der Wal, W., Novák, P., Ebbing, J., & Vermeersen, L. L. A. (2015). Glacial isostatic adjustment in the static gravity field of Fennoscandia. *Journal of Geophysical Research: Solid Earth*, *120*(1), 503–518.

Rosentau, A., Harff, J., Oja, T., & Meyer, M. (2012). Postglacial rebound and relative sea level changes in the Baltic Sea since the Litorina transgression. *Baltica*, *25*(2), 113–120.

Rosentau, A., Klemann, V., Bennike, O., Steffen, H., Wehr, J., Latinović, M., Bagge, M., Ojala, A., Berglund, M., & Becher, G. P. (2021). A Holocene relative sea-level database for the Baltic Sea. *Quaternary Science Reviews*, *266*, 107071.

Rovira-Navarro, M., van der Wal, W., Barletta, V. R., Root, B. C., & Sandberg Sørensen, L. (2020). GRACE constraints on Earth rheology of the Barents Sea and Fennoscandia. *Solid Earth*, *11*(2), 379–395. https://doi.org/10.5194/se-11-379-2020

Roy, K., & Peltier, W. R. (2018). Relative sea level in the Western Mediterranean basin: a regional test of the ICE-7G_NA (VM7) model and a constraint on late Holocene Antarctic deglaciation. *Quaternary Science Reviews*, *183*, 76–87.

Rudolph, M. L., Lekić, V., & Lithgow-Bertelloni, C. (2015). Viscosity jump in Earth's mid-mantle. *Science*, *350*(6266), 1349–1352.

Rushby, G. T., Richards, G. T., Gehrels, W. R., Anderson, W. P., Bateman, M. D., & Blake, W. H. (2019). Testing the mid-Holocene relative sea-level highstand hypothesis in North Wales, UK. *The Holocene*, *29*(9), 1491–1502. https://doi.org/10.1177/0959683619854513

Sabadini, R., Yuen, D. A., & Portney, M. (1986). The effects of upper-mantle lateral heterogeneities on postglacial rebound. *Geophysical Research Letters*, *13*(4), 337–340.

Samrat, N. H., King, M. A., Watson, C., Hooper, A., Chen, X., Barletta, V. R., & Bordoni, A. (2020). Reduced ice mass loss and three-dimensional viscoelastic deformation in northern Antarctic Peninsula inferred from GPS. *Geophysical Journal International*, *222*(2), 1013–1022.

Sasgen, I., Konrad, H., Ivins, E. R., Van den Broeke, M. R., Bamber, J. L., Martinec, Z., & Klemann, V. (2013). Antarctic ice-mass balance 2003 to 2012: regional reanalysis of GRACE satellite gravimetry measurements with improved estimate of glacial-isostatic adjustment based on GPS uplift rates. *The Cryosphere*, *7*(5), 1499–1512.

Schaeffer, A. J., & Lebedev, S. (2013). Global shear speed structure of the upper mantle and transition zone. *Geophysical Journal International*, *194*(1), 417–449. https://doi.org/10.1093/gji/ggt095

Schiffer, C., & Nielsen, S. B. (2016). Implications for anomalous mantle pressure and dynamic topography from lithospheric stress patterns in the North Atlantic Realm. *Journal of Geodynamics*, *98*, 53–69. https://doi.org/https://doi.org/10.1016/j.jog.2016.03.014

Schmeling, H. (1987). On the interaction between small- and large-scale convection and postglacial rebound flow in a power-law mantle. *Earth and Planetary Science Letters*, *84*(2), 254–262.

Schmidt, P., Lund, B., Näslund, J.-O., & Fastook, J. (2014). Comparing a thermo-mechanical Weichselian Ice Sheet reconstruction to reconstructions based on the sea level equation: aspects of ice configurations and glacial isostatic adjustment. *Solid Earth*, *5*(1), 371–388.

Schrama, E. J. O., Wouters, B., & Rietbroek, R. (2014). A mascon approach to assess ice sheet and glacier mass balances and their uncertainties from GRACE data. *Journal of Geophysical Research: Solid Earth*, *119*(7), 6048–6066.

Schumacher, M., King, M. A., Rougier, J., Sha, Z., Khan, S. A., & Bamber, J. L. (2018). A new global GPS data set for testing and improving modelled GIA uplift rates. *Geophysical Journal International*, *214*(3), 2164–2176. https://doi.org/10.1093/gji/ggy235

Seguinot, J., Ivy-Ochs, S., Jouvet, G., Huss, M., Funk, M., & Preusser, F. (2018). Modelling last glacial cycle ice dynamics in the Alps. *The Cryosphere*, *12*(10), 3265–3285. https://doi.org/10.5194/tc-12-3265-2018

Seroussi, H., Nakayama, Y., Larour, E., Menemenlis, D., Morlighem, M., Rignot, E., & Khazendar, A. (2017). Continued retreat of Thwaites Glacier, West Antarctica, controlled by bed topography and ocean circulation. *Geophysical Research Letters*, *44*(12), 6191–6199.

Shapiro, N. M., & Ritzwoller, M. H. (2002). Monte-Carlo inversion for a global shear-velocity model of the crust and upper mantle. *Geophysical Journal International*, *151*(1), 88–105. https://doi.org/10.1046/j.1365-246X.2002.01742.x

Shen, W., Wiens, D. A., Anandakrishnan, S., Aster, R. C., Gerstoft, P., Bromirski, P. D., Hansen, S. E., Dalziel, I. W. D., Heeszel, D. S., Huerta, A. D., Nyblade, A. A., Stephen, R., Wilson, T. J., & Winberry, J. P. (2018). The Crust and Upper Mantle Structure of Central and West Antarctica From Bayesian Inversion of Rayleigh Wave and Receiver Functions. *Journal of Geophysical Research: Solid Earth*, *123*(9), 7824–7849. https://doi.org/https://doi.org/10.1029/2017JB015346

Shen, W., Wiens, D. A., Lloyd, A. J., & Nyblade, A. A. (2020). A geothermal heat flux map of Antarctica empirically constrained by seismic structure. *Geophysical Research Letters*, *47*(14), e2020 GL086955.

Shennan, I., Bradley, S. L., & Edwards, R. (2018). Relative sea-level changes and crustal movements in Britain and Ireland since the Last Glacial Maximum. *Quaternary Science Reviews*, *188*, 143–159.

Shepherd, A., Gilbert, L., Muir Alan S.and Konrad, H., McMillan, M., Slater, T., Briggs, K. H., Sundal, A. V, Hogg, A. E., & Engdahl, M. E. (2019). Trends in Antarctic Ice Sheet elevation and mass. *Geophysical Research Letters*, *46*(14), 8174–8183.

Shepherd, A., Ivins, E., Rignot, E., Smith, B., van den Broeke, M., Velicogna, I., Whitehouse, P., Briggs, K., Joughin, I., Krinner, G., Nowicki, S., Payne, T., Scambos, T., Schlegel, N., A, G., Agosta, C., Ahlstrøm, A., Babonis, G., Barletta, V., … team, T. I. (2018). Mass balance of the Antarctic Ice Sheet from 1992 to 2017. *Nature*, *558*(7709), 219–222. https://doi.org/10.1038/s41586-018-0179-y

Siegert, M. J., & Dowdeswell, J. A. (2004). Numerical reconstructions of the Eurasian Ice Sheet and climate during the Late Weichselian. *Quaternary Science Reviews*, *23*(11–13), 1273–1283.

Simms, A. R., Best, L., Shennan, I., Bradley, S. L., Small, D., Bustamante, E., Lightowler, A., Osleger, D., & Sefton, J. (2022). Investigating the roles of relative sea-level change and glacio-isostatic adjustment on the retreat of a marine based ice stream in NW Scotland. *Quaternary Science Reviews*, *277*, 107366. https://doi.org/10.1016/j.quascirev.2021.107366

Simon, K. M., & Riva, R. E. M. (2020). Uncertainty Estimation in Regional Models of Long-Term GIA Uplift and Sea Level Change: An Overview. *Journal of Geophysical Research: Solid Earth*, *125*(8), e2019JB018983. https://doi.org/https://doi.org/10.1029/2019JB018983

Simon, K. M., Riva, R. E. M., & Broerse, T. (2022). Identifying geographical patterns of transient deformation in the geological sea level record. *Journal of Geophysical Research: Solid Earth*, *127*(7), e2021JB023693.

Simon, K. M., Riva, R. E. M., & Vermeersen, L. L. A. (2021). Constraint of glacial isostatic adjustment in the North Sea with geological relative sea level and GNSS vertical land motion data. *Geophysical Journal International*, *227*(2), 1168–1180. https://doi.org/10.1093/gji/ggab261

Simon, K., & Riva, R. (2020). Constraint of GIA in Northern Europe with Geological RSL and VLM Data. *EGU General Assembly*, 19774.

Spada, G. (2017). Glacial Isostatic Adjustment and Contemporary Sea Level Rise: An Overview. In A. Cazenave, N. Champollion, F. Paul, & J. Benveniste (Eds.), *Integrative Study of the Mean Sea Level and Its Components* (pp. 155–187). Springer International Publishing. https://doi.org/10.1007/978-3-319-56490-6_8

Spada, G., Barletta, V. R., Klemann, V., Riva, R. E. M., Martinec, Z., Gasperini, P., Lund, B., Wolf, D., Vermeersen, L. L. A., & King, M. A. (2011). A benchmark study for glacial isostatic adjustment codes. *Geophysical Journal International*, *185*(1), 106–132.

Spada, G., & Galassi, G. (2012). New estimates of secular sea level rise from tide gauge data and GIA modelling. *Geophysical Journal International*, *191*(3), 1067–1094. https://doi.org/10.1111/j.1365-246X.2012.05663.x

Stacey, F. D., & Davis, P. M. (2008). *Physics of the Earth*. Cambridge University Press.

Steffen, H., Denker, H., & Müller, J. (2008). Glacial isostatic adjustment in Fennoscandia from GRACE data and comparison with geodynamical models. *Journal of Geodynamics*, *46*(3), 155–164. https://doi.org/https://doi.org/10.1016/j.jog.2008.03.002

Steffen, H., & Kaufmann, G. (2005). Glacial isostatic adjustment of Scandinavia and northwestern Europe and the radial viscosity structure of the Earth's mantle. *Geophysical Journal International*, *163*(2), 801–812. https://doi.org/10.1111/j.1365-246X.2005.02740.x

Steffen, H., Kaufmann, G., & Wu, P. (2006). Three-dimensional finite-element modeling of the glacial isostatic adjustment in Fennoscandia. *Earth and Planetary Science Letters*, *250*(1–2), 358–375. https://doi.org/10.1016/j.epsl.2006.08.003

Steffen, H., & Wu, P. (2011). Glacial isostatic adjustment in Fennoscandia-A review of data and modeling. In *Journal of Geodynamics* (Vol. 52, Issues 3–4, pp. 169–204). https://doi.org/10.1016/j.jog.2011.03.002

Tamisiea, M. E., Mitrovica, J. X., & Davis, J. L. (2007). GRACE gravity data constrain ancient ice geometries and continental dynamics over Laurentia. *Science*, *316*(5826), 881–883.

Tanaka, Y., Klemann, V., Fleming, K., & Martinec, Z. (2009). Spectral finite element approach to postseismic deformation in a viscoelastic self-gravitating spherical Earth. *Geophysical Journal International*, *176*(3), 715–739.

Tarasov, L., Dyke, A. S., Neal, R. M., & Peltier, W. R. (2012). A data-calibrated distribution of deglacial chronologies for the North American ice complex from glaciological modeling. *Earth and Planetary Science Letters*, *315*, 30–40.

Tesauro, M., Kaban, M. K., & Cloetingh, S. A. P. L. (2009). A new thermal and rheological model of the European lithosphere. *Tectonophysics*, *476*(3), 478–495. https://doi.org/https://doi.org/10.1016/j.tecto.2009.07.022

Thompson, W. B., Griggs, C. B., Miller, N. G., Nelson, R. E., Weddle, T. K., & Kilian, T. M. (2011). Associated terrestrial and marine fossils in the late-glacial Presumpscot Formation, southern Maine, USA, and the marine reservoir effect on radiocarbon ages. *Quaternary Research*, *75*(3), 552–565.

Trampert, J., & Van Der Hilst, R. D. (2005). Towards a quantitative interpretation of global seismic tomography. *Geophysical Monograph Series*, *160*, 47–62.

Turcotte, D. L., & Schubert, G. (2002). *Geodynamics*. Cambridge university press.

Van Calcar, C. J., Van De Wal, R. S. W., Blank, B., De Boer, B., & Van Der Wal, W. (2023). Simulation of a fully coupled 3D glacial isostatic adjustment–ice sheet model for the Antarctic ice sheet over a glacial cycle. *Geoscientific Model Development*, *16*(18), 5473–5492.

van Casteren, R. (2019). *A 3D Glacial Isostatic Adjustment model for Northwestern Europe*. MSc dissertation, Delft University of Technology

van der Wal, W., Barletta, V., Nield, G., & van Calcar, C. (2023). Glacial isostatic adjustment and post-seismic deformation in Antarctica. *The Geochemistry and Geophysics of the Antarctic Mantle, Geological Society, London, 56(1), 315-341, https://doi.org/10.1144/m56-2022-13*

Van Der Wal, W., Barnhoorn, A., Stocchi, P., Gradmann, S., Wu, P., Drury, M., & Vermeersen, B. (2013). Glacial isostatic adjustment model with composite 3-D Earth rheology for Fennoscandia. *Geophysical Journal International*, *194*(1), 61–77. https://doi.org/10.1093/gji/ggt099

Van Der Wal, W., & IJpelaar, T. (2017). The effect of sediment loading in Fennoscandia and the Barents Sea during the last glacial cycle on glacial isostatic adjustment observations. *Solid Earth*, *8*(5), 955–968.

van der Wal, W., Whitehouse, P. L., & Schrama, E. J. O. (2015a). Effect of GIA models with 3D composite mantle viscosity on GRACE mass balance estimates for Antarctica. *Earth and Planetary Science Letters*, *414*, 134–143.

van der Wal, W., Whitehouse, P. L., & Schrama, E. J. O. (2015b). Effect of the GIA models with 3D composite mantle viscosity on GRACE mass balance estimates for Antarctica. *Earth and Planetary Sciences Letters*, *414*, 134–143.

van der Wal, W., Wu, P., Sideris, M. G., & Shum, C. K. (2008). Use of GRACE determined secular gravity rates for glacial isostatic adjustment studies in North-America. *Journal of Geodynamics*, *46*(3–5), 144–154.

van der Wal, W., Wu, P., Wang, H., & Sideris, M. G. (2010). Sea levels and uplift rate from composite rheology in glacial isostatic adjustment modeling. *Journal of Geodynamics*, *50*(1), 38–48.

Velicogna, I., Sutterley, T. C., & Van Den Broeke, M. R. (2014). Regional acceleration in ice mass loss from Greenland and Antarctica using GRACE time-variable gravity data. *Geophysical Research Letters*, *41*(22), 8130–8137.

Velicogna, I., & Wahr, J. (2013). Time-variable gravity observations of ice sheet mass balance: Precision and limitations of the GRACE satellite data. *Geophysical Research Letters*, *40*(12), 3055–3063.

Wahl, T., Jensen, J., & Frank, T. (2010). On analysing sea level rise in the German Bight since 1844. *Nat. Hazards Earth Syst. Sci.*, *10*(2), 171–179. https://doi.org/10.5194/nhess-10-171-2010

Wang, H., & Wu, P. (2006). Effects of lateral variations in lithospheric thickness and mantle viscosity on glacially induced relative sea levels and long wavelength gravity field in a spherical, self-gravitating Maxwell Earth. *Earth and Planetary Science Letters*, *249*(3–4), 368–383.

Wang, J., Church, J. A., Zhang, X., Gregory, J. M., Zanna, L., & Chen, X. (2021). Evaluation of the Local Sea-Level Budget at Tide Gauges Since 1958. *Geophysical Research Letters*, *48*(20), e2021GL094502. https://doi.org/https://doi.org/10.1029/2021GL094502

Ward, I., Larcombe, P., & Lillie, M. (2006). The dating of Doggerland–post-glacial geochronology of the southern North Sea. *Environmental Archaeology*, *11*(2), 207–218.

Watts, A. B., Zhong, S. J., & Hunter, J. (2013). The behavior of the lithosphere on seismic to geologic timescales. *Annual Review of Earth and Planetary Sciences*, *41*, 443–468.

Weerdesteijn, M. (2019). *The implementation of glaciation-induced rotational behavior of the Earth in a numerical model.* MSc dissertation, Delft University of Technology

Weerdesteijn, M., Hu, H., van der Wal, W., & Riva, R. (2019). The potential of numerical modeling for glaciation-induced true polar wander of the Earth. *Geophysical Research Abstracts*, *21*.

Whitehouse, P. L., Bentley, M. J., Milne, G. A., King, M. A., & Thomas, I. D. (2012). A new glacial isostatic adjustment model for Antarctica: calibrated and tested using observations of relative sea-level change and present-day uplift rates. *Geophysical Journal International*, *190*(3), 1464–1482. https://doi.org/10.1111/j.1365-246X.2012.05557.x

Whitehouse, P. L., Gomez, N., King, M. A., & Wiens, D. A. (2019). Solid Earth change and the evolution of the Antarctic Ice Sheet. *Nature Communications Volume* , *10*(503).

Wolstencroft, M., King, M. A., Whitehouse, P. L., Bentley, M. J., Nield, G. A., King, E. C., McMillan, M., Shepherd, A., Barletta, V., & Bordoni, A. (2015). Uplift rates from a new high-density GPS network in Palmer Land indicate significant late Holocene ice loss in the southwestern Weddell Sea. *Geophysical Journal International*, *203*(1), 737–754.

Wong, M. C., & Wu, P. (2019). Using commercial finite-element packages for the study of Glacial Isostatic Adjustment on a compressible self-gravitating spherical earth–1: harmonic loads. *Geophysical Journal International*, *217*(3), 1798–1820.

Wu, P. (2023). *Sensitivity of GIA Observations on 3D Viscosity Variations: Perturbation Method versus Adjoint Method*.

Wu, P. (2001). Postglacial induced surface motion and gravity in Laurentia for uniform mantle with power-law rheology and ambient tectonic stress. *Earth and Planetary Science Letters*, *186*(3–4), 427–435.

Wu, P. (2002). Mode coupling in a viscoelastic self-gravitating spherical earth induced by axisymmetric loads and lateral viscosity variations. *Earth and Planetary Science Letters*, *202*(1), 49–60. https://doi.org/https://doi.org/10.1016/S0012-821X(02)00750-1

Wu, P. (2004). Using commercial finite element packages for the study of earth deformations, sea levels and the state of stress. *Geophysical Journal International*, *158*(2), 401–408.

Wu, P., Wang, H., & Steffen, H. (2013). The role of thermal effect on mantle seismic anomalies under Laurentia and Fennoscandia from observations of Glacial Isostatic Adjustment. *Geophysical Journal International*, *192*(1), 7–17. https://doi.org/10.1093/gji/ggs009

Yousefi, M., Milne, G. A., & Latychev, K. (2021). Glacial isostatic adjustment of the Pacific Coast of North America: the influence of lateral Earth structure.

Geophysical Journal International, *226*(1), 91–113. https://doi.org/10.1093/gji/ggab053

Yuen, D. A., Sabadini, R. C. A., Gasperini, P., & Boschi, E. (1986). On transient rheology and glacial isostasy. *Journal of Geophysical Research: Solid Earth*, *91*(B11), 11420–11438.

Zhang, R. (2005). *Numerical Simulation of Solid-state Sintering of Metal Powder Compact Dominated by Grain Boundary Diffusion*. Doctoral Dissertation, Penn State.

Zhong, S., Kang, K., A, G., & Qin, C. (2022). CitcomSVE: A Three-Dimensional Finite Element Software Package for Modeling Planetary Mantle's Viscoelastic Deformation in Response to Surface and Tidal Loads. *Geochemistry, Geophysics, Geosystems*, *23*(10), e2022GC010359. https://doi.org/https://doi.org/10.1029/2022GC010359

Zhong, S., Paulson, A., & Wahr, J. (2003). Three-dimensional finite-element modelling of Earth's viscoelastic deformation: effects of lateral variations in lithospheric thickness. *Geophysical Journal International*, *155*(2), 679–695.

Zienkiewicz, O. C., Taylor, R. L., & Zhu, J. Z. (2005). *The finite element method: its basis and fundamentals*. Elsevier.

Curriculum vitae

Experience

Utrecht University, Physics Department
07/2024 – Present
Post-doc
Topic: Modelling surging tide-water glaciers

Het Cristelijk Lyceum Delft
12/2022 – 07/2024
Mathematics teacher

Instituut voor Publieke Sector Efficiëntie (IPSE) Studies
01/2020 – 12/2021
Researcher (0.4 fte)
Topic: Efficiency research on ministries and implementation bodies of the public sector

TU Delft, Faculty of Aerospace Engineering
09/2015 – 03/2025
PhD Candidate
Topic: Glacial Isostatic Adjustment models with 3D rheology for Europe and Antarctica

Het Lyceum Vos
08/2014 – 12/2014
Mathematics teacher

Royal Observatory of Belgium
11/2013 – 02/2014
Intern
Topic: Implementation of a thin shell model for Martian edifices

Education

Master of Science (MSc), Aerospace engineering, Delft University of Technology	**2011-2015**
Bachelor of Science (BSc), Aerospace engineering, Delft University of Technology	**2007-2011**
Bachelor of Education (Bed), Mathematics, Delft University of Technology	**2010-2011**

Publications

Journal publications

Uplift and RSL data constraints on 3D upper mantle viscosity in Northern Europe (TBP)

B Blank, S L Bradley, W van der Wal

Geophysical Journal International, -

Two phases of accelerated sea-level rise in the Early Holocene revealed from North Sea peats (TBP)

Hijma, **Blank**, Bradley, Cohen, Van der Wal, Barlow, Frechen, Hennekam, …

Nature, -

Simulation of a fully coupled 3D glacial isostatic adjustment–ice sheet model for the Antarctic ice sheet over a glacial cycle (2023)

CJ Van Calcar, RSW Van De Wal, **B Blank**, B De Boer, W Van Der Wal

Geoscientific Model Development 16 (18), 5473-5492

A global, spherical finite-element model for post-seismic deformation using *Abaqus* (2022)

GA Nield, MA King, R Steffen, **B Blank**

Geoscientific Model Development 15 (6), 2489-2503

Effect of lateral and stress-dependent viscosity variations on GIA induced uplift rates in the Amundsen Sea Embayment (2021)

B Blank, V Barletta, H Hu, F Pappa, W van der Wal

Geochemistry, Geophysics, Geosystems 22 (9), e2021GC009807

The impact of lateral variations in lithospheric thickness on glacial isostatic adjustment in West Antarctica (2018)

GA Nield, PL Whitehouse, W van der Wal, **B Blank**, JP O'Donnell, ...

Geophysical Journal International 214 (2), 811-824

Conference Contributions

A 3D lithospheric model of Antarctica and its implications on mantle viscosity (2018)

F Pappa, J Ebbing, F Ferraccioli, W van der Wal, **B Blank**

EGU General Assembly Conference Abstracts, 4939

Simulating the evolution of the Antarctic Ice Sheet including 3D GIA feedback during the Last Glacial Cycle (2022)

C van Calcar, R van de Wal, **B Blank**, B de Boer, W van der Wal

EGU General Assembly Conference Abstracts, EGU22-4786

The effect of the GIA feedback loop on the evolution of the Antarctic Ice sheet over the last glacial cycle using a coupled 3D GIA-Ice Dynamic model (2021)

C van Calcar, B de Boer, **B Blank**, R van de Wal, W van der Wal

EGU General Assembly Conference Abstracts, EGU21-15773

Feedback between ice dynamics and bedrock deformation with 3D viscosity in Antarctica (2020)

W van der Wal, C van Calcar, B de Boer, **B Blank**

EGU2020

a New Method to Simulate the Antarctic Ice Sheet Over the Last Glacial Cycle Using a Coupled 3d Gia–Ice Dynamic Model (2020)

CJ van Calcar, B de Boer, **B Blank**, W van der Wal

Geological Society of America Abstracts 52, 359854

The influence of high resolution 3D Earth structure in West Antarctica on Glacial Isostatic Adjustment (2018)

G Nield, P Whitehouse, W van der Wal, **B Blank**, A Lloyd, D Wiens, ...

EGU General Assembly Conference Abstracts, 634

A 3D Finite Element Model with Improved Spatial Resolution to Investigate the Effect of Varying Viscosity on Antarctica (2017)

B Blank, W van der Wal, F Pappa, J Ebbing

AGU Fall Meeting Abstracts 2017, G21B-0865

The Sensitivity of Glacial Isostatic Adjustment in West Antarctica to Lateral Variations in Earth Structure (2017)

G Nield, PL Whitehouse, **B Blank**, W van der Wal, JP O'Donnell, ...

AGU Fall Meeting Abstracts 2017, G12A-05

A benchmark study of the sea-level equation in GIA modelling (2017)

Z Martinec, V Klemann, W van der Wal, R Riva, G Spada, K Simon, ... , **B Blank**, …

EGU General Assembly Conference Abstracts, 8681

Linking GIA and Lithospheric Structure of Antarctica with Satellite Gravity Gradients (2017)

J Ebbing, F Pappa, V Barletta, **B Blank**, F Ferraccioli, R Forsberg, ...

4th Swarm Science Meeting & Geodetic Missions Workshop

A 3D INTEGRATED LITHOSPHERIC MODEL OF ANTARCTICA AND ITS IMPACT ON GIA ESTIMATES (2017)

F Pappa, J Ebbing, F Ferraccioli, W van der Wal, **B Blank**

Polar Systems under Pressure, 141